Properties and Interactions of Type III Intermediate Filaments with CRYAB

ELLIOTT, JAYNE,LOUISE

Abstract

Properties and Interactions of Type III Intermediate Filaments with CRYAB

Jayne L Elliott

Glial fibrillary acidic protein is a type three intermediate filament found within astrocytes in the central nervous system and mutations have been found as the cause of Alexander disease, resulting in protein aggregates of Rosenthal fibers with αB-crystallin. Here two glial fibrillary acidic protein mutants of R79C and R239H, located in the LNDR and rod 2A domain respectively, were assembled *in vitro* and their morphology, assembly competence and interactions with αB-crystallin were assessed. Both mutants were unable to form usual filament lengths but instead were similar to unit length filaments with R239H forming aggregates due to such high protein interactions and the R79C mutant having much lower assembly competent protein interactions. R239H had a much greater affinity for αB-crystallin, likely a reflection that it has one of the most severe phenotypes. An absence of divalent cations equally affected GFAP assembly resulting in compromised compaction and increased filament-filament interactions. The R120G αB-crystallin mutant results in cardiomyopathy and cataract due to aberrant interactions with desmin intermediate filaments, due to an increased oligomer size and therefore these interactions were studied and compared to wild-type interactions. Temperature and pH also alter the oligomer size of αB-crystallin and were therefore investigated with αB-crystallin-type III intermediate filament interactions. It was found that ischemic conditions and increased temperatures promote their association, demonstrated by increased co-pelleting under high speed sedimentations. There was a preference for binding to desmin filaments thus showing how desmin-wild-type αB-crystallin interactions are important for homeostasis in muscle. Passive microrheology was used to complement this and investigate how αB-crystallin may be modulating desmin filaments under equilibrium. From these experiments wild-type αB-crystallin reduced the frequency-dependent passive viscosity $\eta(f)$ and the G', whereas the cardiomyopathy- and cataract- causing R120G mutant increased the $\eta(f)$.

Properties and Interactions of Type III Intermediate Filaments with CRYAB

Jayne L Elliott

A thesis submitted at Durham University for the Degree of Doctor of Philosophy

Department of Biological and Biomedical Sciences

Durham University, September 2012

Table of contents

List of tables

List of figures

List of abbreviations

Ab	antibody
Aβ	β-amyloid peptide
AD	Alzheimer's disease
ADPRT	mono-ADP-ribosyltransferase
AFM	atomic force microscope
ALS	amyotrophic lateral sclerosis
AMPARS	AMPA-type glutamate receptors
AOD	acoustic optical deflector
AxD	Alexander disease
BCA	bichinchoninic acid
BFA	brefeldin A
BFSP1	beaded filament structural protein 1
BFSP2	beaded filament structural protein 2
CaMKII	calcium/calmodulin-dependent protein kinase II
CCP	caspase-cleavage product
cdk-5	cyclin-dependent kinase 5
CMT	Charcot-Marie-Tooth disease
CNS	central nervous system
CoM	centre-of-mass
CRYAB	αB-crystallin
DC	direct current
DCM	dilated cardiomyopathy
DLS	dynamic light scattering
DTT	dithiothreitol
DWS	diffusing-wave-spectroscopy
EAAT2	excitatory amino acid transporter 2
EBS	epidermolysis bullosa simplex
eccDNA	extrachromosomal circular DNA
ECM	extracellular matrix
EDTA	ethylenediaminetetraacetic acid
EF1α	elongation factor 1 alpha
EMD	Emery-Dreifuss muscular dystrophy
ER	endoplasmic reticulum

FDT	fluctuation-dissipation theorem
FPLD	Dunnigan-type familial partial lipodystrophy
FRET	fluorescence resonance energy transfer microscopy
G'	real storage modulus
G''	imaginary loss modulus
GFAP	glial fibrillary acidic protein
GSER	generalised Stokes-Einstein relation
HEPES	4-(2-Hydroxyethyl)piperazine-1-ethanesulfonic acid
HFS	high-frequency stimulation
HGPS	Hutchinson-Gilford progeria syndrome
Hr	hour
HSB	high salt buffer
I	ionic strength
IFs	intermediate filaments
INM	inner nuclear membrane
IPD	idiopathic Parkinson's disease
IPTG	isopropyl β-D-1-thiogalactopyranoside
IR	infrared
LB	Luria broth
LFS	low-frequency stimulation
LGMD1B	limb girdle muscular dystrophy type 1B
LTD	long term depression
LTP	long term potentiation
MFs	microfilaments
mGluRs	metabotropic glutamate receptors
Min	minutes
Mj	*Methanococcus jannaschii*
MS	multiple sclerosis
MSD	mean square displacement
MTs	microtubules
MWCO	molecular weight cut-off
NA	numerical aperture
NEF	nucleotide exchange factor
NFs	neurofilaments

NF-H	neurofilament heavy
NF-L	neurofilament light
NF-M	neurofilament medium
NLS	nuclear localisation signal
M-domain	middle domain
Para-	parallel
PBS	phosphate buffered saline
PD	Parkinson's disease
PEG-PLL	PLL(20)-g[3.5]-PEG(2)
PEI	polyethyleneimine
Perp-	perpendicular
p-INV	protostomic invertebrate
PMSF	phenylmethanesulfonyl fluoride
QPDs	quadrant photo diodes
SAXS	small angle X-ray scattering
SB	sample buffer
SBD	substrate binding domain
SD	standard deviation
SDS	sodium-dodecyl sulphate
SDS-PAGE	sodium dodecyl sulfate polyacrylamide gel electrophoresis
Sec	seconds
sHSP	small heat shock protein
TCP-1	t-complex polypeptide 1
TEM	transmission electron microscope
TEMED	N,N,N'N'-tetramethylethylenediamine
TEN	Tris, EDTA and NaCl
Tris	tris(hydroxy-methyl)aminomethane
ULFs	unit length filaments
UV	ultraviolet
V	volts
WT	wild-type
WWS	Walker-Warburg syndrome

Declaration

I declare that the material contained in this thesis hasn't been previously submitted for a higher degree and that the experiments described in this thesis were carried out by myself.

Jayne Elliott

Acknowledgements

A great thank you to my supervisor Roy Quinlan for his help and guidance throughout my studies.

I would like to thank John Girkin (University of Durham, UK) and Gijsje Koenderink (FOM Institute AMOLF, NL) for their collaboration and giving me the opportunity to work in their laboratories. Special thanks to Scott Silburn (University of Durham, UK) for his invaluable help in providing data analysis scripts and discussions on optical trapping and Karin Jansen (FOM Institute AMOLF, NL) who showed me how to use the ProteinScope for optical trapping and explained the data analysis methods.

Special thanks also go to Ming Der Perng, Andrew Landsbury, Antal Tapodi, Frederique Tholozan, Terry Gibbons and Weiju Wu who worked in the laboratory and contributed to useful discussions throughout my PhD.

Thanks also to my family and friends for being supportive.

Chapter 1; Introduction

1.1 Intermediate filament (IF) structure.

There are three main cytoskeleton networks found within metazoan cells that consist of actin microfilaments (MFs) responsible for cell motility, microtubules (MTs) that enable cell division and IFs (Bayless and Johnson, 2011). IFs were initially identified by Ishikawa et al. in 1968 within myogenic cells localised between myofibrils and this was also the first IF to be sequenced fully as the desmin IF (Geisler and Weber, 1982, Ishikawa et al., 1968). There are about 70 different genes that encode for IFs highlighting that it is a large protein family (Szeverenyi et al., 2008). IFs were originally considered as being just scaffolds within cells but now it appears that they are also involved with bearing stress and thus also act to provide the cell with support against mechanical stress. There are six well known main types of IF I-VI (Omary, 2009) with type VII and VIII having filaments that share similar characteristics with previous types and they are very dynamic structures with variable mass-per-lengths (Engel A, 1985). IFs share a common structure of a central α-helical rod domain with an N-terminal head domain and C-terminal tail region, both of which are non-α-helical. The rod domain is composed of four major units of 1A, 1B, 2A and 2B, with three linker domains of L1, L1-2 and L2 to connect them, as shown in Figure 1.1 (Parry and Steinert, 1995). LNDR and YRKLLEGE motifs are located at the beginning of rod 1 and the end of rod 2, respectively. These are conserved across all IFs and are essential for assembly competence. Found within the type III IFs there is an RP box (RLSL-RM-PP) located at the end of the head domain that contains phosphorylation and proteolytic cleavage sites (Ralton et al., 1994). A pre-coil domain is also found within glial fibrillary acidic protein (GFAP) at the beginning of the rod 1A region, in common with the other IFs (Strelkov et al., 2002). In contrast to other IFs, nuclear lamins contain a nuclear localisation sequence (NLS) that accommodates interactions with chromatin and a globular domain at its centre, which is in addition to the chromatin binding site present in the rod domain (Glass et al., 1993). These features are common to all lamins except the CaaX sequence is present only in lamins A, B1 and B2 since lamin C is a truncated splice variant of lamin A with an alternative ending. There are two other minor forms of lamins, which include lamin C2 and AΔ10 (Nakajima and Abe, 1995, Machiels et al., 1996). The globular domain has Ig folds consisting of nine β-

strands and binds to chromatin, however it works in concert with the NLS and itself requires a positive charge. Mutations in the globular domain have been linked to Dunnigan-type familial partial lipodystrophy (FPLD) (Stierle et al., 2003). There are six additional heptad repeats in coil 1B which makes the rod domain 42 amino acids longer in all of the lamins (Conway and Parry, 1988). A variant of chick CP49 known as CP49ins has been discovered with a similar 41 amino acid insertion in coil 1B which is the first discovery of a vertebrate IF with a lamin-like insertion resulting in a 5-6 nm extension of the rod domain (Sawada et al., 1995). Lamins also have a predicted rod domain, which is entirely α-helical, unlike IF types I-IV, which are predicted to have non-α-helical linkers in the rod domain (Conway and Parry, 1988). The N-terminal head domain of lamins is also different to other IFs with a lower quantity of basic amino acids in a shorter spanning length.

Nestin and synemin, as with lamins, have a longer C-terminal tail domain, with synemin also having a shortened head domain. NF-M and NF-H also have a long tail domain although unlike the tail in lamins containing many domains for specialised interactions, neurofilament (NF) tail regions do not appear to have such specific binding regions however NF-M and NF-H have repeats of Lys-Ser-Pro, which are sites for phosphorylation from Erk1 and 2 (Veeranna et al., 1998). Synemin has similarities to type III IFs but the beginning of the 2A rod domain and the head domain are different, with a very short head domain. NFs consist of three main groups of NF light (NF-L), NF medium (NF-M) and NF heavy (NF-H) chains. Their structures differ to other IFs with having a much longer tail region and the chain weight corresponds to the length of the tails with NF-L having the shortest and NF-H having the longest. Type VII IFs include filensin and CP49. CP49 is closely related to type I keratins, specifically K18 (Pittenger et al., 2007), despite having a divergence from conserved motifs with cytokeratins and the absence of a C-terminal tail region, although keratin 19 also lacks a C-terminal tail. However filensin is likely to be a novel IF, although is most closely related to type II keratins (Hess et al., 1998). Filensin also differs from other IFs with a shortened rod domain, by 29 amino acids, within helix 2 and a much shorter head domain (Gounari et al., 1993).

Nematodes and mollusks of protostomes have an extended 1B coil domain and a lamin-homologous section within their C-terminal tail, which lacks the usual NLS and CaaX box observed in lamins (Bovenshulte et al., 1995). Thus, protostomic invertebrate (p-INV) IFs have a longer rod domain due to extra amino acids in the

1B domain, in common with nuclear lamins, compared to other IFs (Geisler et al., 1998).

Type	Proteins
I	Acidic keratins simple epithelial (K18-21, K23-28) stratified epithelial (K9-17) hair keratins (K31-40)
II	Neutral and basic keratins simple epithelial (K7-8, K71-75) stratified epithelial (K1-7, K76-80) hair keratins (K81-86)
III	GFAP, desmin, vimentin, peripherin, syncoilin
IV	NFs, α-internexin
V	Lamins
VI	Nestin, synemin
VII	Filensin/beaded filament structural protein 1 (BFSP1) and CP49/ beaded filament structural protein 2 (BFSP2)
VIII	Invertebrate IF proteins (both protostomic and deuterostomic)

Table 1.1 **IF types**.

BFSP1 and 2 are categorised in an "orphan" class VII and invertebrate IFs have been placed in class VIII. Keratins are the only IFs spanning two different classes (I and II).

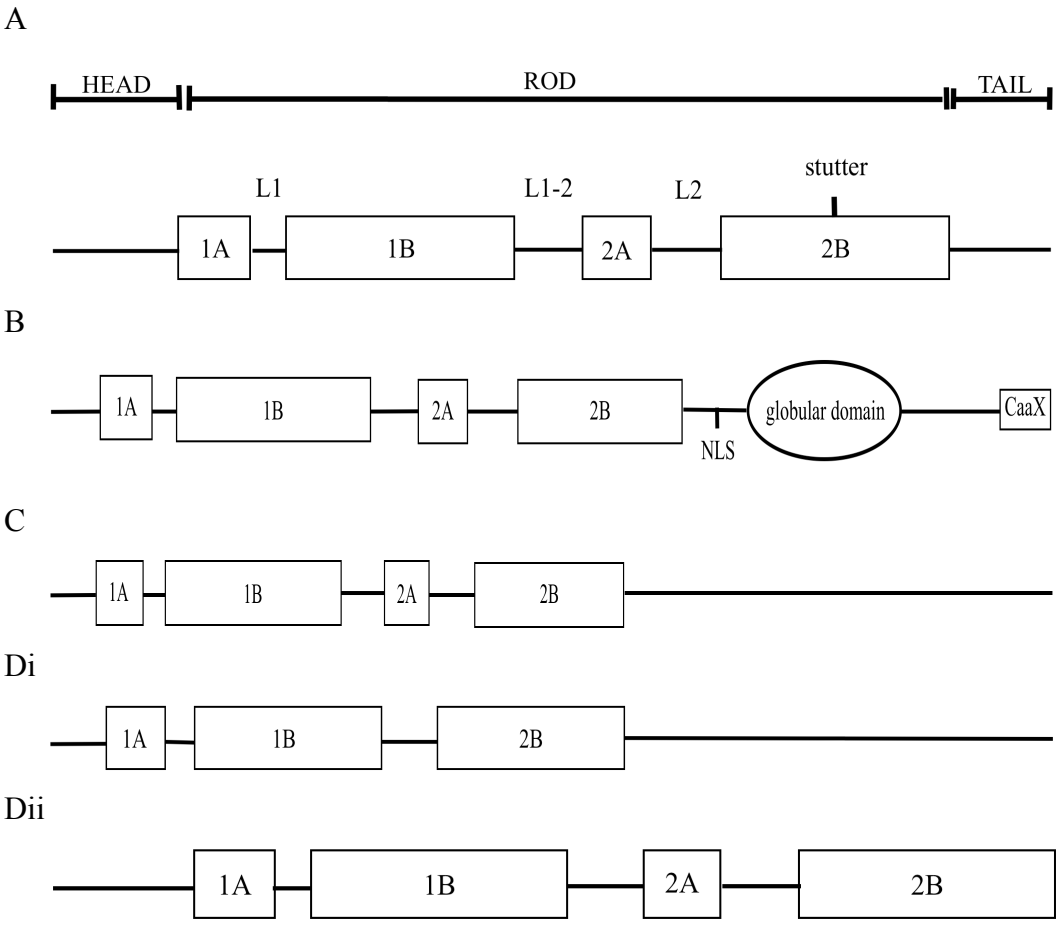

Figure 1.1 General structures of IF proteins.

IF monomers are comprised of a rod domain with four left-handed coiled coils of 1A, 1B, 2A and 2B, separated by linkers of L1, L1-2 and L2. Region 2B also contains a centralised stutter, which is conserved across all IFs (Conway and Parry, 1988). An N-terminal head and C-terminal tail region, both of which are globular structures, flank the rod domain. Each monomer forms a right-handed α-helix. Two monomers form a dimer with a left-handed α-helix and the tetramers (protofilaments) form left-handed coils. Finally the tetramers anneal to produce an overall right-handed coiled-coil structure (Parry and Steinert, 1995). A) The general structure of IFs in groups I-IV is shown (NF-L is represented but NF-M and NF-H have longer C-terminal tails) alongside B) the general structure of group V lamins with the 42 amino acid extension of coil 1B, a globular C-terminal tail domain, a CaaX box and a NLS, C) group VI nestin with a long tail region which is 1306 amino acids in the human sequence and synemin is similar with a tail domain of approximately 1250 amino acids in humans and a very short head domain of 11 amino acids and thus both proteins have a C-terminal tail 8-10 times longer than other IFs apart from NF-

H and also D) i BFSP1 with a shortened helix 2 and long tail and ii BFSP2 with the absence of a C-terminal tail domain and a long head domain. The different domains within each IF type are to approximate proportions, within each individual IF class.

1.2 IFs; locations, functions and disease.

Type III IFs are the main focus of this study and will be discussed initially, looking specifically at GFAP, desmin and vimentin, alongside overviews of the other types of IFs. GFAP mutants and the CRYAB mutant that are studied in this thesis will also be mentioned. All IFs are tissue-specific and as demonstrated in the following sections, mutations in IFs are useful for diagnostic pathology (Omary, 2009).

GFAP is usually found within glial cells but has other locations such as in retinal astrocytes (Bozˇanic´ et al., 2006, Bongcam-Rudloff E, 1991). Its stage of initial expression within the nervous system occurs in radial glia that are responsible for dendrite and axon growth and neuronal migration, replacing vimentin near the end of gestation and then in astrocytes where it also gradually replaces vimentin levels (Middeldorp and Hol, 2011, McCall et al., 1996). Its function is not fully understood although it has been linked to regulating many different aspects within the central nervous system (CNS), such as blood brain barrier maintenance and involvement in plasticity of the brain such as with decreases in the strength of synapses known as long-term depression (LTD) and increases in the strength of synapses, known as long-term potentiation (LTP) (Hughes et al., 2004). Both LTD and LTP are involved in loss and gain of memory and learning processes, respectively. LTD can be activated by many different receptors; metabotropic glutamate receptors (mGluRs) are a common mechanism and are activated by paired-pulse low-frequency stimulation (LFS) in the hippocampus and in the cerebellum requires the combination of parallel and climbing fibre stimulation leading to parallel fibre-Purkinje cell LTD (Ito and Kano, 1982, Brasno and Otis, 2001). LTP results from pre-synaptic high-frequency stimulation (HFS) where calcium enters the post synapse and binds to calmodulin thus activating calcium/calmodulin-dependent protein kinase II (CaMKII), resulting in phosphorylation of AMPA-type glutamate receptors (AMPARs). This increases conductivity and also phosphorylation of stargazin, which enables more AMPARs to traffic to the synapse (Lengyel et al., 2004). When GFAP is absent in astrocytes, there is an increase in synaptic plasticity

(changes in structure and function of synapses) and LTP, shown in GFAP null mice. However CNS morphology and development are the same as wild-type (WT) control mice (McCall et al., 1996). There is a reduction in cerebellar LTD in GFAP null mice, which is likely due to an increase in the astrocytic excitatory amino-acid transporter 2 (EAAT2) protein, responsible for glutamate uptake from synapses (Hughes et al., 2004). However in the hippocampus there is not the same increase in EAAT2 protein (glutamate transporter) expression at synapses, despite EAAT2 total protein levels having been increased, thus showing that the absence of GFAP has inhibited the usual trafficking of EAAT2 to the surface of the cells (Hughes et al., 2004). GFAP levels are also altered in reactive gliosis, which is associated with an upregulation in GFAP levels, in response to brain insult (Vargova and Sykova, 2009). As well as the levels of GFAP protein being linked to different pathological states, mutations in GFAP have been linked to Alexander disease (AxD), which is discussed in more detail in section 1.5. GFAP filaments have also been linked to inhibition of GTP-dependent chaperone-mediated autophagy and potential upregulation of macroautophagy, as seen with AxD when GFAP levels are high (Bandyopadhyay et al., 2010). The presence of GFAP within astrocytes is important for modifying the extracellular matrix (ECM) and its absence leads to a more homogenous laminin distribution, contrasting +/+ cells that have laminin expressed in only certain cells, which influences astroglial differentiation (Menet et al., 2001). Within reactive astrocytes (injured astrocytes found in glial scars), GFAP is responsible for their positioning during prion disease. Demonstrated by the irregular constricted processes in reactive astrocytes with few glial filaments compared to extended processes in normal astrocytes rich in glial filaments (Gomi et al., 2010). GFAP is also always an assembly partner of vimentin and in its absence leads to collapse of vimentin networks (Eliasson et al., 1999).

Desmin is found within muscle fibers and acts to provide mechanical support and integrity (Chen et al., 2003). One of the main roles is to provide force transmission within striated muscle fibers by attaching and aligning sarcomeres (Shah et al., 2012). It also aids in positioning of costameres, which are the sites where the sarcolemma makes contact with the internal myofibrils (Pardo et al., 1983). Mutations in desmin have been linked with myopathies, including skeletal and cardiac and the mutant protein is seen to form aggregates as opposed to normal 10 nm filaments in some cases and other mutations result in assembly-incompetent

protein. Desminopathies are classed as part of the myofibrillar myopathies and result in weakening of muscles, including respiratory and heart if cardiomyopathy is present, in patients and is characterised by accumulated protein aggregates (Selcen et al., 2004). Some of the most severe mutations occur in the N-terminal head domain in the nonapeptide motif "SSYRRTFGG", which is highly conserved between vimentin and desmin, as shown by aggregate formation for the S13F and R16C desmin mutants (Sharma et al., 2009). K8 and 19 also form filaments at costameres, which they organise but are distinct from desmin as they are more important for sarcolemmal stability, whereas desmin is primarily involved in force transmission (Lovering et al., 2011). Desmin interacts with many other cytoskeletal proteins at the costameres, such as plectin and syncoilin (Moorwood, 2008). Importantly, desmin interacts with αB-crystallin (CRYAB) and mutations in CRYAB such as the R120G mutant are also responsible for cardiomyopathy and lead to aggregates of desmin, which phenocopies the pathology caused by desmin mutations (Perng et al., 2004, Vicart et al., 1998). As well as helping to mediate interactions between myofibrils and other proteins, such as with the dystroglycan protein complex, desmin has been implicated in helping to position nuclei and mitochondria (Shah et al., 2004). Desmin knock-out mice display many phenotypes for a diseased state including cardiac muscle hypertrophy and death. When the desmin null phenotype is rescued by specific targeting of desmin to cardiac tissue only, there is removal of the pathological features, such as calcium deposits, fibrotic lesions, mitochondrial malfunction and misalignment of myofibrils (Weisleder et al., 2004). Desmin has also been found localised in the nuclear matrix alongside lamin B and vimentin is also known to bind to lamin B in mesenchymal nuclear matrices. IF assembly is believed to be initiated (nucleated) from the nuclear membrane (Georgatos et al., 1987).

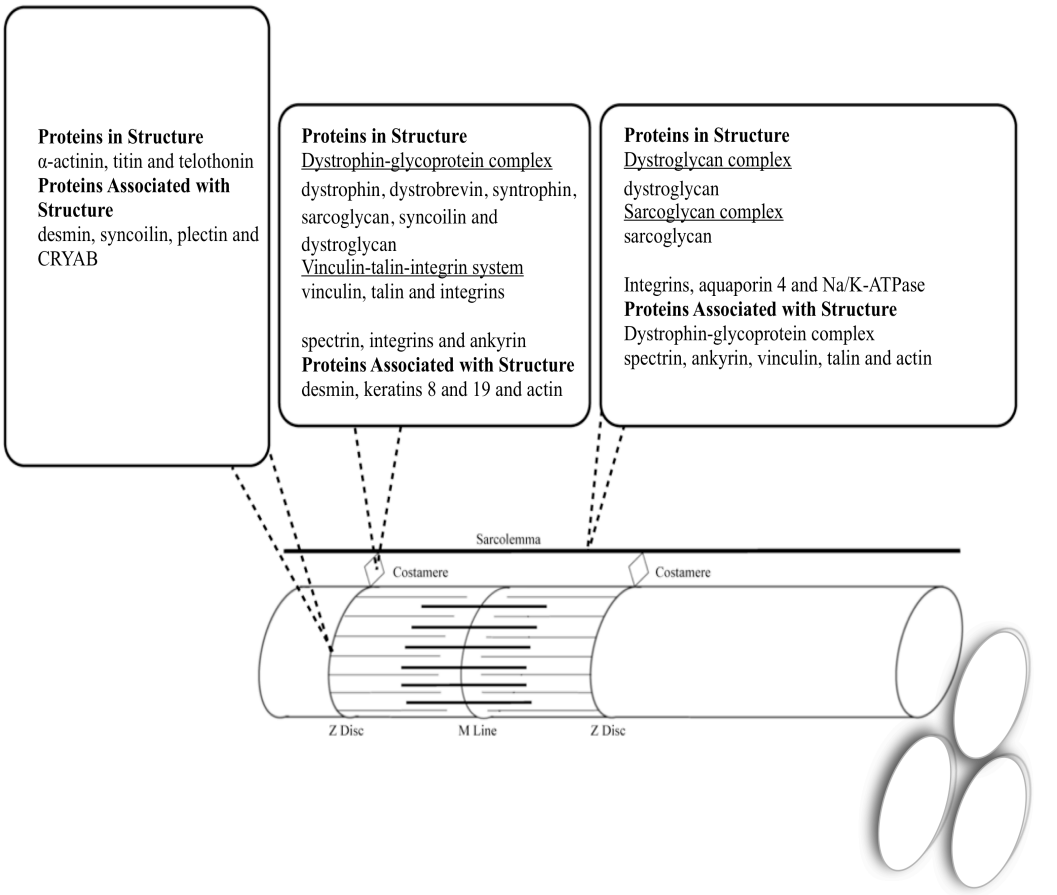

Figure 1.2 Schematic image of skeletal striated muscle and associated proteins.
A single sarcomere (Z-disc to Z-disc) is shown in a myofibril, composed of thin actin filaments attached to Z-discs, which overlap with thick myosin filaments. Magnified views are represented by dashed lines and show cytoskeletal proteins that have been found in these structures, however are unlikely to show all the proteins present especially in the case of the Z-disc which is composed of a large group of different proteins (Zou et al., 2006). Desmin can be seen to be associated with both the Z-disc and costameres.

Vimentin, as mentioned earlier, can be expressed within astrocytes but is found predominantly in cells of embryological mesenchymal origin, such as fibroblasts found in connective tissues, which are the support tissues in the body including blood vessels. There is also a high level of a soluble pool of vimentin in the lens in the differentiated fiber cells and undifferentiated lens epithelium and also vimentin filaments in smooth muscle cells as independent or co-dependent populations of filaments with desmin (Nicholl and Quinlan, 1994, Wang et al., 2006). Within smooth muscle cells, vimentin is attached to the desmosomes and downregulation

impairs plakoglobin (a major desmosomal protein) membrane localisation (Wang et al., 2006). Vimentin is associated with cell motility and expression is correlated with invasiveness (Pana et al., 2012). This has been shown by an increase in motility and invasiveness of cancer cells induced by the presence of vimentin (Hendrix et al., 1997). Vimentin is also found in cells responsible for regulation of mechanical stress (Kuna, 2012). The tail region of vimentin is able to bind to actin microfilaments (MFs) but also vimentin is able to bind to the actin-binding protein fimbrin and thus is able to indirectly interact with MFs (Correia et al., 1999, Cary et al., 1994). MTs can also bind to vimentin and this interaction results in collapse (centripetal movement of filaments into a dense coil near the nucleus) of vimentin networks when MTs have depolymerised (Cary et al., 1994). As well as other cytoskeletal proteins, vimentin is able to interact with other cellular structures such as organelles and in particular the Golgi complex (Gao and Sztul, 2001). One recent study showed that vimentin may be responsible for stabilising collagen mRNA levels, by binding to LARP6 at the 5' stem-loop sequence of collagen mRNA and may help to maintain collagen levels (Challa and Stefanovic, 2011). Vimentin can therefore interact specifically with RNA but also DNA (Traub et al., 1983). It is likely that vimentin and GFAP also play roles as nuclear matrix proteins as they have both been shown to be able to bind to DNA Holliday junctions, with a lesser extent with GFAP and they can induce secondary cruciform branch points in DNA, however they can't enter the nucleus and likely therefore interact with DNA during mitosis (Li et al., 2003). After non-ionic detergents have been used on eukaryotic cells, the cytoplasmic IFs remain associated with the outside of the nucleus showing that there is binding occurring. Vimentin is carried into the nucleus via a binding partner, examples of which are oligo $(dG)_{25}$ and double-stranded DNA, such as superhelical extrachromasomal circular DNA (eccDNA) and once in the nucleus it will likely act to help the cell respond to different environmental pressures (Hartig et al., 1998). No diseases have been reported in humans due to mutations in vimentin, however a few studies generating mutated vimentin in regions similar with other IFs associated with disease have shown that vimentin disruption can lead to disease in mice. This was demonstrated with posterior cataracts in the eye lens fibers (Bornheim et al., 2008). Citrullinated vimentin, as mentioned in section 1.4, however has been found associated with rheumatoid arthritis and results in collapse of IF networks (Kuna, 2012).

IF	Function	Disease	Cause/ correlation	Reference
Keratins	Support epithelial cells against stress	Epidermolysis bullosa simplex (EBS) Epidermolytic ichthyosis Palmo-plantar keratoderma	Mutation in: K5 and 15 K1 or 10 K9	(Bchetnia et al., 2012, Ishida-Yamamoto et al., 1995, Chamcheu et al., 2011, Sybert et al., 1999)
Peripherin	Regeneration of axons and neurite elongation	Amyotrophic lateral sclerosis (ALS)	Mutation	(Eriksson et al., 2008, McNulty and Saunders, 1992)
Syncoilin	Lateral force transmission	Congenital muscular dystrophy	Increased levels	(Brown et al., 2005)
NFs	Axon radial growth	Alzheimer's disease (AD) Parkinson's disease (PD) ALS	Lower NF-L Lower NF-L Phosphorylated NFs	(McLachlan et al., 1988, Hill et al., 1993, Manetto et al., 1988)
α-internexin	Axonal outgrowth	Oligodendrogl-iomas	1p19q codeletion	(Ducray et al., 2009)
Lamins	Nuclear shape and stability	Hutchinson-Gilford progeria syndrome (HGPS)	Mutation in LMNA	(Yang et al., 2011)

Table 1.2 **Summary of IFs and associated diseases**.

Here is a summary of IFs, apart from the three studied in this thesis, showing function and correlated disease.

IF	Function	Disease	Cause/ correlation	Reference
Nestin	Promotes muscle differentiation; inhibits pro-apoptotic cdk-5 activity	Pancreatic and breast cancer	Increased levels of nestin	(Su et al., 2011, Sahlgren et al., 2006, Ishiwata et al., 2011)
Synemin	Muscle integrity	Walker-Warburg syndrome (WWS)	Decreased levels of synemin	(Tawk et al., 2003)
BFSP1	Transparency of eye lens	Cataract	BFSP1 mutation	(Ramachandran et al., 2007)
BFSP2	Transparency of eye lens	Cataract	BFSP2 mutation	(Cui et al., 2007)

Table 1.3 **Summary of IFs and associated diseases**.

Here is a continuation of the summary of IFs, apart from the three studied in this thesis, showing function and correlated disease.

Keratin, peripherin, syncoilin, NFs, lamins, nestin, synemin, BFSP1 and BFSP2 disease associations are reviewed in Table 1.2 and 1.3 since the main focus of the thesis is on the type III IFs desmin, GFAP and vimentin.

1.3 IF assembly and influence of divalent ions.

IF assembly occurs in a sequential process and the main theory of assembly involves the initiating building block being the result of hydrophobic interactions and is the dimer, of which two become associated in a tetramer in the A_{11}, A_{22}, A_{12} or A_{CN} conformation (protofilament), experimentally derived c.f. Figure 1.3.

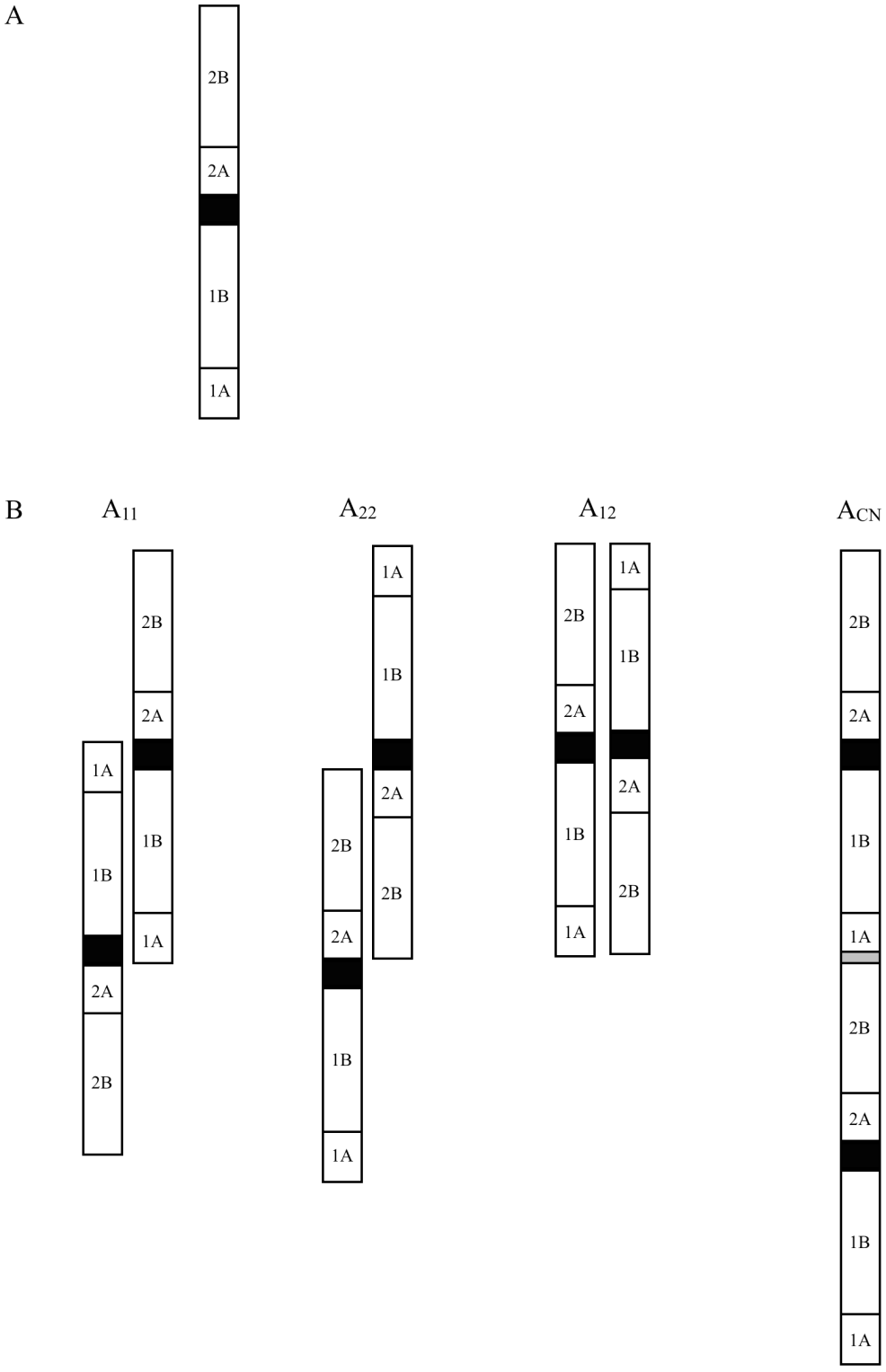

Figure 1.3 Type III and NF IF tetramer assembly.
A) A single α-helical dimer associates B) in either the A_{11}, A_{22}, A_{12} or A_{CN} conformation (protofilament) with another dimer. The grey region represents the overlap of regions 1A and 2B in the A_{CN} conformation.

The monomeric central rod domain has a heptad repeat $(a\text{-}b\text{-}c\text{-}d\text{-}e\text{-}f\text{-}g)_n$ where amino acids in positions a and d are apolar and mediate the hydrophobic interactions that are parallel with the axes of the dimers and ionic interactions occur between amino acids of opposite charges in positions e and g (Parry and Steinert, 1995). Two tetramers then associate together to form an octamer and four octamers then form a thirty two-mer. Thirty two-mers, known as unit-length filaments (ULFs), then anneal longitudinally with other thirty two-mers and finally compact to form the mature filament. It has been proposed however that the A_{12} alignment is unlikely to mediate interactions between the dimers but it is rather just an arrangement of the molecules for adjacent protofilaments (Meng et al., 1996). NFs and vimentin are believed to assemble according to the proposed method outlined above with the initial lateral alignment of tetramers which then lengthen, however heteropolymers of type I (acidic) and type II (basic) keratins initially form octamers which anneal longitudinally, thus lengthening the filament before the usual thirty two-mer formation step, as seen with vimentin filaments (Herrmann et al., 1999). The RP-box is essential for GFAP assembly and is conserved also in desmin and vimentin. Its sequence of RLSL-RM-PPLP is just before the rod domain and removal of the first half of the RP-box results in shortened, less stable filaments (Ralton et al., 1994). As mentioned earlier there are also the LNDR and TYRKLLEGE conserved sequences essential for IF assembly. Mutations in the LNDR sequence are associated with different diseases such as EBS and corneal dystrophy with a high proportion occurring at the arginine residue, most likely due to conversion of cytosine to thymine due to deamination. Mutations in the latter TYRKLLEGE sequence are associated with impaired filament elongation as seen with the substitution of tyrosine for alanine in keratins 8 and 18 *in vitro* (Hess et al., 2005, Hatzfeld and Weber, 1991). The N-terminal head domain is essential for filament formation and is not only required for cytoplasmic IF assembly but also nuclear lamin assembly and the C-terminus likely modulates the assembly (Heitlinger et al., 1992). The assembly of apolar IFs is different to MTs and actin, which both have

been modeled as having subunits associated in a treadmilling process mediated by polarity. Actin exists, for F-actin, in a plus and minus ended state with ATP being hydrolysed and ADP-actin dissociation occurring from these regions, respectively (Fujiwara et al., 2002). MTs are similar to actin filaments except GTP and GDP are used for the growth and shortening ends. Contrary to this, IFs do not metabolise nucleotides and it has been shown that addition of nucleoside triphosphates to bovine GFAP filament networks hinders filament formation likely due to introduction of a negative charge to the assembly buffer (Yang and Babitch, 1988). There is another model in addition to the treadmilling model, also known as the Wegner model or differential dynamic instability model that proposes phases of sustained growth and rapid shortening of tubules and filaments, however both models are predicted to occur for MFs and MTs (Grego et al., 2001).

Nuclear lamins are different to other IFs in that their assembly involves head-to-tail association of dimers prior to their longitudinal assembly. The C-terminal domain is more crucial for lamin formation than other IFs as its deletion results in aggregate formation (Moir et al., 1991). Nuclear lamins do not form tetramers but instead have an NC-overlap of dimers which is distinct only to non-cytoplasmic IFs (Geisler et al., 1998). P-INV IFs are similar to lamins in that they initially form octamers, which then laterally associate and finally form the mature filament, however whilst nuclear lamins form head-to-tail polymers which lengthen and laterally align, the protostomic IFs form tetramers which lengthen and laterally align (Geisler et al., 1998).

Recombinant BFSP1 and 2 assembly *in vitro* results in beaded filaments (filaments with a 6-8 nm backbone that appear to be regularly decorated with 12-15 nm beads or nodules) although they appear different to native beaded filaments assembled *in vitro* and are thought to consist of BFSP1/BFSP2 tetramers that are released from the inner core of the filaments with BFSP1 tails facing the exterior. When α-crystallin is added to the two proteins, the beads appear more similar to the native structures (Goulielmos et al., 1996, Carter et al., 1995). The beaded filament proteins BFSP1 and 2 can form 10 nm diameter filaments although the optimal conditions for assembly are different to the cytokeratins, which they are predicted to be most similar to due to sequence similarities. The reason why BFSP1 and 2 assemble together in a non equimolar ratio, whereas the cytokeratins do not, is likely due to a number of factors such as the inherent shorter rod 2 domain of BFSP1 compared to

BFSP2, the LNDC sequence replacing LNDR in BFSP2 that is unique amongst IFs and LNER replacing LNDR in human BFSP1 alongside RYHRIIE(I/N)EG replacing YRKLLEGE. BFSP1 can form 10 nm short filaments whereas BFSP2 forms predominantly aggregate structures with a few short filaments and it is only until the two proteins are co-assembled (2:1 molar ratio of BFSP2: BFSP1) that 10 nm filaments result (Carter et al., 1995, Perng et al., 2007).

Some IFs are able to form filaments as homopolymers such as type III IFs, α-internexin and NF-Ls. However many others need another IF to form filaments. This includes synemin, keratins, nestin and NF-M and NF-H chains, which both need NF-L (Steinert et al., 1999, Lee et al., 1993). Desmin can form heteropolymers with vimentin and also synemin and most of the type III IFs can co-polymerise with other type III proteins, such as GFAP with vimentin (Quinlan and Franke, 1982, Sharp et al., 1982). Nestin and synemin both need other IFs to assemble and the details of assembly are not fully known at this moment, in addition to how BFSP1 and BFSP2 form filaments, therefore Figure 1.4, which details comparisons between the different types of IF assemblies, excludes type VI and VII.

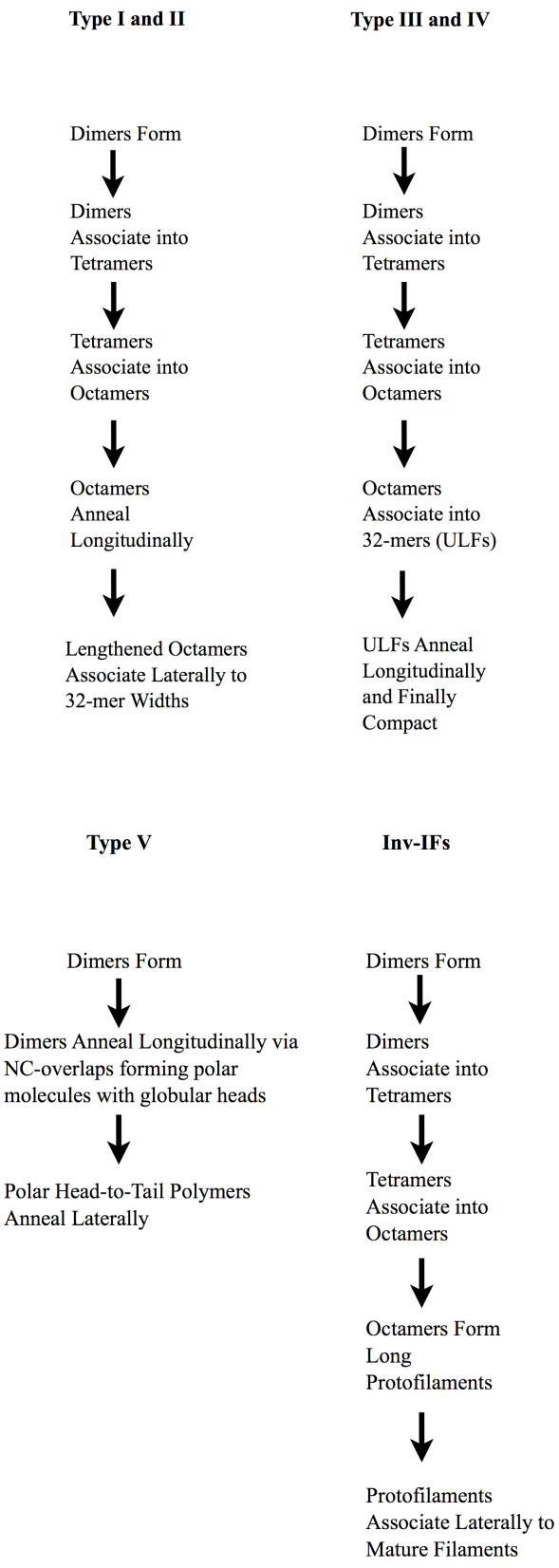

Figure 1.4 Comparison of different IF assembly mechanisms.

Only type I and II and type III and IV IFs share a common mechanism of assembly thus highlighting how variable assembly is between the different classes. This likely reflects their sites of expression and specific functions required. The assembly process will influence the surface structure of the filaments and how sHSPs are able to interact. Type VI and VII IF assembly processes are omitted, as it is not clear at this moment in time as to the full details of how filament assembly occurs.

Cells such as Bergmann and Schwann cells co-express GFAP with vimentin and this association of the two filament networks is required to maintain the stability of the GFAP filaments, as it was shown in $Vim^{-/-}$ mouse cerebellar extracts that there was an increase in the soluble pool of GFAP compared to Vim^{+} control mice (Galou et al., 1996).

The N-terminal head domain appears to be essential for most IF assembly and the C terminal tail regulates filament formation. This has been demonstrated from the splice variant GFAP ε, which has the usual exons 1-7 plus an additional exon 7a alongside missing exons 8 and 9, which forms aggregates. However it is most likely that the absence of the tail domain has no significant effect on filament formation on its own, demonstrated from when the tail region of GFAP ε was transfected into cells with GFAP α and there was no effect on filament formation. Therefore the combined interactions between the tail, head and rod domains must mediate the disruptive effects (Nielsen and Jorgensen, 2004). The head domain is crucial for GFAP assembly, particularly the MERRRITS-ARRSY sequence which when removed by thrombin results in an inability to form filaments (Ralton et al., 1994).

Different IFs require different assembly conditions, for instance vimentin does not form usual IFs when assembled in low pH, as used for NF-L filaments. Also the assembly rodlets of vimentin in tris(hydroxy-methyl)aminomethane (Tris)-HCl (pH 8.4) are different to those soluble structures formed with simple epithelial keratins that require a higher pH to begin filament formation, although epidermal keratin 5 and 14 are able to form filaments at pH 8.4 (Herrmann et al., 1996). When vimentin filaments are assembled in a 25 mM Tris-HCl (pH 7.5) and 50 mM NaCl buffer, after two seconds ULFs are observed whereas the simple epithelial keratins 8 and 18 have already formed long IFs. In addition, different IFs form filaments with differing numbers of molecules per cross-section despite being assembled in the

same buffer conditions, thus highlighting differences in assembly which are likely due to differences in interactions between the N-terminal head and rod domains, the result of sequence differences (Herrmann et al., 1999).

Divalent cations are essential for the formation of IFs and have an influence on how many monomers undergo annealing. Amphibian vimentin assembled with 5 mM Ca^{2+} ions forms twice as thick filaments compared to usual 10 nm widths, although retaining the usual 20 nm cross-striation pattern (Hofmann et al., 1991). There is a high-affinity Ca^{2+}- Mg^{2+} binding site in coil 2B of GFAP that is highly important for mediating assembly, showing that these divalent cations are crucial for normal IF assembly (Yang Z W., 1988). In addition there is a Ca^{2+}- Mg^{2+} binding site in the C-terminal tail that mediates cross-linking (Lin et al., 2010a). Monovalent cations do not promote filament formation as well as divalent cations and regarding Cu^{2+} and bovine GFAP assembly, there is an induction of aggregates instead of filaments (Yang and Babitch, 1988). When bovine GFAP is assembled at physiological pH 7.4 without divalent cations, only rod structures are formed. However, when divalent cations are added, filament formation results (Tanaka et al., 1989). Also thicker GFAP filaments are observed at lower pH and upon addition of higher concentrations of Ca^{2+} divalent cations, which likely reflects a reduction in the negative charges of the acidic amino acids thus restricting repulsive forces between the residues (Tanaka et al., 1989). IFs consist predominantly of negatively charged amino acids and similar to the effects seen with actin filaments and viruses, addition of divalent magnesium cations acts to attract parallel fibres and virus particles (Wen and Tang, 2006). They act as effective molecular cross-links in IFs by interacting with the negative sidearms of the IFs which comprise the tail regions (Lin et al., 2010b). Desmin is also influenced by different divalent cations and has been assembled in Cu^{2+} and Ni^{2+} ions which were shown to promote increased filament widths compared to Ca^{2+} and Mg^{2+} ions (Stromer et al., 1987). Divalent cations mediate cross-links between the final 11 amino acid residues in the tail region of vimentin (tails of separate vimentin IFs bind to each other) showing their importance in modulating filament interactions. Therefore, it appears that the C-terminal tail is highly important for binding to divalent cations and this will be the reason why with desmin filaments if the C-terminal tail is truncated there is an absence of strain stiffening (measure of toughness and stiffening of IFs due to their stress state) (Lin et al., 2010a, Bar et al., 2010). The C-terminal domain has been shown to mediate

forces upon the vimentin network toward the cell periphery, which opposes the head domain forces towards the nucleus, which can result in nuclear import and supports the idea that vimentin binds to DNA and thus the tail region has very specific mechanisms (Lowrie et al., 2000). As well as the ionic environment, temperature has been shown to be an important factor in regulating species variability in assembly, with the example of frog vimentin, which has partially unraveled sections of filaments at 4 ^{0}C in contrast to normal filaments with trout vimentin (Herrmann and Aebi, 1999). GFAP filaments are also dependent upon assembly temperature, demonstrated with 23 ^{0}C resulting in shortened filaments compared to 37 ^{0}C in the absence of cations (Tanaka et al., 1989).

1.4 IFs; modifications.

There are many potential modifications of IFs such as phosphorylation, acetylation, ribosylation, O-glycosylation, myristoylation and cleavage. Unlike MTs and MFs that are mainly modified by other proteins, IFs are predominantly phosphorylated when modified (Westermann and Weber, 2003, Kawauchi et al., 2006). An example of modulation of microfilaments is where Cdk5 and p27 act to suppress phosphorylation of cofilin and increase its activity thus resulting in actin reorganisation via direct interactions between cofilin and the actin filaments (Kawauchi et al., 2006). Phosphorylation of vimentin has been linked to axonal growth and *in vivo*, results in depolymerisation of the filaments (Eriksson et al., 2004, Chang et al., 2012). GFAP has key phosphorylation sites in its N-terminal head domain (serine and threonine residues) for cAMP-dependent protein kinase and protein kinase C, which when phosphorylated result in disassembly of the filaments and this is also common to vimentin and desmin which also have their phosphorylation sites located in the head domain (Inagaki et al., 1990). This is relevant to mediate cytoskeletal framework remodeling within mitotic cells (Takemura et al., 2002). The RP box, at the end of the head domain, in GFAP is also phosphorylated at anaphase (Matsuoka et al., 1992). Therefore in summary, it is the phosphorylation leading to global disassembly of IFs that enables the filaments to become solubilised and free for future IF polymerisation, which is the result of changes in the charge of the head domain with the introduction of a negative phosphate group (disrupting the charges of amino acids crucial for ionic

interactions). Regarding myopathy-linked desmin mutations, most involve replacement of serines with hydrophobic residues, which will ablate key phosphorylation sites thus implicating a deregulation in phosphorylation of desmin as a potential factor in the disease state (Sharma et al., 2009). NFs are known to be phosphorylated within their C-terminal tail domain, which will affect their transport (through axons) and function (Parry and Steinert, 1995). Also they are phosphorylated in the N-terminal head domain alongside O-glycosylation, however NF-M head domain phosphorylation inhibits the phosphorylation of the C-terminal tail showing that different domains can modulate each other in an IF (Zheng et al., 2003, Dong et al., 1993). O-glycosylation is likely to influence how axons grow and interactions of NFs with other filaments (Ludemann et al., 2005). Phosphorylation also affects the assembly status of other IFs in the type III group and also type VI, keratins and lamins, however there are no phosphorylation sites in the central domain of any IFs as the coiled coils restrict kinase access. With EBS it is thought that the mutations in the keratin proteins will increase or restrict how kinases are able to phosphorylate the proteins due to conformational changes in the tertiary structures (Jerábková et al., 2010). During a normal cell cycle, keratins 8 and 18 are phosphorylated to enable disassembly and then interactions with the regulatory protein 14-3-3. Keratin 18 is phosphorylated at Ser33 and interacts with dephosphorylated 14-3-3 proteins (Ku et al., 1998). 14-3-3 proteins also influence GFAP and vimentin filaments and have specific binding to each, independent of each other. The binding occurs mostly at the S and G2/M stages of the cell cycle when hyperphosphorylation of the filaments occurs via cell cycle-dependent kinases (Li et al., 2006). Nestin is phosphorylated by cdk5 in myogenic differentiation resulting in reorganisation and it is thought that this may be linked to migration of cancer cells (Sahlgren et al., 2003, Kleeberger et al., 2007). Synemin is also known to be phosphorylated (Sandoval et al., 1983). BFSP1 and 2 are both phosphorylated with the main sites located in the tail domain of BFSP1 and in the head domain of BFSP2. This will mediate the localisation of the proteins as it has been shown with BFSP2 that phosphorylation increases its lens fiber membrane localisation (Ireland et al., 1993). Vimentin is ADP ribosylated in the N-terminal head by the mono-ADP-ribosyltransferase (ADPRT) SpyA, which mediates disassembly of filament networks (Icenogle et al., 2012). This ribosylation of vimentin can be induced by brefeldin A (BFA) however is not involved with mediating the downstream bundling

effects of vimentin filaments after administration (Styers et al., 2006). Citrullination, the result of deimination of arginines, appears to occur with GFAP and levels may be correlated with multiple sclerosis (MS) (Nicholas et al., 2003). Citrullination has also been found with vimentin and correlated with rheumatoid arthritis (Kuna, 2012). Deimination of arginine residues also occurs with desmin and vimentin resulting in filament disassembly (Inagaki et al., 1989). Truncation (due to proteolytic processing) is another process, which is the result of aging lenses and results in two main fragments of BFSP1. The first one includes the N-terminal head domain, the rod domain and part of the C-terminal domain (53 kDa). The second contains the rest of the C-terminus (29 kDa) (Sandilands et al., 1995b). Another C-terminal fragment of 51 kDa has also been found within the nucleus of the lens and other varying molecular weight fragments of the C-terminal tail have been identified up to 62 kDa (Brunkener and Georgatos, 1992). Truncation seems to be important for mediating the posttranslational N-myristoylation in BFSP1, which implicates apoptotic events occurring within the lens and helps mediate binding of the proteins within membranes. The apoptotic caspases are responsible for normal lens organelle degradation (Zandy et al., 2005). The truncation process is thought to stabilise the beaded filament proteins (they localise from the cytoplasm to the membranes) and for BFSP1 the truncated 53 kDa form is still able to co-assemble with BFSP2 and forms distinct secondary structures to full-length BFSP1 (Sandilands et al., 1995b). In young lens fibre cells where differentiation is a relatively recent process, BFSP1 and 2 are predominantly in the plasma membrane (Sandilands et al., 1995a). Acetylation also occurs after truncation, which results in a charge change and potential structural changes (Wang et al., 2010). Therefore aging results in various modifications of the BFSP1 protein, which likely help maintain the transparency of the lens.

Caspases are involved in cleaving different proteins and have been found to target GFAP, vimentin and desmin. They are classified within two main groups of initiator (caspases-2, 8, 9 and 10) and executioner (caspases-3, 6 and 7) caspases, which are involved in either the intrinsic pathway for apoptosis where intracellular signals initiate the pathway, or the extrinsic pathway which is started from death receptors binding to ligands (Amarante-Mendes and Green, 1999). Desmin is cleaved by caspase-6 in response to apoptosis and the N-desmin that results acts to dominantly inhibit desmin and vimentin assembly (Chen et al., 2003). Most caspase cleavage

sites are found within the linker 1-2 domain of IFs (Caulin et al., 1997). GFAP can be cleaved by caspase-3 in AD brain and this can also be induced in acute postnatal injured rat brain alongside cleavage of vimentin in the reactive astrocytes (Mouser et al., 2006). AxD mutant GFAP also induces the cleavage and thus activation of caspase-3, which in turn results in its cleavage (Chen et al., 2011). Vimentin has been found to be cleaved by caspase-4 in situations leading to apoptosis, releasing p53 usually bound in a complex and activation of pro-apoptotic *bax* after its translocation into the nucleus (Yang et al., 2005). Therefore it can be seen that caspases act on many different IFs.

Response	IF	Modification	Reference
Disassembly of IFs and binding to 14-3-3	GFAP	Phosphorylation	(Inagaki et al., 1990, Li et al., 2006)
Reactive gliosis		Caspase-3 cleavage	(Chen et al., 2011)
Lymphocyte migration and axonal growth.	Vimentin	Phosphorylation	(Chang et al., 2012, Nieminen et al., 2006, Icenogle et al., 2012)
Disassembly of IFs		Ribosylation	(Icenogle et al., 2012)
Release of cytosolic p53 and apoptosis		Caspase-4, caspase-6 and caspase-3/7-like protease cleavage	(Yang et al., 2005, Byun et al., 2001)
Disassembly of IFs	Desmin	Phosphorylation	(Inagaki et al., 1988)
N-desmin (dominant inhibitor of assembly)		Caspase-6 cleavage	(Chen et al., 2003)

Table 1.4 **Summary of IF modifications**.

Here is a summary of the most common modifications noted of IFs and all IFs have been documented as having the potential to be phosphorylated (Chou et al., 1989).

Response	IF	Modification	Reference
Binding to mitochondria and axonal transport	NFs	Phosphorylation	(Wagner et al., 2003) (Parry and Steinert, 1995)
Surface modulation		O-glycosylation	(Dong et al., 1993)
Disassembly of IFs	Lamins	Phosphorylation	(Hennekes et al., 1993)
Surface modulation		O-glycosylation	(Ferraro et al., 1989)
Membrane affinity		Isoprenylation	(Hofemeister et al., 2000)
Protein interactions and localisation	Keratin -18	O-glycosylation	(Ku et al., 2010)
Localisation	BFSP1	Phosphorylation	(Wang et al., 2010)
Membrane binding and regulation of the cytoskeleton in apoptosis		N-myristoylation	(Wang et al., 2010)
Structural changes		N-acetylation	(Wang et al., 2010)
Membrane affinity	BFSP2	Phosphorylation	(Ireland et al., 1993)
Structural changes		N-acetylation	(Wang et al., 2010)

Table 1.5 **Summary of IF modifications**.
Here is a continuation of some common modifications.

As can be seen from the above potential IF modifications, whether it be physiological or pathological, many different processes require IFs to be altered and this highlights how varied their roles are within cells.

1.5 AxD and GFAP mutants.

AxD is a fatal disease, the result of a heterozygous mutation within the GFAP gene. W.Stewart Alexander first identified the disease in 1949, 51 years after Rosenthal fibers were noted by the German pathologist Werner Rosenthal (Alexander, 1949). The most common mutations occur at positions R79 and R239 in the GFAP protein, accounting for more than half of all documented mutations and it is believed that they act in a gain-of-function manner (Hagemann et al., 2005). These are commonly mutated due to the presence of a cytosine next to a guanine in the DNA sequence, separated by a phosphate group (Cooper and Youssoufian, 1988). Patients present with seizures, macrocephaly, dysphagia and Rosenthal fibers, which contain GFAP predominantly alongside CRYAB and p62, which is a ubiquitin-binding protein (Shiroma et al., 2001). In addition, GFAP is over-expressed in AxD, likely resulting in inhibition of chaperone mediated autophagy and upregulation of macroautophagy (increases in p38 signaling down regulates mTOR). Chaperone mediated autophagy is a form of the autophagic and lysosomal degradation system which involves the binding of the foldase hsc70 to mis-folded proteins which are brought to lysosomes and are then translocated via the lysosome-membrane protein type 2A (LAMP-2A) receptor complex, through lysosomal membranes, destined for degradation in the lysosomal compartment (Chiang et al., 1989). Macroautophagy is different to this process since autophagosome vesicles are involved which transport cargo to lysosomes where fusion of membranes occurs and contents are released into the lysosomes for degradation (Itakura and Mizushima, 2010).

There are many mutations associated with AxD with three main types of infantile, juvenile and adult onset and all three have been associated with mutations occurring throughout the whole of the GFAP molecule. Over-expression of WT GFAP leads to protein aggregates, however mutant GFAP is more prone. Despite the three different ages of onset, the same mutation can lead to different ages of onset and thus it is difficult to pinpoint the exact determining factors leading to the development and presentation of the disease. It is therefore likely that environmental and additional genetic factors contribute to disease development. Mutant GFAP leads to an upregulation in the MLK2-JNK pathway and accumulation of CRYAB; it is likely that there is upregulation of JNK downstream pathways (causing direct increases in GFAP levels) and inhibition of proteasome function also leading to accumulation of

GFAP protein which is supported by the finding of activated JNK (phosphorylated JNK) being shown to interact direct with over expressed WT and mutant GFAP in cells (Tang et al., 2006). R239C mutant GFAP can inhibit the proteasome system and it has been proposed that the larger oligomer complexes may bind to the proteasomes and thus not be effectively degraded. The mutant GFAP reduces the cytosolic stores of the ubiquitin-proteasome system and is inefficiently degraded within proteasomes (Tang et al., 2010). Cdc42 and rac small GTPases are known to activate the stress-induced JNK pathway alongside the p38 MAPK pathway, which is regulated by rho (Lim et al., 1996). In AxD, both of these pathways are upregulated and since the cause of AxD is mutated GFAP, some intermediary stages will be required for activation of these signaling pathways and it is thus possible that the upstream signaling initiators of the GTPases are involved with interacting with the altered filament surface, the result of mutations. As well as certain signaling molecules being affected in AxD, transporter proteins can also be altered such as glt1, which is a glutamate transporter found in astrocytes and has reduced levels in mice heterozygous for the R236H mutated GFAP, likely due in part to upregulation of the MAPK pathway, however expression of CRYAB is able to increase Glt1 expression (Hagemann et al., 2009).

Many other neurodegenerative diseases have also been correlated with inefficient autophagy mechanisms, such as Huntington's, AD and Parkinson's disease (Cheung and Ip, 2011). These diseases are also associated with insoluble protein aggregates, similar to AxD. In the AD brain there is also induction of the caspase cleavage of GFAP, which results in the GFAP caspase-cleavage product (CCP) antibody (Ab), directed towards the C-terminal cleavage product after $DLTD^{266}$, colocalising with activated caspase-3 in astrocytes. In response to reactive gliosis, astrocytes cluster around senile plaques, which consist of β-amyloid peptide (Aβ) and release inflammatory mediators. The upregulation of activated caspase-3 in AD brain reflects most likely the increase in turnover of the GFAP as opposed to an increase in apoptotic cell death (Mouser et al., 2006). Figure 1.5 highlights the structure of a monomer of GFAP, including AxD documented missense mutations discovered to date, including the two mutations looked at in this study of R79C and R239H.

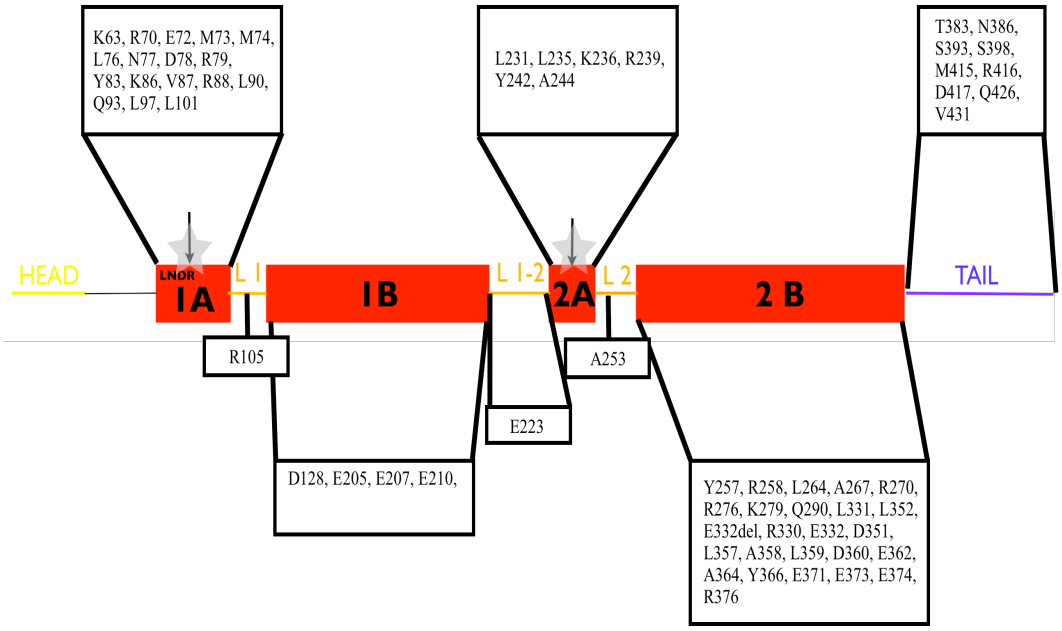

Figure 1.5 Schematic diagram of a human GFAP monomer alongside known mutations.

A diagram of human GFAP is shown above. The yellow line represents the head domain, the gray line represents the pre-coil domain, the red boxes represent the rod coiled-coil domains, the orange lines represent the linker regions and the blue line represents the tail domain. The R79C and R239H mutation points are highlighted with vertical arrows, with R79C located within the LNDR motif in the 1A region of the rod domain and the R239H mutation located within the 2A region. Other mutations are listed in the boxes and it is shown that most mutations occur in the rod domain with very few in the tail region and the only mutation documented so far before coil 1A is K63Q, which is positioned in the pre-coil domain. No mutations have been documented in the head domain (Brenner et al., 2009, Messing, 2012, Li et al., 2005).

1.6 Rheological properties of filament networks.

Filament networks are viscoelastic showing both solid (elastic) and viscous (liquid) components. Microrheology is a method assessing the properties of colloidal substances, which are generally microspheres in the range of 0.001 μm to several μm, within a soft material; it specifically looks at the thermal fluctuations of particles

to derive linear response functions of the material, utilising the generalised Stokes-Einstein relation (GSER). Passive microrheology involves deriving the response functions of a material using tweezers to hold the particles in place. There are a few other rheological methods, not using probe particles, such as the utilisation of a rotating plate that applies force to a material held against another parallel stationary plate and measures the strain (Dhori et al., 1997). Diffusing-wave-spectroscopy (DWS) is similar to single-particle video tracking microrheology except light is measured after being scattered from many microspheres to derive an autocorrelation function which is then used in the GSER; it measures the properties of isotropic solutions (Palmer et al., 1999). Dynamic light scattering (DLS) involves a laser beam illuminating a sample, which is then deflected and the scattered light intensity is then converted into an auto-correlation function (Chastek et al., 2008). The atomic force microscope (AFM) applies relatively high forces to a material using a tip attached to a cantilever and deformations in the material are used to derive the shear modulus (Radmacher et al., 1993). From all methods, the dynamic shear modulus G can be derived which is composed of both the real storage (G') and imaginary loss (G'') moduli in the equation $G = G' + iG''$. Optical tweezers were first demonstrated in 1986 allowing manipulation of objects, which could be trapped by a Gaussian laser beam (Ashkin et al., 1986). Microrheology has many advantages over standard rheology such as minimal invasive disruption in the samples and the ability to measure a wide range of frequencies, since rotational rheometers generally are limited to frequencies below 100 Hz (Willenbacher and Oelschlaeger, 2007).

Various rheological methods have been used to assess the properties of filament networks, such as displacement and stretching of filaments to discover that they likely act as shock absorbers in cells (Kreplak et al., 2005).

From strain stiffening experiments *in vitro* it has been shown that different filaments have different strain-stiffening properties, which are conducive to the different responses required of the filaments dependent upon where they are situated, such as vimentin within fibroblasts and desmin found in muscle cells (Schopferer et al., 2009). The importance of different regions of desmin on filament function has also been derived from strain-stiffening experiments giving important biophysical information on filament properties (Bar et al., 2010). Comparing desmin and vimentin networks it has been shown that desmin has greater attractive forces and strain stiffening at low salt concentrations that is absent with vimentin filaments

(Schopferer et al., 2009). A more in-depth insight into filament assembly for vimentin has also been gathered using strain-stiffening experiments with divalent cations showing that these act as cross-linkers within the tail region of the IF (Lin et al., 2010a).

IFs are semi-flexible polymers; however there also exist flexible and rigid polymers. Semi-flexible polymers have a persistence length (a length scale for the decay of tangent-tangent correlations) which is equivalent to their contour length (total filament length) and completely elastic and rigid polymers are either made up of a greater contour length with an entirely entropic elastic response or a greater persistence length with no entropic elasticity, respectively (Storm et al., 2005). Rheology gives a general overview of the properties of filament networks that need to be supplemented with other methods to assess more local changes (individual filaments), such as thermal fluctuation measurements (Noding and Koster, 2012).

1.7 Heat shock proteins.

There are five main classes of heat shock protein, c.f. Table 1.6, with classes 1-4 utilising ATP and known as foldases and class 5 corresponding to the small heat shock protein (sHSP) family, which are ATP-independent and known as holdases (Karplus et al., 2005).

Class I, also known as chaperonins, consists of groups II and I. Group I includes the bacterial HSP60 and GroEL, which is found in *E.coli* and consists of two rings each composed of seven subunits, both of which are referred to as having a double donut quaternary shape. GroES binds to GroEL at the apex in the presence of ATP binding to the central parts (equatorial regions) of the GroEL rings. A mixed population of singly and doubly capped GroEL chaperones result. Mis-folded substrates enter the central *cis* ring cavity after ATP initiation, GroES binds resulting in a bigger cavity and ATP is then hydrolysed and there is a release of the denatured and GroES protein and ADP after binding of the denatured protein and ATP to the *trans* ring (Karplus et al., 2005). Group II chaperonins are found in archaea and eukaryotes and consist of two rings, each containing eight to nine subunits. They are similar to group I as they have an equatorial ATP binding domain and in addition bind to substrates at the apex and have a connecting domain (intermediate domain) between the apical and equatorial regions. They have a similar donut shape with double rings,

each of which constitute eight subunits (Kalisman et al., 2012). The apical domain is quite different in group II chaperonins compared to group I as it moves (rotates), when ATP is bound to the central region and results in a decrease in size of the central folding chamber. The intermediate domain then has a hydrolytic aspartic acid residue that moves towards the ATP binding site and upon hydrolysis the apical and intermediate regions rock forward using the equatorial hinge and close the chamber (Zhang et al., 2011). Therefore there are lids that open and close the central domain. The t-complex polypeptide 1 (TCP-1) is an example and is made up of TriC, CCT and C-cpn and is 1-MDa, with tubulin and actin as its substrates (Sternlicht et al., 1993).

Class II covers the HSP70s, which consist of a nucleotide binding domain (NBD) and a substrate binding region (SBD) and like chaperonins from group I, their activity is dependent on allostery. For instance, Hsc70 binds to the cochaperone J (Jiang et al., 2005). Eukaryotic Hsp70 requires Hsp40 and nucleotide exchange factor (NEF) and prokaryotic DnaK requires DnaJ and GrpE (Miot et al., 2011). The interactions of HSP70s with their target substrates are transient and the cochaperones act to promote the hydrolysis of ATP and thus increase the affinity of the chaperones for their client proteins (Raviol et al., 2006). The re-folding of the substrates is believed to occur through release and re-binding cycles within the central cavity (Mayer et al., 2000).

HSP90s are within class III and have three domains: an ATP binding domain, a central SBD and a C-terminal domain for dimerisation. The N- terminal and central regions are connected by linker amino acids, which provide flexibility and modulate chaperone activity of the protein. The linker region confers a negative charge to the protein and aids in Hsp90 domain organisation. Cochaperones also interact with Hsp90s such as HSP70, isomerases and S100A1 and the linker region aids in placing the interaction domains in the correct place (Okada et al., 2004). Aha1 is a cochaperone and interacts with Hsp90-Pf-CL to increase the activity of ATPases (Tsutsumi et al., 2012). HSP90 function is predominantly to mediate correct protein folding of signal transduction proteins.

Hsp100s can un-fold insoluble, aggregated proteins and are found in class IV. They have four main domains consisting of: an N-terminal region, two NBDs and a middle domain (M-domain), with a central channel and hexameric ring structure and exist in a double ring structure. In the case of the prokaryote ClpB and its eukaryotic

homologue Hsp104, their activities require DnaK, DnaJ and GrpE or Hsp70 and Hsp40, respectively (Miot et al., 2011). For Hsp104, the NBD1 domain is mainly responsible for ATPase activity and NBD2 primarily for oligomer formation and communication occurs via a coiled coil between the two domains (Wendler et al., 2007).

sHSPs are present in all organisms, in all the kingdoms and have diverged early in evolution with the most divergence occurring in *Arabidopsis thaliana* (Waters et al., 1996). sHSPs act in concert with HSPs, since once the sHSPs have bound to their client proteins; the release of the substrates usually requires the larger chaperones which utilise ATP, with the exception of HSP27 for example which has low affinity sites that can easily release substrate without any input of energy (McDonald et al., 2012). They therefore act as a store for incorrectly and mis-folded proteins but do not have the ability to re-fold the proteins, as seen with foldases. They consist of three main domains of an N-terminal region, an α-crystallin central domain and a C-terminal domain (Haslbeck et al., 2008). The α-crystallin domain is composed of seven to nine β-strands structured as a sandwich and this domain is conserved across all the sHSPs. There are α-helices within the N-terminal head and α-crystallin domain.

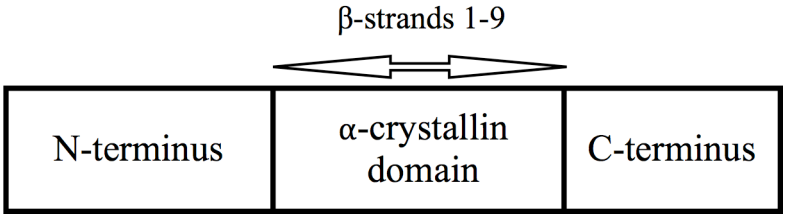

Figure 1.6 Diagram of CRYAB structure.

Variability between the different sHSPs exists in the N-terminal arm and C-terminal domain, except there is a I/L-X-I/L conserved motif in the C-terminus that is crucial for oligomer formation and this contacts the hydrophobic patch in the α-crystallin domain of adjacent subunits to form the oligomers (Poulain et al., 2010, van Montfort et al., 2001). They consist of between 4-40 subunits and rely on the ATP-dependent functions of HSP60, 70 and 100 for re-folding of the client proteins (McDonald et al., 2012). The variation in the number of subunits per oligomer is a key property of sHSPs, which is most likely the result of dissociation of tetramers (Bova et al., 2000). Binding of substrates is initiated via presentation of hydrophobic

surfaces on the sHSPs. Their response to increase affinity for client proteins is not only due to mis-folded client proteins but also due to changes in their oligomeric structures; often the result of temperature rises as part of a heat stress response. In the case of HSP18.1, increased temperatures result in a preference of higher-order oligomer formation over monomers and dimers (Stengel et al., 2010). Phosphorylation also influences substrate interactions and phosphorylation of CRYAB increases its affinity for unfolded substrates (Koteiche and McHaourab, 2003). Wheat (*T. aestivum*) sHSP16.9 has been crystallised and found to contain 12 subunits composed of two rings, each containing six α-crystallin domains in a barrel-shape complex. The N-termini are important in mediating hydrophobic interactions with proteins within the oligomeric structure due to intertwining and knot formations (Aquilina et al., 2004, van Montfort et al., 2001). However, *Methanococcus jannaschii* (Mj) HSP16.5 contains 24 subunits and is a hollow ball-shaped structure as shown from its crystal structure and all sHSPs have an α-crystallin domain in common, believed to be important for interacting with client proteins (Haslbeck et al., 2008).

Class	Molecular Weight (kDa)	Proteins
I (chaperonins)	Group I: 60 Group II: 1000	GroEL TCP-1 (TRiC/CCT/C-cpn complex)
II (Hsp70s)	70	DnaK Hsc70
III (Hsp90s)	90	Hsp90
IV	100	Hsp104 ClpB ClpC
V (sHSPs)	12-43	CRYAB Hsp16.5 Hsp20.2

Table 1.6 **Heat shock protein types**.

1.8 CRYAB; chaperone and cell protector.

CRYAB is part of the sHSP family, which consists of proteins having the smallest molecular weights within the heat shock protein superfamily, as detailed in the previous section. It is a holdase small heat shock protein that has the capability to chaperone, preventing aberrant structures and aggregates of proteins, acting as a cell protector upon increased associations with interacting target proteins. It is also found as part of the larger α-crystallin complex, which is in the vertebrate eye lens and consists of αA-crystallin and CRYAB in a 3:1 or 2:1 molar ratio (Srinivas et al., 2008, Swamy and Abraham, 1991). This complex constitutes more than 50% of the total water-soluble proteins present within the lens and has greater stability towards increased temperatures compared to either αA-crystallin or CRYAB alone (Srinivas et al., 2008, Bova et al., 2000). Total protein in the lens can be at a concentration of up to 450 $mgml^{-1}$ and thus there are many proteins with the potential for unfolding, necessitating the actions of the crystallin complex to bind to the mis-folding substrates (Fagerholm et al., 1981). The α-crystallin complex binds irreversibly to other crystallin structures thus aiding in the prevention of light scattering (Hanson et al., 2000). CRYAB has a polydisperse structure and its basic unit consists of a dimer, as with HSP20. When the higher order oligomers dissociate to reveal the dimers, these smaller units have more peptide binding sites exposed thus increasing affinity for substrates (Bagneris et al., 2009). The structure of the oligomers has been proposed using knowledge gained from the crystal structures of the Mj HSP16.5 and *T. aestivum* HSP16.9 proteins and many different models have been suggested (Murugesan et al., 2008). It is thought that the CRYAB oligomers have a central cavity (Haley et al., 1999). Cryo-EM has been used to generate the quaternary structure of CRYAB to reveal 16 subunits, although this varies (Haley et al., 1999). The β-strands 4 and 8 form pockets in which the I-X-I motif within the C-terminal tail of adjacent monomers is able to dock and aid in building oligomers (Laganowsky et al., 2010, Jehle et al., 2010).

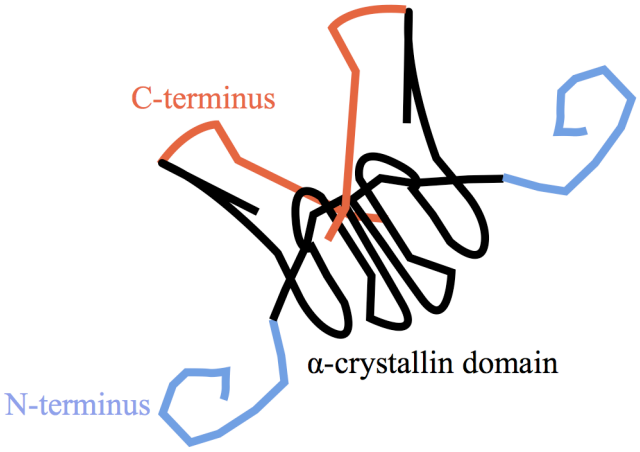

Figure 1.7 Diagram of CRYAB dimer.
The C-terminal I-X-I motif interacts with an adjacent monomer's β-4 and 8 strands.

The interaction of the C-terminal tail with the α-crystallin domain is also crucial for determining the architecture and symmetry of the oligomers, such as with Hsp16.9 and 16.5, dependent upon orientation and rotation of the tail in relation to the α-crystallin domain (McHaourab et al., 2012). CRYAB has been shown to increase its binding affinity to IFs upon an increase in stress imposed upon the filament networks, seen with an increase in temperature imposed upon *in vitro* formed networks. In addition, with particular reference to the R120G mutation in CRYAB located in the α-crystallin domain resulting in cardiomyopathy, desminopathy and cataracts, an altered structure of the chaperone also lends itself to increased associations with the filament networks (Perng et al., 2004). In this situation it acts in a dominant gain of function manner to promote aggregation instead of preventing it and the mutant dimer is more stabile at low pH compared to WT CRYAB (Bagneris et al., 2009). The arginine is replaced with a glycine removing a positive charge within the dimer interface already sensitive to pH changes in the physiological range, due to a high number of histidines (Clark et al., 2011). Therefore it can protect networks in the normal wild-type conformation but if this is altered by a mutation, the filament-filament interactions can be increased. CRYAB interactions are important with desmin filaments for muscle homeostasis. It has the ability to prevent damage in muscle by increasing its associations with titin in response to ischemic stress as it is usually only found as part of the soluble fraction (Bullard et al., 2004). As well as mutation resulting in decreased chaperone abilities,

phosphorylation has also been shown linked to certain diseases with specific relevance to aging in the lens with a reduction in chaperone ability (Aquilina et al., 2004). WT CRYAB is likely able to transition between dimeric and monomeric forms; this has been shown to be pH dependent as acidosis results in a dimer-monomer conversion of the α-crystallin domain only (Jehle et al., 2009), which correlates with an increase in binding to desmin and actin in muscle cells. Also in ischemic conditions there is an increase in phosphorylation of CRYAB and despite there being an increase in translocation and increased binding of CRYAB to IFs at the low pH, it appears that the chaperone ability has been reduced, alongside a decrease in oligomer size (Eaton et al., 2001). This is unusual as it would be expected in ischemia that since the CRYAB is binding more to the unfolding substrates, there would be an increase in the prevention of their aggregation (Ito et al., 2001). However the increased phosphorylation seen in hypoxic conditions is likely to mediate CRYAB interactions with caspase-3 and other signaling molecules to prevent apoptosis and thus even if the ability to sequester the filaments, which potentially mis-fold is reduced, the increased binding of CRYAB to the filaments likely mediates its interactions with other proteins (Morrison et al., 2003). However studies have shown that CRYAB does protect and stabilise titin and other members of the cytoskeleton upon increased binding and thus the ability to chaperone or prevent heat-induced aggregation of a protein is different to the effects of stabilising the cytoskeleton (Bullard et al., 2004).

CRYAB acts to protect C6 glioma cells from apoptosis as the result of oxidative stress, in response to increased p38β levels (Shin et al., 2011). CRYAB and αA-crystallin can both bind to the pro-apoptotic Bax and Bcl-X_s proteins thus halting their mitochondrial translocation, in response to staurosporine (Mao et al., 2004). CRYAB is additionally important in responding to ischemia-reperfusion (I/R) that results in stress, with increased levels of CRYAB that protect the myocardium from damage. Serine 59 is a target for phosphorylation, present within the N-terminal region (amino acids 1-65) and CRYAB translocates and binds to the outside and also enters mitochondria thus potentially binding unfolding mitochondrial proteins (Jin et al., 2008). In relation to AxD, it has been shown that CRYAB can reverse the inhibitory effects of toxic mutant GFAP oligomer build-up on proteasome activity (Tang et al., 2010).

1.9 Aims and objectives.

In this thesis I have focused on the interactions of CRYAB with type III IFs to gain more understanding about how filament structure and CRYAB structure can influence the two independent processes of binding of CRYAB to filaments and also prevention of filament-filament interactions by CRYAB. The main objectives included looking at desmin and GFAP interacting with CRYAB since oligomer size of CRYAB appears to be crucial in mediating binding and any alterations in CRYAB oligomers, such as with the R120G mutant, leads to a diseased state that alters its interactions with IFs. The fact that the R120G mutation in CRYAB results in desminopathies and cardiomyopathies but not gliopathies highlights how crucial the WT CRYAB-desmin interactions are for maintaining homeostasis in muscles. Therefore a greater understanding of how CRYAB interacts with the IFs is crucial for understanding how pathological states occur and therefore different conditions were investigated, hypothesised to alter the oligomer size of CRYAB and also shift the equilibrium of IF assembly. Also rheological and sedimentation experiments were carried out to see if the CRYAB-desmin interactions are functional. Divalent cations, temperature and pH changes were studied. Another aim of this thesis was to investigate how the AxD mutants of R239H and R79C human GFAP proteins assemble *in vitro*, alongside the previously studied R416W mutant and how the morphology may be explained using hypothesised predictions based upon the mutations' locations within the coiled coils' heptad repeats and random coils. As mentioned earlier, passive microrheology with optical tweezers was used to probe the mechanical properties of WT desmin networks, as a non-invasive technique, to assess the frequency-dependent viscosity and elasticity (*G'*) of the filament networks as another method compared to sedimentation assays to see how the cardiomyopathy-causing R120G CRYAB mutant results in increased filament-filament interactions and how WT CRYAB changes the biomechanical properties of desmin IF networks. These rheological experiments add more information in an equilibrium situation, as to the nature of the CRYAB-IF interactions, to non-equilibrium sedimentation assays that have been used thus far as the standard method of assessing CRYAB's effect upon filament networks.

Chapter 2; Interactions between WT and mutant GFAP with CRYAB

2.1 Introduction and aims

The aim of this study was to find out what effects the known heterozygous mutated human GFAP proteins, involved in the etiology of AxD, had on filament properties compared to WT GFAP filaments and how this influenced their interactions with the small heat-shock protein CRYAB. In addition the interactions of CRYAB with WT GFAP was investigated under different assembly methods. The hypothesis was that the R79C and R239H mutated GFAP would have increased associations with CRYAB since this has been shown previously for the R416W mutant in astrocytoma cells (Der Perng et al., 2006). Amino acid position 239 in human GFAP is the most common hotspot for amino acid substitution non-conservative mutations in AxD. Both amino acid positions 239 and 79 were investigated, as they are included in the most severe phenotypes. In addition the R416W mutant was compared as a control, having been studied previously in this laboratory (Der Perng et al., 2006). Also using different assembly methods the interactions of CRYAB with WT filaments was investigated.

2.1.2 Materials and methods.

Analytical grade chemicals were used throughout the chapter unless otherwise stated and were from Sigma-Aldrich (Poole, UK), Fisher (UK), VWR International Ltd. (UK) or Melford Laboratories Ltd. (Suffolk, UK).

2.1.2.1 Construct production.

Recombinant GFAP DNA was kindly given by Terry Gibbons. R79C human GFAP was originally in pcDNA 3.1 (-) (Invitrogen, UK) between XbaI and HindIII restriction sites and transferred into a pET-23b vector (Novagen, UK) using the same restriction sites. R416W human recombinant GFAP originally in pcDNA 3.1 (-) between XbaI and BamHI sites was transferred into pET-23b using the same sites. WT human GFAP was inserted in a pET-23b vector between NdeI and EcoRI sites and R239H human GFAP was between the same sites in a pET-23b vector. Human

WT desmin (pET-23) was kindly received as a glycerol stock from Andrew Landsbury alongside human WT CRYAB (pET-23d) and R120G CRYAB (pET-23d) in BL21 (pLysS) (Novagen, UK). Human recombinant WT vimentin was derived from a pET-7 vector in BL21 (pLysS) within a glycerol stock.

DNA was transformed into DH5α bacteria using 50 µL of bacteria and 1 µL (approximately 100 ng) of purified DNA sample. They were left to incubate on ice for 10 minutes (min) and then heat shocked at 42 ^{0}C for 50 seconds (sec). The samples were again cooled to 4 ^{0}C for 10 min; 250 µL Luria broth (LB) (1% (w/v) bacto-tryptone, 0.5% (w/v) bacto-yeast extract, 1% (w/v) sodium chloride (NaCl)) was added and they were put on the shaker at 37 ^{0}C for 1 hour (hr) before being plated out onto LB agar plates with the antibiotic selection marker of 50 µg/mL ampicillin.

2.1.2.2 BL21 *E.coli* transformation and protein expression.

BL21 (pLysS) (Novagen, UK) competent cells were transformed with DNA plasmids through heat shock; involving 50 µL of BL21 (pLysS) being incubated with 1 µL of plasmid miniprep (Sigma-Aldrich, UK) purified DNA in an ice bath for 10 min. These were then put in a polystyrene float in a water bath set at 42 ^{0}C for 50 sec and transferred back onto the ice bath for 10 min and 250 µL of LB was added. The cells were incubated for a further 1 hr at 37 ^{0}C on the shaker at 250 rpm, 37 ^{0}C and plated out onto LB agar plates with 34 µg/mL chloramphenicol (to select for the pLysS vector in host cells) and 50 µg/mL carbenicillin (to select for the pET vectors). Single colonies were picked into 5 mL LB broths with the same antibiotics and 0.05% (w/v) glucose concentrations and then grown overnight for 16 hr at 37 ^{0}C. The next day these were diluted 100-fold for scaling up the growth within 2 litre (L) capacity Fernbach flasks. The bacteria were grown at 37 ^{0}C, 250 rpm for approximately 4 hr until an optical density at 600 nm (OD_{600}) of 0.6 was reached and then they were induced with a final concentration of 0.5 mM isopropyl β-D-1-thiogalactopyranoside (IPTG). They were grown for a further 4 hr for protein expression. After a 1 mL post-induction sample was removed, spun down and the pellet resuspended in 100 µL 2x sample buffer (SB) (100 mM Tris-HCl (pH 6.8), 2% (w/v) sodium-dodecyl sulphate (SDS), 10 mM ethylenediaminetetraacetic acid (EDTA), 10 mM dithiothreitol (DTT), 20% (v/v) glycerol, 0.2% (w/v) bromophenol

blue), the remaining majority was spun down at 6,200xg_{av} in the JLA-8.1000 rotor for 30 min, 4 ^{0}C (Beckman JA-20-I centrifuge). Protein expressed in bacteria are either mainly present in their native conformation in a soluble state such as for human WT and R120G CRYAB where the final bacterial pellet was resuspended in 20 mL of 50 mM Tris-HCl (pH 8.0), 1 mM EDTA, 300 mM NaCl and 0.2 mM phenylmethanesulfonyl fluoride (PMSF), spun and frozen ready for a soluble protein extraction, or alternatively the protein has been folded in such a way as to make them insoluble and located in the insoluble inclusion body portions and so the final pellet was resuspended in 20 mL of a modified Tris, EDTA and NaCl (TEN) buffer of: 10 mM Tris-HCl (pH 7.4), 150 mM NaCl and 5 mM EDTA, for GFAP, vimentin and desmin, then spun again at 5,000xg_{av}, 15 min, 4 ^{0}C in the JA-20 rotor (Beckman JA-20-I centrifuge) and frozen as a cell pellet at -20 ^{0}C ready for an insoluble protein extraction.

2.1.2.3 GFAP, desmin and vimentin insoluble protein preparation.

The bacterial pellet was freeze-thawed three times for bacterial cell wall disruption and then resuspended in 20 mL of a TEN buffer (10 mM Tris-HCl (pH 8.0), 5 mM EDTA, 100 mM NaCl and 1 mM PMSF with one complete protease inhibitor cocktail tablet (Roche Diagnostics, UK) and incubated on ice for 15 min. This was homogenised to a bacterial suspension with a 40 mL Dounce homogeniser (Wheaton, USA) so the suspension became cloudy and viscous. The lysates were then centrifuged at 30,000xg_{av}, for 30 min at 4 ^{0}C in the JA-20 rotor (Beckman JA-20-I). The pellet was resuspended in 20 mL high salt buffer (HSB) (1.5 M KCl and 1% (w/v) Triton X-100 in TEN buffer with 1 mM PMSF) and homogenised on ice with one hundred strokes using the tight pestle. The homogenates were centrifuged again at 30,000xg_{av}, 20 min, 4 ^{0}C in the JA-20 rotor (Beckman JA-20-I) and the HSB stage was then repeated to aid in complete removal of all DNA contaminants. As a final step the pellet was washed with phosphate buffered saline (PBS) to remove excess salts and centrifuged again. Extraction of the pellet was then carried out due to the insoluble nature of the proteins.

2.1.2.4 Purification of GFAP, desmin and vimentin insoluble protein.

Can be found detailed in the purification methods for chapter 2 in the appendix.

2.1.2.5 Purification of WT and R120G CRYAB.

Can be found detailed in the purification methods for chapter 2 in the appendix.

2.1.2.6 GFAP, desmin and vimentin TMAE anion and COO^- cation exchange chromatography.

Can be found detailed in the purification methods for chapter 2 in the appendix.

2.1.2.7 WT and R120G CRYAB TMAE anion and size exclusion chromatography.

Can be found detailed in the purification methods for chapter 2 in the appendix.

2.1.2.8 Gel electrophoresis.

Samples were taken from dissolved samples in 1x final concentration denaturing Laemmli SB (50 mM Tris-HCl (pH 6.8), 1% (w/v) SDS, 5 mM EDTA, 5 mM DTT, 10% (v/v) glycerol and 0.2% (w/v) bromophenol blue), boiled for 5 min at 95 ^{0}C and in some cases centrifuged if taken from bacterial cells and finally vortexed for a few sec ready for running on a 0.75 mm spacer plate thickness 10% (w/v) (0.375 M Tris-HCl (pH 8.8), 10% (w/v) acrylamide, 0.3% (w/v) bis-acrylamide, 0.1% (v/v) SDS, 0.05% (w/v) ammonium persulphate and 0.06% (w/v) N,N,N'N'-tetramethylethylenediamine (TEMED)) or 12% (w/v) acrylamide separating gel, with a 4% (w/v) acrylamide (0.123 M Tris-HCl (pH 6.8), 4% (w/v) acrylamide, 0.12% (w/v) bis-acrylamide, 0.1% (v/v) SDS, 0.05% (w/v) ammonium persulphate and 0.06% (w/v) TEMED) stacking gel using a Bio-Rad 15-well comb and Mini-PROTEAN 3 cell (Bio-Rad, UK). The separating gel was initially placed between short and spacer glass plates held flush together by Mini-PROTEAN 3 gel casting frames (Bio-Rad, UK), held in place by pressure cams, on Mini-PROTEAN 3 gel casting stands (Bio-Rad, UK). A layer of water-saturated butanol was placed on top of the separating gel to give a flat surface ensuring samples entered the separating gel

at the same time. Once the separating gel was set, the water-saturated butanol was removed using de-ionised water and tissue and the stacking gel was placed on top with a comb and left to set. For gel running, combs were removed and the gels were placed into a clamping stand, mini tank and 1x running buffer (0.1% (v/v) SDS, 0.192 M glycine, 0.0275 M Tris) added. The samples were loaded into the wells using gel tips and 2 µL of a pre-stained Pageruler^{TM} protein ladder #SM0671 (Fermentas, UK) was run in the left most lane of the gels. Once the samples were loaded, the lid was attached to the banana plugs of the electrode assembly. The lid was connected to a direct current (DC) voltage power supply (Bio-Rad, UK) and run at a constant 250 volts (V) for 30 min. The gels were then removed from the tank and glass plates, placed into an empty tip box on a shaker and initially fixed for 15 min in 50% (v/v) methanol and 10% (v/v) acetic acid, then stained for 15 min using 0.25% (w/v) Coomassie brilliant blue R-250, 50% (v/v) methanol and 10% (v/v) acetic acid. Finally the gels were destained using 10% (v/v) methanol with 5% (v/v) acetic acid for a few changes on a shaker and then finally a digitising picture was taken with a Fuji digital camera system, using the Luminescent image analyser LAS-1000 plus (Fuji Film, Japan). Gel images were imported into Adobe Photoshop CS5 version 12.0.2 (Adobe Systems Inc., US) and Keynote version 5.1.1 (Apple Inc, US) for processing to adjust brightness, contrast and merge samples from separate gels as necessary.

2.1.2.9 Semi-dry immunoblotting.

Gel electrophoresis was carried out. Gels were removed from the tank after electrophoresis and then immediately transferred into buffer B (0.025 M Tris and 20% (v/v) methanol), alongside an equal dimension 0.45 µm pore size nitrocellulose membrane. 18 pieces of Whatman 3MM Chr chromatography papers were cut per gel transfer. 6 pieces were soaked in buffer A (0.3 M Tris and 20% (v/v) methanol), 3 pieces in buffer B (0.025 M Tris and 20% (v/v) methanol) and 9 pieces in buffer C (0.025 M Tris, 14 mM glycine and 20% (v/v) methanol). The Transblot SD Semi-Dry Transfer Cell machine (Biorad, Herts, UK) was set up as follows from bottom to top: papers soaked in buffer A, papers soaked in buffer B, nitrocellulose from buffer B, gel from buffer B and finally the papers soaked in buffer C. Transfer was carried out at a constant 0.8 mA per cm^2 for 90 min. Membranes were removed, washed

extensively in water in a weighing boat on a shaker and then stained in the absence of light in Ponceau stain (0.5% (w/v) Ponceau S and 1.0% (v/v) acetic acid) for 5 min. The membranes were rinsed again and transfer assessed. The membranes were then blocked at room temperature for 2 hr in blocking solution (3% (w/v) BSA, 5% (w/v) non-fat milk powder in TTBS (0.1% (w/v) Tween-20, 25 mM Tris-HCl (pH 7.4) and 150 mM NaCl)). The membranes were removed and washed three times in TTBS for 5 min intervals. Then primary antibodies (Abs) were incubated with the membranes in polyethylene bags, sealed with a sealer (Mercier Corporation, Taiwan), diluted in 5% (w/v) BSA in TTBS overnight at 4 ^{0}C, on a rotating wheel (Agar Scientific, UK). The membranes were washed three times in 5% (w/v) non-fat milk powder in TTBS for 5 min intervals and then incubated with secondary Abs for 2 hr at 4 ^{0}C using a 1000-fold dilution in 5% (w/v) BSA-TTBS solution with polyclonal goat anti-mouse IgG immunoglobulins.HRP (1.3 g/L) (Dakocytomation, Denmark). Five washes with 5% (w/v) non-fat milk powder-TTBS was then carried out and the membranes developed in the absence of light for 5 min with ECl I (100 mM Tris-HCl (pH 8.0), coumaric acid and luminol) and ECl II (100 mM Tris-HCl (pH 8.0) and 0.02% (v/v) H_2O_2) solutions mixed together. The LAS-1000plus Fuji luminescent image analyser (FujiFilm, Japan) was used with the chemiluminescence setting and enhanced chemiluminescence for a minimum of 1 min for development.

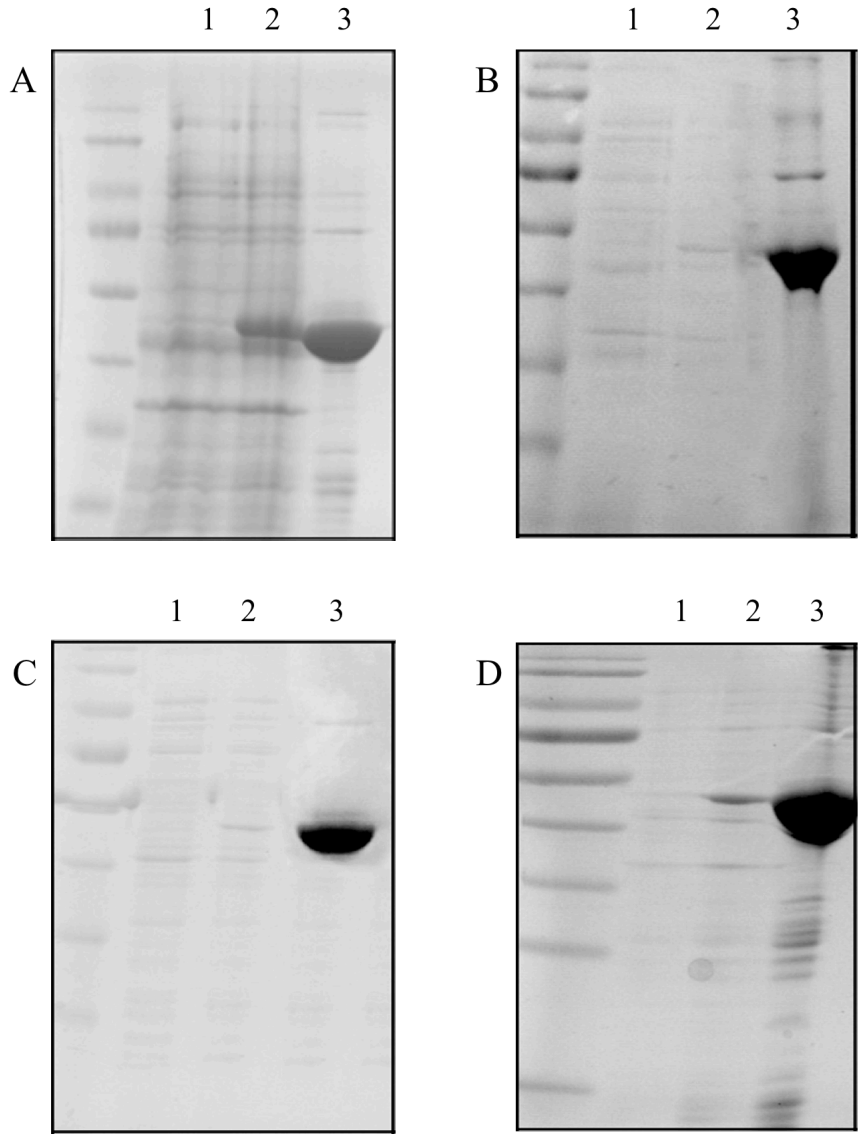

Figure 2.1 GFAP inductions and extractions.

A) WT, B) R79C, C) R239H and D) R416W human GFAP pre- (lane 1), post- (lane 2) IPTG inductions and solubilised proteins after inclusion body preparations (lane 3) were run on gels. Pre- and post- inductions from 1 mL bacterial culture samples, taken from the larger cultures, were spun at $420xg_{av}$ for 5 min and the pellets were resuspended in 100 µL of 2X SB. 5 µL pre- and 2.5 µL post- inductions were loaded to the 12% (w/v) acrylamide gel. The solubilised fraction obtained after an inclusion body preparation, extraction, homogenisation and centrifugation is in the final lane constituting 1 µL of sample with 1 µL 2X SB and as can be seen, the target protein constitutes more than 80% of the total protein. Protein ladder molecular weights are from the pre-stained Pageruler^{TM} protein ladder #SM0671 and are: 170, 130, 95, 72, 55, 43, 34, 26, 17 and 10 kDa, from the top to the base of the gel.

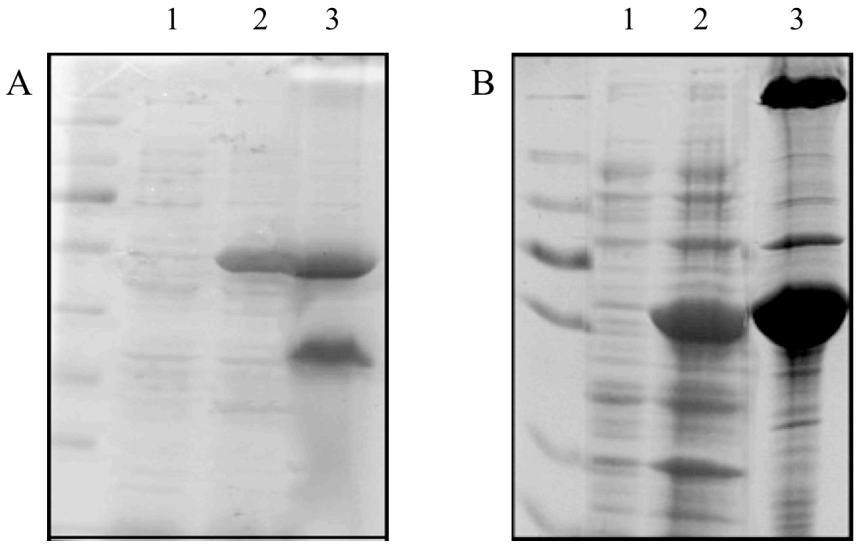

Figure 2.2 Desmin and vimentin inductions and extractions.

In gel A) WT human desmin and in gel B) WT human vimentin pre- (lane 1), post- (lane 2) IPTG inductions and solubilised proteins (lane 3) are shown. The marker lane on the left-hand side of the gel corresponds to the same marker weights mentioned in Figure 2.1. Pre- and post- inductions from 1 mL bacterial culture samples were taken from 500mL cultures, spun at 2,000 rpm ($420xg_{av}$) for 5 min and the pellets were resuspended in 100 µL 2X SB. 5 µL pre- and 2.5 µL post-inductions were loaded to the 12% (w/v) acrylamide gel. The solubilised fraction is in the final lane constituting 1 µL of sample with 1 µL 2X SB.

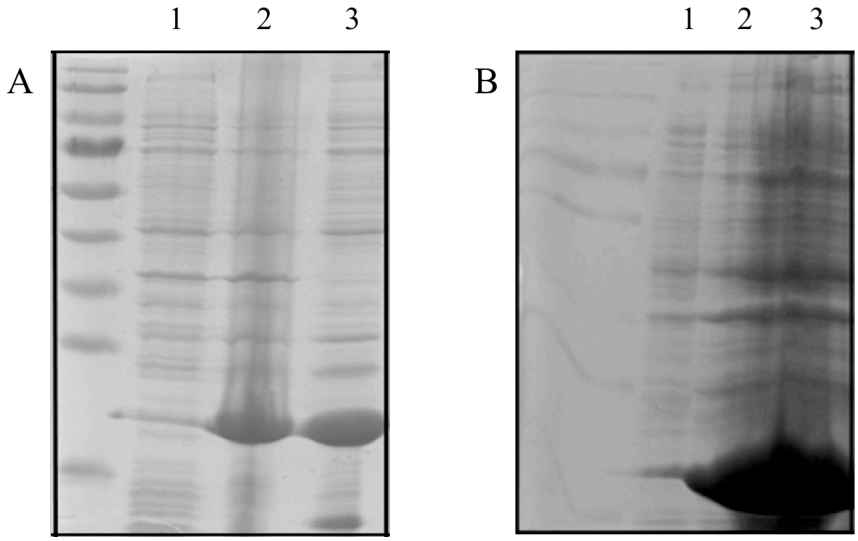

Figure 2.3 CRYAB inductions and extractions.

A) WT human CRYAB and B) R120G human CRYAB pre- (lane 1), post- (lane 2) IPTG inductions and solubilised proteins (lane 3) are shown. Pre- and post-inductions from 1 mL bacterial culture samples were taken from 500mL cultures, spun at 2,000 rpm ($420xg_{av}$) for 5 min and the pellets were resuspended in 100 µL 2X SB. 5 µL pre- and 2.5 µL post- inductions were loaded to the 12% (w/v) acrylamide gel. The solubilised fraction is in the final lane constituting 1 µL of sample with 1 µL 2X SB.

A

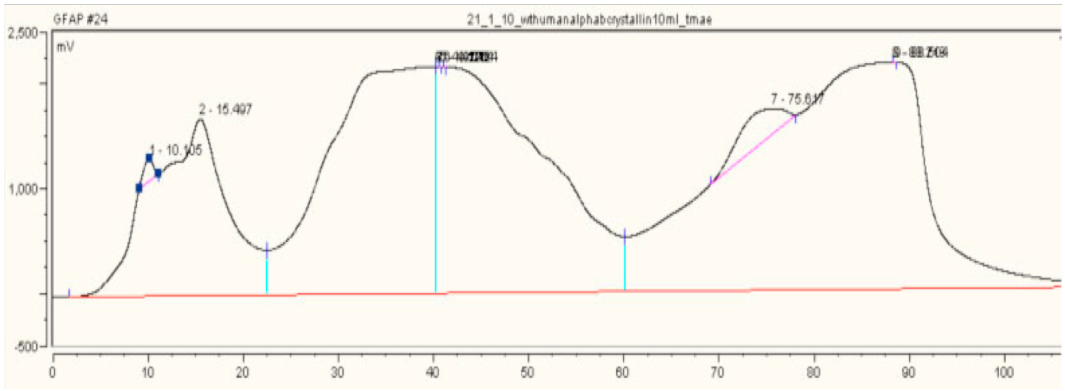
GFAP #24
21_1_10_withumanalphabcrystallin10ml_tmae
mV
2,500
1,000
-500
2 - 16.497
7 - 75.647
0
10
20
30
40
50
60
70
80
90
100

B

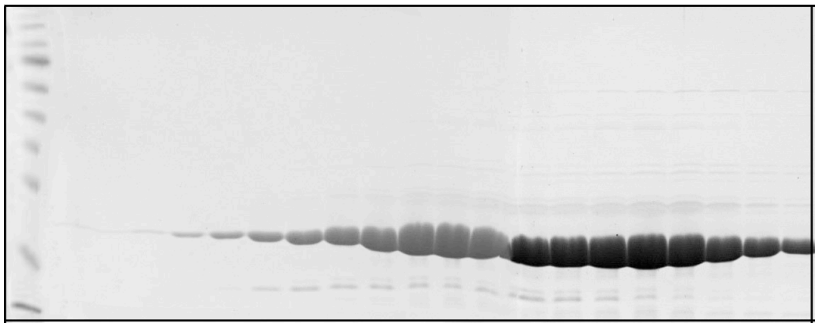

C

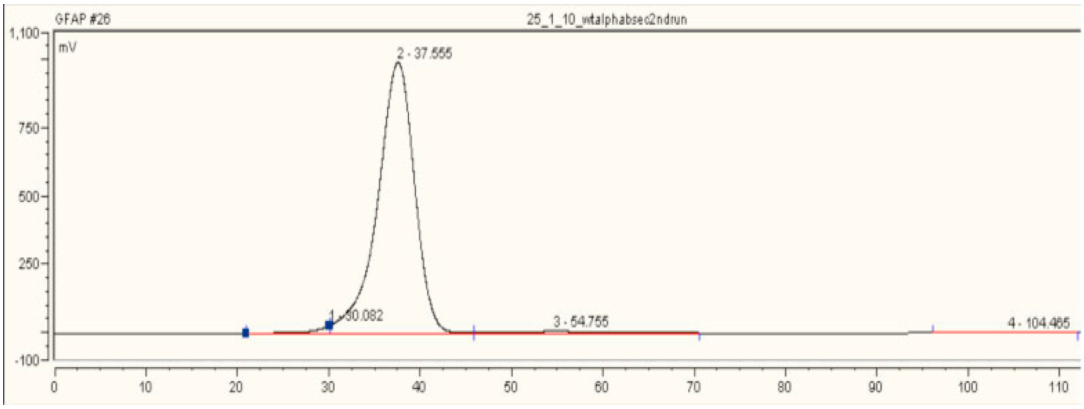
GFAP #26
25_1_10_wtalphabsec2ndrun
mV
1,100
750
500
250
-100
2 - 37.555
3 - 54.755
4 - 104.465
0
10
20
30
40
50
60
70
80
90
100
110

D

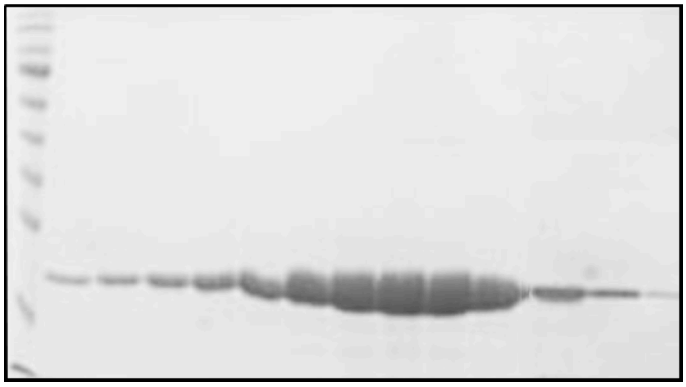

Figure 2.4 WT CRYAB purification.

The A) human WT CRYAB TMAE purification chromatogram (the y-axis shows the absorbance (mV) and the x-axis shows the time (min)) and B) gel of the elution of fractions 1-20 are shown. Fractions 4-20 were pooled together from the TMAE column and then applied to a size exclusion column deriving the C) human WT CRYAB size exclusion column purification chromatogram and D) gel of the elution of fractions 30-42. Fractions 30-42 were pooled from the size exclusion column. Gel fractions were run as 10 µL from 20 µL sample + 20 µL 2x SB.

A

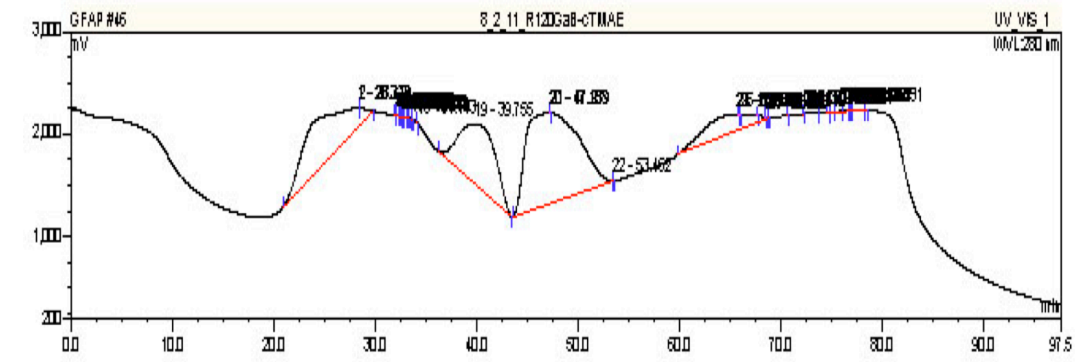
GFAP #45
8_2_11_R120Gal8-cTMAE
UV_VIS_1
mV
WVL:280 nm
3,000
2,000
1,000
200
0.0
10.0
20.0
30.0
40.0
50.0
60.0
70.0
80.0
90.0
97.5
min

B

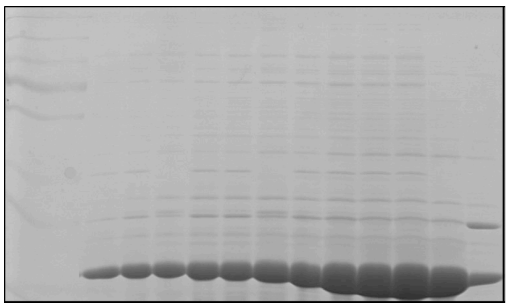

C

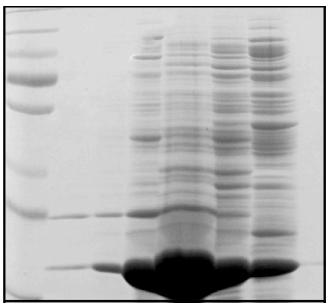

D

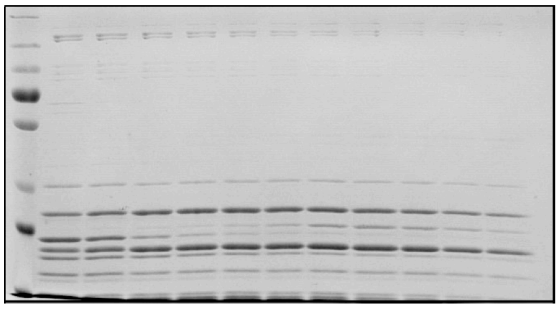

E

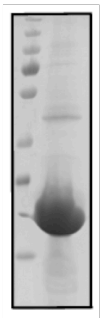

F

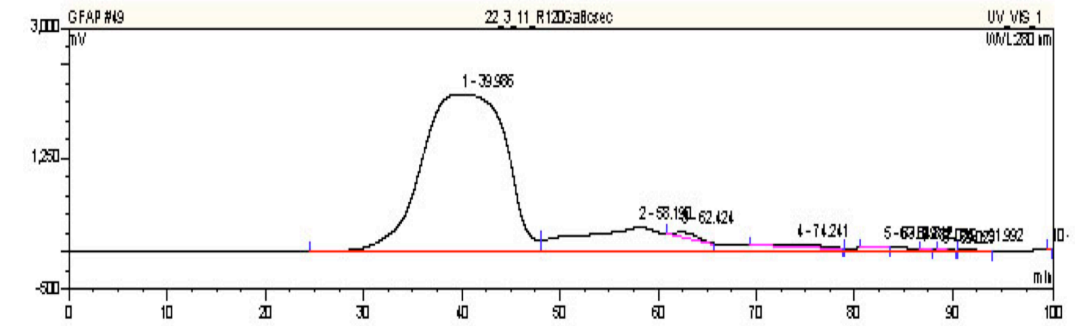
GFAP #49
22_3_11_R120Gal6sec
UV_VIS_1
mV
WVL:280 nm
3,000
1,250
-500
1 - 39.986
2 - 58.198
62.424
4 - 74.241
0
10
20
30
40
50
60
70
80
90
100
min

Figure 2.5 R120G CRYAB purification.

The A) human R120G CRYAB TMAE purification chromatogram alongside B) the first gel of the elution of fractions 1-23 (every other fraction), C) the second gel with fractions 14-39 (every fifth fraction) and D) the third gel of fractions 59-69 is shown. Fractions 1-15 and 24-34 were pooled from the TMAE column and then applied to a second column deriving the F) human R120G CRYAB size exclusion column purification chromatogram and E) gel of the pooled fractions 37-46. Note how the size exclusion peak for R120G CRYAB is much broader than for WT CRYAB thus showing there is more polydispersity.

A

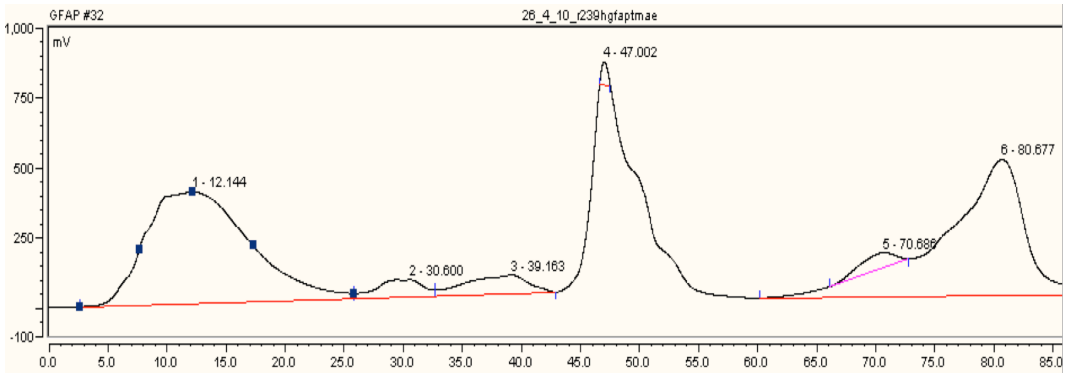

B

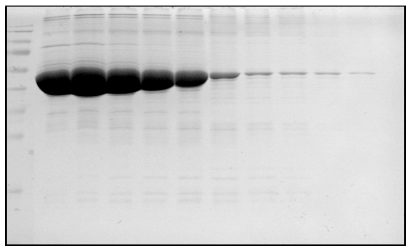

C

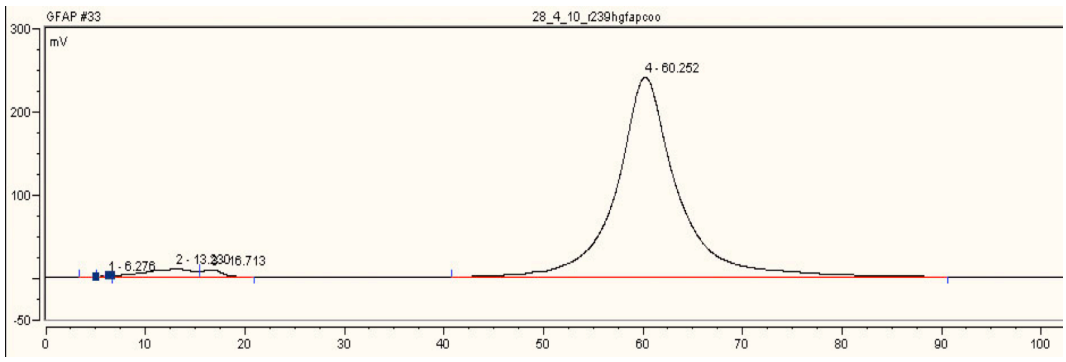

D

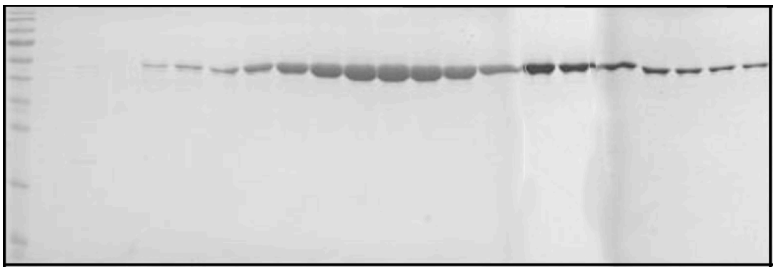

Figure 2.6 R239H GFAP purification.

The A) human R239H GFAP TMAE purification chromatogram is shown alongside the B) gel of the elution of fractions 46-55. Fractions 45-51 were pooled from the TMAE column and run over a second column to derive the respective C) R239H GFAP COO^- column purification chromatogram and D) gel of the elution of fractions 51-71. Fractions 56-70 pooled from COO^- column.

A

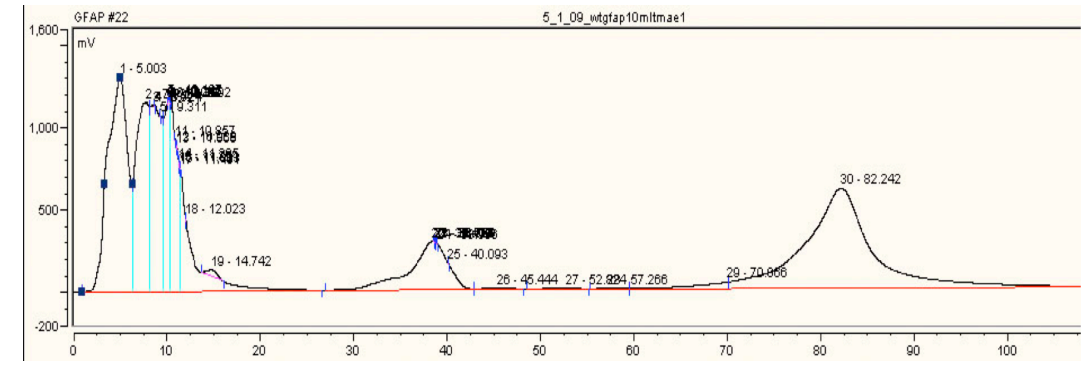

B

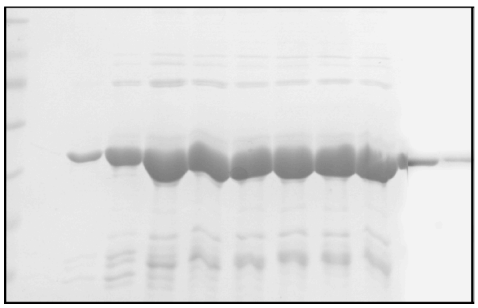

C

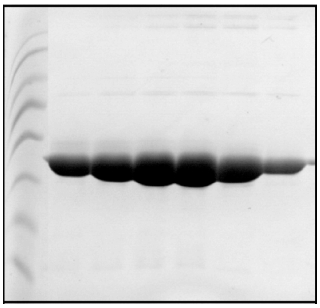

D

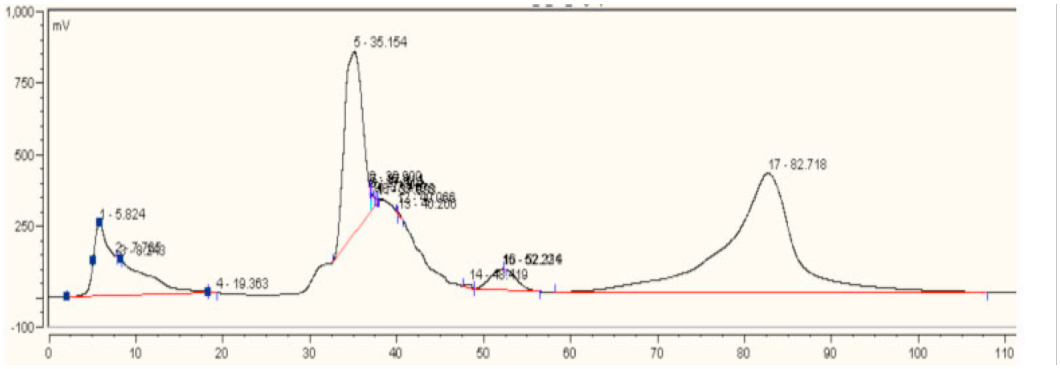

E

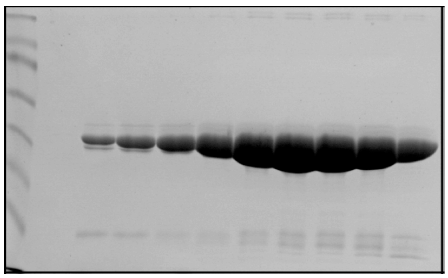

Figure 2.7 WT GFAP purification.

The A) human WT GFAP TMAE purification chromatogram is shown alongside B) the first gel of the elution of fractions 1-2, 5 and 6-13 and the C) second gel with fractions 35-40. Fractions 2-12 and 35-40 were pooled from the TMAE column and a second column was used to derive the D) WT GFAP COO^- column purification

chromatogram and E) gel of the elution of fractions 35-44. Fractions 36-46 were pooled from the COO^- column.

A

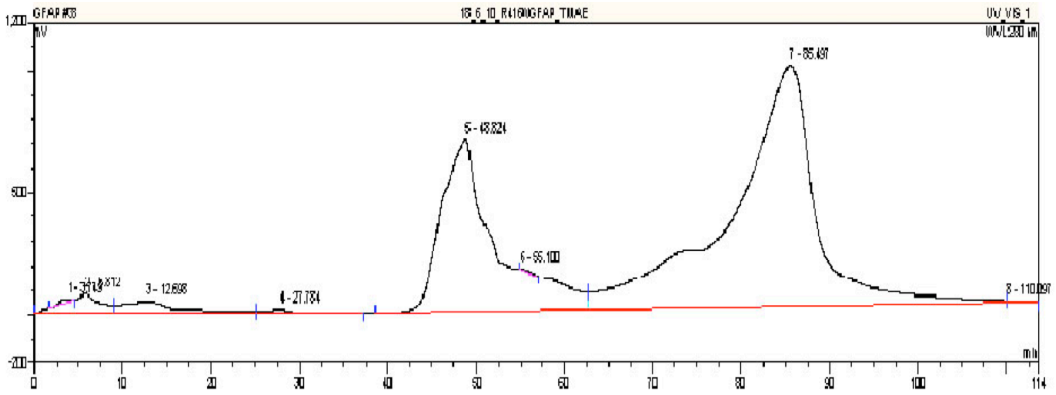

B

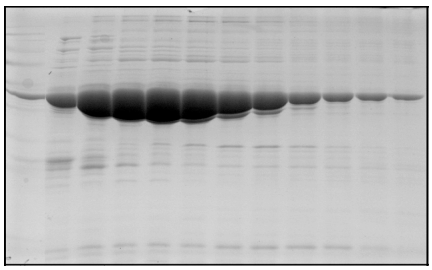

C

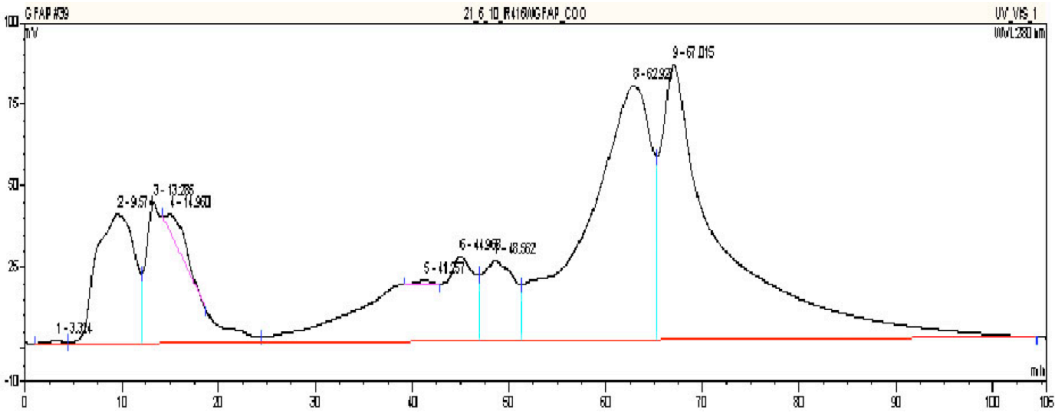

D

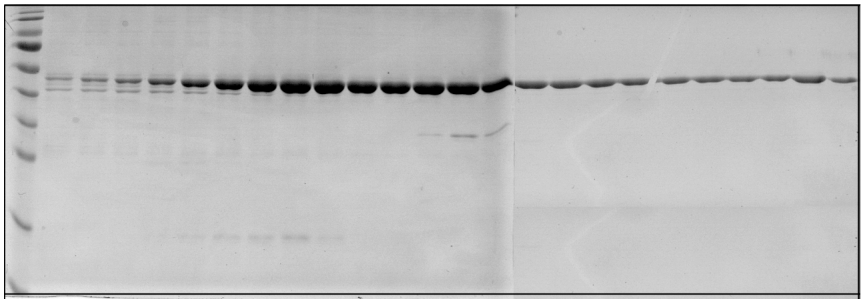

Figure 2.8 R416W GFAP purification.

The A) human R416W GFAP TMAE purification chromatogram is shown and the B) eluted fractions 46-56. Fractions 46-56 were pooled. The second column C) R416W GFAP COO^- purification chromatogram is also shown and D) the gel of the eluted fractions 56-79. Fractions 58-79 were pooled from the COO^- column.

A

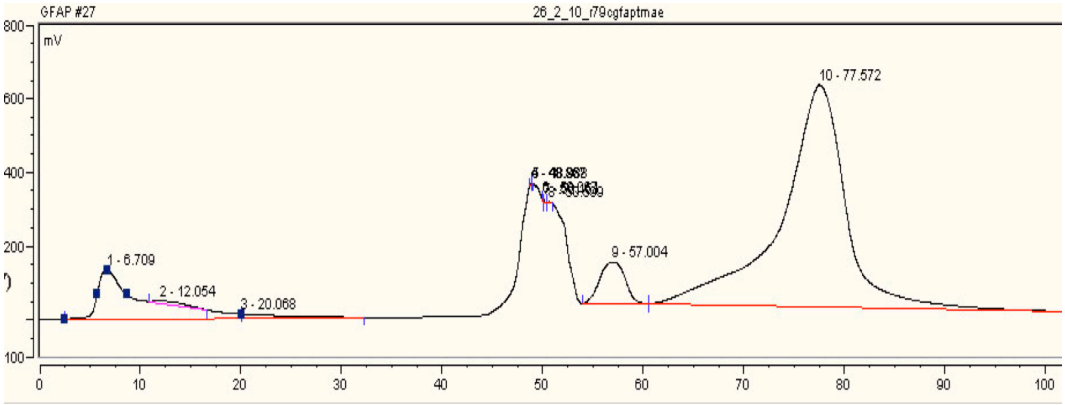

B

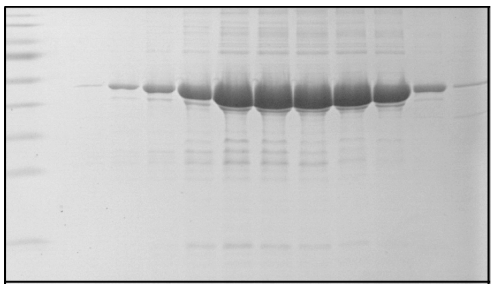

C

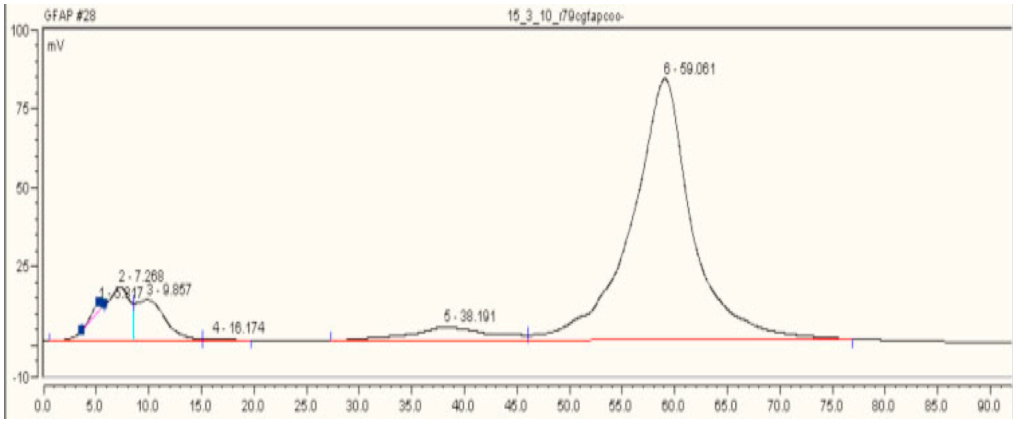

D

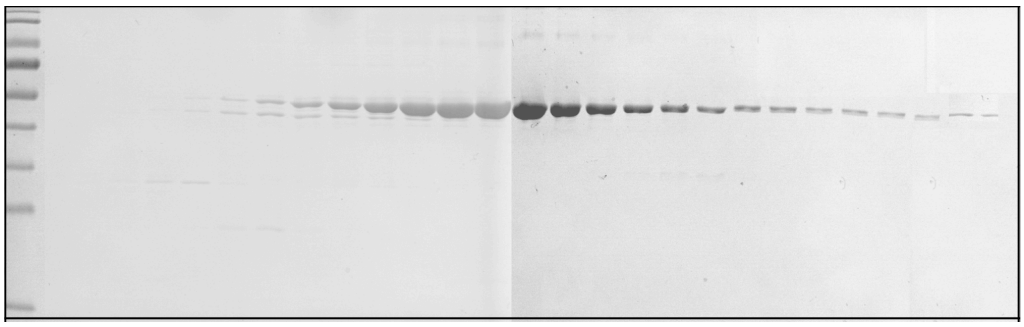

Figure 2.9 R79C GFAP purification.

The A) human R79C GFAP TMAE purification chromatogram is shown with the B) gel of the eluted fractions 45-56. Fractions 47-55 were pooled from the TMAE. The C) R79C GFAP COO^-column purification chromatogram and D) the gel of the elution of fractions 49-75 is shown. Fractions 58-74 were pooled from the COO^- column.

A

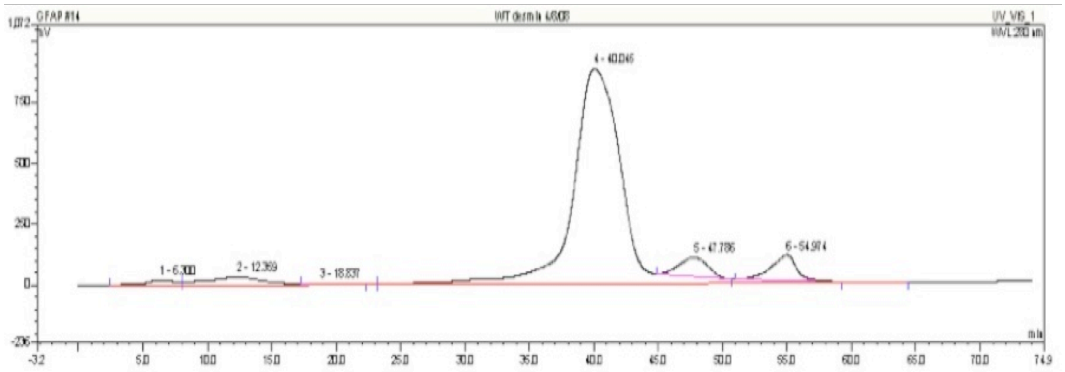

B

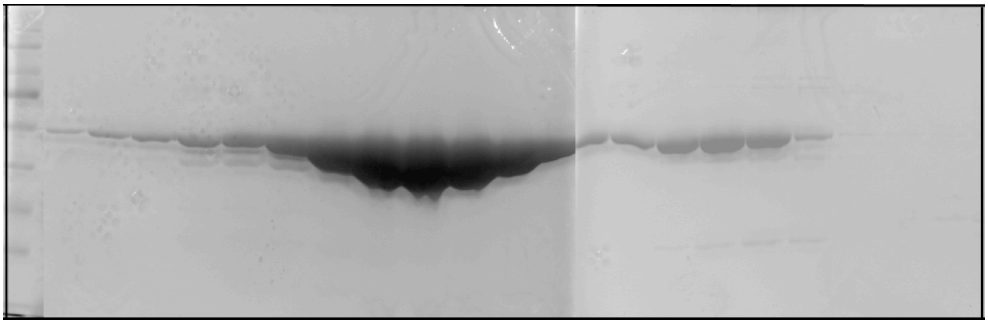

Figure 2.10 WT desmin purification.

The A) human WT desmin TMAE purification chromatogram is shown alongside the B) gel of eluted fractions 33-53. Fractions 35-49 were pooled. The desmin was already more than 90% pure and therefore no COO^- column was used.

A

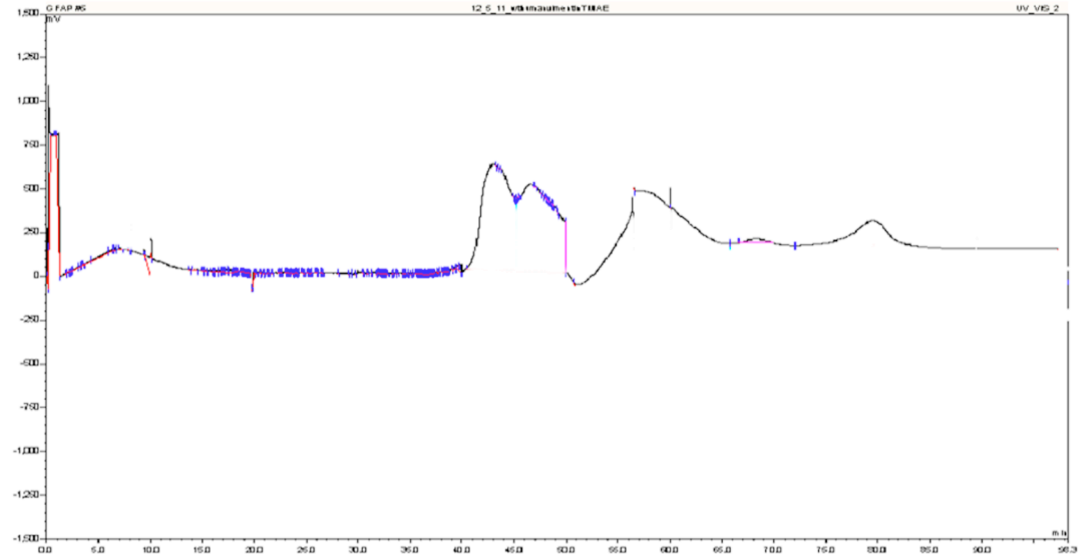

B

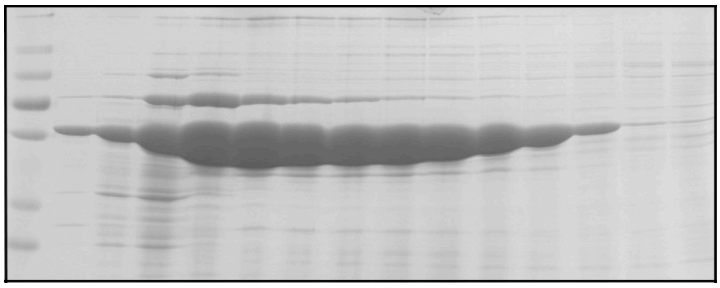

C

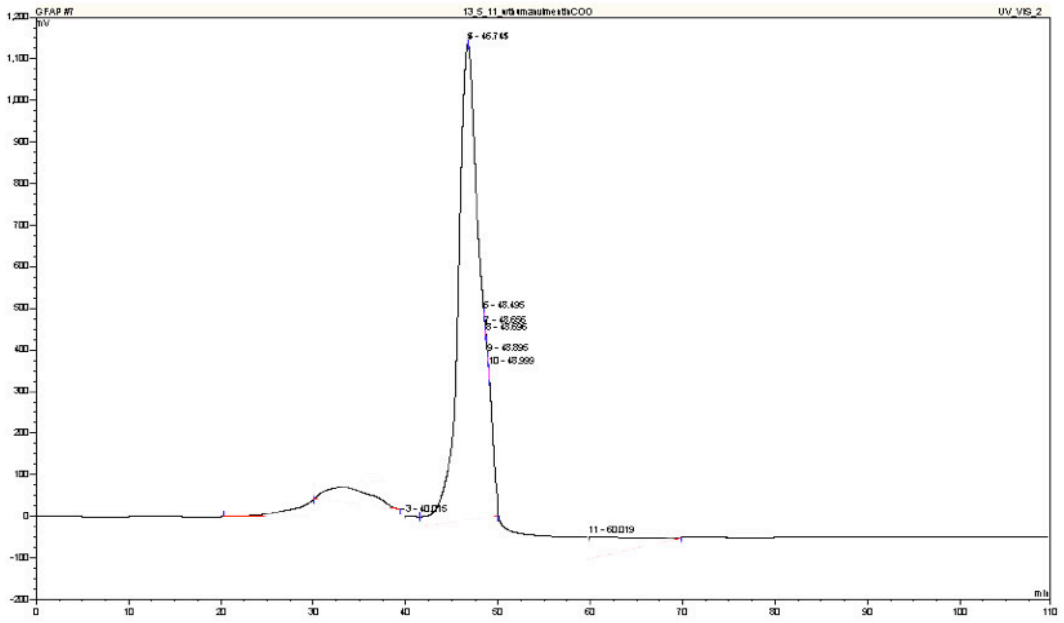

D

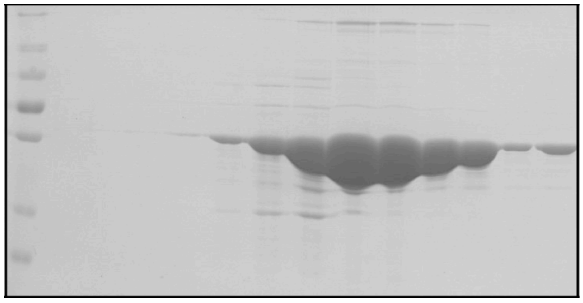

Figure 2.11 WT vimentin purification.

The A) human WT vimentin TMAE purification chromatogram is shown with the B) gel of the eluted fractions 40-53. Fractions 40-51 were pooled from the TMAE. The second purification column C) WT vimentin COO^- column purification chromatogram is shown with the D) gel of the elution of fractions 40-52. Fractions 44-52 were pooled from the COO^- column.

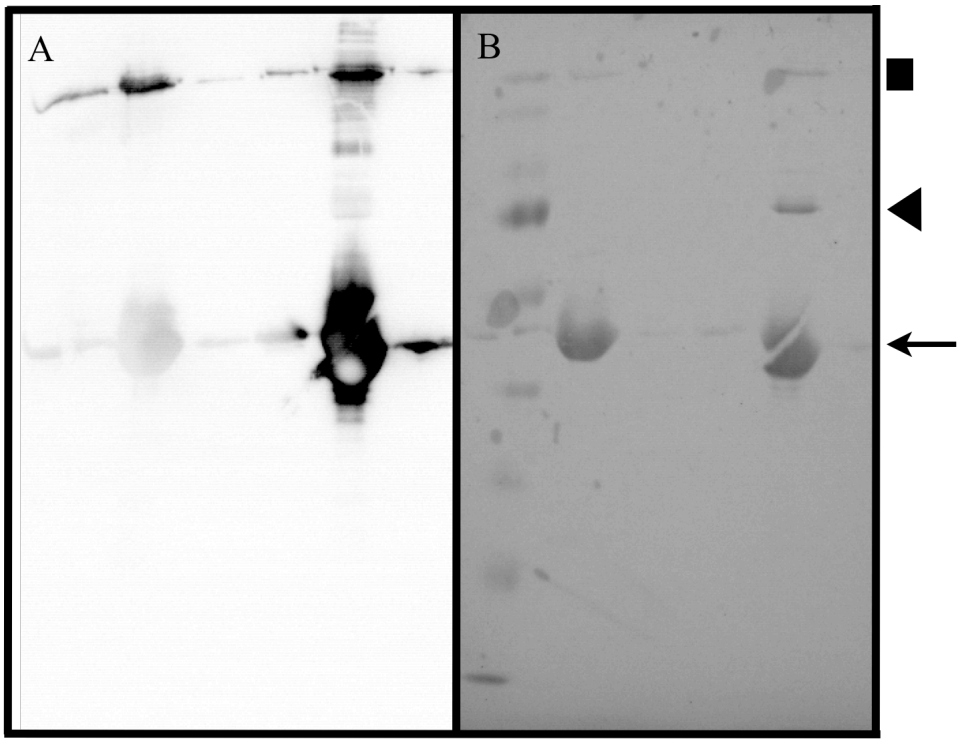

Figure 2.12 WT GFAP dimers.

An A) immunoblot of two pooled purified fractions from a TMAE column of WT GFAP is shown alongside its corresponding B) Ponceau-stained membrane with the GFAP monomer bands (in line with the arrow), the *E.coli* contaminating band (in line with the arrowhead and the 72 kDa marker band) and the GFAP dimer (in line

with the square) being shown (Quinlan and Franke, 1983). The GFAP monomer from the left lane in A) hasn't been detected on the blot likely due to irreversible luminol substrate exhaustion caused by too much HRP in its vicinity, the result of too much sample. Primary mouse monoclonal SMI-21 anti-human GFAP Ab was used at a 5000-fold dilution.

For all of the different protein TMAE gel fractions run, it can be seen that there are many other bands present in the lanes alongside the target protein bands. In the case of WT and R79C GFAP TMAE column fractions, the band in alignment to the 72 kDa marker band was analysed as to whether it consisted of a higher oligomer of GFAP protein or whether it was a different protein and was sent for MALDI analysis. It was shown that the band corresponded most likely to a Hsp70 chaperone in the *Shigella flexneri* 2a str. 301, using a MASCOT search (Matrix science) however the heat shock protein will be from the *E.coli* BL21 transformation host. The band above the 170 kDa marker corresponds to a dimer of GFAP since an immunoblot using the SMI-21 GFAP-specific monoclonal Ab gave a signal positive for this band. The COO^- column separated this from the GFAP protein on further purification. The second COO^- column in all cases appeared to remove most of the contaminating bands from the target proteins (Figure 2.4-2.9, 2.11) and these fractions were then pooled and used in the assembly experiments.

2.1.2.10 Assemblies.

Pooled protein fraction concentrations were estimated using a bichinchoninic acid (BCA) protein assay kit (Thermo Scientific Pierce®, Rockford, USA) and in some instances these were concentrated using an Amicon Ultra Centrifugal filter device with a 10 kDa molecular weight cut-off filter (Millipore, Bedford, MA). Pooled protein fractions were defrosted, vortexed and mixed with the initial buffer solution relevant to the assembly method being used and with any other proteins if co-assembly was being carried out. The protein samples were then put into 9.3 kDa molecular weight cut-off rehydrated cellulose membrane dialysis tubing (Sigma-Aldrich, UK) after rinsing with de-ionised water from storage at 4 ^{0}C in 20% (v/v) ethanol and clipped with dialysis clips at both ends. The samples were then

transferred into the buffer solutions. Each buffer solution had a magnetic flee and was placed on a magnetic stir bar so that buffer exchange was promoted across the dialysis tubing membranes of the samples, using a minimum of a 1:1000 ratio of sample: buffer volume.

GFAP was assembled at 0.4 mg/mL through a series of buffer changes to remove the chaotropic denaturant urea and increase the salt ionic strength (*I*) promoting the association of the coiled coils in the protein in much a similar manner used by others (Der Perng et al., 2006). This method was used in the imidazole assembly method (Figure 2.14) and in addition a Tris assembly method (Figure 2.13), similar to Hsiao et al. (2005), was used and comparisons made between the two (Hsiao et al., 2005). For co-assemblies with WT CRYAB, a 1:1 molar ratio of WT CRYAB (20.2 kDa): WT GFAP (49.9 kDa) was used with a 0.16 mg/mL concentration of sHSP. All buffer steps were carried out at 23 ^{0}C (room temperature) except the final overnight assembly buffer dialysis that was carried out at increased temperatures of 37 and 44, in some cases and the 10 mM Tris-HCl (pH 8.3) penultimate step in the GFAP imidazole assembly method, at 4 ^{0}C. The final temperatures were of the incubator ambient temperature not accounting for local heating effects from the magnetic stirrer, which resulted in approximately 5 ^{0}C increases. The times taken for each buffer change in the assembly protocols were a minimum of 2 hr, but no longer than 4 hr, apart from the final buffer dialysis which took 16 hr overnight in all cases. The pH values refer to those of the stock Tris-HCl solutions and not the final pHs upon addition of salt, which follows the previous standard methodology of assembly carried out in this laboratory (Perng et al., 1999a). $MgCl_2$ was included in the Tris final assembly buffer, as it has been shown to be necessary for GFAP filament formation (its absence results in defective compaction) however it was not necessary for the imidazole method as this chemical already binds magnesium ions that are present on the plastic surfaces of the beakers used for assembly.

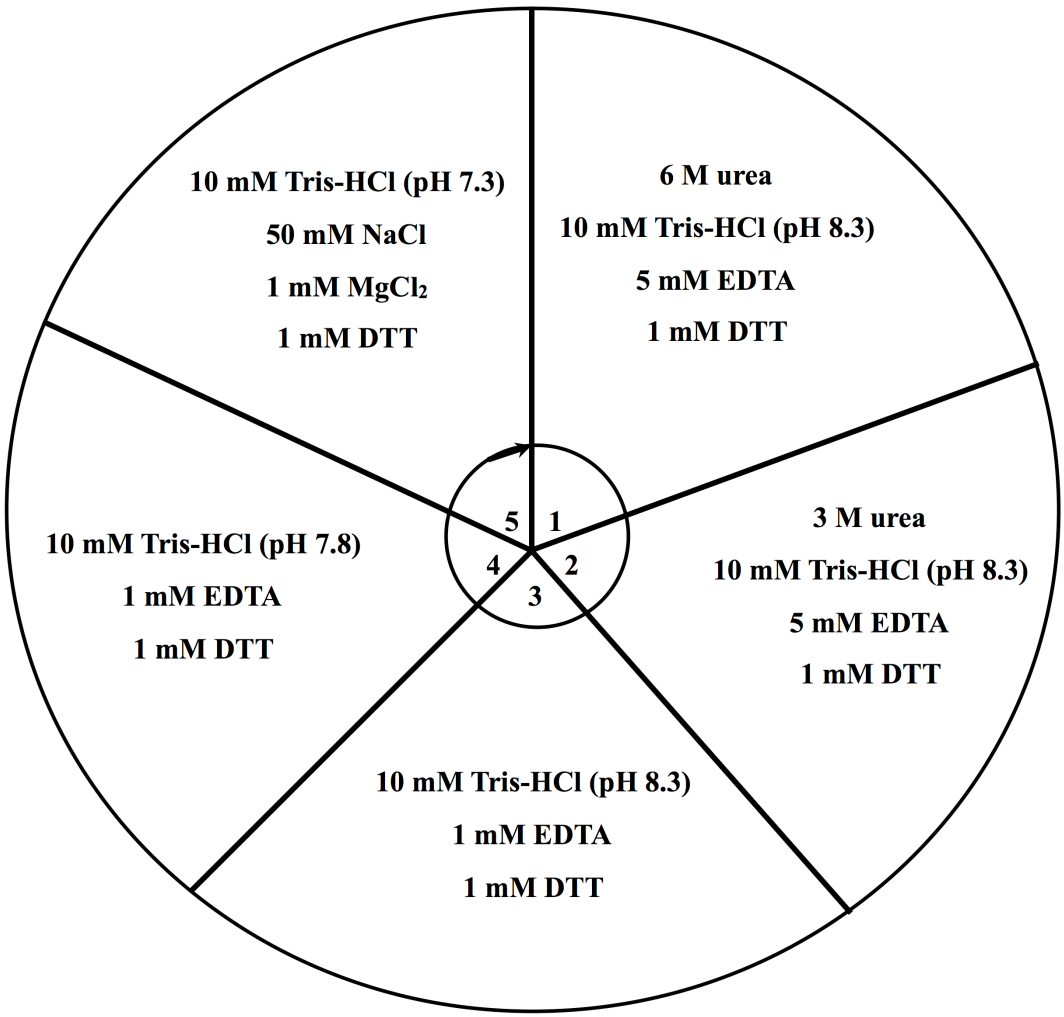

Figure 2.13 GFAP Tris assembly method.

Assembly was carried out sequentially clockwise through steps 1-5. Buffer volumes were 0.5 L for the initial buffer (with a 2,500-fold excess of dialysis buffer to sample volume) and then 1 L (with a 5,000-fold excess of dialysis buffer to sample volume) for all the buffers after with dilutions made for the 6 to 3 M drop in concentration of urea. The final pH was measured after all of the salts were added to buffer 5 and it was found to have increased to pH 7.4. The *I* of buffer 5 is equal to 0.0607 M (3 sf), as detailed in the appendix.

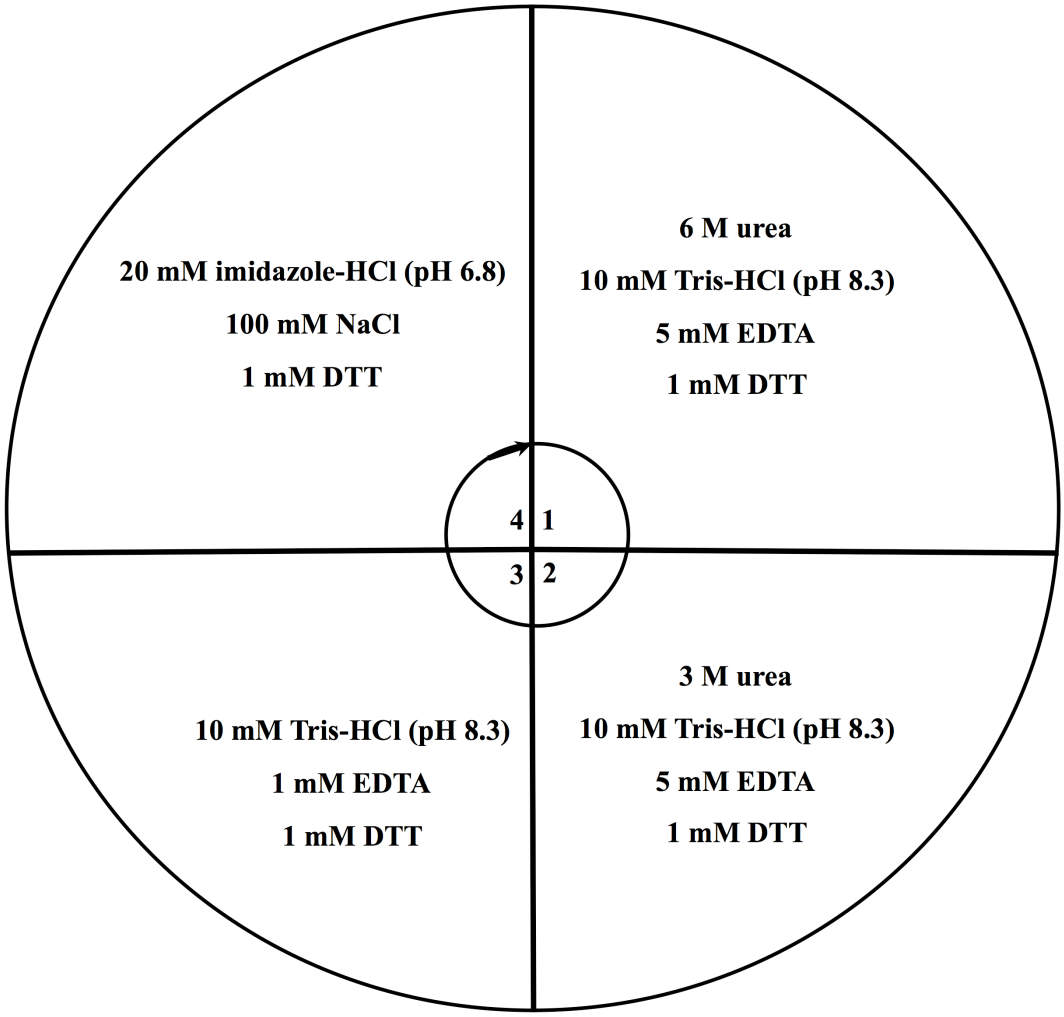

Figure 2.14 GFAP imidazole assembly method.

Assembly was carried out sequentially clockwise through steps 1-4. Buffer volumes were 0.5 L (with a 2,500-fold excess of dialysis buffer to sample volume) for the initial buffer and then 1 L (with a 5,000-fold excess of dialysis buffer to sample volume) for all the buffers after. The *I* for buffer 4 in this method is 0.111 M (3 sf).

WT human recombinant GFAP was assembled through either the Tris assembly or imidazole assembly protocol forming 10 nm width filaments as shown below (Figure 2.15). CRYAB forms oligomers of 1-2 nm in width. The lengths of the WT GFAP filaments seemed to be in the approximate range of 2 to 6 μm. The filaments are morphologically very similar imaged with the transmission electron microscope (TEM), assembled through either of the two assembly procedures although the sedimentation assay data show that there are differences apparent in the filament properties.

2.1.2.11 TEM grid preparation and image collection.

Cleaved mica (Agar Scientific, UK) was placed onto a microscope slide on double-sided sticky tape (Scotch, USA), with the clean side facing upwards and carbon coated using the Cresington evaporation supply LT750 308 (Cresington Ltd., UK), alongside a Cresington MTM10 thickness monitor (Cresington Ltd., UK). 20 μL of assembled material was added to 320 μL final overnight assembly buffer in an eppendorf lid (20 μg/mL final concentration) and mixed thoroughly, then using Valentine's method a carbon-coated mica sheet was used to trap some sample between the mica and carbon film which was lifted off by surface tension, rinsed in water and then finally placed into a 1% (w/v) uranyl acetate solution (Harris and Horne, 1991). Between each step the edge of the mica was placed carefully against some Whatman 3MM Chr chromatography paper (Whatman, NJ, USA) to remove excess liquid by capillary action. A 400 square copper grid (Agar Scientific, UK) was used to lift some of the final negatively stained sample off the surface of the uranyl acetate solution for viewing using the Hitachi H7600 TEM, with an accelerating voltage of 100kV.

2.1.2.12 Sedimentation assays.

To assess filament-filament interactions, low speed sedimentation assays were carried out utilising 50 μL of assembled protein material. These were centrifuged for 10 min at 2,450xg_{av} and 23 ^{0}C in an Eppendorf 5417R centrifuge (Eppendorf, US). The supernatant was carefully separated from the pellet and 150 μL 1X SB added to the pellet and 100 μL 1.5X SB added to the 50 μL supernatant, to make the two

fractions equivalent. Then the sample was loaded as 10 µL of supernatant and pellet fraction per gel lane, after resuspension of the pellet and vortexing and boiling of both fractions at 95 ^{0}C for 5 min.

For high speed sedimentation assays a similar method was used to before (Djabali et al., 1997). 50 µL of assembled sample was layered on top of 50 µL of a 0.85M sucrose cushion and centrifuged at 59,875.2xg_{av}, 23 ^{0}C for 30 min, in the TLS-55 rotor, in the TL-100 Bench Top ultracentrifuge (Beckman Coulter, UK). The supernatant was carefully removed from the pellet and 150 µL 1X SB was added to the pellet and 50 µL 3X SB added to the 100 µL supernatant. 10 µL of supernatant and pellet fractions were loaded per gel lane, after resuspending the pellet and vortexing and boiling both fractions at 95 ^{0}C for 5 min.

2.1.2.13 Gel protein band quantification.

Digitising pictures of the gels run of sedimentation assays were taken and analysed in the ImageGauge V4.23 program (FujiFilm, Japan). Boxed areas were made around the sample bands and these were duplicated and positioned close to each protein band for use as a background reading, using the Quant mode. The Quant Result option then presented a table with each box and their absorbance units so each sample band and its respective background could be grouped together. The background absorptions were then subtracted from each of the sample band absorptions by assigning the background box as the blank to give a final reading of absolute values (AU-BG) used to calculate proportions in the supernatant and pellet fractions.

2.1.2.14 Statistical analysis.

For Student's T test analysis, data derived from gel quantifications (independent repeats of a minimum of n = 3) were transformed using an arcsine-square root transformation (using ASIN and SQRT functions in Excel 2008 (Microsoft Corporation, US)), taking the arcsine of the square root of numbers, for converting the proportional data into normalised data for T-test analysis, as proportions are distributed binomially (Zar, 1996). Data were tested for normality in the SPSS Statistics version 21 programme (IBM, US) using a Shapiro-Wilk test and those

groups which didn't have a normal distribution were tested using a Mann-Whitney U test as explained in the appendix.

For data with a normal distribution, a two-tailed F test was then used to verify the variances were similar between the two samples of data compared for each test (Fowler Jim, 1998), using n-1 degrees of freedom v_1 and v_2 and p = 0.05. F values were calculated as s^2_1/s^2_2 with s^2_1 being the greater variance. For those samples that had an F value lower than the critical F value, a two-sided, type-2 (equal variance) Student's T-test was used and p values calculated for significance using Excel (Microsoft Corporation, US). Raw data and results are shown in the appendix. Averages of the data are represented as bar charts in the text, prepared using Keynote version 5.1.1 (Apple Inc., US).

2.1.3 Results.

	Observations	Page #s
Filament morphology	Mutant R79C GFAP forms ULF-like filaments. Mutant R239H GFAP forms aggregates made up of ULF-like filaments.	65
CRYAB influence on filament-filament interactions	CRYAB reduces R239H interactions after assembly in Tris buffer. CRYAB increases WT GFAP interactions after assembly in imidazole buffer.	69 72
CRYAB influence on filament assembly	CRYAB hinders WT GFAP formation through Tris assembly buffer, which is not seen after imidazole buffer assembly.	76 74
CRYAB-filament interactions (binding)	CRYAB increases its binding to GFAP with increased temperatures. Most binding is seen with the R239H mutant. The greatest binding to WT GFAP filaments occurs with imidazole buffer.	79 82
Influence of AxD-causing mutants R79C and R239H on WT GFAP filament assembly	R239H alters filament morphology at a 10% level whereas R79C alters filaments at a 50% level. The dominant effect is observed only at a 50% mutant level for R239H from low speed sedimentation assays.	85 84 87

Table 2.1 **Summary of chapter's main findings**.

2.1.3.1 WT and mutant GFAP morphology.

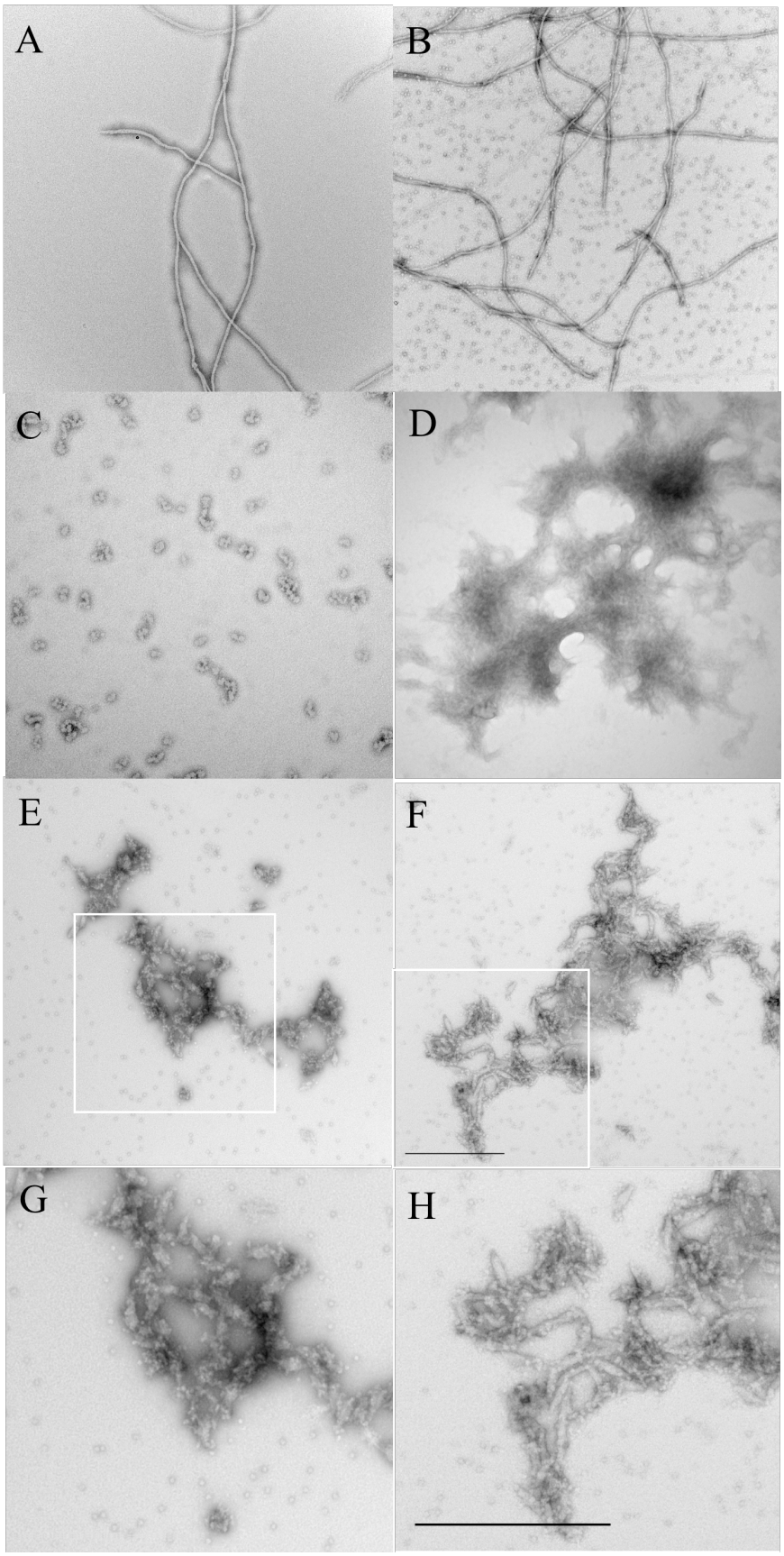

Figure 2.15 WT and mutant GFAP morphologies.

A) WT GFAP formed usual 10 nm wide filaments of a few μM in length and in B) were surrounded by CRYAB particles. Whereas C) R79C GFAP formed shortened filaments of similar lengths to ULFs. D) R239H formed aggregates when assembled alone. In the presence of CRYAB shown in E) and its inset of G), R79C had shorter filaments that could be seen to cluster together and in F) and the inset H) the substructure of the R239H aggregates could be seen more clearly with CRYAB, consisting also of shorter filaments. The scale bar is equal to 500 nm.

Two different buffer systems were used to assess WT and mutant GFAP, according to Figure 2.13 and 2.14.

The R239H GFAP forms aggregates that are difficult to see the sub-structure of (Figure 2.15 D)), however when CRYAB is added in a 1:1 molar ratio the filaments are separated much more and it can be seen that the filaments are much shorter in length than WT filaments; ranging approximately between 60-100 nm as measured in ImageJ 1.43r (National Institutes of Health, USA) (Colakoglu and Brown, 2009). It has been shown already that R239C forms filaments similar to WT GFAP and thus the positively charged, basic histidine group in the R239H mutant must influence how the unit length filaments anneal and compact (Hsiao et al., 2005). The R79C GFAP is assembly incompetent and forms unassembled protein that appear to be similar in length to unit length filaments and R239H; ranging approximately between 60-100 nm as measured in ImageJ 1.43r (National Institutes of Health, USA) (Figure 2.15 C)) and it appears to have an increased solubility in comparison to WT GFAP. WT CRYAB can be seen to form oligomers of approximately 20 nm in length (Figure 2.15 B)). Upon an increase in temperature to 44 ^{0}C, the R79C mutant GFAP can be seen to have more associations between the unassembled material (Figure 2.16 D)). WT GFAP filaments were also assembled through the imidazole assembly procedure (Figure 2.14) and the TEM images show the filaments are similar to those formed through Tris assembly (Figure 2.17).

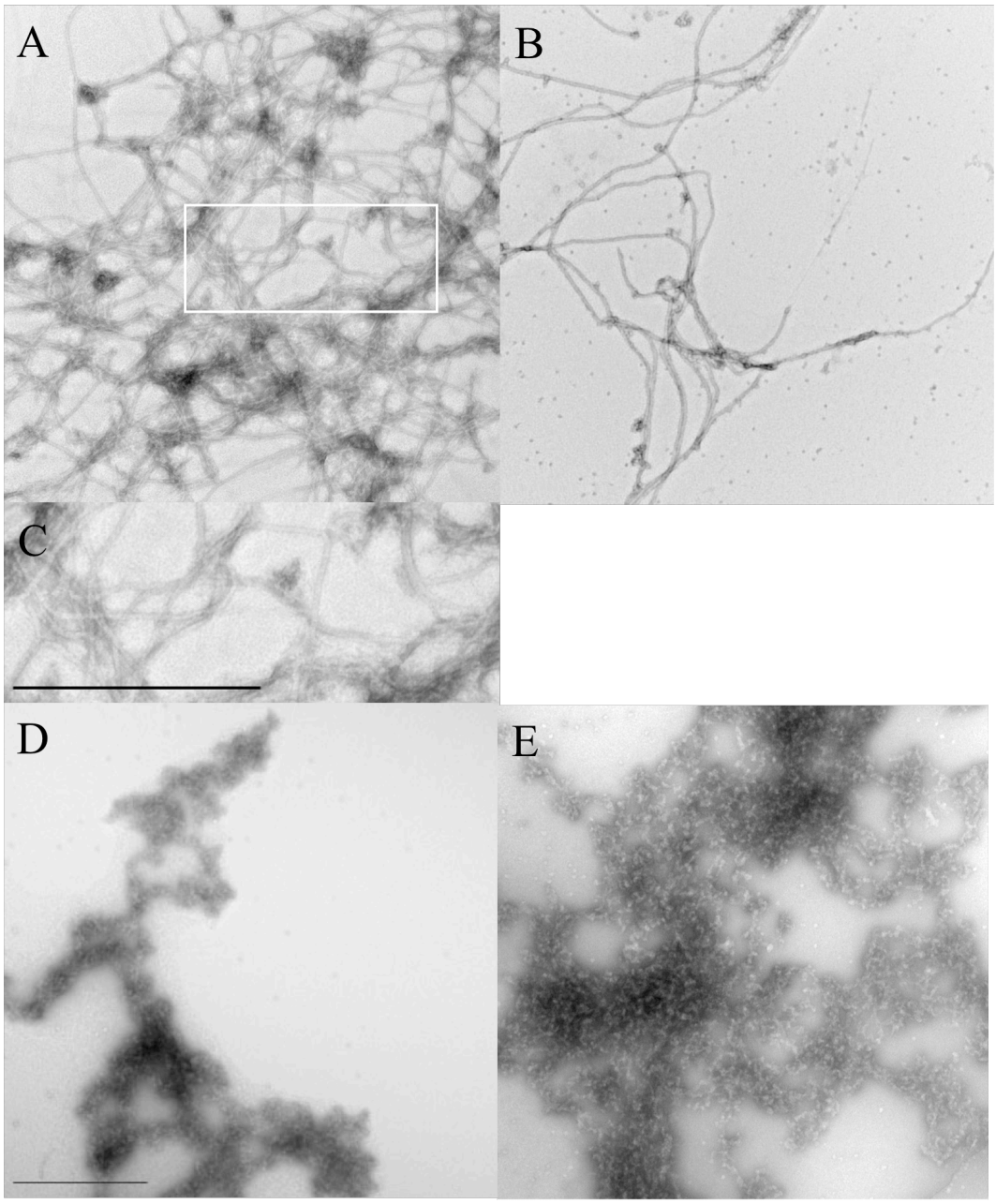

Figure 2.16 WT and mutant GFAP morphologies at 44 ^{0}C.

A) and C) WT GFAP forms similar filaments to those formed at room temperature. B) WT GFAP with CRYAB is also shown. D) R79C GFAP with CRYAB appears to have increased associations compared to room temperature assembled material and in E) the sub-structure of the aggregates can no longer be seen as clearly for R239H GFAP with CRYAB. The scale bar is equal to 500 nm.

The WT GFAP filament morphology from imidazole assembly (Figure 2.17) appears very similar to that from Tris assembly (Figures 2.15 and 2.16). Thus no apparent differences are obvious from TEM analysis. However sedimentation assay analysis in the following sections shows the different filament properties.

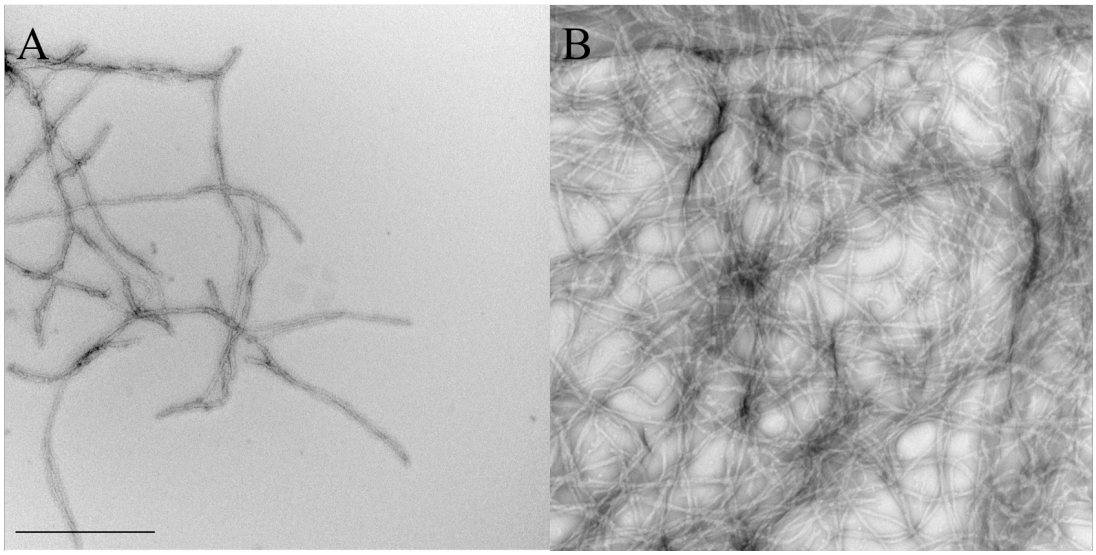

Figure 2.17 WT GFAP filaments after imidazole assembly.
A) WT GFAP and B) WT GFAP with CRYAB at 23 ^{0}C are shown. The filaments are morphologically similar to those assembled with Tris and there is no obvious increase in spacing between the filaments in the presence of CRYAB. The scale bar is equal to 500 nm.

2.1.3.2 CRYAB reduces mutant GFAP filament-filament interactions.

CRYAB was co-assembled with GFAP in a 1:1 molar ratio with 0.4 mg/mL GFAP and 0.16 mg/mL CRYAB through long assembly, according to Figure 2.13, to see how the sHSP influences filament interactions. As seen in Figure 2.18, it acts to reduce interactions of the mutant R239H GFAP. In addition to the Tris assembly method, comparisons were made for WT GFAP only, with an imidazole assembly method to show that the CRYAB could also increase filament interactions depending on the assembly buffer environment.

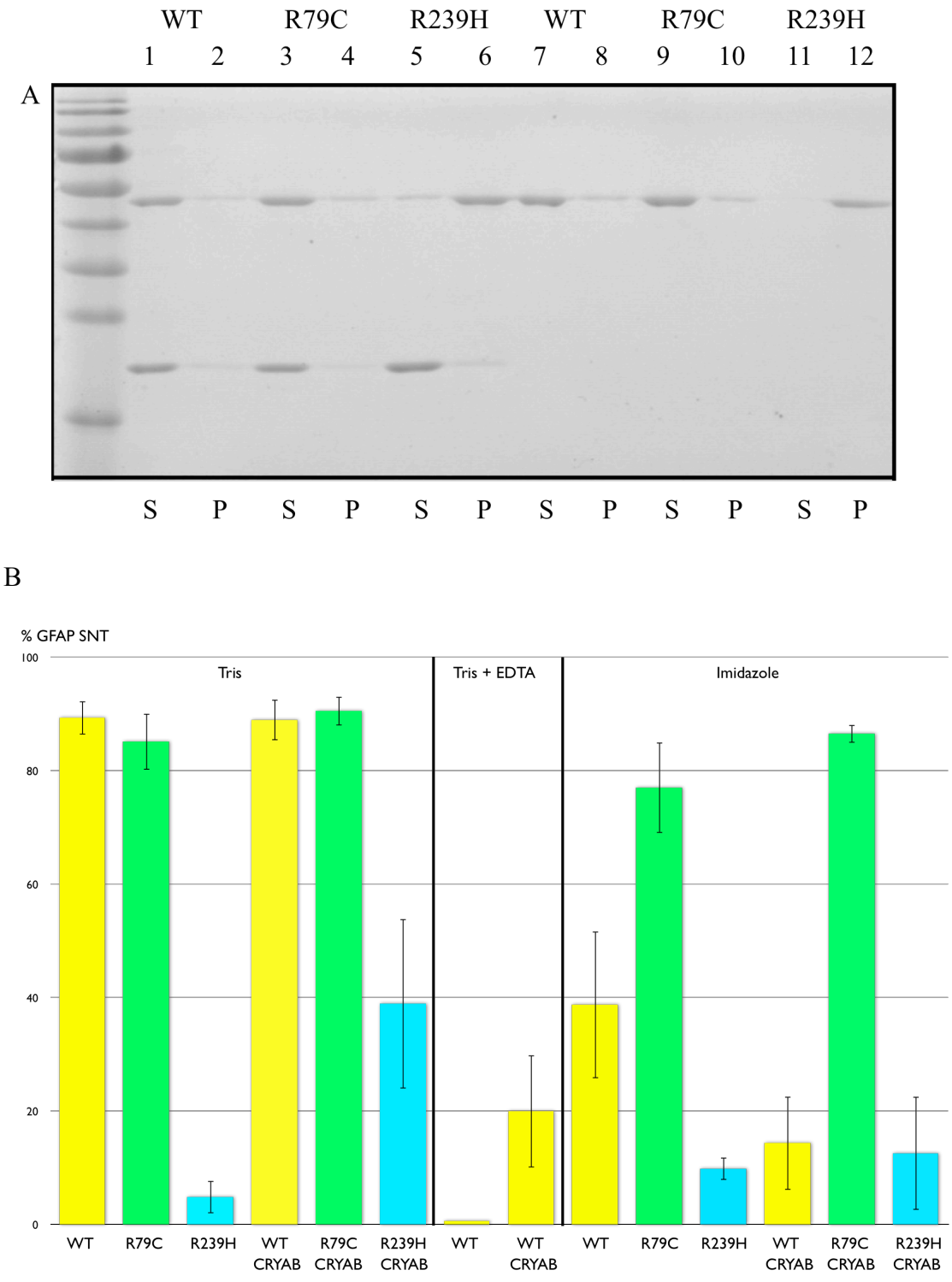

Figure 2.18 WT CRYAB reduces R239H mutant GFAP filament-filament interactions through Tris assembly.

A low speed sedimentation assay gel is shown alongside quantification results. Molecular weights of the protein standard are from top to bottom: 170, 130, 100, 70, 55, 40, 35, 25 and 15 kDa. In the appendix, Table A.2 and A.3 show the statistical tests carried out. The quantification data in the chart are from at least three

independent repeats, shown with error bars representing +/- one standard deviation (SD). Within the chart, the % GFAP SNT refers to the percentage of GFAP (top bands) present in the supernatant after low speed sedimentation. Only for R239H through Tris assembly is the ability to reduce filament interactions significant statistically ($p<0.05$) and it appears that with imidazole buffer the CRYAB acts to promote increased filament interactions. The Tris + EDTA section is discussed in the next chapter. SNT and S= supernatant and P= pellet.

Temperature increases appear to reduce the amount of GFAP in the supernatant as seen from Figure 2.19, through Tris assembly. The imidazole assembly leads to CRYAB acting to promote more filament-filament interactions since in its presence there is an increase in pelleting of filaments compared to when filaments are assembled alone (Figure 2.20). At 44 ^{0}C, CRYAB in the presence of WT GFAP increases its proportion pelleted under low speed sedimentation conditions compared to 23 ^{0}C, shown in Figure 2.19. This is seen to be an effect of interactions with the filaments since its assembly alone at this temperature still results in most of the CRYAB being present in the supernatant fraction (Figure 2.22).

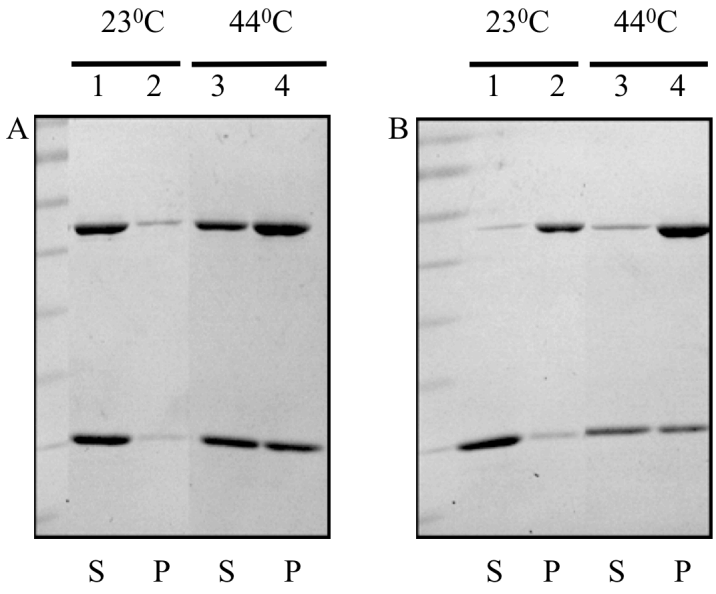

Figure 2.19 Increasing the temperature from 23 to 44 ^{0}C increases filament-filament interactions of WT GFAP in the presence of WT CRYAB through Tris assembly.

Low speed sedimentation assay gels were run of samples, assembled through A) Tris and B) imidazole assembly of WT GFAP with CRYAB. With the Tris assembled filaments, most of the protein is in the supernatant portion at room temperature. Upon an increase in temperature the opposite is seen and also for imidazole assembly most of the filaments are in the pellet portions. There is a positive correlation between an increase in the filament-filament interactions and an increase in the interactions of CRYAB with the filaments as seen in Figure 2.25 and 2.26. S= supernatant and P= pellet.

Imidazole buffer appears to result in WT filaments that tangle and have more increased associations amongst them as shown by a reduction in the amount of GFAP in the supernatant fraction at low speed, compared to WT GFAP assembled through Tris assembly (Figures 2.18A and 2.20B).

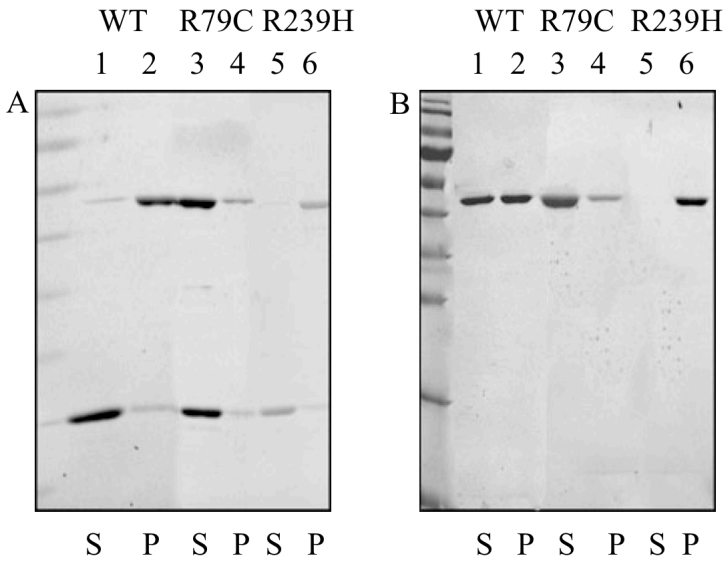

C

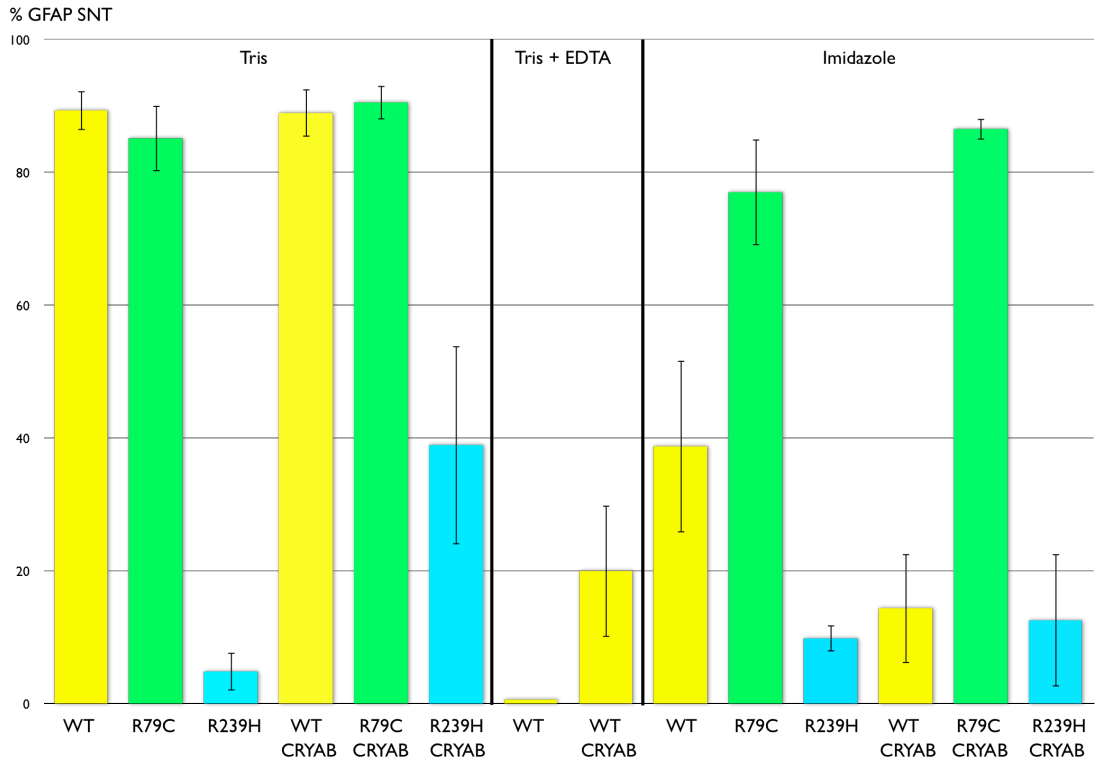

Figure 2.20 WT CRYAB increases filament-filament interactions of WT GFAP through imidazole assembly.

Low speed sedimentation assay gels were run of samples from 23 ^{0}C. From gel B) there is approximately 50% WT GFAP present in the S portion, which is then reduced upon addition of CRYAB, as shown in gel A), significant with a p value of 0.05 (Table A.4). The addition of CRYAB to R79C and R239H GFAP has no influence on their solubility in imidazole buffer. The same quantification chart from Figure 2.18 is shown. SNT and S= supernatant and P= pellet.

GFAP is not the only IF in which CRYAB can reduce filament interactions as shown in Figure 2.21 where CRYAB acts to reduce desmin filament-filament interactions.

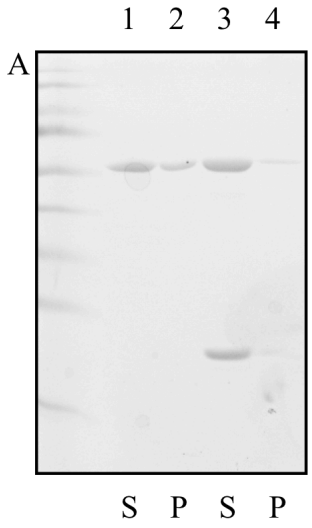

Figure 2.21 WT CRYAB reduces WT desmin filament-filament interactions through Tris assembly.

A low speed sedimentation assay gel A) was run of samples assembled through the method in Figure 2.13, from left to right, of WT desmin and WT desmin + CRYAB, at 23 ^{0}C. Comparing lanes 2 and 4, it can be seen that desmin filaments alone have more pelletable material than when co-assembled with CRYAB. S= supernatant and P= pellet.

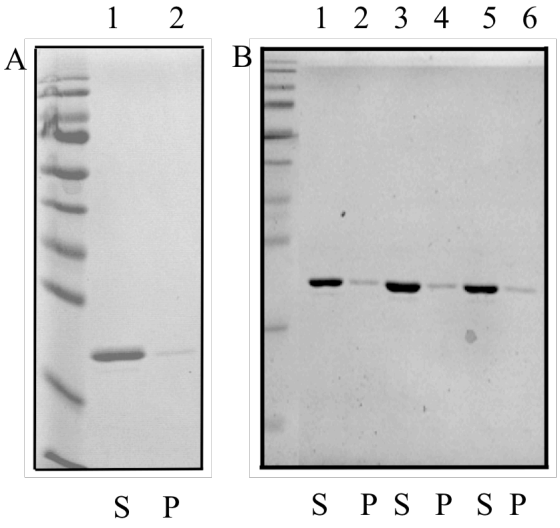

Figure 2.22 WT CRYAB is predominantly in the supernatant fraction after low speed sedimentations from imidazole and Tris assemblies.

A low speed sedimentation assay gel A) was run of WT CRYAB after assembly according to Figure 2.13 at 23 ^{0}C and also a gel was run of B) WT CRYAB,

assembled according to Figure 2.14, at 23, 37 and 44 ^{0}C. Most of the CRYAB is present in the S portions through both assembly conditions. S= supernatant and P= pellet.

2.1.3.3 CRYAB impairs WT human GFAP assembly.

Next the ability of CRYAB to inhibit WT GFAP assembly was assessed from high speed sedimentation assays, which assess assembled (insoluble) and unassembled (soluble) material in the pellet and supernatant fractions respectively and this was compared between Tris and imidazole assemblies at 23 ^{0}C (Ralton et al., 1994). The effect of crystallins on bovine GFAP assembly have shown previously that crystallins inhibit assembly of filaments, therefore the effect of CRYAB on human GFAP assembly was assessed (Nicholl and Quinlan, 1994).

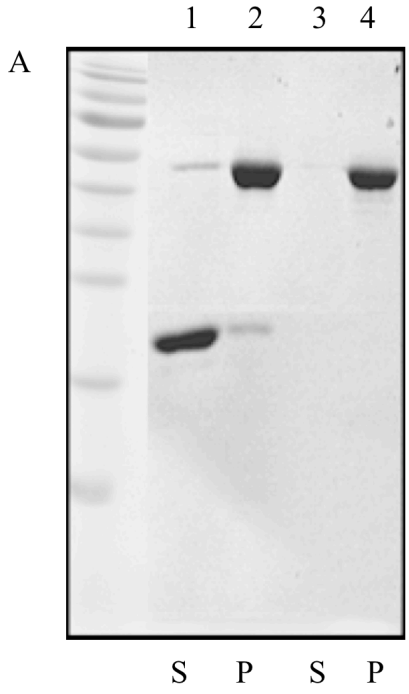

Figure 2.23 WT CRYAB does not inhibit WT GFAP assembly through imidazole assembly.

WT CRYAB does not act to significantly increase the amount of WT GFAP in the supernatant at high speed through imidazole assembly, shown from three independent experiments as quantified in the chart in Figure 2.24, which is contrary

to the findings when GFAP and CRYAB are assembled in a Tris buffer as shown in Figure 2.24. S= supernatant and P= pellet.

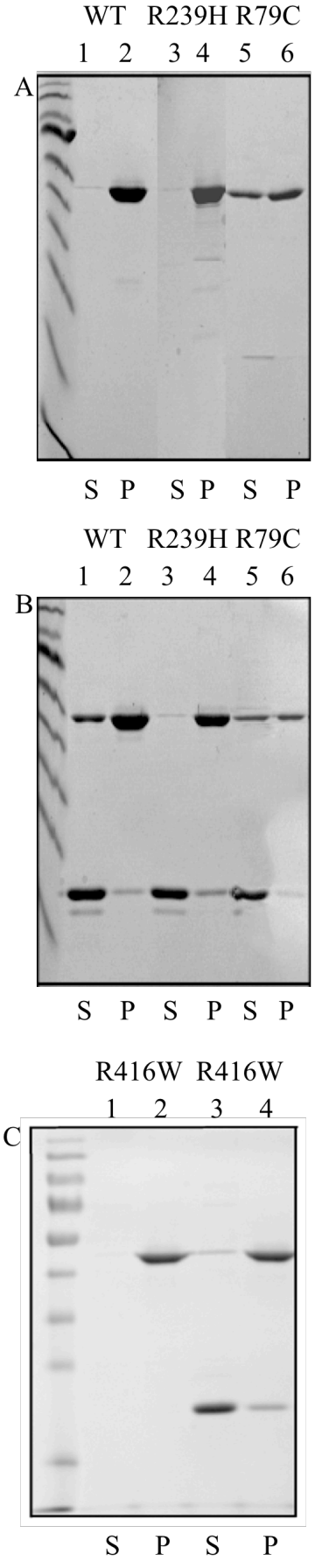
WT R239H R79C
1 2 3 4 5 6
A
S P S P S P
WT R239H R79C
1 2 3 4 5 6
B
S P S P S P
R416W R416W
1 2 3 4
C
S P S P

D

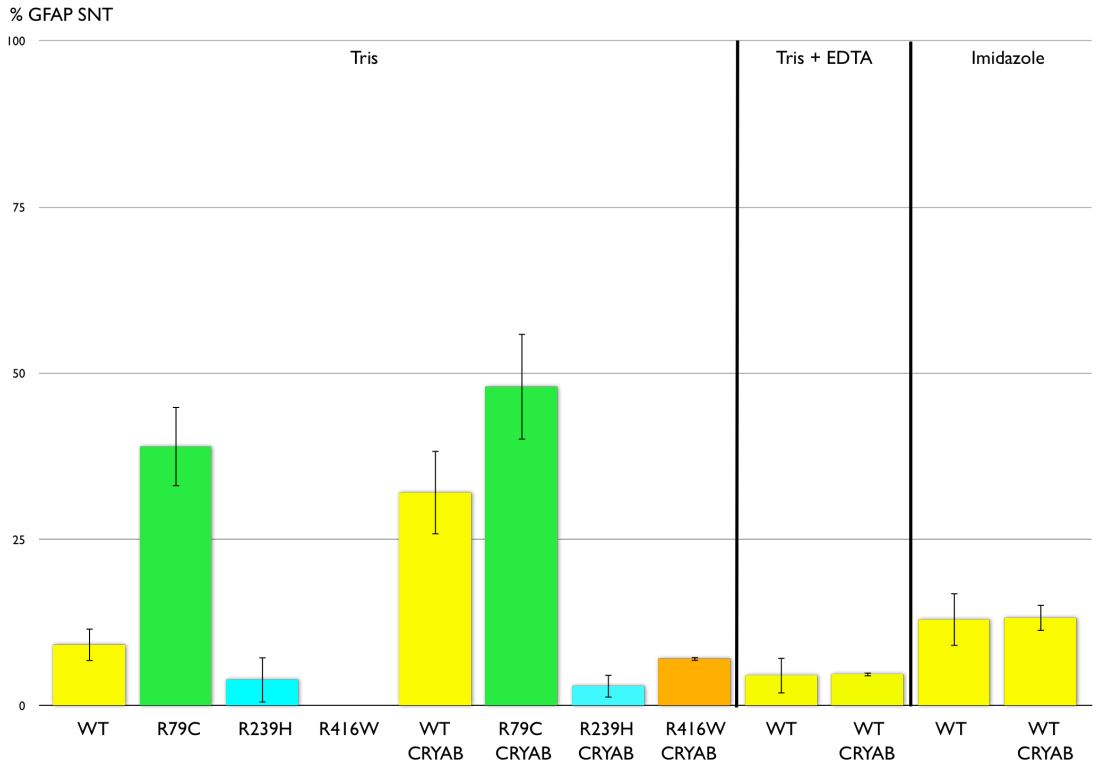

Figure 2.24 WT CRYAB inhibits WT GFAP formation through Tris assembly. High speed sedimentation assay gels (A-C) are shown highlighting how WT CRYAB acts to increase the amount of WT GFAP in the SNT portion at 23 ^{0}C by 20%, showing that it can inhibit the assembly of human GFAP. There is no statistically significant difference in the amount of GFAP in the S portions for R239H and R79C in the presence of CRYAB, compared to its absence (c.f. appendix Table A.6 and A.7). P = 0.001 for the increased amount of WT GFAP in the S in the presence of CRYAB compared to when CRYAB is not present. WT CRYAB also inhibits R416W assembly competency as demonstrated from a Mann-Whitney U test in Table A.7. The quantification data of the average values of protein present in the supernatant fractions, after high speed sedimentations, from at least three independent repeats is shown with error bars representing +/- one SD. The Tris + EDTA section is discussed in the next chapter. Only for WT GFAP through Tris assembly is the ability to inhibit filament assembly significant statistically where p = 0.001 (c.f. appendix, Table A.6) and it appears that with imidazole buffer the CRYAB does not have this effect. SNT and S= supernatant and P= pellet.

2.1.3.4 CRYAB has increased interactions with GFAP as a result of AxD-causing mutations, elevated temperatures and a higher *I*.

It was found that CRYAB interacts the least with WT GFAP filaments, as shown by the lowest proportion of CRYAB co-sedimenting with GFAP compared to the R239H mutant, seen in Figure 2.25 for 39 and 44 ^{0}C with the Tris assembly buffer. Increased temperatures also increase the interactions between CRYAB and the WT and mutant GFAP protein.

Comparing the interactions of CRYAB with WT GFAP from the Tris and imidazole assemblies, imidazole buffer with its lower pH and higher *I* results in more interactions than Tris buffer.

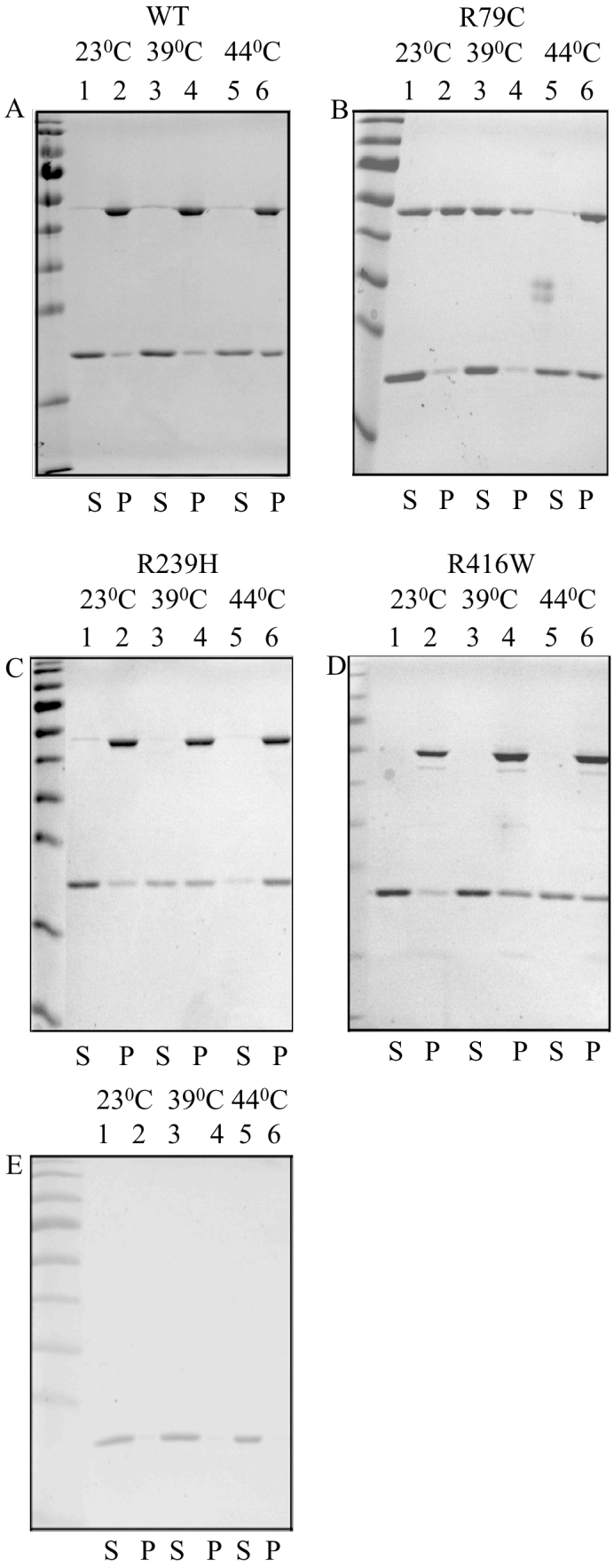
WT
23⁰C 39⁰C 44⁰C
1 2 3 4 5 6
A
S P S P S P
R79C
23⁰C 39⁰C 44⁰C
1 2 3 4 5 6
B
S P S P S P
R239H
23⁰C 39⁰C 44⁰C
1 2 3 4 5 6
C
S P S P S P
R416W
23⁰C 39⁰C 44⁰C
1 2 3 4 5 6
D
S P S P S P
23⁰C 39⁰C 44⁰C
1 2 3 4 5 6
E
S P S P S P

F

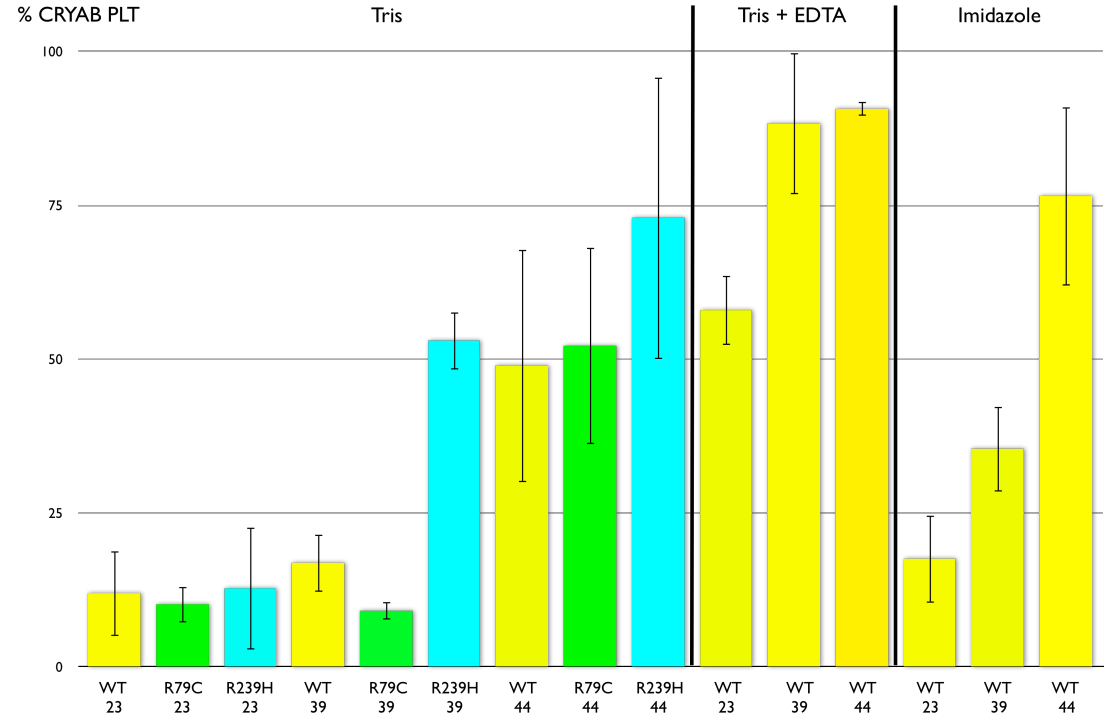

G

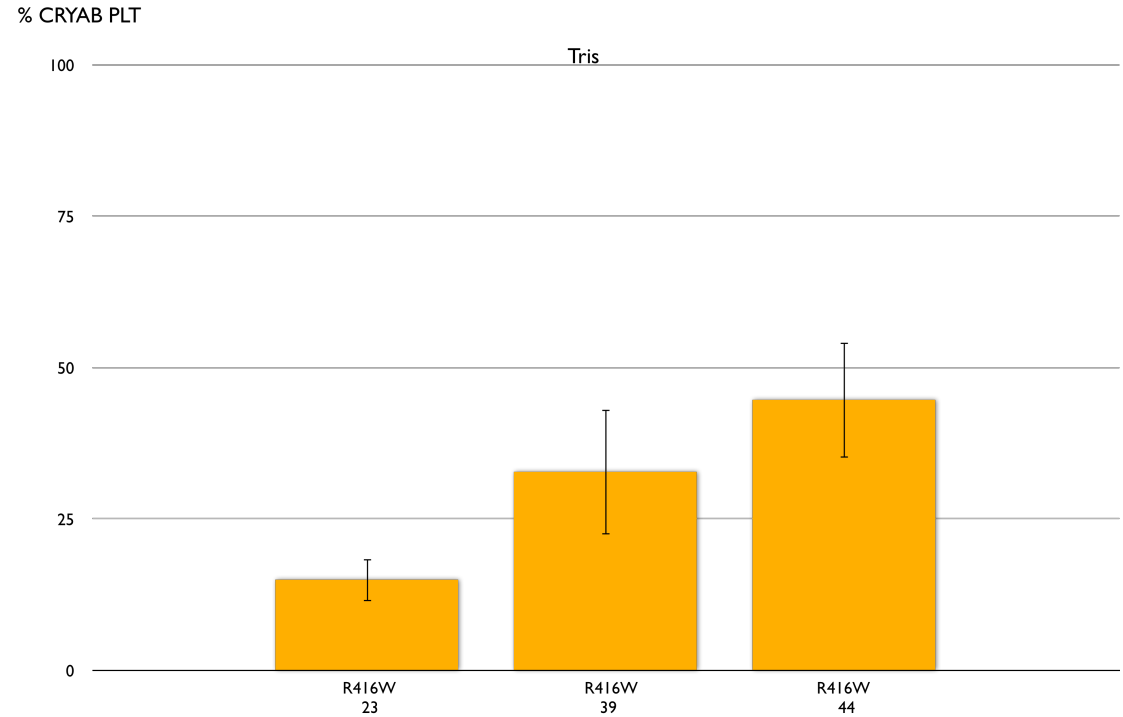

Figure 2.25 The AxD-causing mutant R239H has increased interactions with CRYAB.

High speed sedimentation assays (A) to E)) are shown from assemblies in Tris buffers, with gel E) as the control of CRYAB assembled in the absence of GFAP.

Most interactions (binding) of CRYAB with GFAP occur with the R239H GFAP as shown in C). The quantification data of the average values of CRYAB present in the pellet fractions, after high speed sedimentations, from at least three independent repeats is shown with error bars representing +/- one SD. CRYAB is predominantly in the supernatant after high speed sedimentation at all three temperatures but in the presence of GFAP there can be seen a temperature-dependent increase in binding which is statistically significant at a 1% probability level for all of the mutants and WT protein assembled through both conditions, comparing 23 with 44 ^{0}C (c.f. appendix, Tables A.8 and A.9). Also there appears to be more binding of CRYAB to WT GFAP assembled through imidazole assembly as opposed to Tris assembly. The Tris + EDTA section is discussed in the next chapter. S= supernatant and PLT and P= pellet.

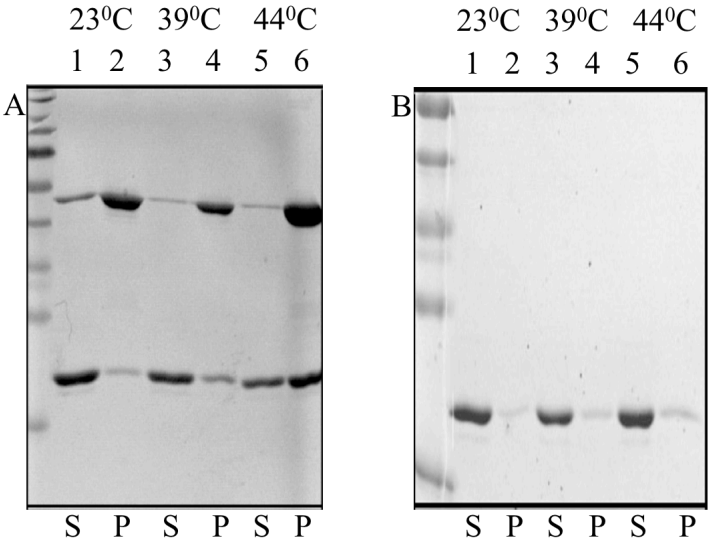

C

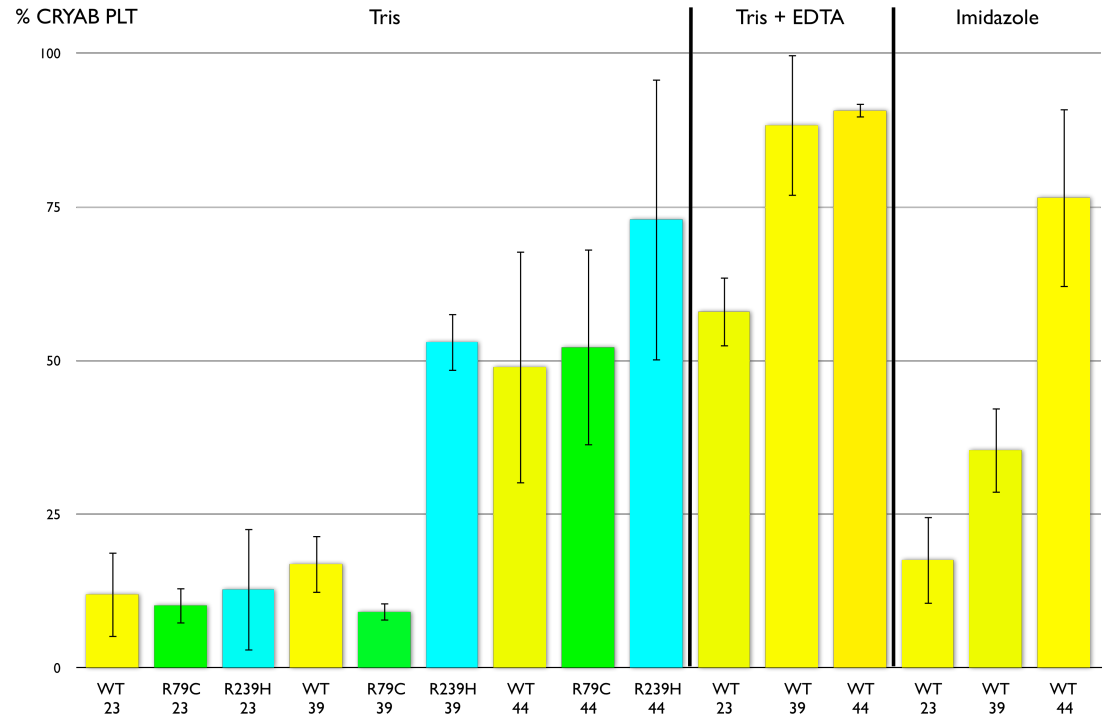

Figure 2.26 Binding of WT CRYAB increases with WT GFAP, at increased temperatures with imidazole assembly.

High speed sedimentation assays of A) WT GFAP assembled with CRYAB and B) WT CRYAB alone are shown. CRYAB is predominantly in the S portion after high speed sedimentation but in the presence of GFAP, it increases its quantity in the P portion and this increases with increasing temperature. There is a greater amount of binding to filaments from assembly in imidazole buffer compared to Tris buffer. S= supernatant and PLT and P= pellet.

2.1.3.5 Dominant effects of mutants on WT GFAP assembly.

WT GFAP was mixed with the mutant GFAP and then assembled through Tris assembly at room temperature. The R416W mutant GFAP studied previously, the result of a point mutation in the tail domain RDGE motif, was also assessed alongside the R239H and R79C mutant proteins (Der Perng et al., 2006). Low speed sedimentation assays were carried out on the assembled proteins to assess the filament-filament interactions. For the R239H mutant GFAP which results in aggregates consisting of small proteins, there is an increase in pelleting of the GFAP material at a 1:1 ratio of WT: mutant GFAP (Figure 2.30). For the R79C mutant, any effect is difficult to observe from sedimentation assays, as the gel pattern is very similar to WT GFAP. However, TEM images of the 1:1 ratio of WT: R79C GFAP show that there is a dominant effect of the mutant over WT filament formation due to the appearance of much shorter lengths of filaments at this level (Figure 2.27). At a 1:1 ratio level for the other two mutants, a clear alteration of filament morphology can be seen from TEM images and for R239H this can be seen at a 10% level however this is not severe enough to alter the low speed sedimentation profile seen for GFAP (Figure 2.30).

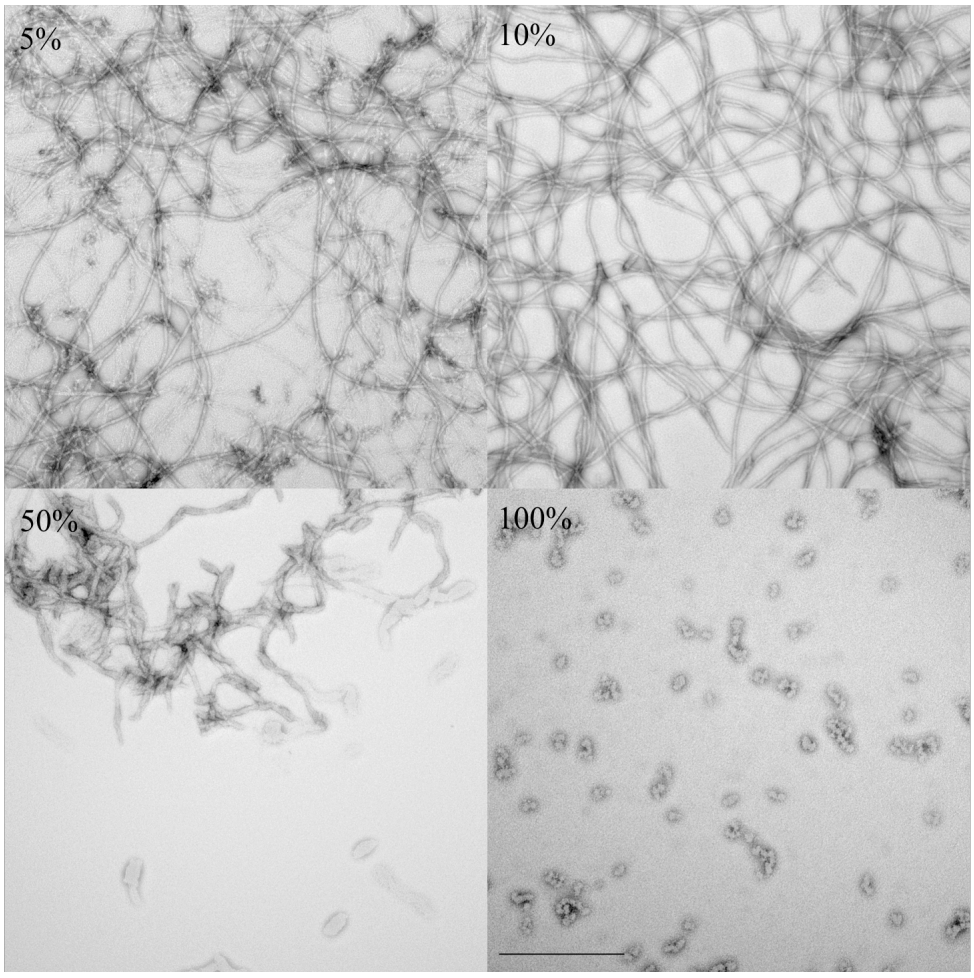

Figure 2.27 Dominant effect of R79C on WT GFAP filament formation.
Mutant GFAP was present in the mentioned %s with WT GFAP. A 50% level of R79C GFAP results in shortened filaments, whereas a 10% level does not have any dominant effect on WT filament formation. The scale bar is equal to 500 nm.

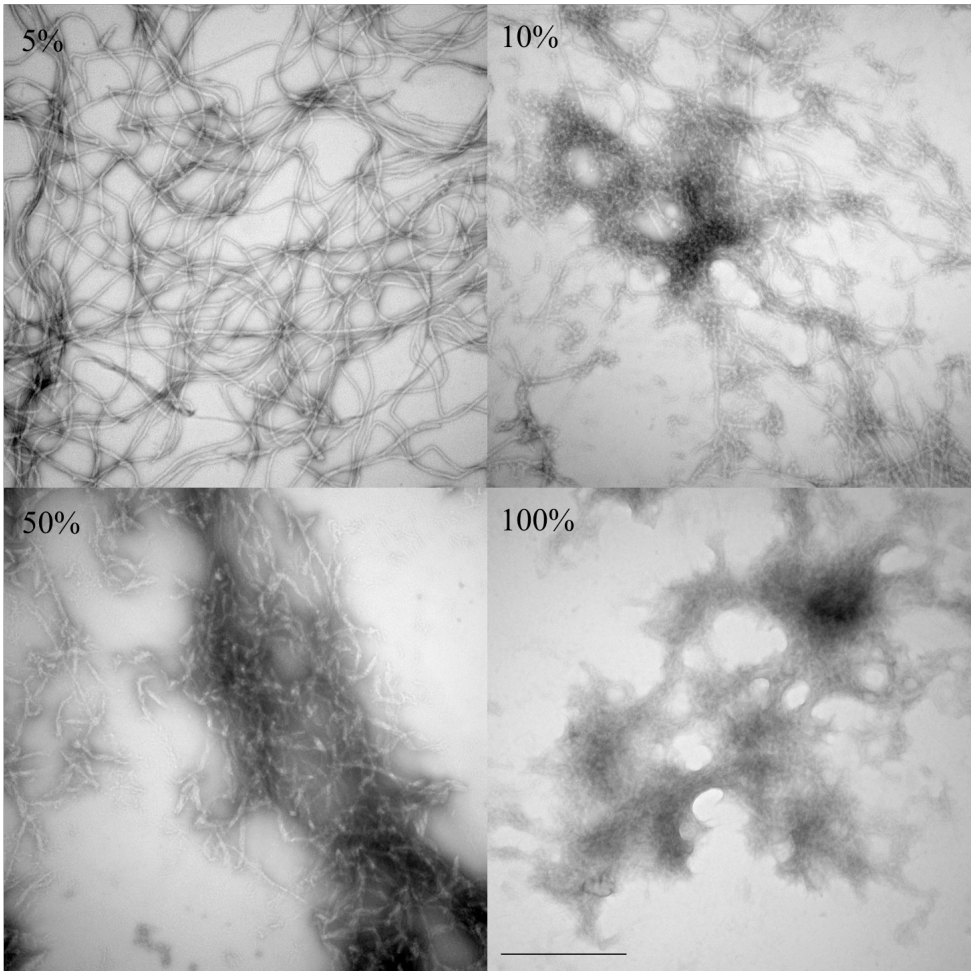

Figure 2.28 Dominant effect of R239H on WT GFAP filament formation.
Mutant GFAP was present in the mentioned %s with WT GFAP. A 50% level of R239H GFAP results in shortened filaments and there appears to be an effect on filament morphology at a 10% level. The scale bar is equal to 500 nm.

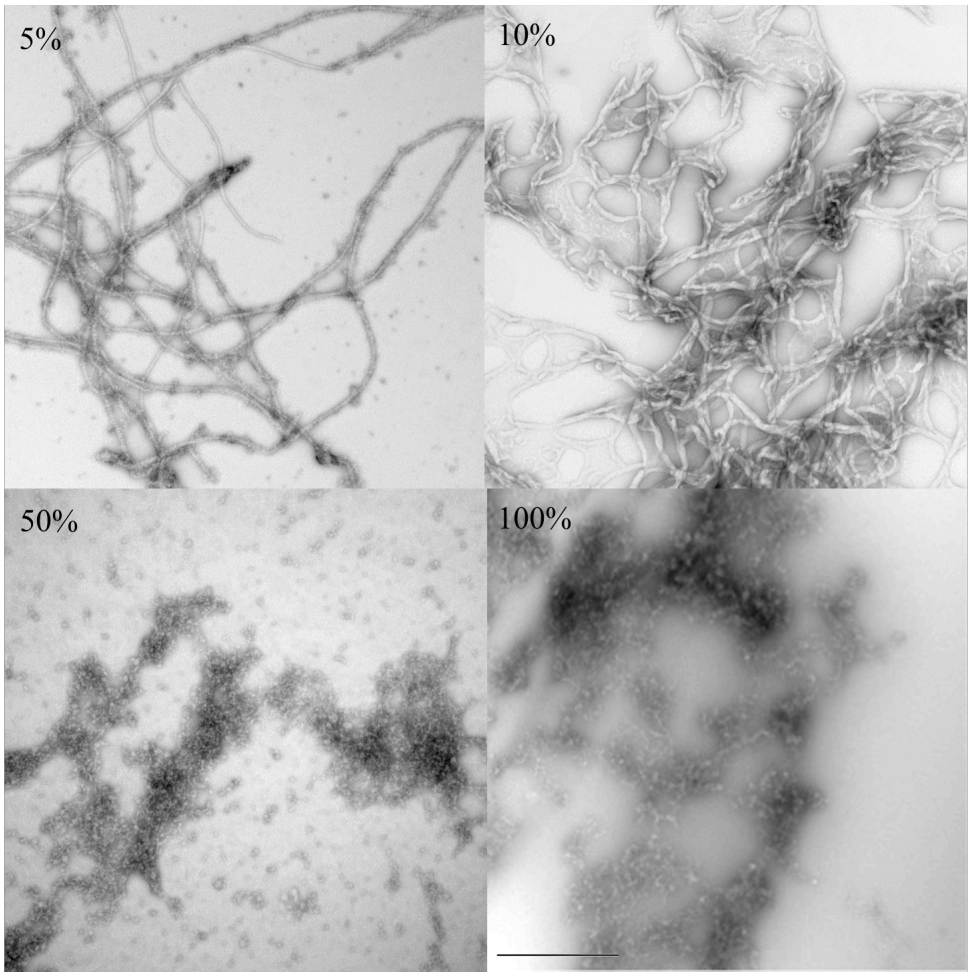

Figure 2.29 Dominant effect of R416W on WT GFAP filament formation.
Mutant GFAP was present in the mentioned %s with WT GFAP. A 50% level of R416W GFAP results in shortened filaments and even at a 10% level the filament structures appear altered. The scale bar is equal to 500 nm.

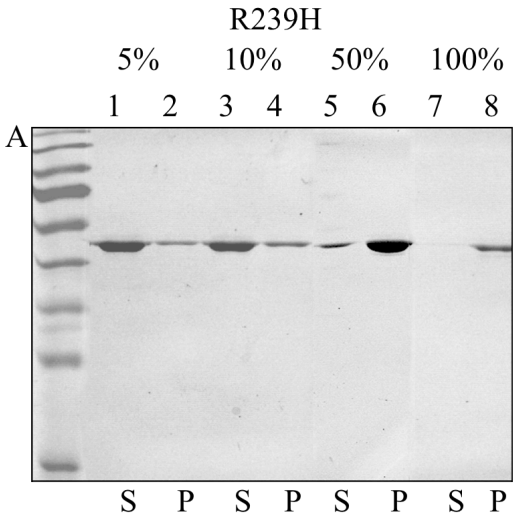
R239H
5% 10% 50% 100%
1 2 3 4 5 6 7 8
A
S P S P S P S P

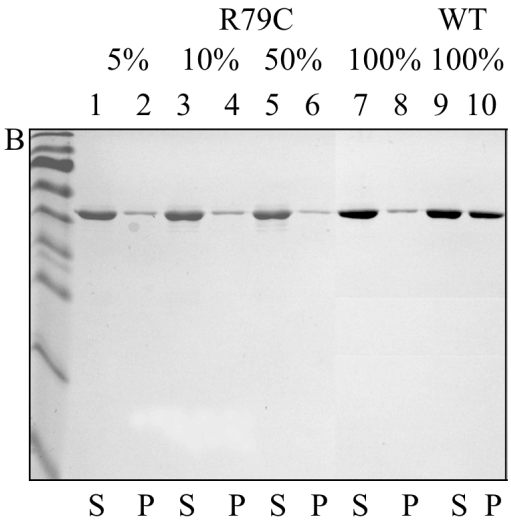
R79C WT
5% 10% 50% 100% 100%
1 2 3 4 5 6 7 8 9 10
B
S P S P S P S P S P

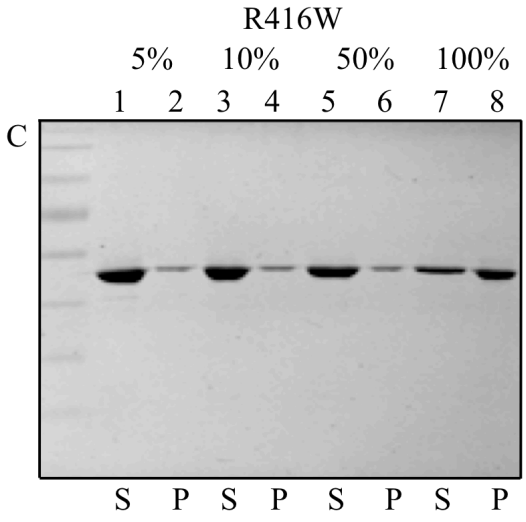
R416W
5% 10% 50% 100%
1 2 3 4 5 6 7 8
C
S P S P S P S P

D

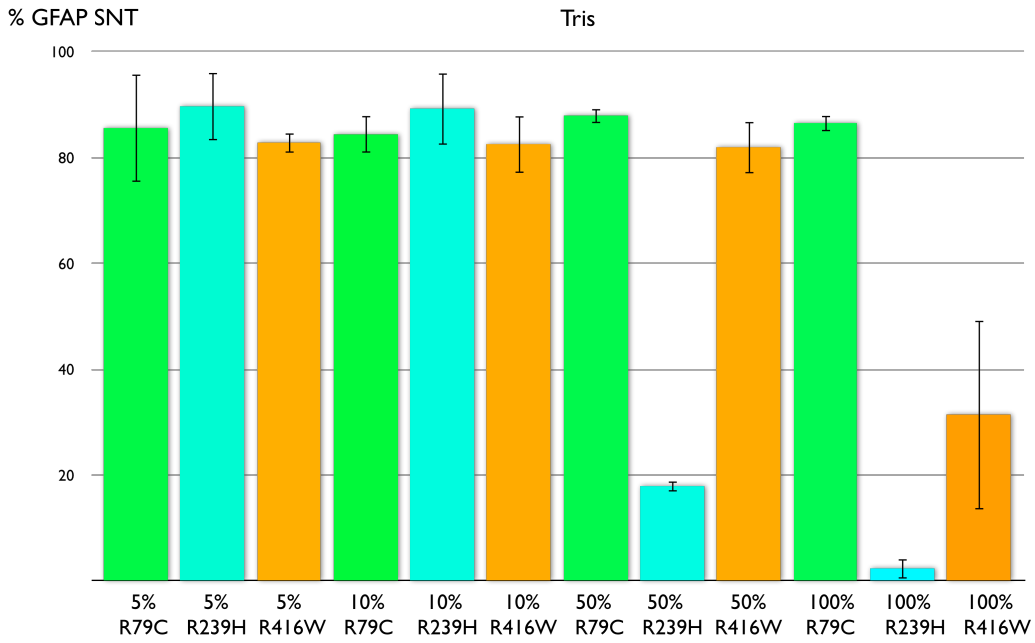

Figure 2.30 R239H mutant GFAP is dominant over WT GFAP at a 50% level for increasing filament-filament interactions.

Low speed sedimentation assays are shown. The dominant effect of R239H can be seen at a 50% level by an increase in GFAP in the P portion. D) the quantification data represent the average values of GFAP present in the supernatant fractions from three independent repeats. The error bars represent +/- one SD. Only at a 50% level is there an apparent reduction in the amount of soluble protein for the R239H mutant GFAP. Regarding R79C the effects are difficult to see as 100% R79C is similar to 100% WT GFAP. SNT and S= supernatant and P= pellet.

High speed sedimentations were carried out to assess assembly efficiency with the varying percentages of the mutant GFAP. It was shown that most of the filaments were pelleted, even at a 50% level with R79C GFAP, despite shorter filaments being observed from TEM images. Therefore low speed sedimentation assays appear to be more sensitive for assessing filament alterations.

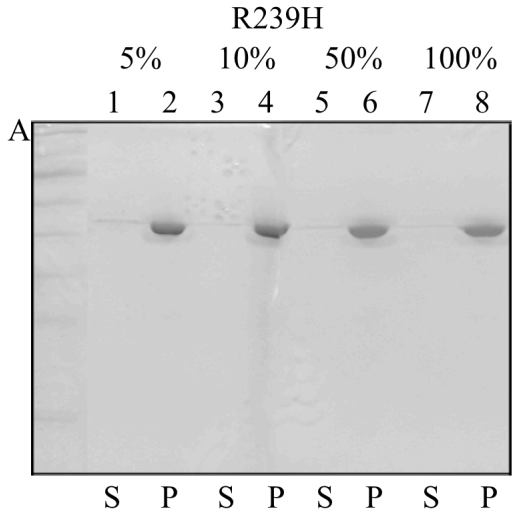
R239H
5% 10% 50% 100%
1 2 3 4 5 6 7 8
A
S P S P S P S P

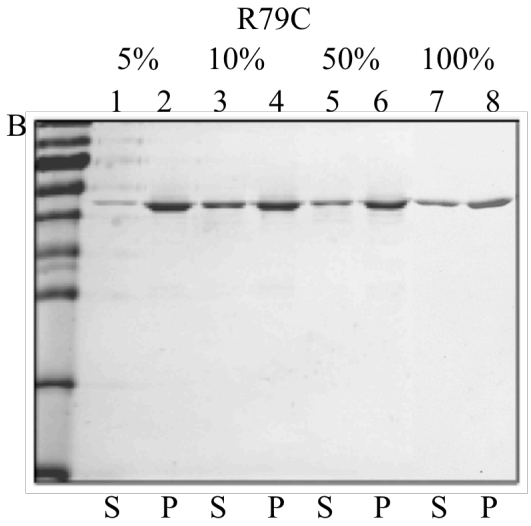
R79C
5% 10% 50% 100%
1 2 3 4 5 6 7 8
B
S P S P S P S P

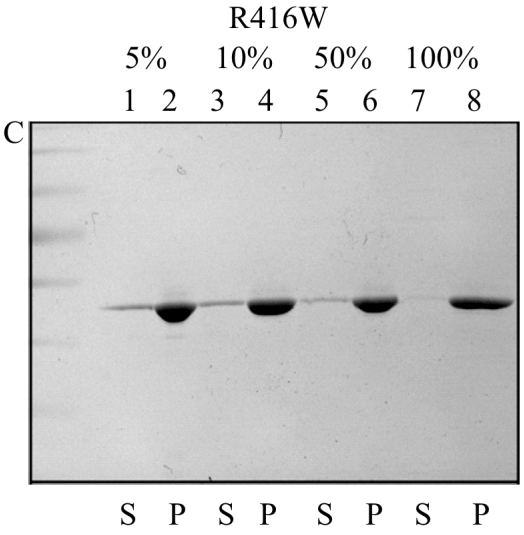
R416W
5% 10% 50% 100%
1 2 3 4 5 6 7 8
C
S P S P S P S P

D

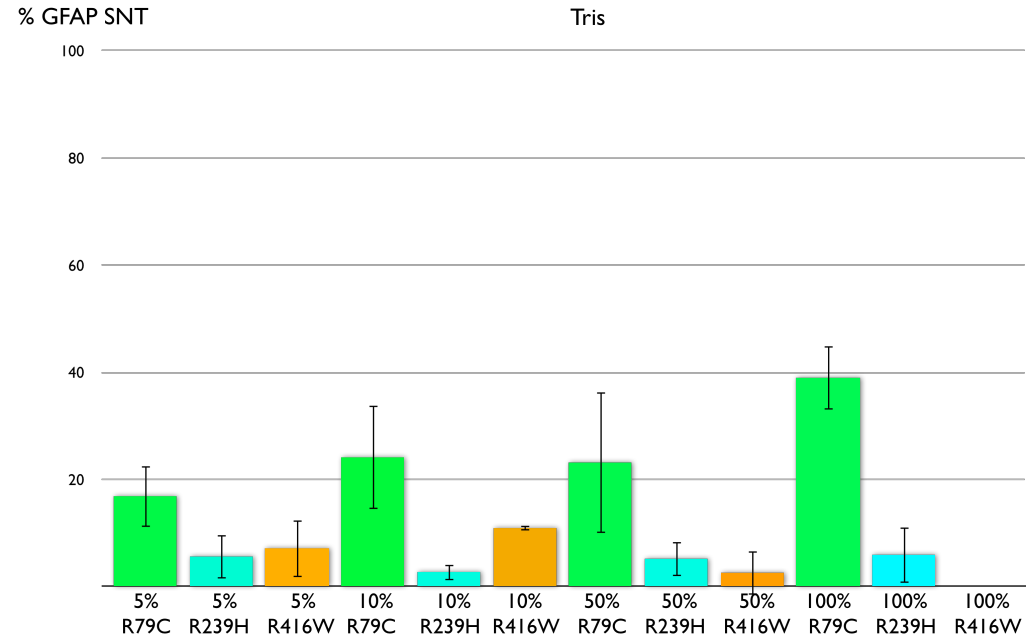

Figure 2.31 R239H and R416W mutant GFAP form protein aggregates.

High speed sedimentation assays are shown. All of the samples are sedimented efficiently apart from 100% R79C GFAP. D) the quantification data represent the average values of GFAP present in the supernatant fractions from at least three independent repeats. The error bars represent +/- one SD. Any difference in pelleting is difficult to assess from high speed sedimentation assay as the mutants result in aggregates, which give a similar sedimentation profile to WT GFAP filaments. However differences can be seen between the R79C mutant and the R239H and R416W mutant proteins. SNT and S= supernatant and P= pellet.

2.1.4 Discussion

Two GFAP mutants of R79C and R239H have been studied in regard to their sedimentation profiles and morphology after TEM. The R79C and R239H both result in distinct properties. The R79C protein assembles inefficiently as observed from high speed sedimentation data, where more than 35% is present in the supernatant fraction. This is in contrast to R239H GFAP, which is predominantly in the pellet due to a promotion of aggregation.

WT and mutant GFAP morphology.

The R79C GFAP forms structures similar to other mutants of GFAP found within the LNDR motif of the protein, such as with the R79H mutant and short fragments, however in this case the inability to form filaments does not lead to aggregates of proteins, instead it results in a large soluble pool of protein, which under high speed sedimentation remains predominantly in the supernatant portion (Figure 2.24) (Long, 2003). Mutations in the LNDR motif in other IFs are associated with severe disease thus showing that this conserved motif is essential for effective filament formation and function, demonstrated with Dowling-Meara EBS due to an identical mutation in K10 and 14 (Coulombe et al., 1991, Brenner et al., 2001). The R239H mutation results in aggregates although it is difficult to identify what they are made up of. However, when CRYAB is added in a 1:1 molar ratio, the substructures can be seen and in fact this mutation also leads to shortened filaments, which are of ULF length or longer (Figure 2.15). Another mutation in human recombinant GFAP at the 239 amino acid position has been studied before, however this did not disrupt the annealing of the protofilaments and instead filament formation was preserved (Hsiao et al., 2005). A reason for this may be because cysteine has a relatively high pK of 8.5 alongside 12.0 for arginine and both will have a net positive charge, whereas histidine has a pI of 6.5 close to physiological pH, under the conditions of assembly with pH 7.3 and thus histidine is more negatively charged than cysteine. R239 is at position e in the heptad repeat pattern in coil 2A of human GFAP and since positions e and g are involved in the inter-ionic interactions between two oppositely charged amino acids, the resulting charge change would be predicted to perturb assembly of dimers and potentially tetramers and in this case the replacement with histidine

appears to have prevented elongation of the filaments (Parry and Steinert, 1995, Stryer, 1996).

CRYAB reduces mutant GFAP filament-filament interactions.

It can be seen that CRYAB acts to reduce filament-filament interactions between R239H GFAP as seen by a statistically significant increase in the amount of GFAP in the supernatant in its presence compared to GFAP alone, through Tris assembly (Figure 2.18). There is not a significant difference in the amount of WT GFAP in the supernatant portion in the presence of CRYAB compared to its absence although there is an effect seen with WT desmin and a reduction in filament-filament interactions (Figure 2.21). However with imidazole assembly the opposite scenario is observed and the CRYAB is acting to increase filament associations for GFAP. There are a few differences between the imidazole and Tris assemblies that may account for the differences in the ability for CRYAB to modify filament-filament interactions. Firstly the pH is much lower for the imidazole buffer having used a pH 6.8 stock compared to pH 7.3 with Tris. Also there is a higher concentration of buffer at 20 mM imidazole compared to 10 mM Tris and a higher amount of NaCl (100 mM) used with the imidazole assembly compared to 50 mM with the Tris assembly; the imidazole buffer has a higher *I* of 0.111 M compared to the Tris buffer of 0.0607 M (c.f. appendix, Ionic strength calculations). No magnesium was included in the imidazole buffer, unlike the Tris assembly final buffer, due to the fact that imidazole binds magnesium. The method used for the imidazole assembly is a standard method used previously in the laboratory and it is therefore interesting to assess how different assembly methods lead to different filament properties. However the lower pH for the imidazole buffer may explain the increased filament-filament interactions as low pH has been shown previously to promote increased interactions of CRYAB with desmin filaments isolated from muscle tissue (Bennardini et al., 1992). The $\Delta pH/\Delta T$ for Tris buffers is -0.028 pH units per degree centigrade increase, therefore at 23 ^{0}C the pH is 7.3, at 39 ^{0}C it is 6.9 and at 44 ^{0}C the pH is 6.7. However for the imidazole buffer at 23 ^{0}C, the pH is 6.8 and this changes to 6.5 at 44 ^{0}C thus showing a $\Delta pH/\Delta T$ of -0.015 per degree centigrade increase. The pH is thus likely to have an effect upon the ability of CRYAB to bind to filaments, therefore not only is temperature influencing the CRYAB-GFAP protein interactions

in the following section at three different temperature values. This information leads into the hypothesis at the end of this chapter as to how pH and temperature may influence CRYAB interactions with the filaments, which is investigated in chapter 3.

CRYAB impairs WT human GFAP assembly.

It was shown that through Tris assembly, CRYAB effects were apparent where there was an increase in the unassembled material in the supernatant portion of the samples after assembly in Tris, with WT GFAP, significant statistically at a 1% probability level. This is represented quantitatively from three independent repeats in Figure 2.24. *In vitro* assembly inhibition of bovine GFAP has been observed from CRYAB using native purified proteins. In this case however the filament assembly was inhibited as there was an absence of long filaments and most of the protein was present in the supernatant portion after a high speed sedimentation, whereas from these experiments with recombinant human protein there are still filaments, in the presence of CRYAB, as shown in Figure 2.15 and there has only been a slight increase in the soluble portion of WT GFAP (from 9 to 32%). However since human and bovine GFAP are 96% identical it would be predicted that they have similar assembly properties, although the difference between these results and those found previously may be due to different post-translational modifications between the *in vitro* and *in vivo* proteins (Nicholl and Quinlan, 1994).

CRYAB has increased interactions with GFAP as a result of AxD-causing mutations, elevated temperatures and a higher *I*.

It was in fact seen that as the temperature was raised, CRYAB did associate more with the protein and this was at greater levels after imidazole assembly compared to Tris assembly (Figure 2.25 and 2.26).

With imidazole and Tris assembly there is binding of CRYAB to the filaments at 39 and 44 ^{0}C since CRYAB alone is 10% in the pellet at all temperatures for Tris assembly (Figure 2.25). For imidazole assembly it is 10% in the pellet at 23 ^{0}C and 20% at 39 and 44 ^{0}C (Figure 2.26). With Tris assembly, the R239H GFAP has a much greater affinity for the CRYAB oligomers compared to even the R416W mutant and may be a reflection on the severity of the mutations. R239H has

appeared only in infantile cases whereas R416W has been observed in infantile, juvenile and adult cases and therefore the R239H is likely to compromise filaments to a greater extent, shown by the younger age of presentation of the disease, than the R416W mutant thus leading to increased interactions with CRYAB (Rodriguez et al., 2001, Kinoshita et al., 2003). There is not a significant difference in the amount of CRYAB binding to WT GFAP and the other mutants at all three temperatures, apart from at 39 ^{0}C where R239H has a much higher affinity, also the maximum binding recorded is greater with the R239H mutant at 44 ^{0}C despite an overlap in error bars (Figure 2.25). Not only does binding increase but also much more for the mutants, this shows that the increase in binding at higher temperatures is due to a combination of both the increased temperature and also altered architecture of the filaments (Figure 2.25). It seems as if the temperature and structural factors are providing the means for the increased interactions and that one is exacerbating the other, otherwise the increase in binding would be linear as the temperature is increased and within each temperature there would be no significant difference in the amount of CRYAB binding to the WT or mutant GFAP.

Dominant effects of mutants on WT GFAP assembly.

As shown from high speed sedimentation quantification, the GFAP filaments have assembled at 5 and 10% mutant proportions with WT GFAP, as shown by approximately 90% of the total GFAP being pelleted. At 50% however the mutated GFAP has had a dominant effect over the WT filaments formed seen from TEM images. The 50% level of R79C GFAP formed very small protein structures, which were very close to the 60 nm length of ULFs. These clumped and overlapped each other (Figure 2.27). The 50% R239H GFAP also formed much shorter filaments that tended to cluster together (Figure 2.28). At a 50% mutant level for all of the mutations, the filaments are shorter and more tangled than wild-type filaments as a result of perturbed longitudinal annealing.

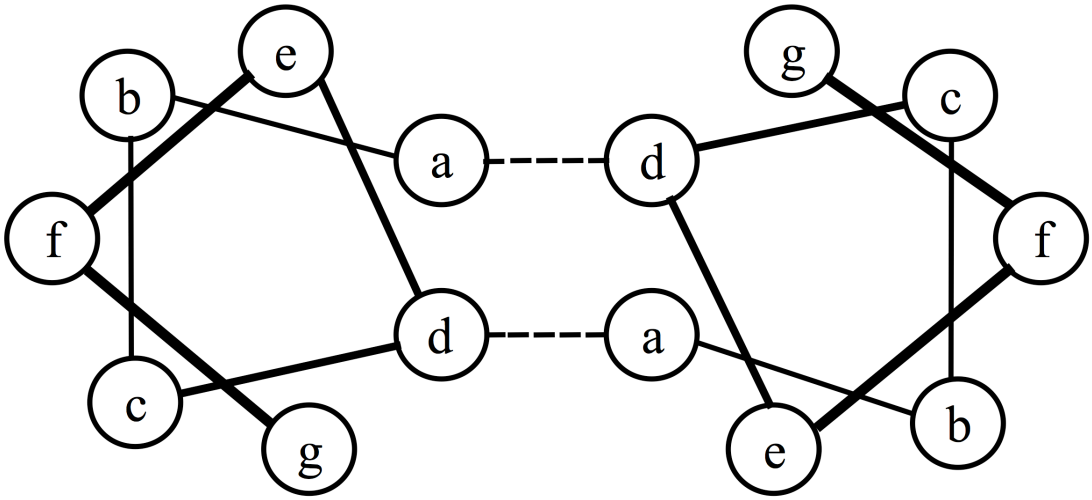

Figure 2.32 Helical wheel projections of coiled coils.

There are 3.3 amino acid residues per 360 degree turn of the helix (an amino acid every 109^0). Hydrophobic residues are in positions a and d and interchain ionic interactions occur between amino acids in the e and g positions.

R239H is in a predicted position e of the heptad repeat in the 2A part of the rod domain; the e and g positions are crucial for specifying interactions between monomers in a coiled coil and this therefore helps to explain why it is the most severe mutant studied here (Parry and Steinert, 1995). However R79C is located in the LNDR portion of the protein in the 1A rod domain but will also affect ionic interactions (predicted to be in a g position of the heptad repeat), as cysteine will be less positively charged than arginine at the physiological pH used in the experiments. Since this was assembled in the presence of 1 mM DTT, any potential disulfide bond formation will have been prevented. These mutations will either introduce or hinder the formation of hydrogen-bonds and ionic bonds and will likely affect van der Waals forces as well (Parry and Steinert, 1995).

Mutation	Predicted location in coiled coils $(a\text{-}b\text{-}c\text{-}d\text{-}e\text{-}f\text{-}g)_n$	Hypothesised alteration on assembly at pH 7.3
R79C	i) position g ii) position g	Reduction in positive charge disturbing ionic interactions between coils
R239H	i) position e ii) position e	Reduction in positive charge thus reducing ionic interactions
R416W	i) random coil ii) random coil	Tryptophan has an aromatic side chain which is bulky and will interfere with how the C-terminal RDGE motif interacts with neighboring coils

Table 2.2 **Summary of the hypothesised effects of GFAP mutations upon filament assembly**.

i) Positions of mutants were derived from the heptad repeat worked out manually (positions a and d are hydrophobic amino acids). ii) The program COILS (SIB, SZ) was used to work out the heptad repeat.

Amino acids in position a are predicted to have their side chains projecting out of the coiled coils whereas those in position d are predicted to have their side chains buried between the coils and therefore any bulky aromatic side groups such as with the imidazole ring in histidine will disrupt how the chains interact. However the R239H mutation is not hypothesised to be in an a or d position but it will alter the charge responsible for ionic interactions. For both the R79C and R239H mutants, the 32-mers have been able to form since ULFs are observed for both but the ionic charge disruptions have prohibited their longitudinal annealing and compaction. The R416W mutation is positioned in a random coil and may be why it is less severe than the R239H mutant as it won't affect the alpha helical coil structures but how the tail domain interacts with neighbouring coils, which influences compaction (Heimburg et al., 1996).

The R416W mutant GFAP has been studied previously where a 25% level of R416W led to a dominant effect over WT filament formation however a similar effect was not seen in this case, only at a 100% level of R416W could the increase in interactions be observed from low speed sedimentation assays (Der Perng et al., 2006). This is likely due to the fact that the imidazole assembly method was used in the paper whereas Tris was used in this case and this supports how the imidazole method leads to increased filament interactions. However the mutant protein morphology is similar, to that reported previously for R416W GFAP. They appear as short filaments, which have aggregated together and when it is mixed with WT GFAP, a clear reduction in filament length can be seen as shown in Figure 2.29. At a 50% level of the mutant, altered structures can be seen from the TEM images. R239H appears to be the more severe mutant, supporting the finding of increased CRYAB binding in the previous section, compared to R416W since the dominant aggregate formation is observed at a 50% level from the low speed sedimentations compared to R416W effects which are not seen until a 100% level from sedimentation.

Due to the variability in filaments when mixtures of mutants are present combined with WT GFAP and also the occasional presence of positive staining on some of the grids, the ability to quantify the lengths and widths of individual filaments accurately was hindered and thus a qualitative approach was taken instead of a quantitative analysis with statistical tests. However a few measurements were made using ImageJ 1.43r (National Institutes of Health, USA), in section 2.1.3.1.

In the next chapter a closer look at the interactions between CRYAB and GFAP and also the other type III IFs of desmin and vimentin will be carried out, to help gain more understanding about how altered filament architecture can lead to increases in CRYAB associations and also why temperature appears to influence these interactions. In addition, since differences in CRYAB interactions with filaments were observed between the two different assembly methods and the observed increased binding of CRYAB to filaments at elevated temperatures and thus lowered pH values, a closer look at the effect of pH on CRYAB-filament interactions will be carried out. The hypothesis is that lowered pH and increased temperatures will act to promote increased CRYAB-filament interactions.

Chapter 3; Conditions influencing WT CRYAB interactions with type III IFs GFAP, vimentin and desmin.

3.1 Introduction and aims

The purpose of this chapter is to assess how different divalent cation environments, temperatures and pH values influence CRYAB interactions with the type III IFs of GFAP, desmin and vimentin. A previous study has assessed the effect of temperature and pH on desmin assembly but only with native desmin protein and also no comparison has been made to vimentin or GFAP. Therefore the purpose of this study was to see how *in vitro* desmin protein was affected and how it compared to GFAP and vimentin (Bennardini et al., 1992). Additionally the effects of different divalent cations on CRYAB-IF interactions have not been assessed from sedimentation assays in great detail before. Type III IFs have the same molecular structure consisting of two non α-helical sections of an N-terminal head and C-terminal tail domain and a central α-helical rod domain split into four main segments of 1A, 1B, 2A and 2B (Strelkov et al., 2002). GFAP is predominantly expressed in glial cells, whereas vimentin is present in mesenchymal tissue and desmin in muscle cells, although desmin is also expressed in posterior capsule opacification within lens epithelial cells (cataract with fibrotic plaques) (Lovicu et al., 2002). Vimentin has been shown capable of co-assembly with either GFAP or desmin and is co-expressed at the same time. CRYAB is a sHSP, which forms large oligomeric complexes either alone or with αA-crystallin to form α-crystallin. The sHSPs are generally upregulated in response to pathological states such as tuberculosis (Yang et al., 1999). CRYAB can prevent aggregation of proteins, demonstrated by a reduction in thermal aggregation of insulin and interacts with other proteins via hydrophobic interactions; at physiological temperatures CRYAB has a greater quantity of hydrophobic regions (responsible for binding to hydrophobic pathches on target unfolded proteins) than αA-crystallin, which reflects its greater ability for chaperone-like activity (Datta and Rao, 1999). IFs interact with sHSPs, as shown by the ability of HSP25 to reduce the gel viscosity of GFAP filaments, as assessed by a falling ball viscosity assay and also CRYAB's ability to also prevent IF gel formation (Perng et al., 1999a, van Boekel et al., 1999). Mutations in CRYAB can alter its interactions with IFs and induce changes in filament-filament interactions such as with the

cataract- and cardiomyopathy-causing R120G mutant, which results in increased clumping of desmin and even GFAP filaments, despite the mutation not being linked to gliopathy (Perng et al., 1999b, Perng et al., 2004).

Magnesium ions are known to play a key role in the formation of assembled GFAP filaments; with a calcium-magnesium binding site having been reported in the 2B rod domain and thus the hypothesis was that removal of magnesium ions would result in perturbed assembly (Yang Z W., 1988). Not much is known about the assembly mechanisms of GFAP filament formation, especially regarding the absolute number of ULFs that are aligned parallel to each other to form the mature filament after final compaction and how the protofilament step is involved. Changes in the concentrations of divalent cations have been linked to pathological states such as increased iron levels within the substantia nigra in PD patients, where degenerated dopaminergic neurons correlate with iron importers being increased and iron exporters decreased in expression levels alongside increased expression of α-synuclein involved in Lewy body formation (Lv et al., 2011). Development of AD, ALS and Huntington's disease have also been correlated with high levels of iron (Pankhurst et al., 2008, Simmons et al., 2007, Jeong et al., 2009). However some drug-induced skeletal muscle myopathies are due to a reduction in the level of muscle metal ions, such as with D-penicillamine administration (Preedy et al., 2001). High levels of manganese are implicated in idiopathic Parkinson's disease (IPD) and in the spinal cord of patients with ALS linked to manganism that is coincidental with increased levels of CRYAB (Wang et al., 2008). Mitochondria are known as a store of manganese ions; these ions are involved in a few processes including association as a chelated ion within the complex of manganese superoxide dismutase, therefore skeletal muscle contains a moderate quantity in addition to the high levels in other tissues such as the liver and pancreas (Calne et al., 1994, Miyata et al., 1983, Murakami et al., 1998). Therefore although not reported so far, it may be the case that accumulated levels of iron or manganese in AxD or desmin-related myopathies, linking in with GFAP and desmin studied here, contributes to increased associations with CRYAB and therefore it was important to study how manganese and other divalent cations may influence these interactions.

Assembly was carried out investigating the influence of different divalent cations (magnesium, manganese and calcium) and their absence on filament structures. The interactions of CRYAB with these filaments were investigated as it has been shown

that mutated GFAP, which forms aggregates, has increased associations with CRYAB. Calcium levels are known to be transiently high in cells when released from the endoplasmic reticulum (ER), but it is more likely that magnesium ions play a role in regulation of GFAP filament networks (Tanaka et al., 1989). It has been shown for Xenopus vimentin that the addition of 5 mM Ca^{2+} ions results in much thicker filaments compared to normal conditions of assembly (Hofmann et al., 1991). Therefore in addition to the role that the physiological divalent magnesium ions play in GFAP assembly, calcium ions were also investigated in this study alongside manganese ions, to assess effects of other physiological divalent cations. It has already been shown that manganese ions result in greater associations of GFAP bovine filaments as revealed from turbidity spectrophotometrical measurements (Yang and Babitch 1988). When bovine GFAP has been assembled in 5 mM $CaCl_2$ it was found to form individual filaments but also filament bundles from side-by-side interactions and divalent cation concentrations above 10 mM resulted in aggregate formation, thus showing that the divalent cation environment is important for influencing the assembly of filaments (Yang and Babitch, 1988). The ability for WT CRYAB to reduce filament-filament interactions was investigated under these conditions with GFAP filaments formed in 1 mM Ca^{2+} and Mn^{2+} ions, showing that manganese ions resulted in the perturbed ability of CRYAB to be able to reduce filament-filament interactions since not as much GFAP was present in the supernatant portion at room temperature compared to assembly in calcium ions. GFAP filaments were found to be most sensitive to their divalent cation environment, compared to desmin and vimentin. Thicker GFAP filaments were observed with 1 mM Mn^{2+} ions, 5 mM Ca^{2+} ions, in the absence of divalent cations and at pH 6.3. Shortened GFAP filaments were observed with 1 mM Mn^{2+} ions, at pH 6.3 and in the absence of divalent cations giving filaments that were prone to aggregation. There is a clear effect upon WT GFAP filament compaction from manganese ions and therefore the effect of this divalent cation on desmin and vimentin type III IFs was also investigated.

To add to the investigation of whether temperature influences the binding of WT CRYAB to 10 nm filaments through assembly with magnesium ions, experiments keeping a constant pH at different temperatures were devised. The hypothesis inferred from the data in chapter 2 was that at lower pH values and increased temperatures the CRYAB would increase its association with the filaments, likely

due to alterations in the filament structure. This follows on from the story in chapter 2, with the question of how CRYAB increases its interactions with filaments at higher temperatures and if it is due to a drop in pH, an increase in temperature or a mixture of the two. Previous studies on CRYAB binding to filaments involved using a shortened assembly method (Perng et al., 2008). Although this has its merits due to ease of controlling the final assembly temperatures using a water bath, in this study the effects of temperature on binding was assessed using overnight assembly as filaments compact a lot better.

3.1.2 Materials and methods.

3.1.2.1 Assembly methods.

3.1.2.1.1 Tris assemblies.

For assembly of GFAP filaments in the absence of magnesium ions, the method used was the same as in Figure 2.13, except 1 mM EDTA (0.0727 mM free Mg^{2+} ions (Ca^{++} and Mg^{++} Calculations programme)) was added. 0.4 mg/mL GFAP was assembled with or without 0.16 mg/mL WT CRYAB (1:1 molar ratio) unless otherwise stated. In addition $MnCl_2$ and $CaCl_2$ were investigated at concentrations of 1 mM and also 5 mM for Ca^{2+}. High and low speed sedimentation assays were carried out as in section 2.1.2.12 and TEM grid preparation was the same. For investigating the influence of different divalent cations on GFAP, desmin and vimentin filament assemblies, the same assembly method was used minus the penultimate buffer step and without EDTA in the final buffer, at 23-28 and 39-44 ^{0}C. A 1 mM concentration of divalent cations was used unless otherwise stated.

3.1.2.1.2 Desmin shortened assembly method.

Filaments were assembled via dialysis using a previous method from the laboratory, through 6, 4, 2 and then 0 M urea in 10 mM Tris-HCl (pH 8.0), 1 mM EDTA and 1 mM DTT and then into 10 mM Tris-HCl (pH 7.0) with 1 mM DTT (Perng et al., 2004). The protein was placed on ice at 4 ^{0}C in a TLS-55 centrifuge tube before the

quick assembly buffer was added with 100 mM imidazole-HCl (pH 6.8) and 1 mM DTT final concentrations and left at 37 ^{0}C for 1 hr (Perng et al., 2008).

3.1.2.1.3 Manganese ion assemblies.

Assemblies of GFAP and vimentin were carried out through a 4-(2-Hydroxyethyl)piperazine-1-ethanesulfonic acid (HEPES) assembly method with Mn^{2+} ions as shown in Figure 3.1. A 1:1 molar ratio of filaments: WT CRYAB was used (0.2 mg/mL vimentin (53.7 kDa) + 0.07 mg/mL WT CRYAB (20.2 kDa) and 0.2 mg/mL GFAP (49.9 kDa) + 0.08 mg/mL WT CRYAB). Below is a table highlighting the pH values used. The HEPES buffers (ΔpKa/^{0}C of -0.014) were made at three different pH values so that they would be pH 6.9 at their respective temperatures.

The three stock HEPES buffers' pH values prepared at 23 ^{0}C			The three final assembly buffer pH values prepared with either buffer 1, 2 or 3 at the temperatures shown		
1	2	3	1 23 ^{0}C	2 39 ^{0}C	3 44 ^{0}C
7.1	7.22	7.29	6.9	6.9	6.9

Table 3.1 **pH values of final HEPES assembly buffers measured with salt and DTT**.

Final assembly buffer pH values are shown, prepared taking into account a ΔpKa/^{0}C of -0.014, for buffer 5 in Figure 3.1 (Beynon and Easterby, 1996).

For the final buffer at 23 ^{0}C with manganese ions, initially the pH dropped to 6.8 when using a pH 7.00 stock solution of HEPES compared to stock pHs of 7.22 and 7.29 which both dropped to pH 6.9 at 39 and 44 ^{0}C in the final assembly buffer conditions. Therefore a pH 7.1 HEPES buffer was prepared and used for the final assembly buffer at 23 ^{0}C to get a final pH of 6.9. In this case when higher temperatures than 23 ^{0}C were used, the manganese ion was behaving as a different Lewis acid. Also, the final assembly buffer pH with 1 mM $MnCl_2$ ions is higher at pH 6.9 than pH 6.8 with $MgCl_2$ at 39 and 44 ^{0}C using pH 7.22 and 7.29 stock

solutions. It is already known that buffers have metal-binding constants, however this is relatively low for HEPES in comparison to phosphates (Sokolowska and Bal, 2005). The HEPES buffer is zwitterionic with the weak acid having both a positive charge on the NH group and a negative charge on the SO_3 group; the conjugate base is negatively charged and thus any free cations will compete with H^+ ions for binding (Good and Izawa, 1972). Magnesium ions exist only in one oxidation state of +2 and manganese can exist in many oxidation states up to +7, however under these conditions the +2 oxidation state will be the most stable; only at higher pH values such as 14 will the higher oxidation states become more stable (Ghosal et al., 2005, Cox, 2004). Importantly, magnesium ions (ionic radius of 0.65 Å) are approximately 20% smaller than manganese ions (ionic radius of 0.80 Å) and thus will have a greater charge density lending itself to stronger interactions with water and thus more capacity for it to accept electrons and act as a Lewis acid (Permyakov and Kretsinger, 2011). Whereas manganese ions will have more covalent interactions, with it being a transition metal, leading to a lower hydration and therefore will be a less effective Lewis acid, thus explaining why the pH is lower when magnesium ions are used instead of manganese, at 39 and 44 ^{0}C (Yoder, 2006).

For anionic phosphate buffers, when cations from salts are added they are attracted to the negatively charged phosphate ions leading to more hydronium ions in solution and thus a drop in pH and the differences in the ability for different ions to drop the pH by different amounts is due to their polarisability. Also anions, which have higher polarisability than cations, will be closer to the phosphates thus reducing release of hydronium ions and leading to higher pH values. However with Tris-HCl buffers, these are cationic and the conjugate Tris base is electrostatically neutral and cations are thought to lead to increases in pH with a lower quantity of free hydroniums, which has been observed in chapter 2 where the addition of NaCl and $MgCl_2$ resulted in a whole pH unit increase for the final Tris assembly buffer (Salis et al., 2007).

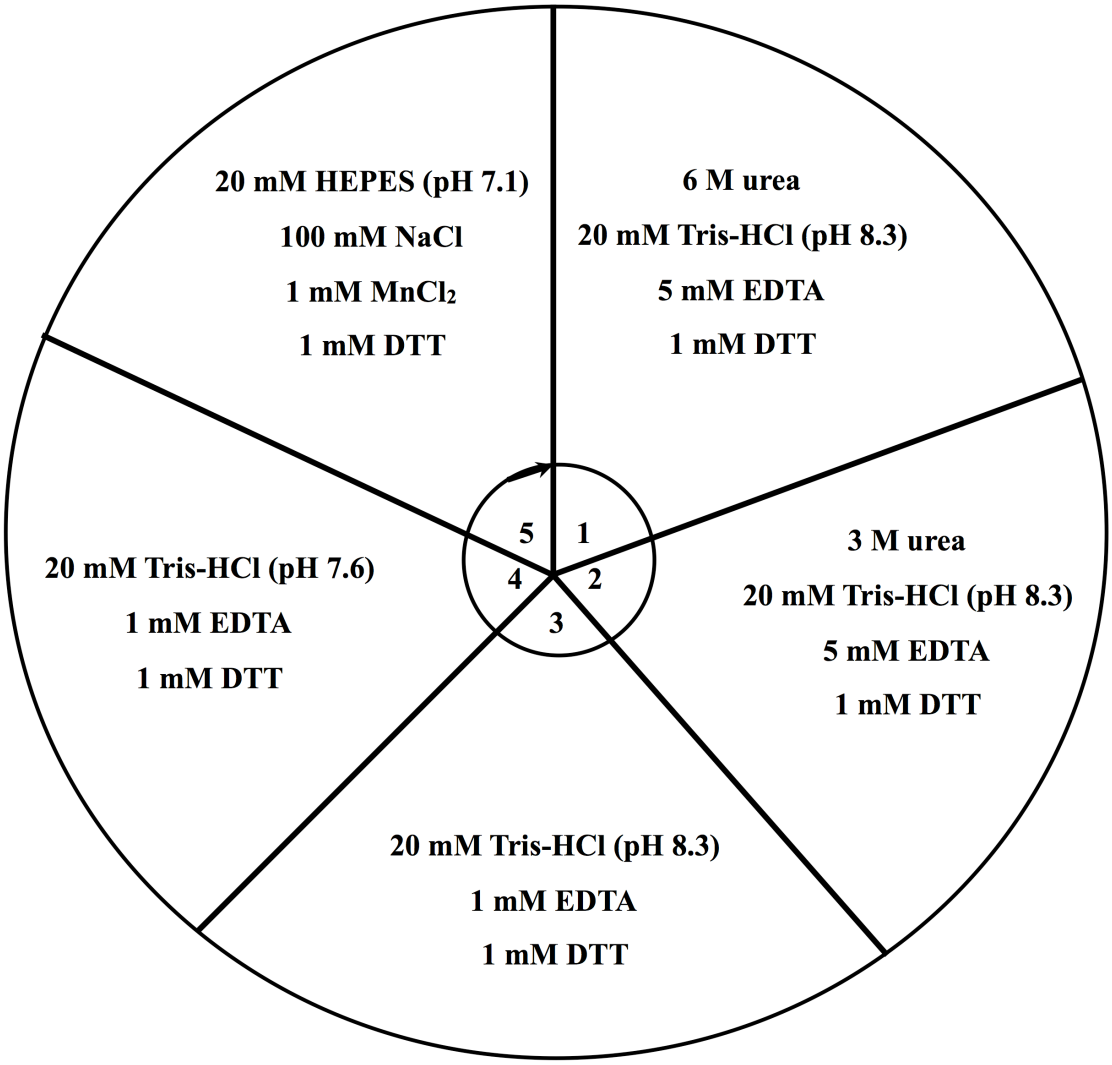

Figure 3.1 GFAP, desmin and vimentin HEPES assembly wheel.

Protein was assembled clockwise within 1 L buffers (with a 5,000-fold excess of dialysis buffer to sample volume) except for buffer 5 (with a 2,500-fold excess of dialysis buffer to sample volume) and assembly was for 2 hr for each step, using a stirring flee on a magnetic stirrer at 28 ^{0}C prior to buffer 5 at 23, 39 and 44 ^{0}C overnight. The final buffer was pH 6.9.

Desmin was excluded from the assemblies here as the manganese ions resulted in such increased interactions of filaments that inevitable sample loss after pipetting on gels occurred.

3.1.2.1.4 HEPES and magnesium ion assemblies; CRYAB addition before filament formation.

To assess the pH and temperature dependence of binding of WT CRYAB to GFAP, vimentin and desmin with its addition prior to filament maturation, an *I* of 20 mM HEPES alongside 100 mM NaCl was used to ensure proper compaction of the filaments. All filaments were assembled using 28 ^{0}C for all the buffers before the final assembly step, which was at 23, 39 or 44 ^{0}C. A 1:1 molar ratio of filaments: WT CRYAB was used (0.2 mg/mL desmin (53.4 kDa)/vimentin + 0.07 mg/mL WT CRYAB and 0.2 mg/mL GFAP + 0.08 mg/mL WT CRYAB). WT GFAP, vimentin and desmin were assembled through the method used in Figure 3.1, except 1 mM magnesium ions were used in place of manganese ions in buffer 5. CRYAB was mixed with the filaments in the column purification buffers before assembly was begun, for the main experiments. To remove temperature-heating effects from the magnetic stirrers for buffer 5 and to ensure accurate temperatures, a polystyrene base was placed between the magnetic stirrers and plastic beakers containing the final assembly buffers and samples, to act as an insulator. All buffers prior to the final buffer were at 28 ^{0}C and the final buffer was pH 7.3, 6.8 or 6.3. The final pHs were checked with the pH meter upon addition of the salts and DTT, at the appropriate temperatures using a thermostatically controlled water bath and are listed in the table below. Calibration of the pH meter was also carried out using two standards either side of the pH being measured, at the same temperatures as the final buffers.

The three stock HEPES buffers' pH values, per row, prepared at 23 ^{0}C			The three final assembly buffer pH values prepared with either buffer 1, 2 or 3, per row, at the temperatures shown			Base: acid ratio of HEPES buffers at final temperatures used
1	2	3	1 23 ^{0}C	2 39 ^{0}C	3 44 ^{0}C	
7.6	7.82	7.89	7.3	7.3	7.3	1:0.8
7.0	7.22	7.29	6.8	6.8	6.8	0.3:1
6.5	6.72	6.79	6.3	6.3	6.3	0.09:1

Table 3.2 **pH values of final assembly buffers measured with salt and DTT**.

As can be seen the pH values were lower in the presence of the salts, similar to the previously found trend of a reduction of pH upon addition of NaCl to phosphate buffer solutions and the discrepancy was different dependent upon the location within the buffering range looked at, dependent upon the different ratios of base/acid as shown in Table 3.2 (calculated using the Henderson-Hasselbach equation with a pKa of 7.51 at 23 ^{0}C) (Robinson, 1929). The largest ΔpH appears to occur at the higher base: acid ratio, which is the opposite of what was found with the effects of addition of NaCl or LiCl on the pH of phosphate buffers (Robinson, 1929). The pHs were the same at the different temperatures for each pH looked at and thus conclusions could be drawn as to temperature and pH changes influencing the binding of CRYAB to filaments.

3.1.2.1.5 HEPES and magnesium ion assemblies; CRYAB addition after filament formation.

As an additional test of the system, experiments at pH 6.3 and 7.3 were carried out with CRYAB oligomers added to assembled GFAP filaments, to see if similar results were apparent to the binding seen when CRYAB was added before filaments had formed. For this case the WT CRYAB was dialysed alongside the filaments into the final assembly buffers of either pH 6.3 or 7.3 overnight at 23 ^{0}C using the same method as Figure 3.1 with magnesium ions, then CRYAB was added at a 1:1 molar ratio to the assembled filaments in the dialysis bags, they were placed into the higher pH buffers as necessary in glass beakers and sonicated for 15 sec (enabling the CRYAB to get within the filament networks), then they were dialysed for 1.5 hr at 23 ^{0}C and incubated at 23 ^{0}C or the increased temperatures for a further 4 hr on rotating wheels, within Eppendorfs positioned perpendicular to the axis of rotation so that the filament solutions didn't come into contact with the inner surface of the Eppendorf lids. Since vimentin bound the least to CRYAB in the first section, only GFAP was looked at to test the hypothesis that the surface of the filaments have changed leading to altered binding and two pH values of 6.3 and 7.3 were studied which gave the greatest contrast in binding. Desmin would have been tested but material was lost from most of the samples on the gels run suggesting that despite sonication being used, the interactions between the filaments were too great, before addition of CRYAB and the filaments were likely sticking to the plastic surfaces and

thus only GFAP could be looked at. Student's T-tests and Mann-Whitney U tests were carried out on the data similar to the analysis carried out in chapter 2 and the data are shown in the appendix, comparing the quantity of CRYAB binding to filaments from its addition to assembled filaments to the binding seen when CRYAB was added before filament formation, at the same pH.

A further test was set up with the filaments assembled at pH 6.3 at 23 ^{0}C and then transferred into pH 7.3 for 1.5 hr, before CRYAB assembled at pH 7.3 was added to assess any potential for the filaments to revert back to a conformation that has lower binding. The solutions were sonicated and incubated for 4 hr in Eppendorfs. This also aids in understanding if it is predominantly the final filament surface structure that has been altered due to a lower pH and increased temperature values, resulting in increased associations with CRYAB, as opposed to both alterations in the CRYAB structure and the filament surface, which could be presumed from CRYAB addition from the same pH.

3.1.2.2 Reduction of GFAP dimer.

20 µg of WT GFAP assembled through Tris assembly with manganese ions at 23-28 ^{0}C was reduced with 50 mM DTT at 37 ^{0}C for 1 hr, similar to a previous method used before and an equivalent mass of 4 µg to that loaded as the supernatant portion from a low speed sedimentation assay was then run on a sodium dodecyl sulfate polyacrylamide gel electrophoresis (SDS-PAGE) gel, alongside the supernatant portion (Dornmair and Mcconnell, 1990).

3.1.2.3 Gel electrophoresis.

Gels were run the same as in 2.1.2.8 except in some instances the Pageruler^{TM} Plus Prestained Protein Ladder #SM1811 (Fermentas, UK) was used, which has the following recombinant protein molecular weights: 250, 130, 95, 72, 55, 36, 28, 17 and 10 kDa, instead of the Pageruler^{TM} Prestained Protein Ladder #SM0671 (Fermentas, UK).

3.1.2.4 Sedimentation assays.

These were carried out the same as in 2.1.2.12.

3.1.2.5 TEM grid preparation and image collection.

Images were prepared and imaged the same as in 2.1.2.11.

3.1.2.6 Semi-dry immunoblotting.

Immunoblotting was carried out the same as in 2.1.2.9.

3.1.2.7 Statistical analysis.

Student T-tests were carried out the same as in 2.1.2.14.

3.1.2.8 Sequence alignments.

The ClustalW2 (EMBL-EBI, UK) alignment of WT human GFAP (GenBank: J04569.1), desmin (GenBank: NM_001927.3) and vimentin (GenBank: NM_003380.3) was carried out from pasting the sequences into the input box on the EMBL-EBI website (Larkin MA, 2007).

Sequence similarities were also assessed in BLAST (National Library of Medicine, US) using the Align option and blastp, after pasting the amino acid sequences. The megablast programme was selected. The alignment showed the % identities.

3.1.2.9 ImageJ filament measurements.

TEM images were imported into ImageJ 1.43r (National Institutes of Health, USA) and initially the straight line tool was selected and used to draw a line the same distance as the scale bar on the image. Then in the Analyze and Set Scale options, the known distance in nm was entered and also the units to drive a scale in pixels/nm. Filament widths and lengths were then measured by using the zoom option and also the line tool to span the length of interest and then the Analyze and Measure options.

3.1.3 Results.

Questions to answer	Information gathered	Page #s
What is the effect of the divalent cations Mg^{2+}, Mn^{2+} and Ca^{2+} on the assembly properties of WT GFAP, vimentin and desmin?	**i)** Mn^{2+} induces higher oligomeric structures to be formed for all three IFs; GFAP dimers are due to oxidative cross-linking. It also increases the interactions between CRYAB and filaments compared to Mg^{2+} ions. **ii)** Mn^{2+} ions increase GFAP and desmin filament-filament interactions, but not for vimentin. **iii)** GFAP filaments are wider than 10 nm when assembled in the presence of 1 mM Mn^{2+} ions and 5 mM Ca^{2+} ions. Human vimentin and desmin appear unaffected in 5 mM Ca^{2+} ions. **iv)** Filaments assembled in 1 mM Ca^{2+} ions appear no different to those assembled in 1 mM Mg^{2+} ions. **v)** The absence of divalent cations leads to disruption in GFAP longitudinal annealing, although lengths appear longer than ULFs and this leads to increased CRYAB binding.	135 133 131 116 128 129 130 123-125 114
Is pH more crucial than temperature of the final assembly buffer to result in increased binding of CRYAB to WT GFAP, vimentin and desmin?	**i)** Low pH is the main determining factor for binding of CRYAB and higher temperature acts to exacerbate this effect, likely due to changes in the structure of the presenting filament and increases in CRYAB hydrophobic surfaces. CRYAB oligomers are wider and more variable at pH 6.3 compared to 6.8 and 7.3. **ii)** CRYAB binds predominantly to desmin filaments with least preference for vimentin. **iii)** GFAP in pH 6.3 buffer has variable widths, implicating a filament structural change is likely responsible for increased interactions with CRYAB. Vimentin in pH 7.3 at 23 ^{0}C is also wider. **iv)** The filament surface is very important for determining interactions with CRYAB, demonstrated from the assembly stage when CRYAB is added where most binding occurs when CRYAB has been present throughout GFAP filament formation. **v)** Filaments appear to have some plasticity in their surface structures for interaction with CRYAB as those assembled at pH 6.3 and put into pH 7.3 bind less CRYAB than those just assembled at pH 6.3.	142 140-141 149-150 153 154
How does temperature influence binding of WT CRYAB to filaments with Mn^{2+} ions?	**i)** With Mn^{2+} ions, temperature rises induce increased binding of CRYAB to the filaments with the preference of binding as vimentin<GFAP. **ii)** Desmin filaments stuck to the plastic surfaces and pipette tips when assembled in HEPES with Mn^{2+} ions thus showing how the interactions between the filaments are greatly increased, more so than even the desmin assembled in Tris buffer with Mn^{2+} ions.	139

Table 3.3 **Summary of findings**.

3.1.3.1 GFAP assembly is susceptible to its divalent cation environment.

WT GFAP forms 10 nm filaments when assembled through the standard assembly procedure. However in this case where divalent cations have been chelated, the filaments are unable to elongate and compact as usual and have changed filament morphologies (Figure 3.4). However there is some capacity for elongation, referring to Figure 1.4 where the assembly mechanism shows type III IFs forming ULFs that are approximately 60 nm in length, since the filaments are longer than ULFs. The filaments are also thicker than normal and often reach over 20 nm. However the elongation is not complete and compaction will also be stalled thus giving the appearance of sheet-like structures and much wider filaments often over 20 nm thick (Figure 3.4). The lengths vary but some of the shorter filaments are approximately 300 nm, measured in ImageJ 1.43r (National Institutes of Health, USA). Despite the increased filament-filament associations as shown below in Figure 3.2 B), displaying average quantification results of the percentages of GFAP in the supernatants after low speed sedimentations, WT CRYAB is able to reduce the filament-filament interactions between these filaments.

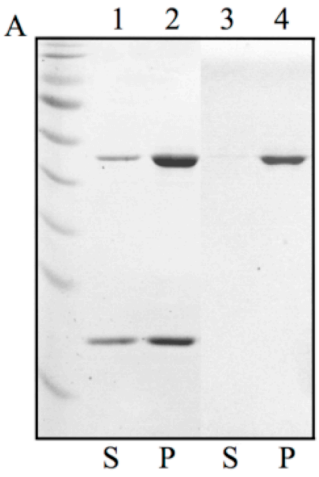

B

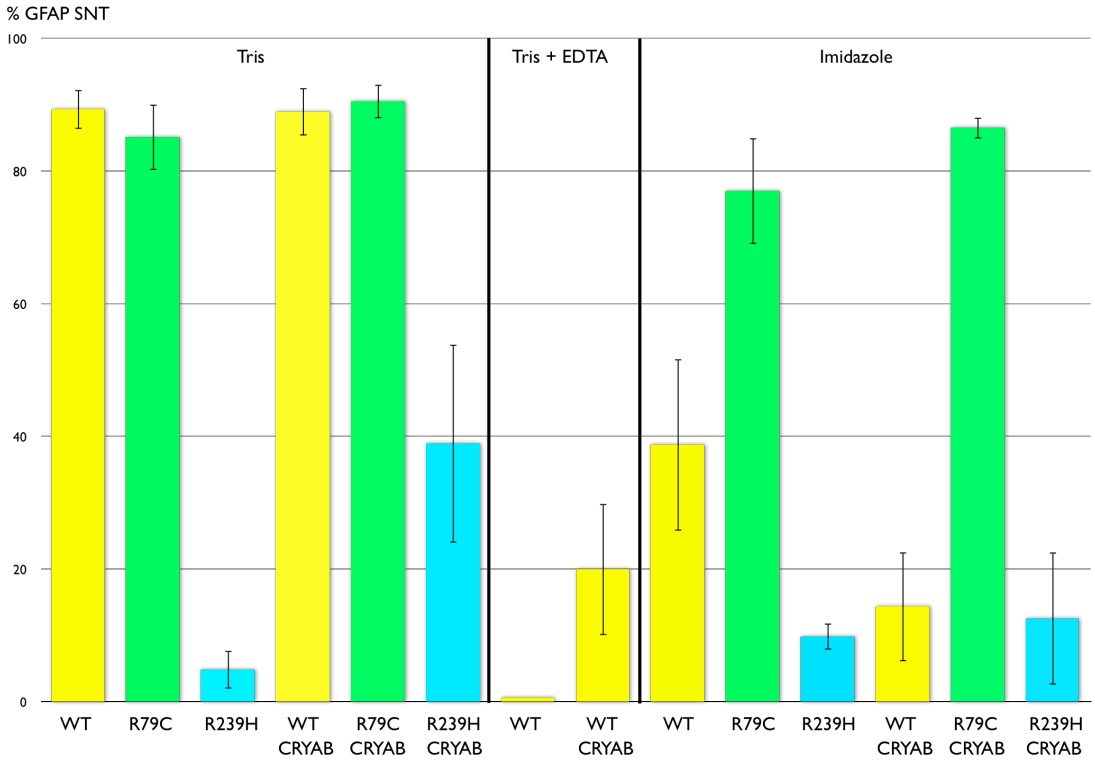

Figure 3.2 CRYAB is able to reduce filament-filament interactions of GFAP assembled without magnesium ions as demonstrated from low speed sedimentation assays.

A low speed sedimentation assay was carried out on WT GFAP samples after assembly according to Figure 2.13 with the addition of 1 mM EDTA to the final assembly buffer. WT GFAP was assembled alone (track 3-4) but when CRYAB is present (track 1-2), there is an increase in the soluble portion of GFAP (compare track 1 to 3), but notice how the chaperone-like activity of CRYAB can't prevent the

full extent of the increased associations since WT GFAP assembled in the presence of magnesium ions has a much lower quantity of material in the pellet fraction, shown in B). S and SNT= supernatant and P= pellet.

In addition to the usual ability of WT CRYAB being able to reduce filament-filament interactions, there is also an increase in the co-pelleting alongside these altered GFAP filaments at increased temperatures, similar to the trend of increased binding to normal GFAP filaments with increasing temperatures, seen in the second chapter. This binding is much greater than the binding seen to usual GFAP filaments, as displayed in Figure 3.3. Also unlike section 2.1.3.3 where WT CRYAB was shown to hinder formation of WT GFAP filaments, in this case CRYAB has no effect upon the pelleting under high speed sedimentation conditions of these altered GFAP filaments, as shown in Figure 3.3.

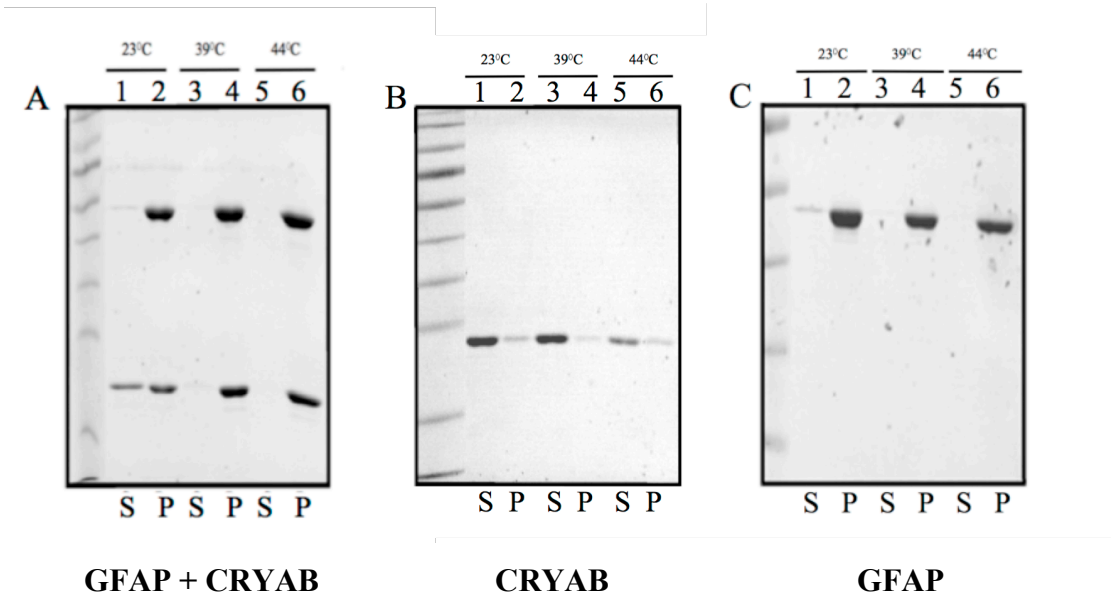

D

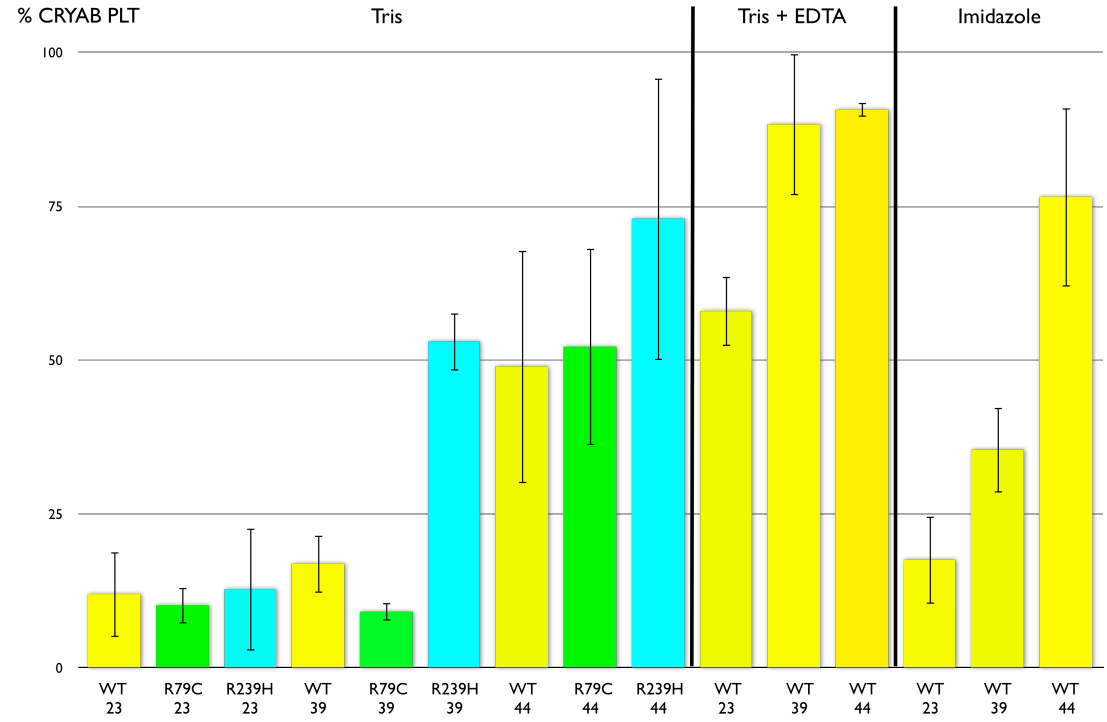

Figure 3.3 CRYAB binds more to GFAP assembled without magnesium ions, compared to with magnesium ions, upon increases in temperature as demonstrated from high speed sedimentation assays.

WT GFAP was assembled A) without magnesium ions in the presence of WT CRYAB at 23, 39 and 44 ^{0}C and quantification results are shown in the Tris + EDTA section of chart D). There is an increase in co-pelleting of CRYAB with GFAP at higher temperatures. The increase in pelleting of CRYAB is due to interactions with GFAP as B) most is present in the supernatant at all three temperatures on its own.

At increased temperatures C) there is also a reduction in the amount of GFAP in the supernatant portions showing an increase in filament interactions. Comparing the amount of GFAP in the supernatant in C) at 23 ^{0}C to that with WT CRYAB at 23 ^{0}C in A) it can be seen that the CRYAB hasn't increased the soluble portion of the assembled GFAP under these conditions and thus has little influence on the assembly status of these structures. S= supernatant and PLT and P= pellet.

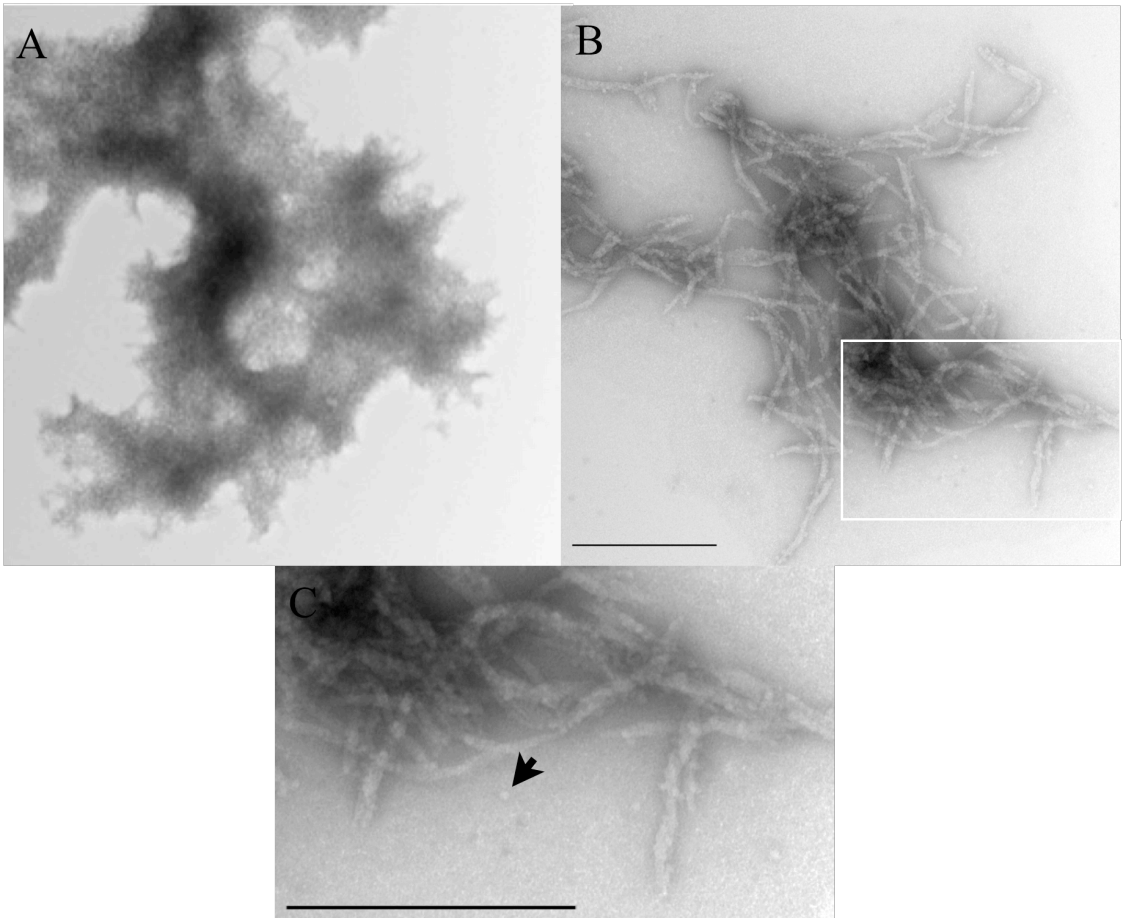

Figure 3.4 WT GFAP assembled without magnesium ions forms altered filaments and CRYAB acts to reduce interactions within these.

TEM images of A) WT GFAP assembled without magnesium and B) and C) WT GFAP with WT CRYAB assembled without magnesium at 28 ^{0}C were taken. The CRYAB has reduced the interactions between the GFAP, enabling the lengths to be discerned which are much shorter than usual WT filaments, but longer than ULFs.

Additionally the filament widths are thicker than 10 nm. The arrow points to a CRYAB particle. The scale bar is equal to 500 nm.

Despite no alteration in pelleting of assembled GFAP in magnesium-free conditions assessed from high speed sedimentation assays, in the presence of CRYAB compared to its absence, CRYAB enables the filament structures to be seen more clearly from TEM images as shown in Figure 3.4.

GFAP filaments were then assembled with manganese ions to see what effect this divalent cation has on assembly as increased levels have been linked to various neurological disorders. It was found that the filaments are assembly compromised and form filamentous sheet structures, even in the presence of CRYAB that is seen in Figure 3.5. However to contrast these findings, when 1 mM Ca^{2+} ions are used there is no apparent alteration in filament formation (Figure 3.6).

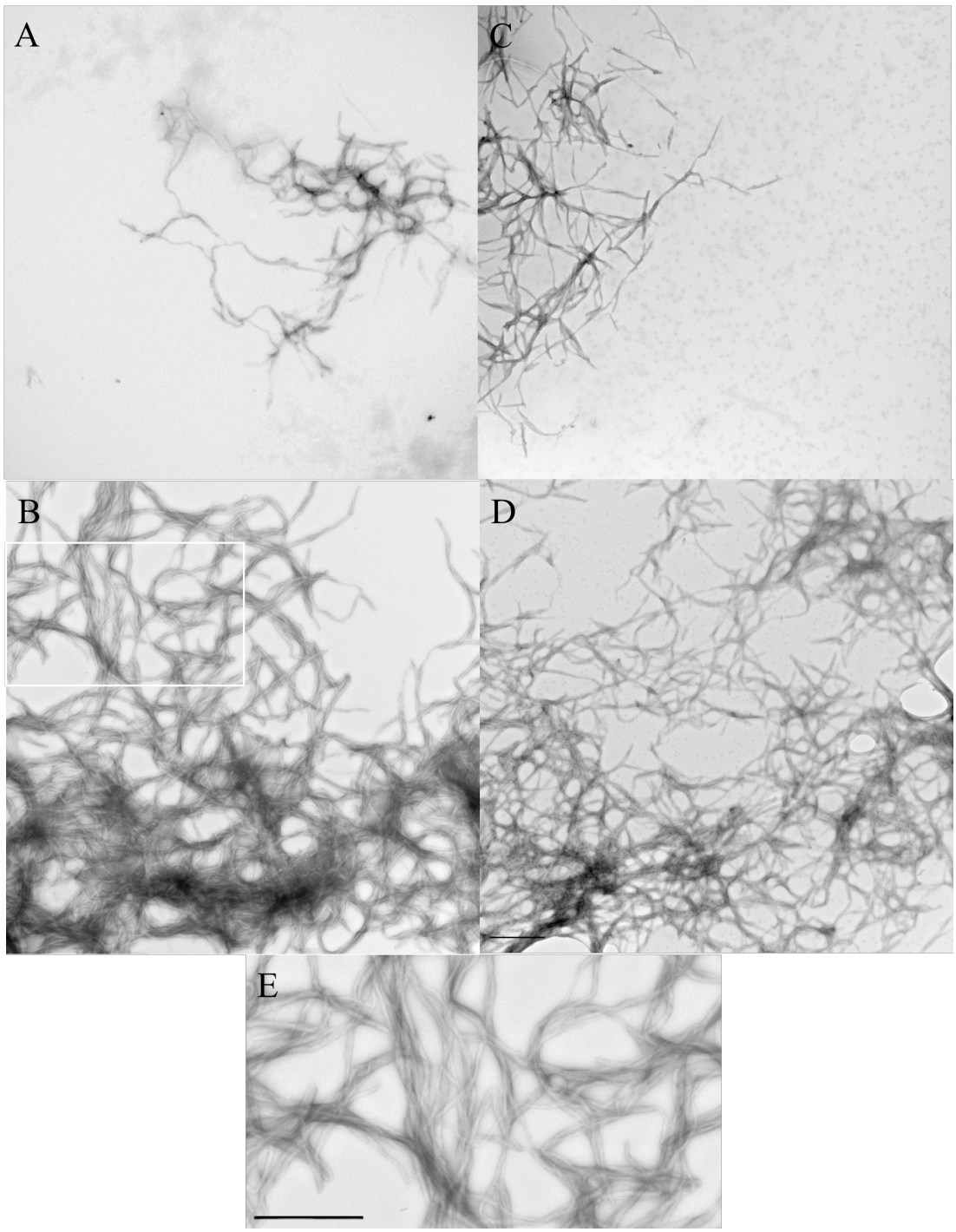

Figure 3.5 Manganese ions promote the formation of sheet-like filament networks of WT GFAP.

TEM images were taken of WT GFAP assembled alone at A) 28 and B) 44 ^{0}C (alongside its inset E)). Images are also shown of WT GFAP with CRYAB at C) 28 and D) 44 ^{0}C. Assembly was according to Figure 2.13 with 1mM Mn^{2+} ions. The GFAP filaments are shorter than normal and do not appear as the usual individual filaments but instead align next to each other much more and thus appear more like

sheets. The filament widths span up to approximately 30 nm, measured in ImageJ 1.43r (National Institutes of Health, USA). The scale bar is equal to 500 nm.

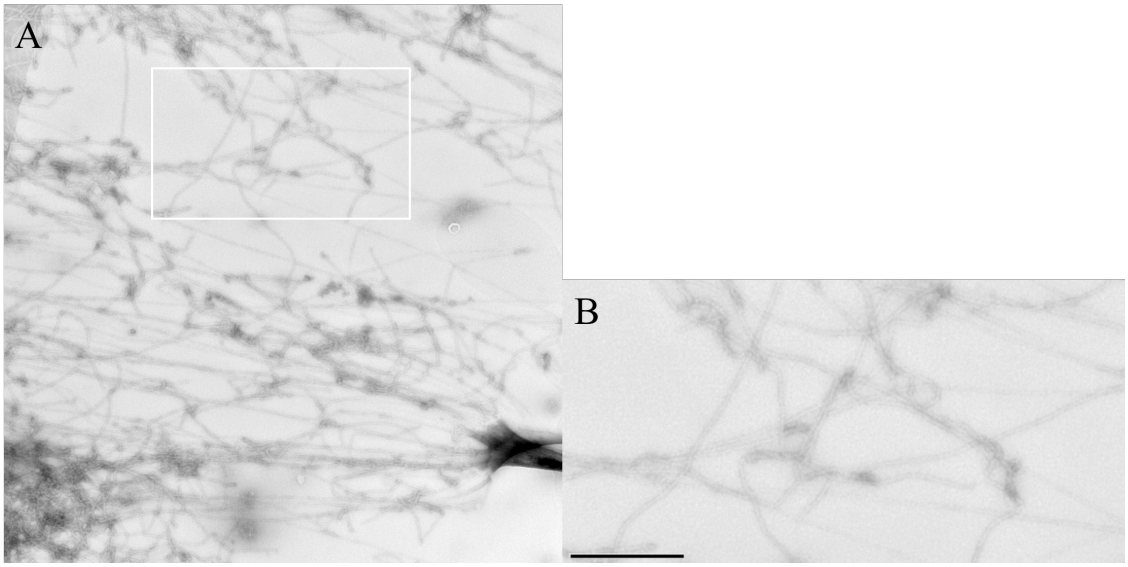

Figure 3.6 WT GFAP assembled with 1 mM Ca^{2+} ions form filaments morphologically similar to those assembled with 1 mM Mg^{2+} ions.
TEM images of WT GFAP assembled in 1 mM Ca^{2+} ions are shown at A) 39 ^{0}C and its inset B). The filaments are 10 nm in width and span up to a few μm thus showing that calcium assembled filaments are similar to magnesium assembled filaments that are unlike manganese assembled filaments. The scale bar is equal to 500 nm.

The action of manganese ions can also be seen biochemically from low speed sedimentation assays with an increase in pelletable GFAP compared to lower filament-filament interactions after assembly with magnesium and calcium ions (Figure 3.7).

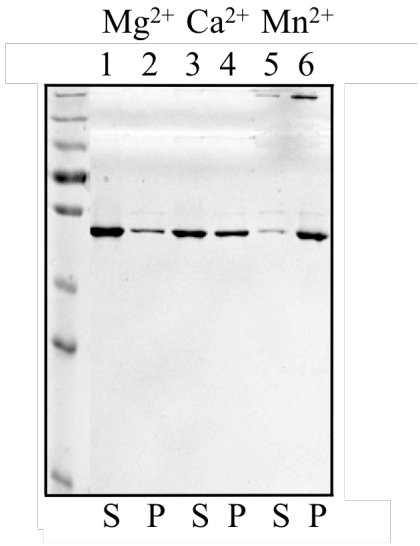

Figure 3.7 Manganese ions promote an increase in filament-filament interactions of WT GFAP.

Low speed sedimentation assays carried out on WT GFAP samples are shown. GFAP is predominantly in the supernatant portion with magnesium and calcium ions whereas with manganese ions most is pelleted showing there has been an increase in filament-filament interactions with the manganese ions. The manganese ions result in greater variability of GFAP in the supernatant fraction compared to the other two ions looked at, varying approximately 10-40% in the supernatant, but in all cases there is a greater amount pelleted compared to the conditions with the other two divalent cations. Manganese ions have also resulted in an upper molecular weight band of GFAP showing a larger complex of GFAP has been formed. S= supernatant and P= pellet.

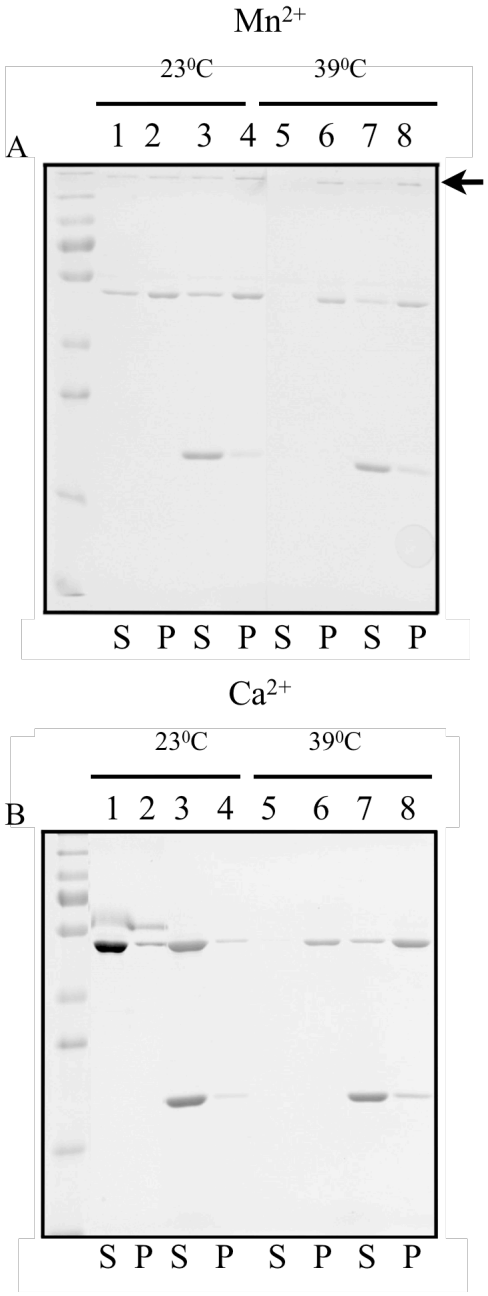

Figure 3.8 Addition of CRYAB to WT GFAP assembled with manganese ions does not prevent the formation of the higher molecular weight oligomer of GFAP.

Low speed sedimentation assay gels are shown. A) With 1 mM Mn^{2+}, the upper molecular weight band corresponding to larger complexes of GFAP, evidenced in Figure 3.17, is shown (arrow) and will be a dimer (Quinlan and Franke, 1983). The increased filament-filament interactions are seen as an increase in the amount of GFAP present in the pellet fraction that can't be reduced at 23 ^{0}C, although as with

calcium CRYAB can reduce GFAP interactions at 39 ^{0}C. B) Most of the GFAP is present in the supernatant at 23^{0}C with 1 mM Ca^{2+} and upon increasing the temperature to 39 ^{0}C there is an increase in the filament-filament interactions that CRYAB is able to reduce in addition to reducing interactions at 23 ^{0}C, as more GFAP is present in the supernatant fraction. S= supernatant and P= pellet.

3.1.3.2 Manganese ions promote increased binding of CRYAB to GFAP, desmin and vimentin filaments.

Previously quick assembly (3.1.2.1.2) has been used to investigate binding interactions of CRYAB with IFs and it can be seen that these filaments (Figure 3.9), in comparison to desmin filaments assembled through Tris assembly (Figure 4.4), have many more filament-filament interactions with similarities to the increased interactions seen with GFAP filaments formed in the presence of 1 mM Mn^{2+} ions (Figure 3.5 E)) (Perng et al., 2004). Therefore Tris assembly was used for these experiments to utilise conditions as close to the *in vivo* filament networks as possible to assess the role of different divalent cations on filament-filament interactions and CRYAB binding.

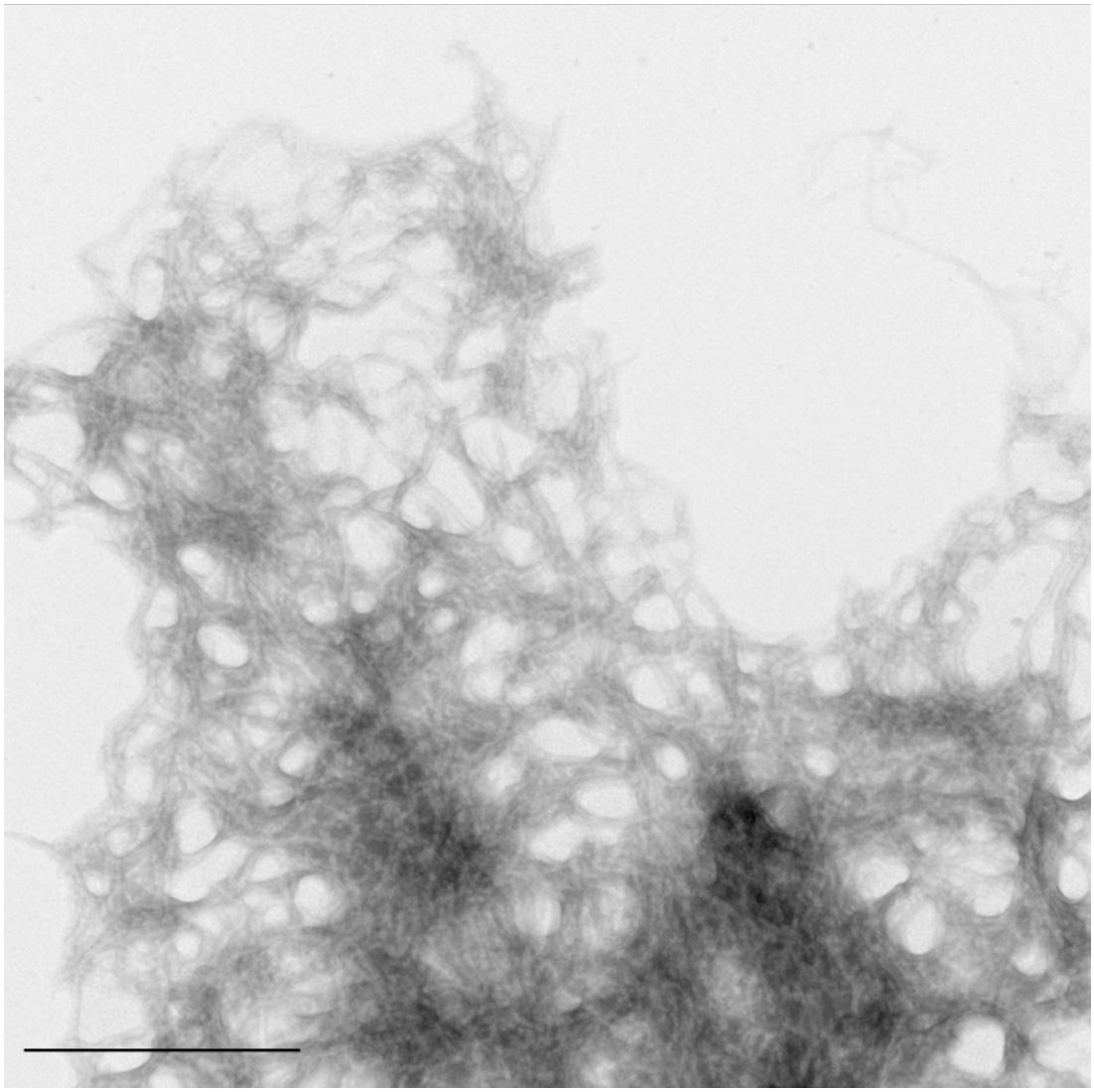

Figure 3.9 WT desmin assembled through the shortened assembly method.
Note how filaments look similar to the WT GFAP filaments assembled without magnesium ions with less spacing between individual filaments, highlighting a lack of proper compaction. The scale bar is equal to 500 nm.

Figure 3.10 shows that desmin and vimentin can form usual 10 nm filaments in 1 mM Ca^{2+} ions as does GFAP however 5 mM Ca^{2+} ions result in thicker filaments for human GFAP, similar to Xenopus vimentin, but not human vimentin or desmin as seen in Figure 3.12. As well as manganese ions promoting increased filament-filament interactions for GFAP and desmin (Figure 3.13) it also promotes an increase in binding of CRYAB to the filaments, shown from the TEM images in Figure 3.11 for desmin filaments where there is a greater density of CRYAB particles

surrounding the filaments compared to those after assembly in calcium ions. This increased binding due to manganese ions is shown from high speed sedimentation assays in Figure 3.15 and is compared to the filaments assembled in the presence of magnesium ions, which have lower binding. From these gel images it can be seen that desmin has the greatest binding to CRYAB, GFAP has an intermediary level and vimentin binds the least. Assembled filaments in 1 mM Ca^{2+} ions also have a relatively low binding to CRYAB (Figure 3.16). The binding with manganese and magnesium ions is also increased at the higher temperature range and is highlighted in the quantifications shown in Table 3.4.

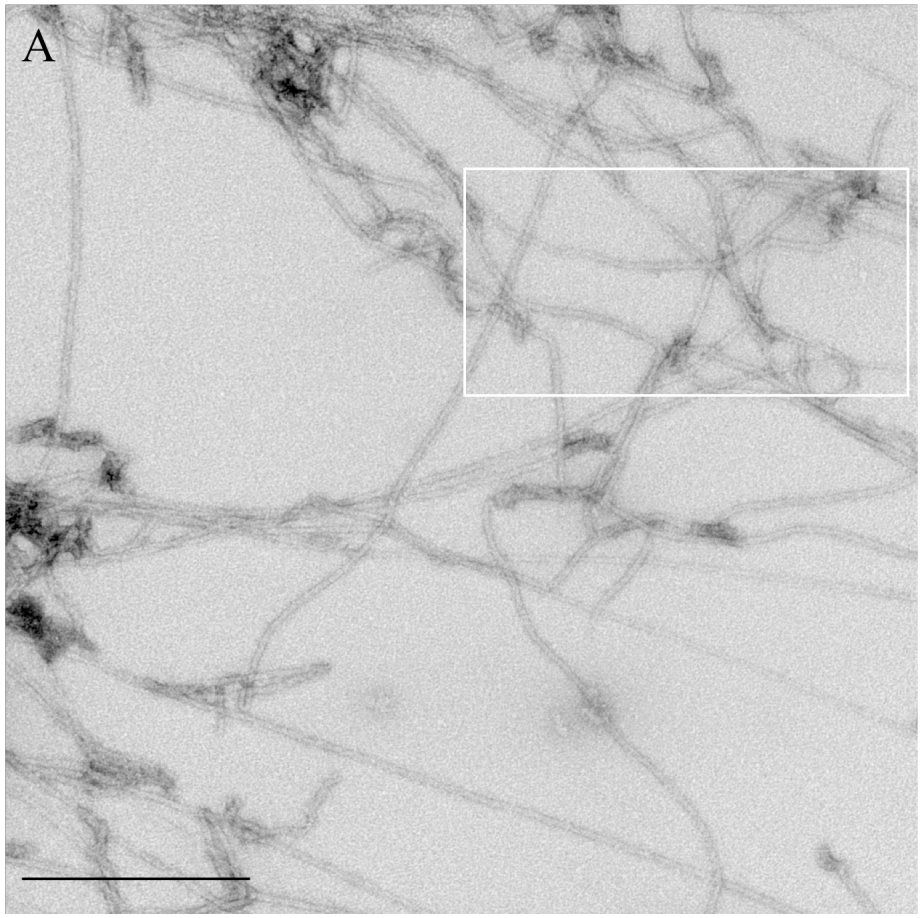
A

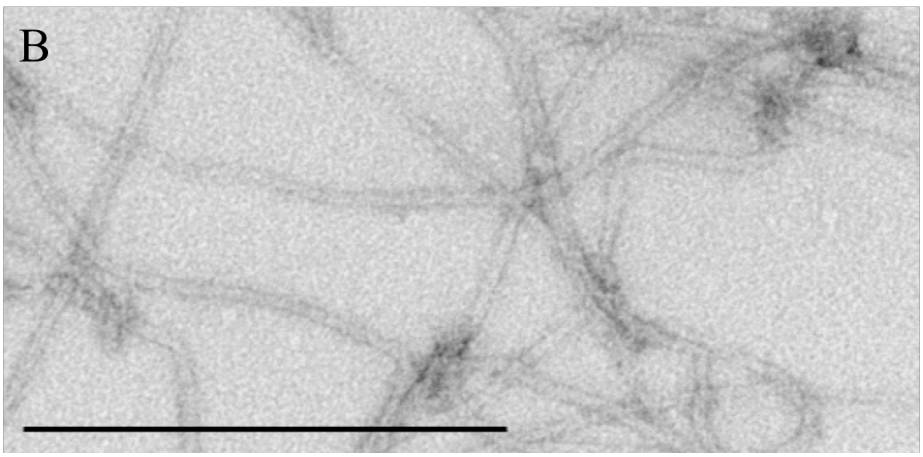
B

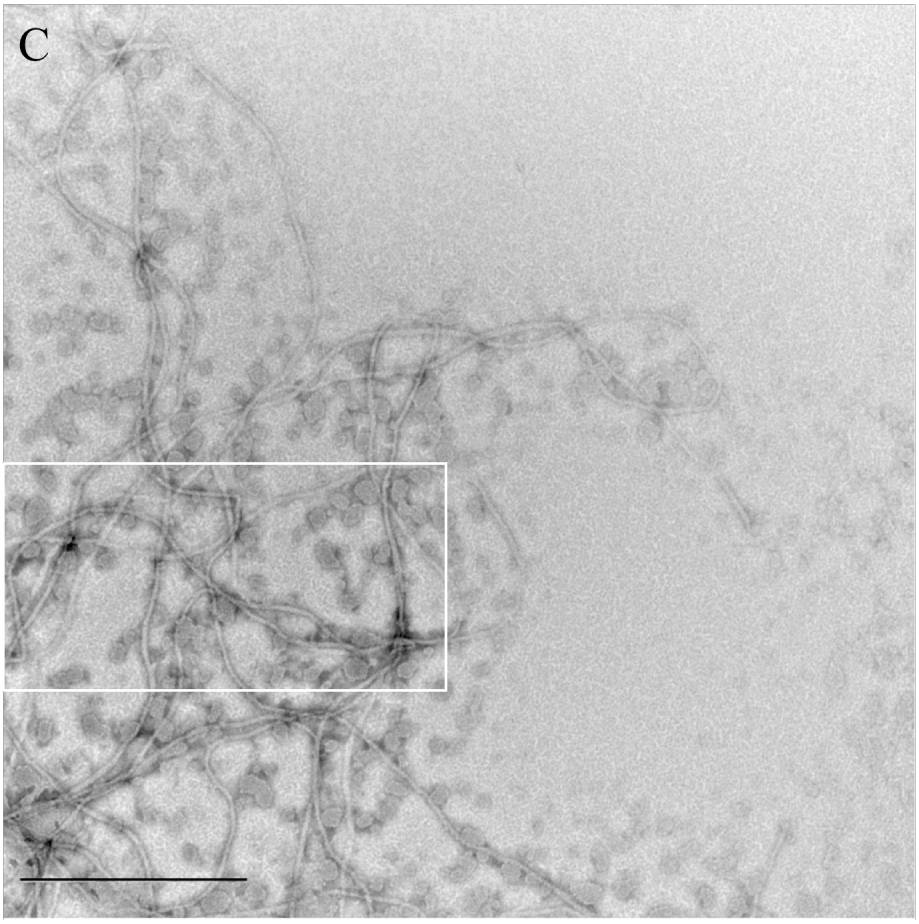
C

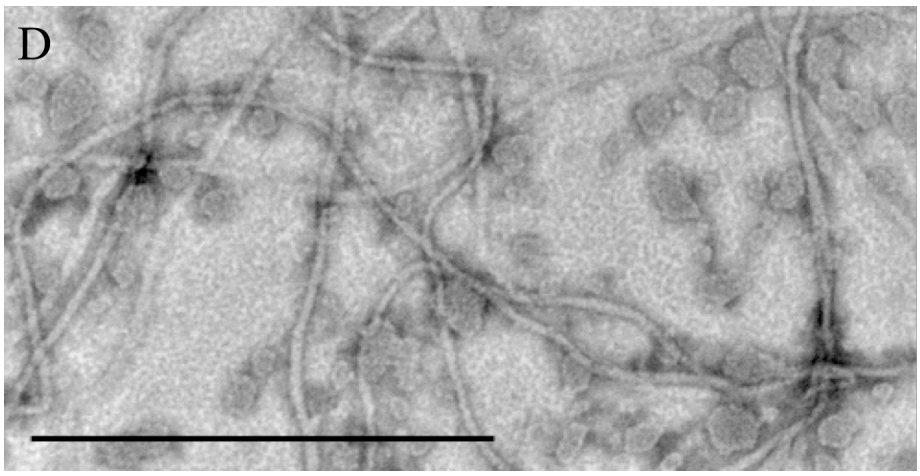
D

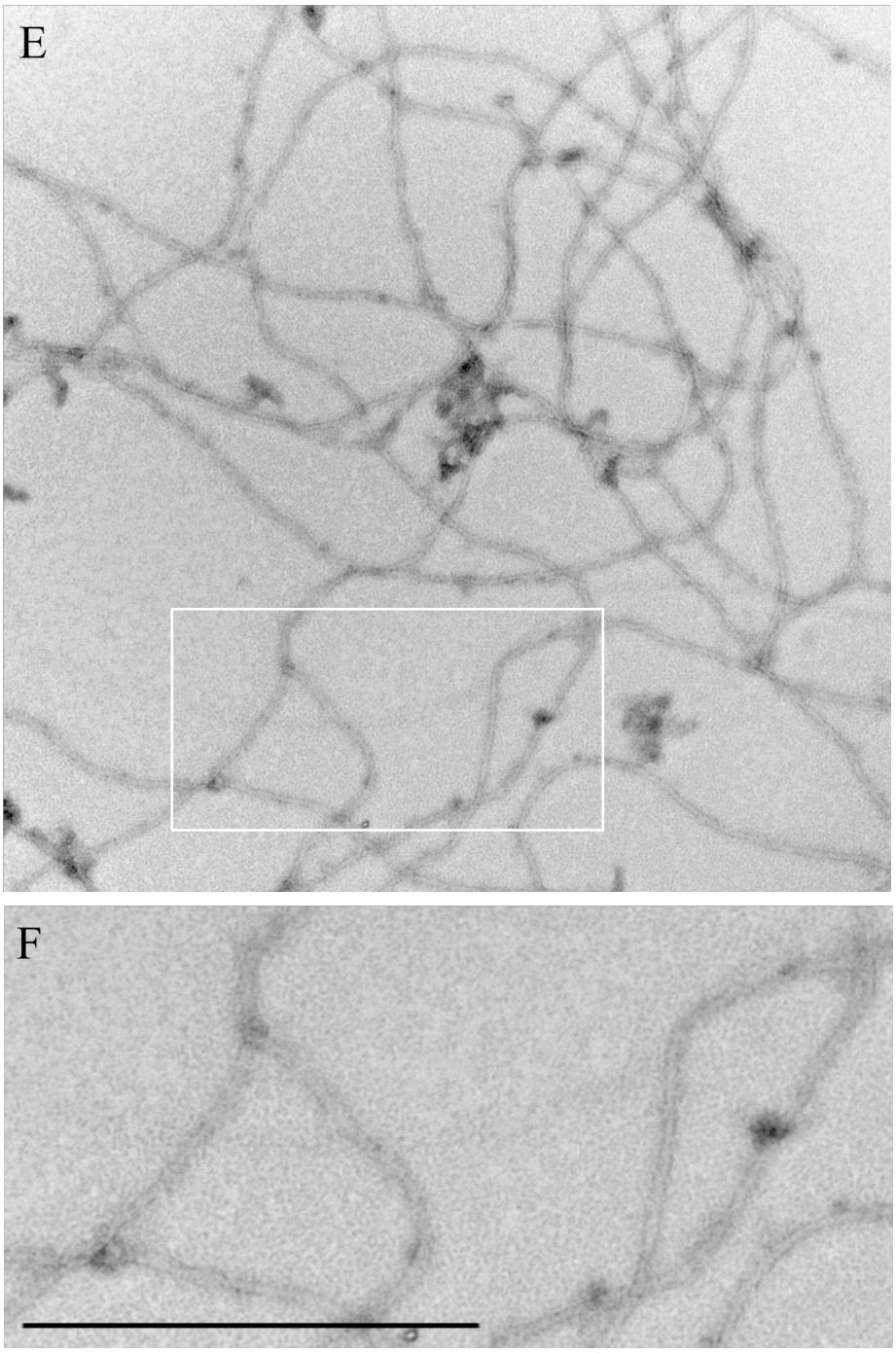

Figure 3.10 Filaments formed with 1mM calcium ions have usual 10 nm diameters.

TEM images are shown of A) and inset B) WT GFAP, C) and inset D) desmin and E) and inset F) vimentin assembled through Tris assembly with 1 mM Ca^{2+} ions at 39-44 ^{0}C. A 10 nm filament width can be observed for all three filament networks. The scale bar equals 500 nm.

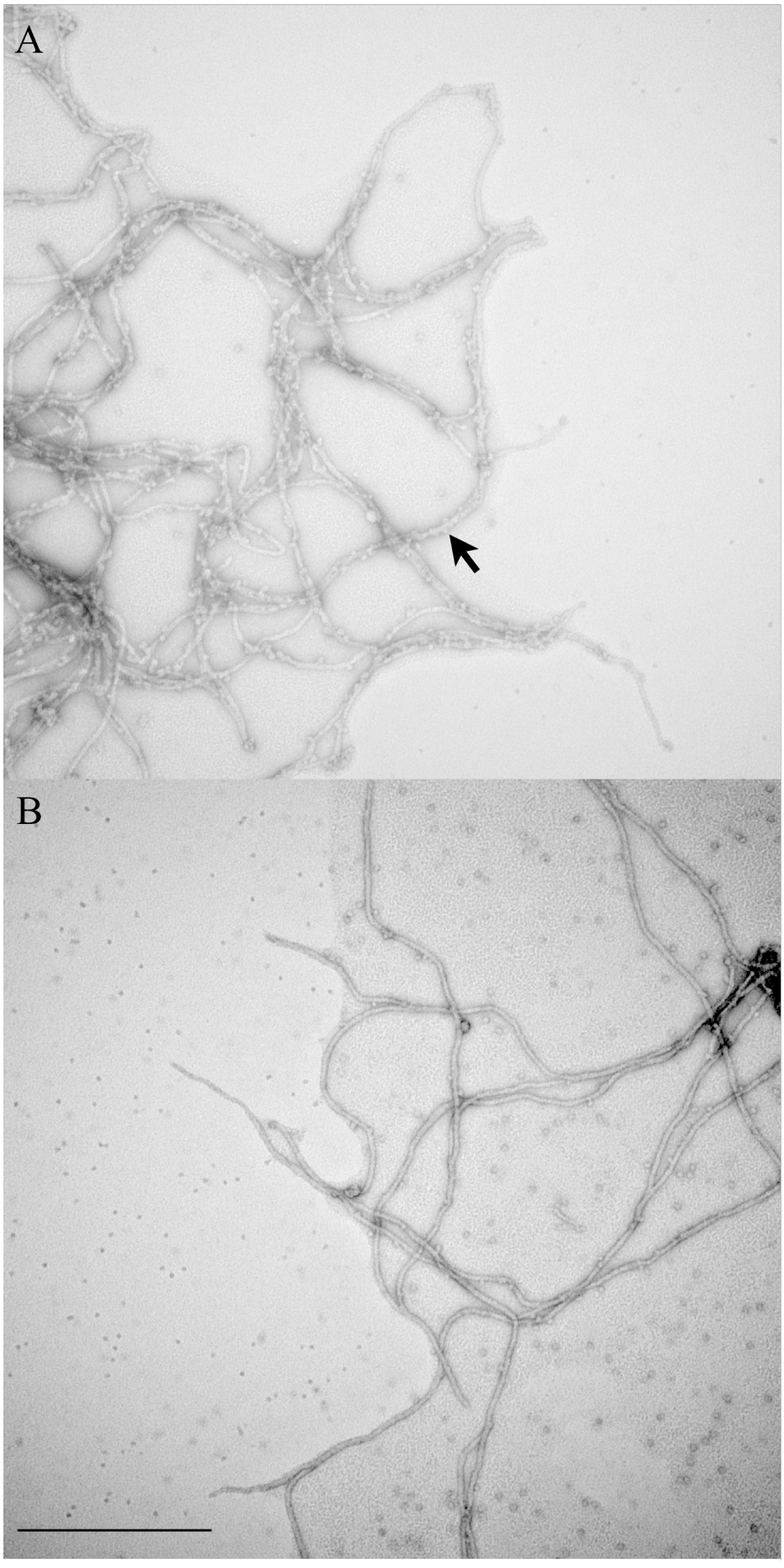
A
B

Figure 3.11 In the presence of manganese ions, CRYAB binding is greater to desmin filaments compared to calcium ions.

TEM pictures of WT desmin assembled with WT CRYAB in the presence of A) 1 mM Mn^{2+} or B) Ca^{2+} ions through Tris assembly at 39-44 ^{0}C are shown. Note how the desmin filaments are coated with CRYAB particles (indicated by arrow) in the presence of manganese compared to calcium ions. The scale bar is equal to 500 nm.

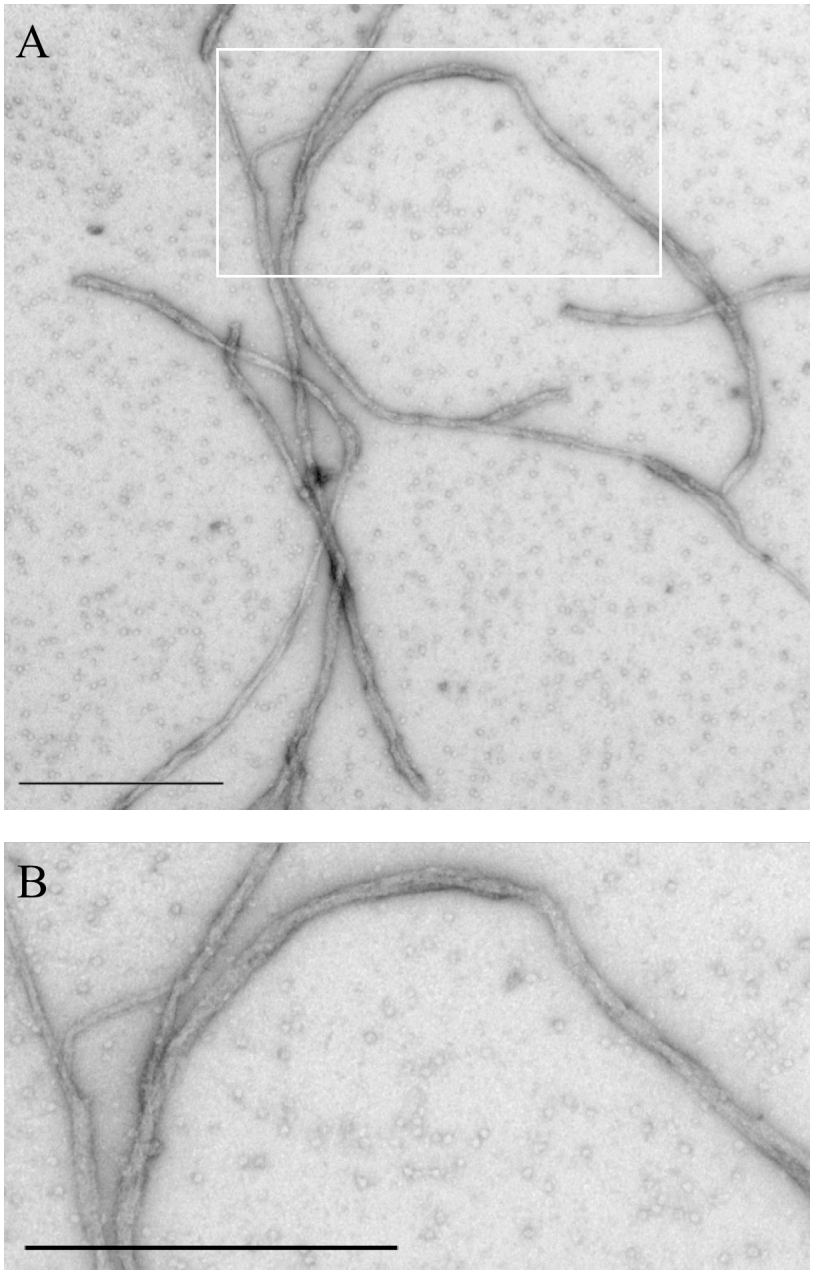
A
B

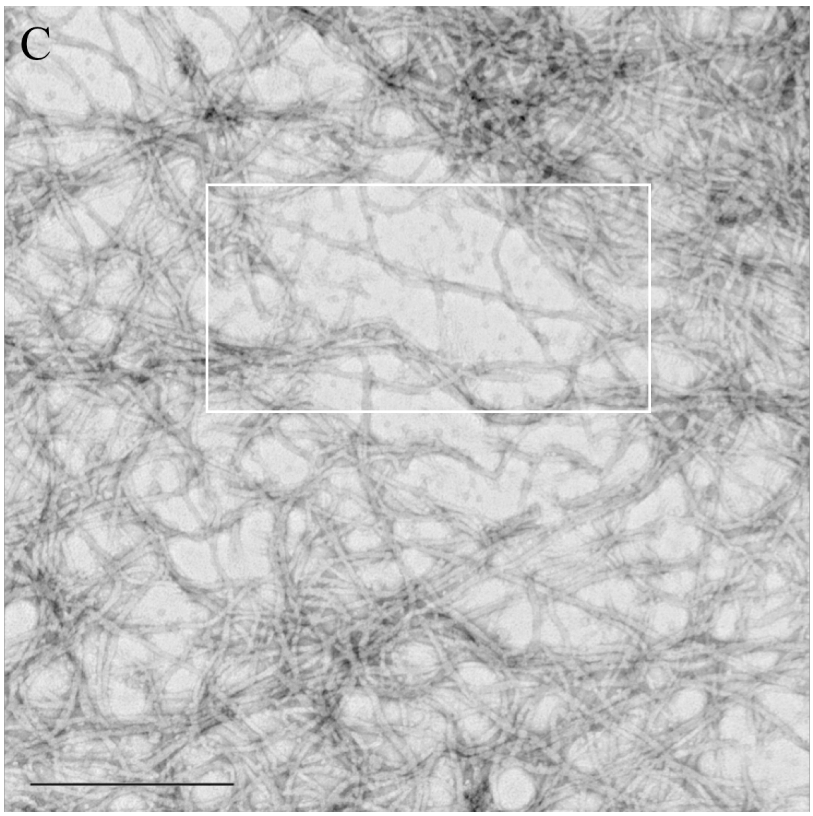
C

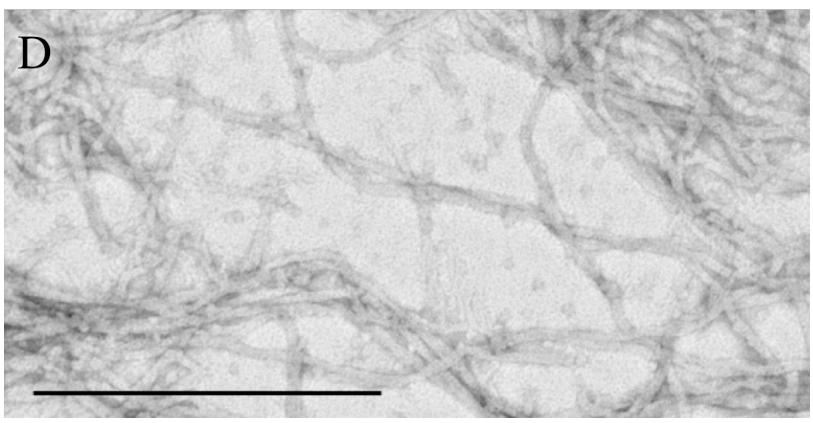
D

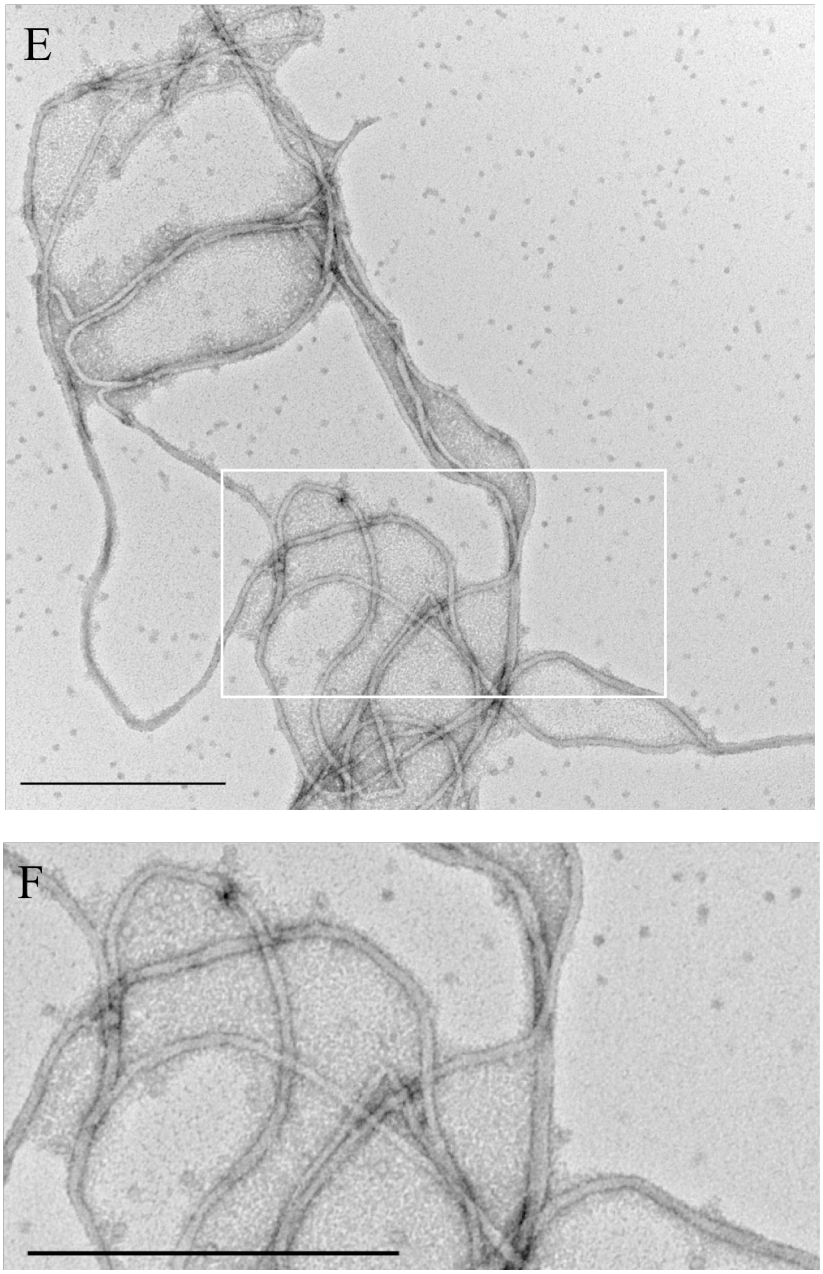

Figure 3.12 WT GFAP forms thicker filaments in the presence of 5 mM Ca^{2+} ions compared to desmin and vimentin that form 10 nm filaments.

TEM pictures of A) and inset B) WT GFAP, C) and inset D) desmin and E) and inset F) vimentin were taken after Tris assembly with WT CRYAB in the presence of 5 mM Ca^{2+} at 23-28 ^{0}C. Human vimentin forms 10 nm filaments in these conditions in contrast to Xenopus vimentin, which forms much thicker and shorter filaments (Hofmann et al., 1991). Desmin also forms usual 10 nm width filaments. However, WT human GFAP forms filaments of varying widths along the lengths, mostly thicker than 10 nm. The scale bar equals 500 nm.

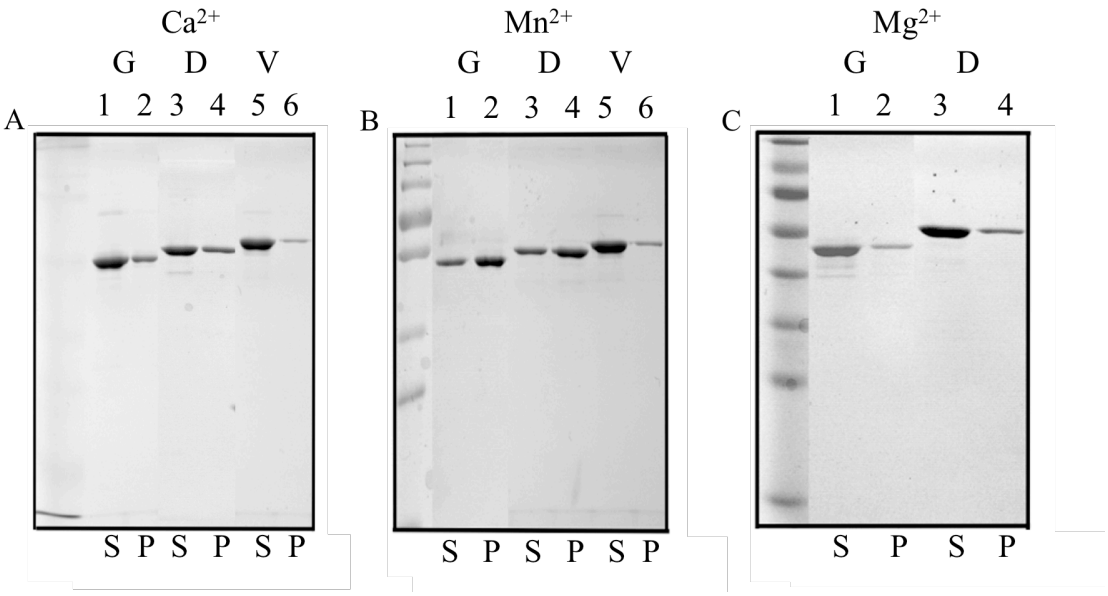

Figure 3.13 Manganese ions promote increased filament-filament interactions for desmin and GFAP but not vimentin.

Low speed sedimentation assays are shown from assembled filaments from three different divalent cation environments at 23-28 ^{0}C. Desmin and GFAP are both affected by an increase in filament-filament interactions from manganese ions and vimentin the least. G= GFAP, D= desmin and V= vimentin. S= supernatant and P= pellet.

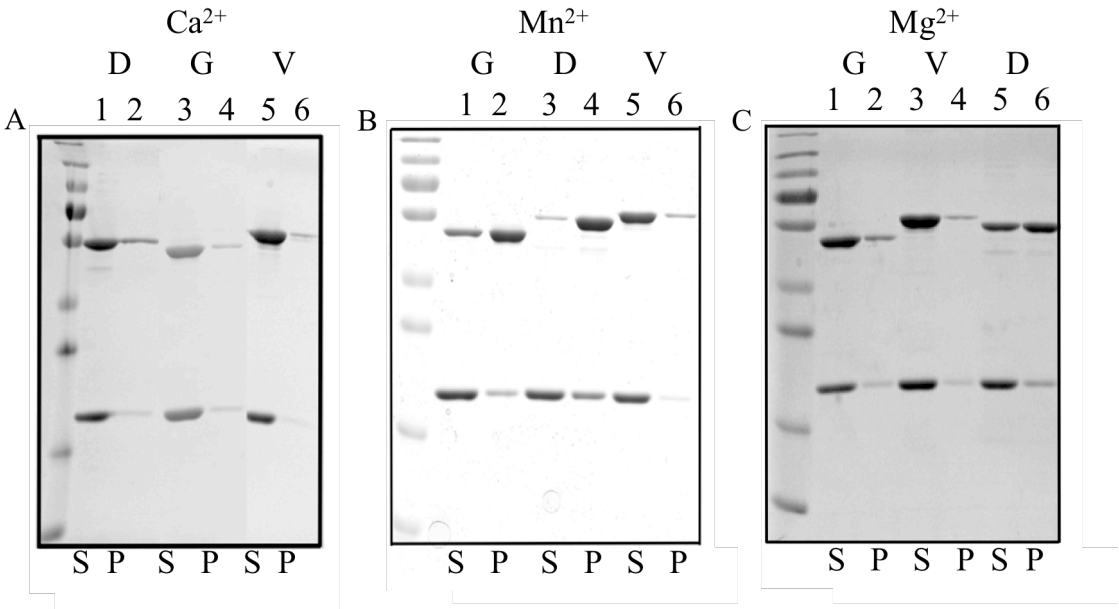

Figure 3.14 CRYAB has no effect upon metal-induced filament-filament interactions.

CRYAB is not able to reduce the filament-filament interactions any further for all three IFs. G= GFAP, D= desmin and V= vimentin. S= supernatant and P= pellet.

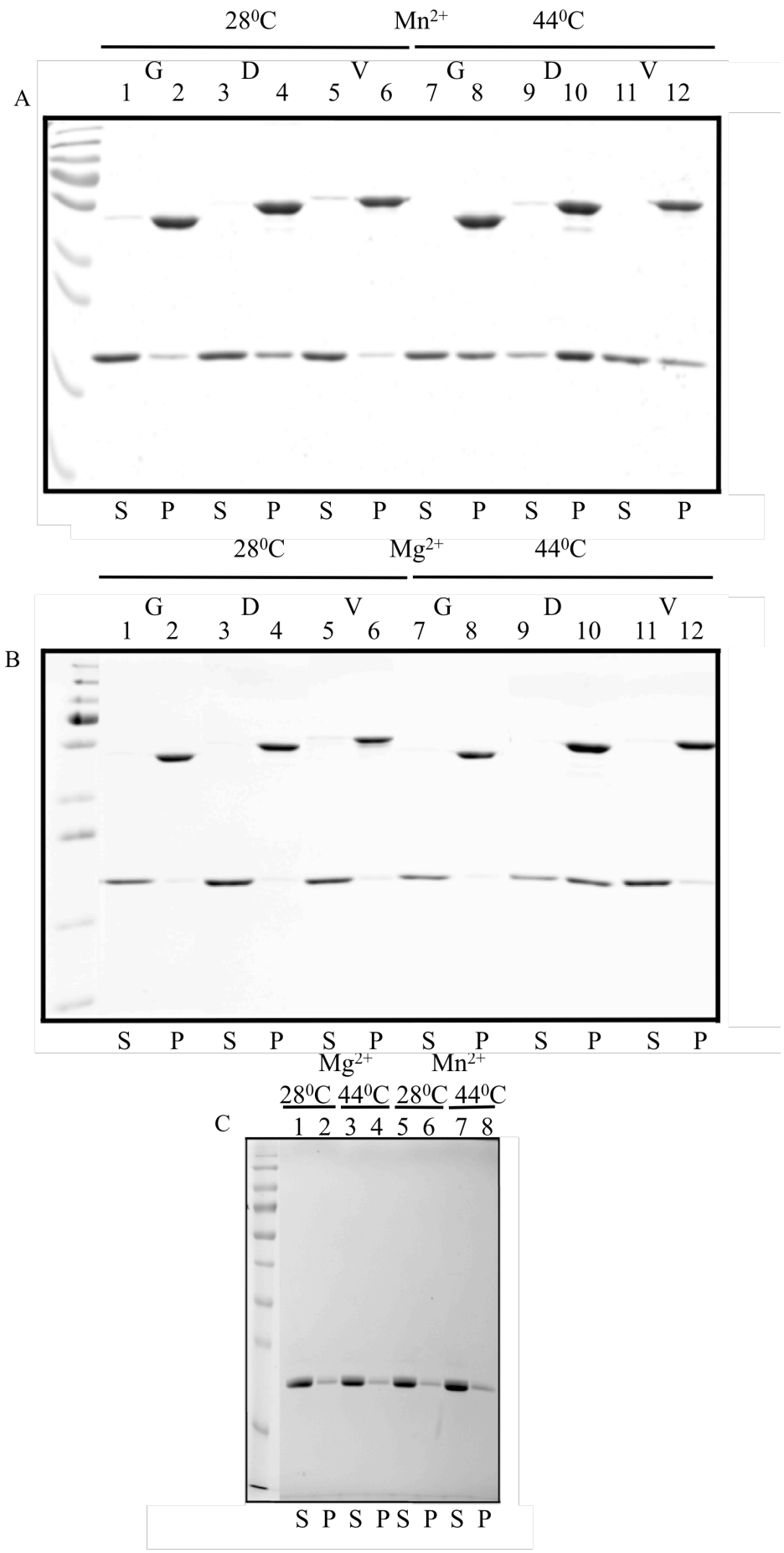
28⁰C
Mn2+
44⁰C
G D V G D V
1 2 3 4 5 6 7 8 9 10 11 12
A
S P S P S P S P S P S P
28⁰C
Mg2+
44⁰C
G D V G D V
1 2 3 4 5 6 7 8 9 10 11 12
B
S P S P S P S P S P S P
Mg2+
Mn2+
28⁰C 44⁰C 28⁰C 44⁰C
C
1 2 3 4 5 6 7 8
S P S P S P S P

Figure 3.15 Filaments assembled with manganese ions have greater binding to WT CRYAB compared to those assembled with magnesium ions.

High speed sedimentation assays are shown. CRYAB binds strongest to desmin filaments and this interaction is increased upon raising the temperature. Note how when CRYAB is assembled alone C) most of the protein is present in the supernatant fraction. G= GFAP, D= desmin and V= vimentin. S= supernatant and P= pellet.

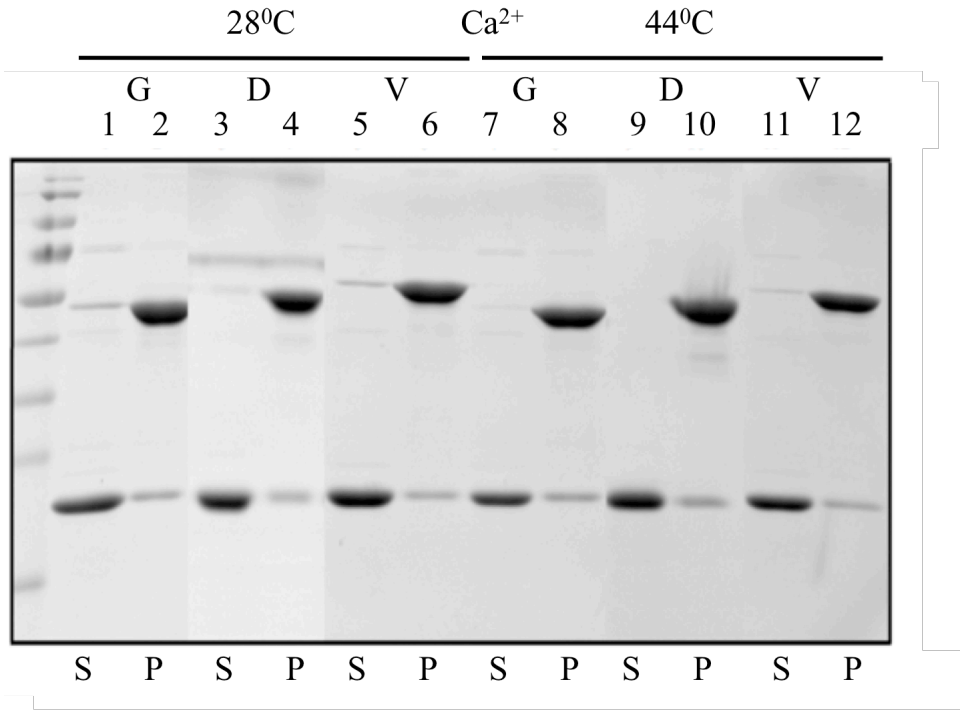

Figure 3.16 Filaments assembled with manganese ions also have greater binding to WT CRYAB compared to those assembled with calcium ions.

High speed sedimentations of assembled material from 1 mM Ca^{2+} ions are shown. CRYAB does not interact as much with the filaments as with manganese ions (Figure 3.15). G= GFAP, D= desmin and V= vimentin. S= supernatant and P= pellet.

The dimer resulting from GFAP assembly in the presence of manganese ions, seen in Figure 3.8 from sedimentation assays, was probed using an anti-GFAP Ab and proven to be GFAP (Figure 3.17). The nature of this band was investigated using reduction to see if oxidation was the cause and it was shown that manganese ions promote oligomers of GFAP due to oxidative cross-linking (Figure 3.18).

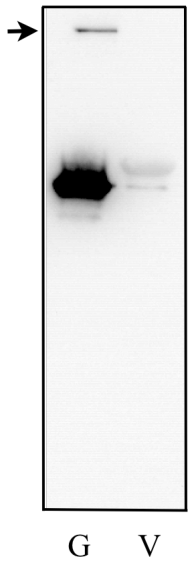

Figure 3.17 Manganese ions result in dimer formation of assembled GFAP.
An immunoblot is shown against 2 μg of each protein. The membrane was probed with the anti-human GFAP SMI-21 1^0 Ab with a 1:50 dilution. A strong band corresponding to the monomer of GFAP can be seen and the absence of a signal for vimentin shows the specificity of the Ab for human GFAP. G= GFAP and V= vimentin. The arrow indicates the position of the GFAP dimer.

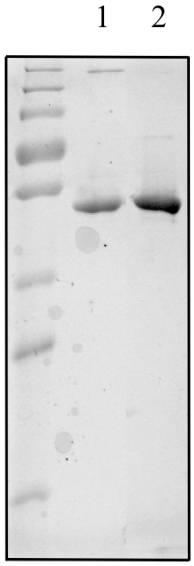

Figure 3.18 Dimer of GFAP in presence of manganese ions is due to oxidation.
WT GFAP after Tris assembly with 1 mM Mn^{2+} ions was either untreated and run from a low speed supernatant as 4 μg of protein (lane 1) or reduced with 50 mM DTT at 37 ^{0}C for 1 hr and loaded as 4 μg of protein (lane 2). There is no dimer present after reduction with DTT under these conditions.

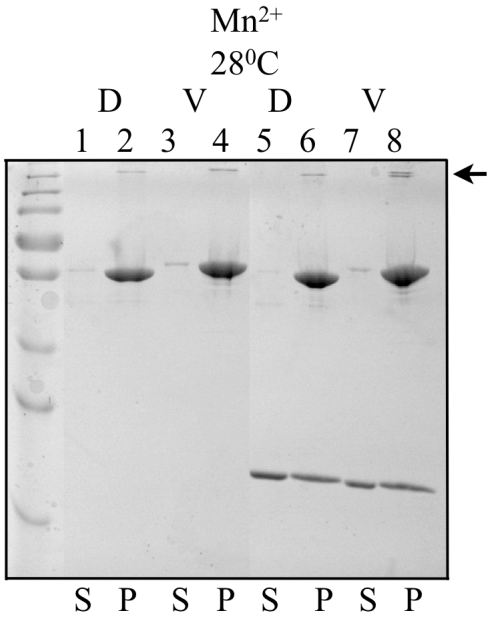

Figure 3.19 Manganese ions promote dimer formation of desmin and vimentin. As well as 1 mM Mn^{2+} ions resulting in WT GFAP dimers, there is also promotion of desmin and vimentin to form dimers shown from the high speed sedimentations and highlighted by the arrow. D= desmin and V= vimentin. S= supernatant and P= pellet.

Gel quantifications were carried out from three independent repeats of co-assembled GFAP, desmin or vimentin with CRYAB to assess the proportion of CRYAB that binds. It can be seen in Table 3.4 that CRYAB binds the most to desmin, at the increased temperatures of 39-44 ^{0}C; GFAP and vimentin appear to bind the least. It is interesting to see that there is no difference in binding of CRYAB to desmin filaments in the presence of magnesium or manganese ions at 39-44 ^{0}C, however this is not the case at 23-28 ^{0}C. Also binding between CRYAB and GFAP is increased at both temperatures when assembled with manganese ions compared to magnesium. However with vimentin the increase in interactions is seen only at 39-44 ^{0}C and not 23-28 ^{0}C, comparing the two different divalent cations.

	% CRYAB pellet Mg^{2+} 23-28 ^{0}C	% CRYAB pellet Mg^{2+} 39-44 ^{0}C	% CRYAB pellet Mn^{2+} 23-28 ^{0}C	% CRYAB pellet Mn^{2+} 39-44 ^{0}C
Vimentin	12 +/- 3	19 +/- 2	15 +/- 12	31 +/- 13
GFAP	8 +/- 4.5	17 +/- 5	28 +/- 2	29 +/- 2
Desmin	13 +/- 4	53 +/- 7	25 +/- 5	64 +/- 10

Table 3.4 **Percentages of WT CRYAB binding to type III IFs**.
Mean values +/- one SD of percentages of CRYAB binding to filaments after Tris assemblies.

An additional test of interactions of CRYAB at increased temperatures with the filaments was carried out in HEPES buffer as outlined in Figure 3.1. In this instance a constant pH 6.9 was investigated at the three temperatures of 23, 39 and 44 ^{0}C. Similar to the changes in morphology of GFAP filaments after Tris assembly with 1 mM Mn^{2+} ions, assembly in HEPES with 1 mM Mn^{2+} also results in altered filament architectures (Figure 3.20 D-F)). However the filaments are longer after the HEPES assembly with 1 mM Mn^{2+} ions compared to Tris assembly, comparing Figure 3.5 A) with Figure 3.20 D).

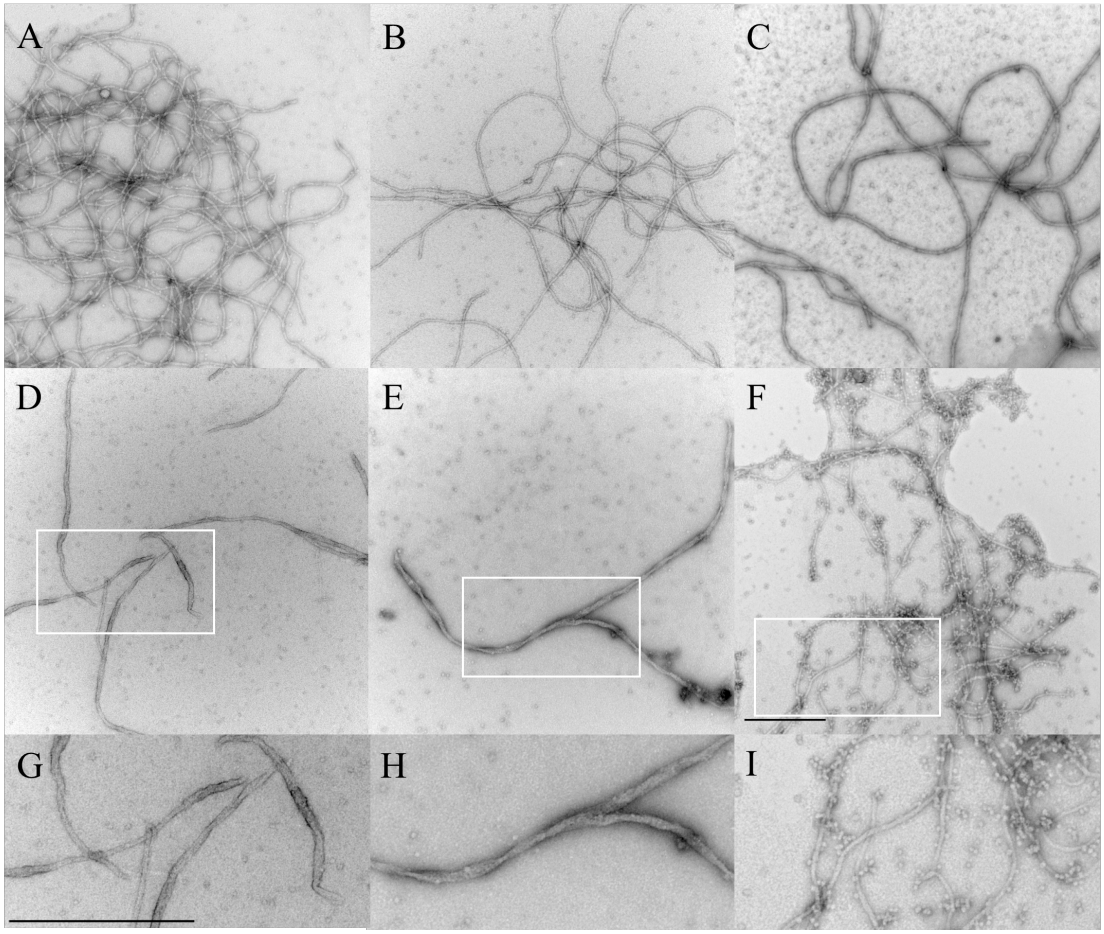

Figure 3.20 Manganese ions alter assembly of GFAP filaments.

TEM pictures are shown of WT GFAP (D-I) and vimentin (A-C) with WT CRYAB after assembly in HEPES buffer at pH 6.9 with 1 mM Mn^{2+} ions at 23 (A and D), 39 (B and E) and 44 ^{0}C (C and F). WT GFAP filaments vary approximately 10-30 nm in width along their lengths, whereas vimentin filaments remain at the usual 10 nm width. The scale bar is equal to 500 nm.

As seen with Tris assembly, CRYAB binds more to GFAP than vimentin filaments (Figure 3.21) in the presence of manganese ions and this increases with increasing temperature. A difference is observed for vimentin and GFAP, comparing pH 6.8 with magnesium ions to pH 6.9 with manganese ions at 39 and 44 ^{0}C for vimentin and 23 ^{0}C for GFAP, c.f. Table A.11 and A.14.

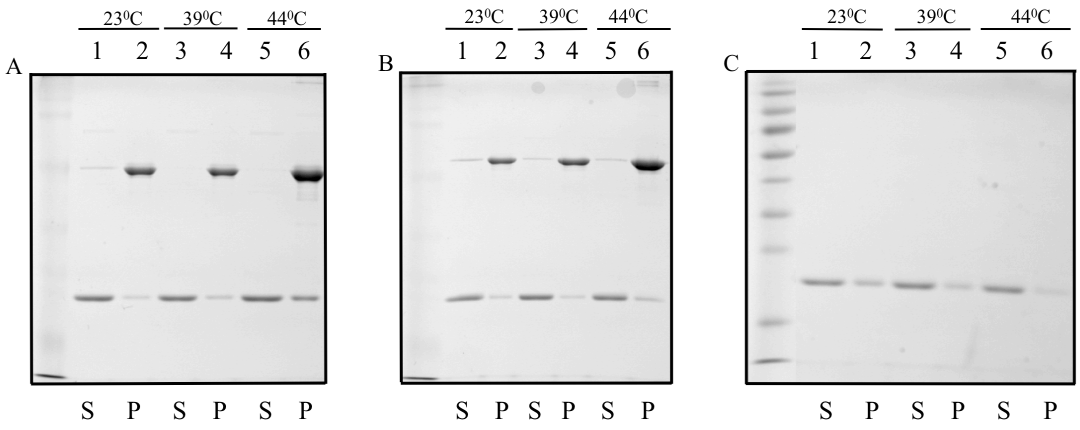

Figure 3.21 CRYAB binds to GFAP and vimentin filaments in a temperature-dependent manner.

High speed sedimentations were carried out on assembled A) WT GFAP with CRYAB, B) WT vimentin with WT CRYAB and C) WT CRYAB alone. CRYAB binds much more to GFAP than vimentin. S= supernatant and P= pellet.

	% CRYAB pellet Mn^{2+} 23 ^{0}C	% CRYAB pellet Mn^{2+} 39 ^{0}C	% CRYAB pellet Mn^{2+} 44 ^{0}C
Vimentin	9 +/- 3	13 +/- 3	18 +/- 2
GFAP	10 +/- 3	13 +/- 3	30 +/- 10

Table 3.5 **% of CRYAB binding to filaments in HEPES buffer at pH 6.9**.

A statistically significant increase was observed for vimentin comparing binding with CRYAB in the presence of manganese to magnesium ions at 39 and 44 ^{0}C ($p = 0.05$) and also GFAP at 23 ^{0}C ($p<0.05$).

3.1.3.3 Lower pH and increased temperatures promote increased binding of CRYAB to GFAP, desmin and vimentin filaments.

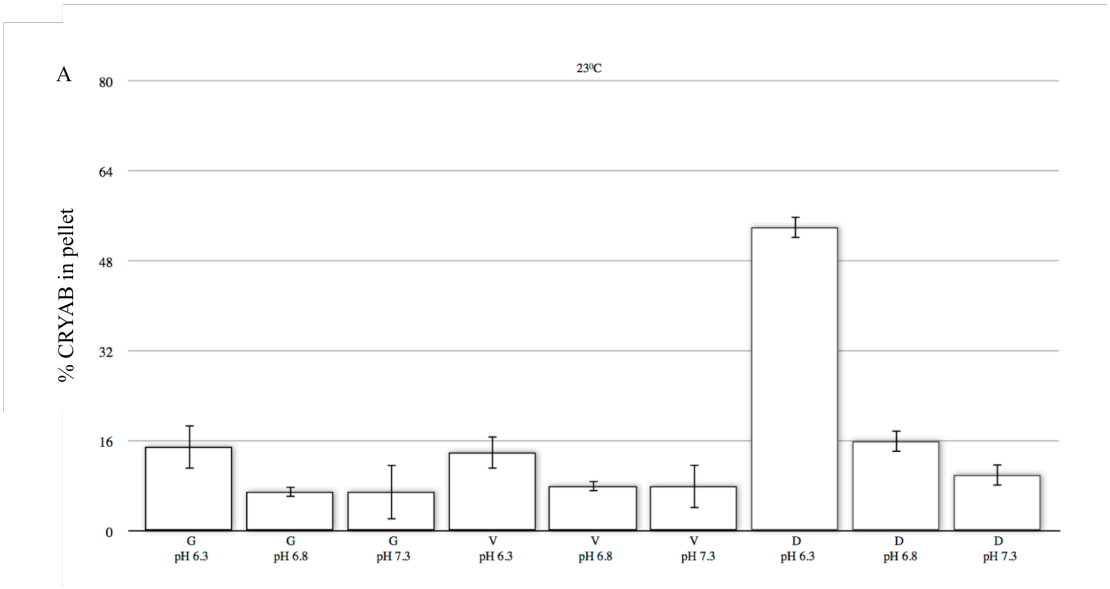

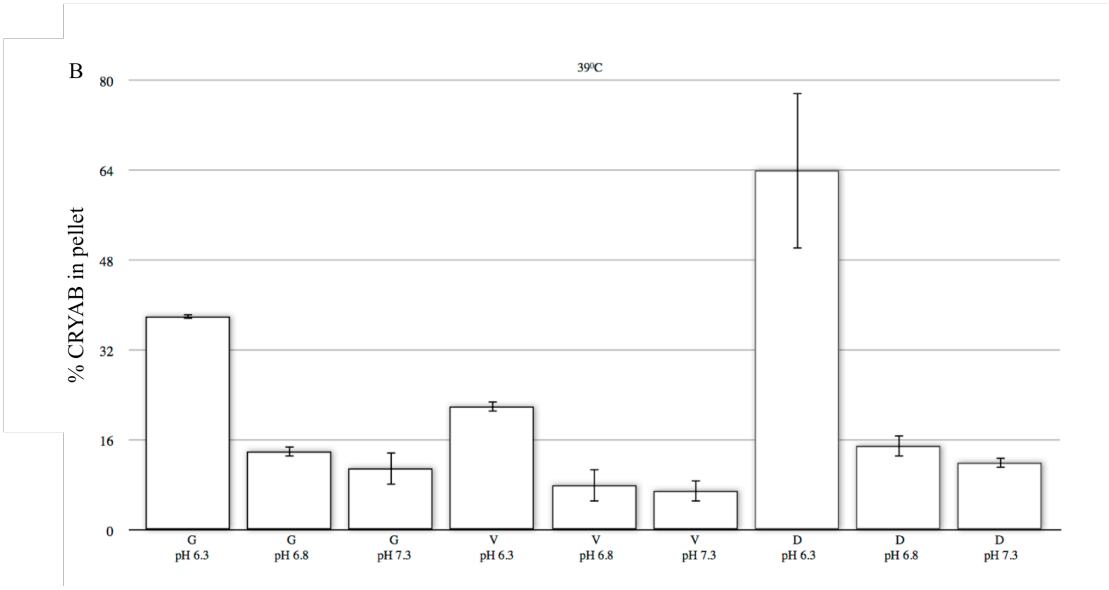

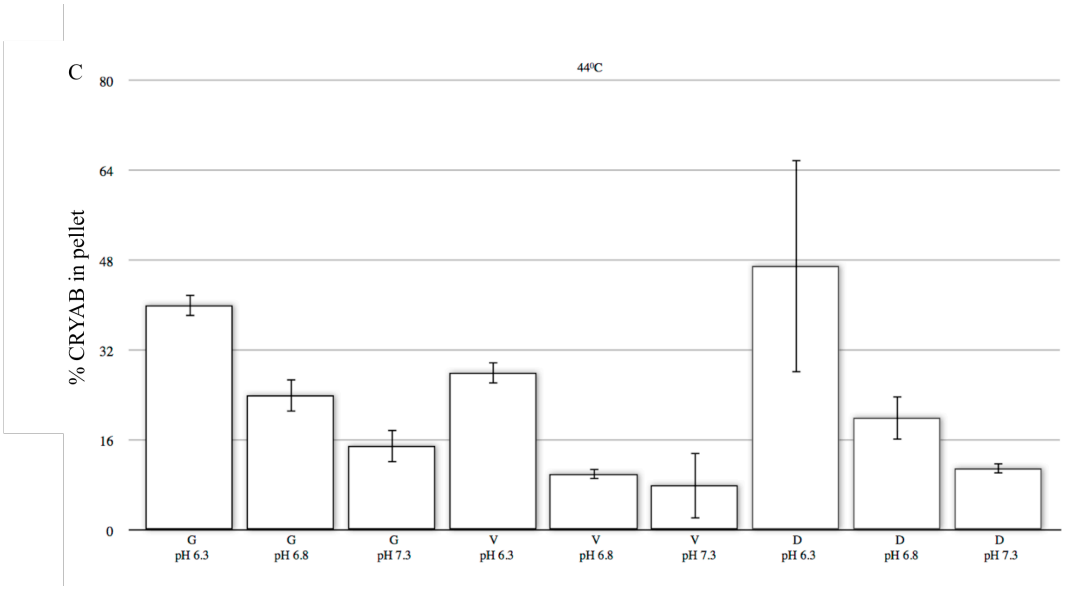

Figure 3.22 Charts of binding of WT CRYAB to type III IFs.

CRYAB was present throughout assembly, carried out at three different pH and temperature values of A) 23, B) 39 and C) 44 ^{0}C. This showed increased binding of CRYAB to the filaments at low pH values and increased temperatures and preference of binding to desmin in comparison to GFAP and vimentin. Data are represented as the average values of three independent experiments with error bars showing +/- one SD. Averaged raw data are shown in Table A.15-A.17. G= GFAP, D= desmin and V= vimentin.

The amount of CRYAB co-pelleting alongside the sedimentable filaments (Figure 3.23) was quantified using ImageGauge (FujiFilm, Japan), from three independent experiments and the average values are represented as bar charts in Figure 3.22. This highlights how CRYAB binds the most to desmin filaments at pH 6.3 and at 39 and 44 ^{0}C.

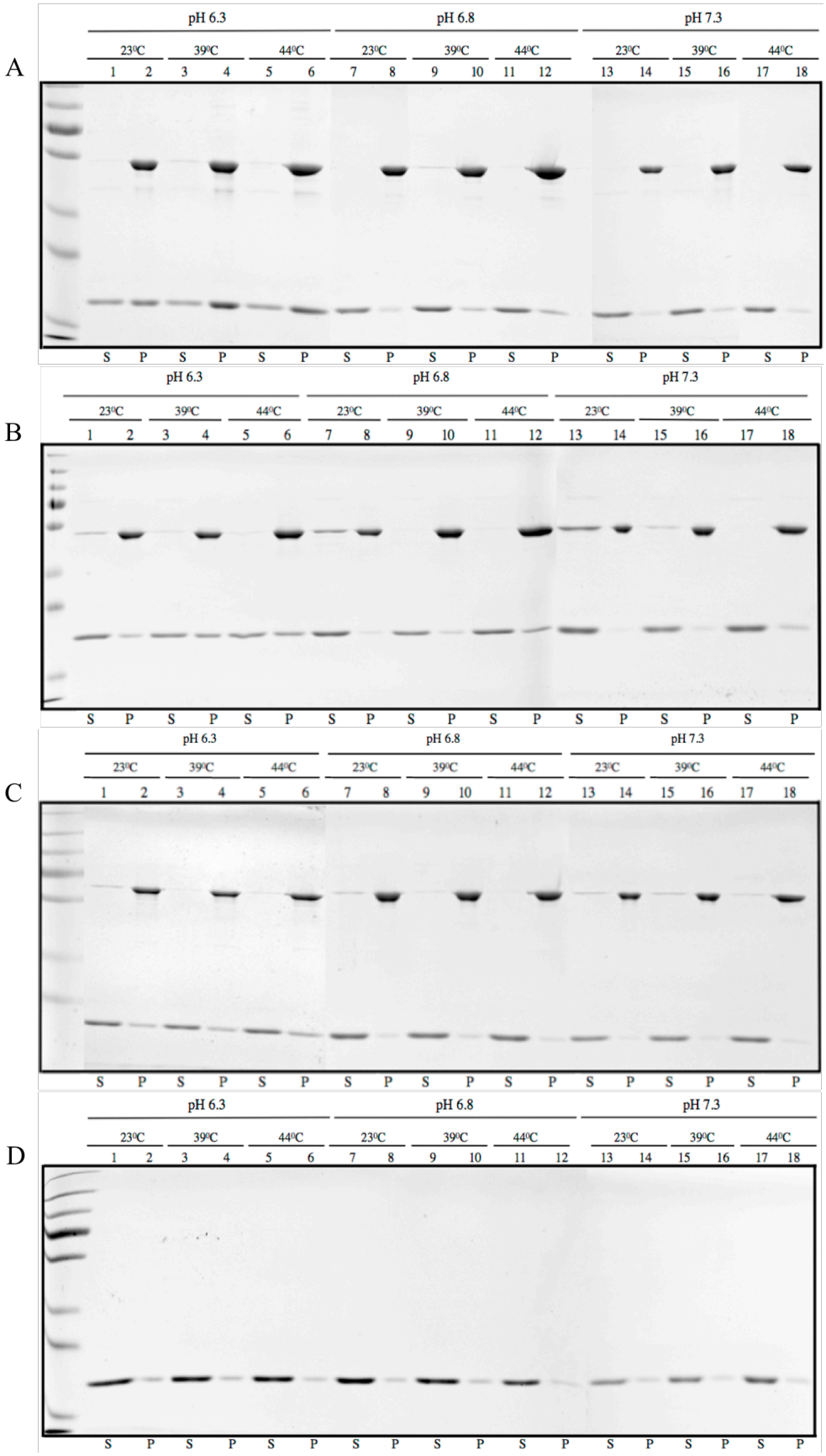

Figure 3.23 Binding of CRYAB to IFs is increased upon a drop in pH and an increase in temperature.

High speed sedimentation assays were carried out on assembled A) WT desmin, B) GFAP and C) vimentin with WT CRYAB after assembly with HEPES buffers set to pH 6.3, 6.8 and 7.3 at 23, 39 and 44 ^{0}C with 1 mM Mg^{2+} ions. These gels are an example of those used for the quantifications in Figure 3.22. A temperature- and pH-dependent effect can be seen with CRYAB binding, to all of the filaments, with a preference for desmin filaments. D) very little CRYAB pellets when assembled alone at all three temperatures. Note how GFAP at 23^{0}C has more protein present in the supernatant compared to desmin and vimentin at pH 6.8 and 7.3, however at pH 6.3 the CRYAB does not appear to have the same inhibitory effect on GFAP filament formation. S= supernatant and P= pellet.

To assess how pH and temperature influence the interactions of CRYAB with type III IFs, three pH and temperature values were assessed ranging from physiological pH 7.3 to ischemic pH 6.3, using pH 6.8 as the mid-point of this range at 23, 39 and 44 ^{0}C. Previous experiments in this laboratory have shown that increased temperature causes increased binding of WT CRYAB to desmin filaments, however this was not accounting for pH changes (Perng et al., 2004). Therefore nine individual pH buffers were used to keep the pH constant at the three temperatures studied. The filaments in the experiments from this section were assembled according to 3.1.2.1.4.

High speed sedimentation assays were used to assess the binding of CRYAB to the filaments. In Figure 3.22 the increased co-pelleting of CRYAB can be seen alongside the filaments at the lower pHs and increased temperatures. The temperature dependency is more obvious at the lower pH values; at pH 7.3 only by comparing the sedimentation of CRYAB with WT GFAP can it be seen that there is an increase in binding from 23 to 44 ^{0}C. There does not appear to be an increase in binding for vimentin and desmin at pH 7.3 upon increasing the temperature, however at pH 6.3 and 6.8 this is not the case.

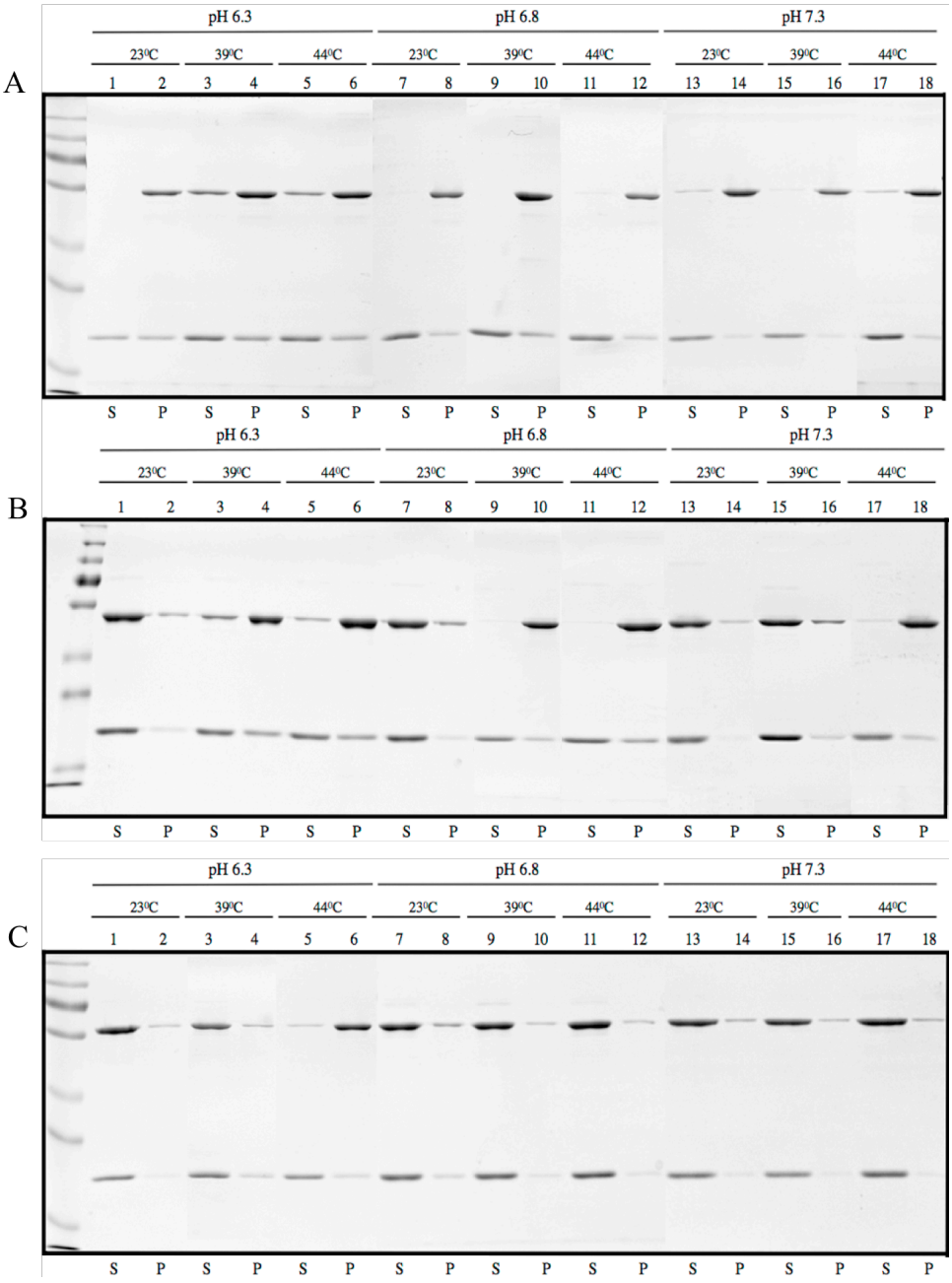

Figure 3.24 A general trend of increased filament interactions occurs upon a drop in pH and an increase in temperature with the exception of desmin.

Low speed sedimentations on assembled A) WT desmin, B) GFAP and C) vimentin with WT CRYAB are shown. A temperature- and pH- dependent effect can be seen with filament interactions. For all three types of filaments, most of the filaments are pelleted at pH 6.3 at 39 and 44 ^{0}C. This is in contrast to pH 6.8 and 7.3 where most of the protein is present in the supernatant portions, with the exception of desmin, which is pelleted under all pH values and temperatures. S= supernatant and P= pellet.

To assess filament-filament interactions within the co-assemblies, low speed sedimentation assays were carried out. With the exception of desmin, increased filament-filament interactions as observed by an increase in the pelletable filaments was seen at the lower pH values and increased temperatures (Figure 3.24). For GFAP the increased interactions were seen at 39 and 44 ^{0}C for pH 6.3 and 6.8. For vimentin these were seen only at 44 ^{0}C in pH 6.3. Desmin filaments had increased filament-filament interactions at all pH values assessed, even when CRYAB binding was relatively low at pH 7.3.

The morphology of the assembled filaments with WT CRYAB was assessed using the TEM. All filaments were morphologically similar at all three pH and temperature values, apart from WT GFAP that had variable widths at pH 6.3 at 23 ^{0}C (Figure 3.28 A)) and vimentin in pH 7.3 buffer at 23 ^{0}C that was also wider. Increasing the temperature restored the vimentin filaments to usual 10 nm widths. Three measurements of filament widths were taken for the three different pH values at 23 ^{0}C (Table 3.6). To further support the sedimentation assay data showing the increased binding of CRYAB at pH 6.3, the TEM images also show an increase in the density of CRYAB oligomers coating the filaments and the arrows in Figure 3.28 point to CRYAB oligomers bound to the surface of the filaments.

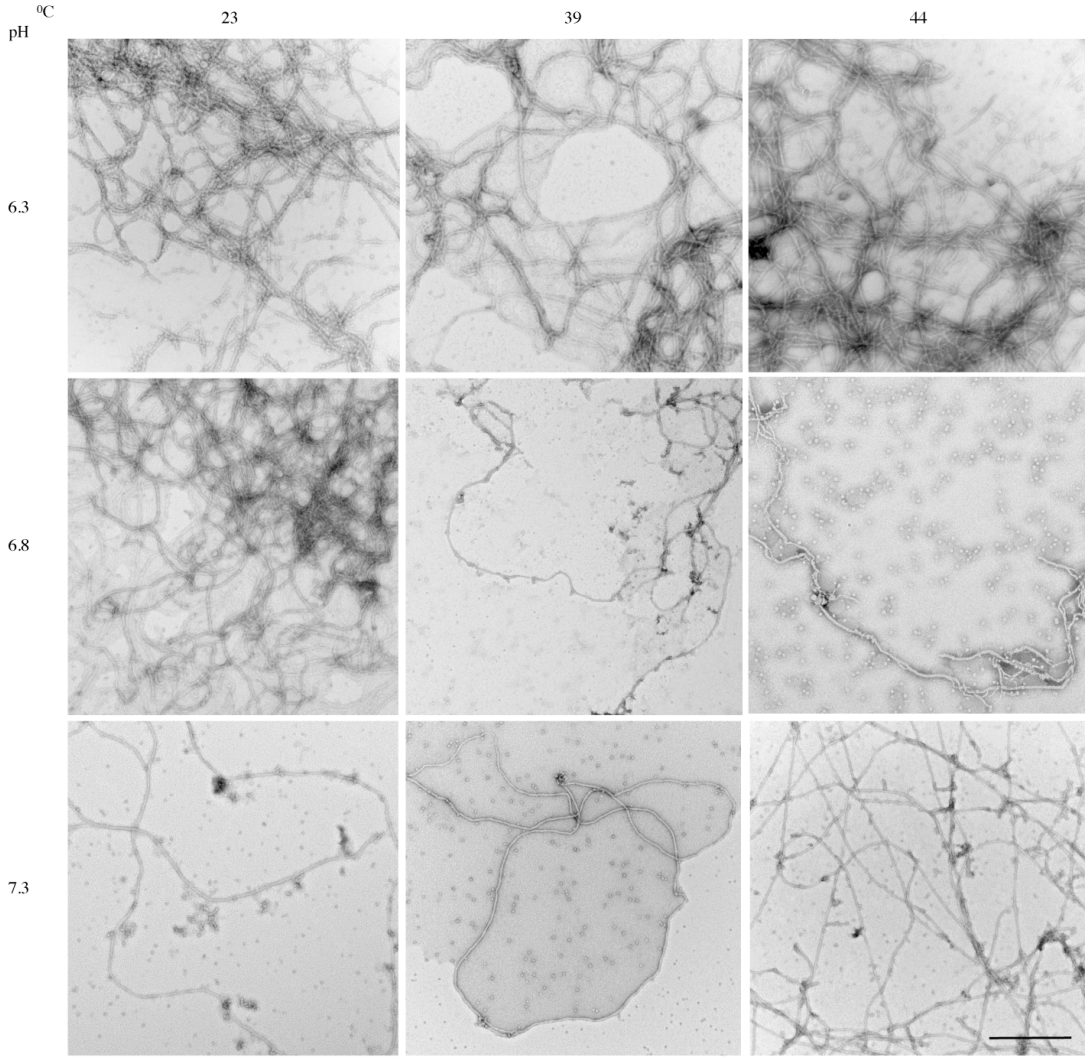

Figure 3.25 Desmin forms usual 10 nm filaments at all three temperatures and pH values.

TEM images of desmin filaments assembled at three temperatures and pH values with WT CRYAB show normal 10 nm IFs at all nine conditions. The scale bar is equal to 500 nm.

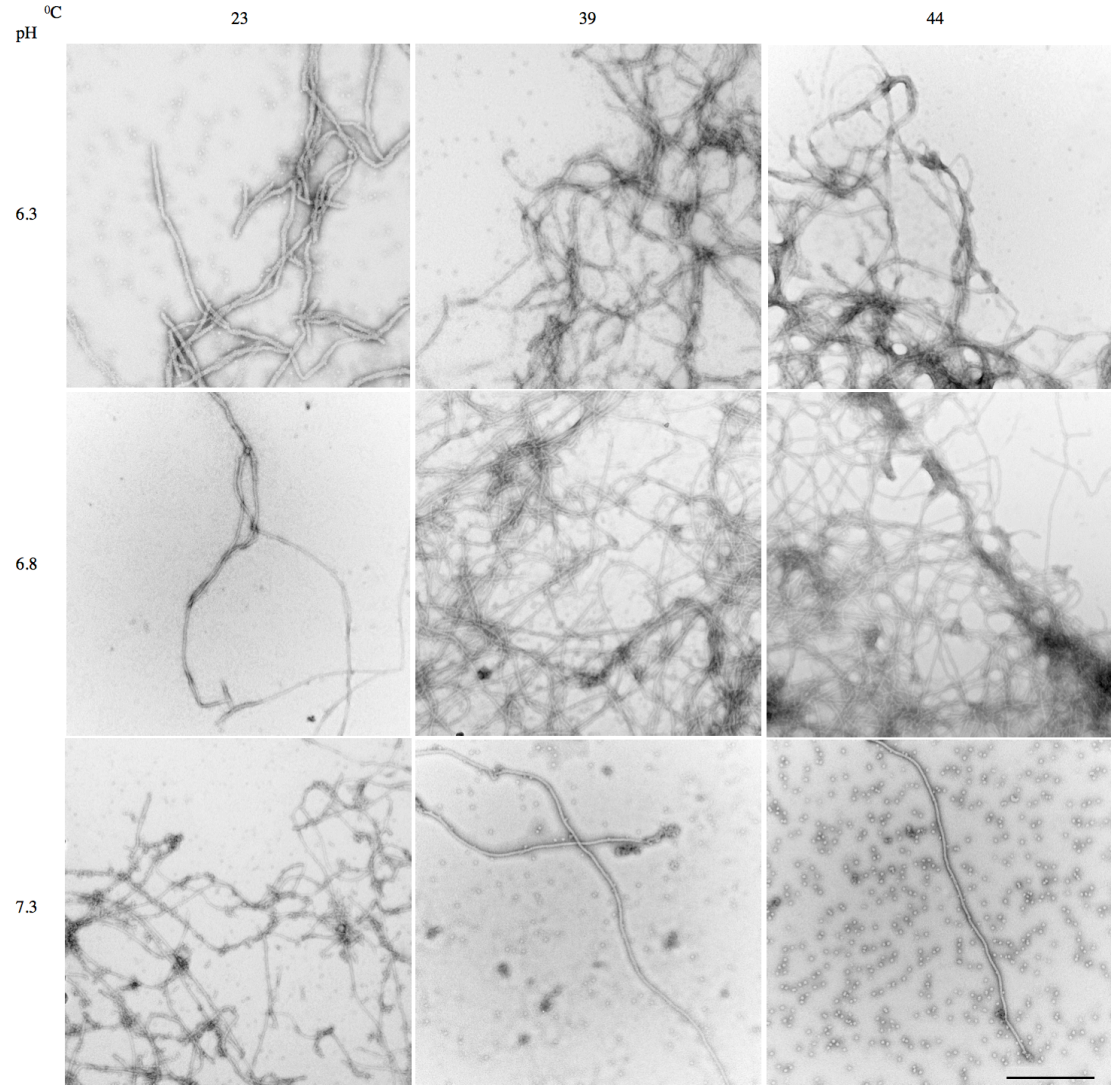

Figure 3.26 GFAP forms 10 nm filaments under all conditions apart from pH 6.3.

TEM images of GFAP filaments assembled at three temperatures and pH values with WT CRYAB show normal 10 nm IFs at all nine conditions apart from thicker widths and shorter lengths at pH 6.3 at 23 ^{0}C. The scale bar is equal to 500 nm.

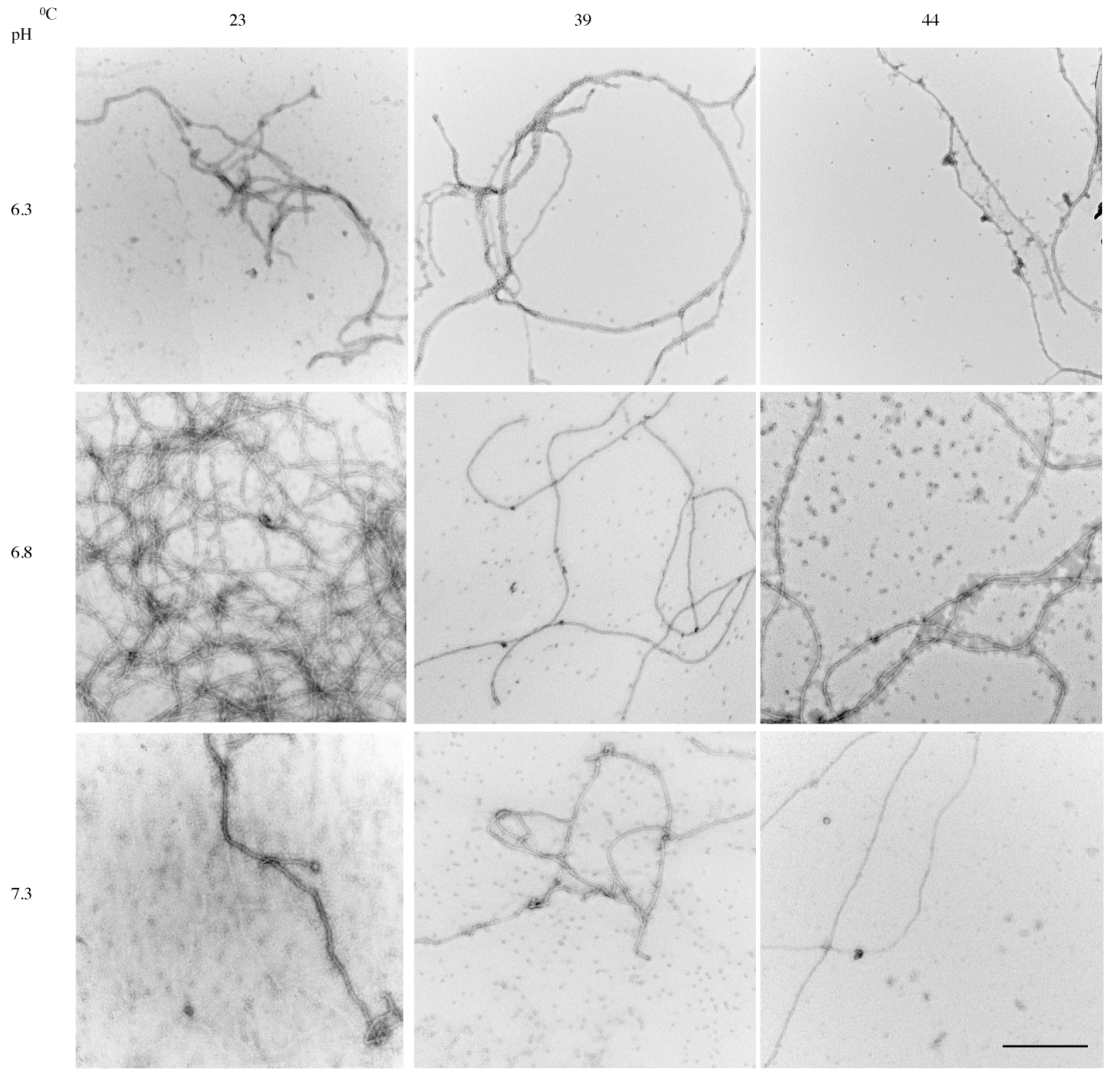

Figure 3.27 Vimentin forms usual 10 nm filaments with most temperature and pH values.

TEM images of vimentin filaments assembled at three temperatures and pH values with WT CRYAB show normal 10 nm IFs with most conditions (Table 3.6 highlights wider filaments at pH 7.3). The scale bar is equal to 500 nm.

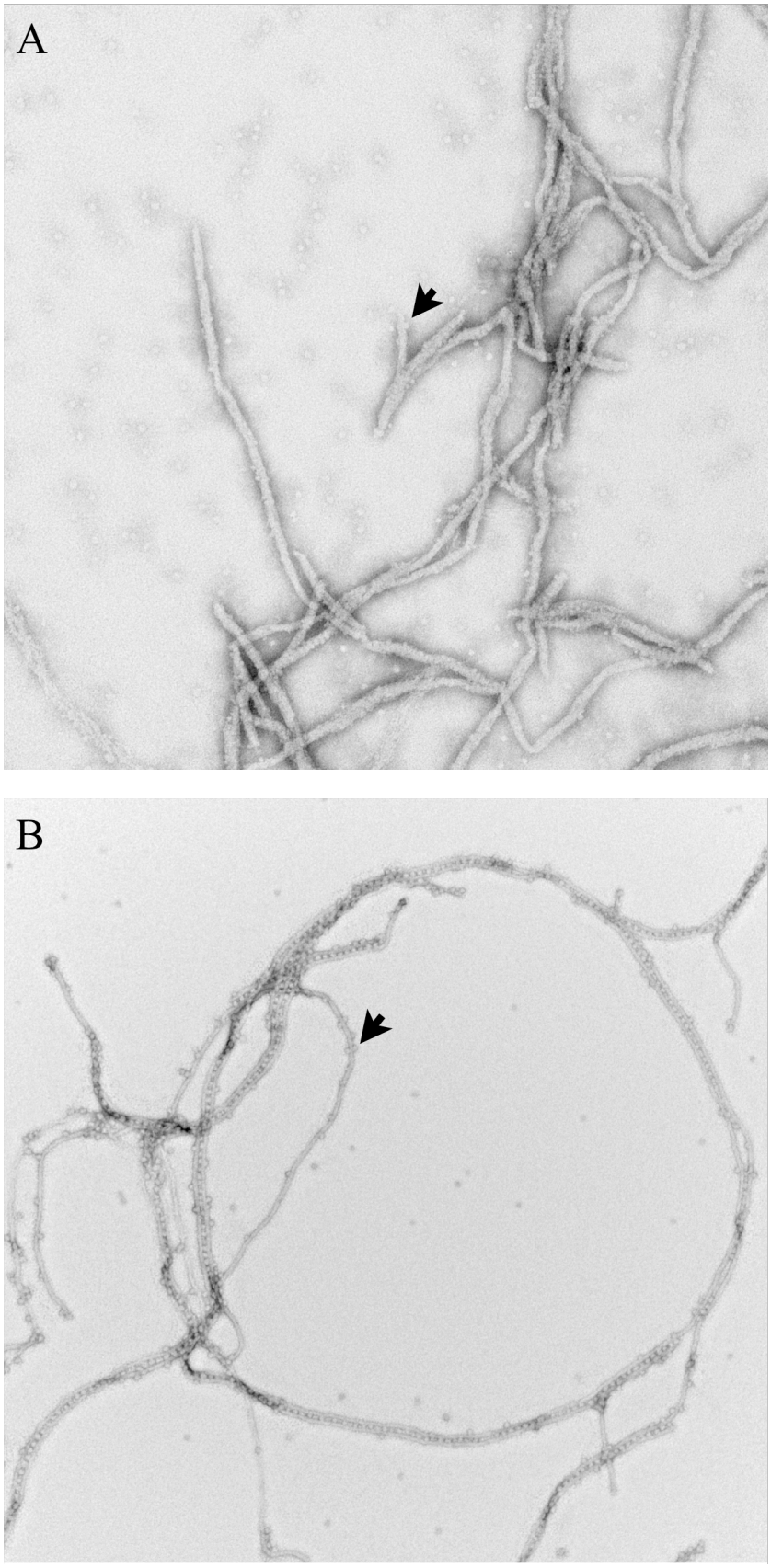
A
B

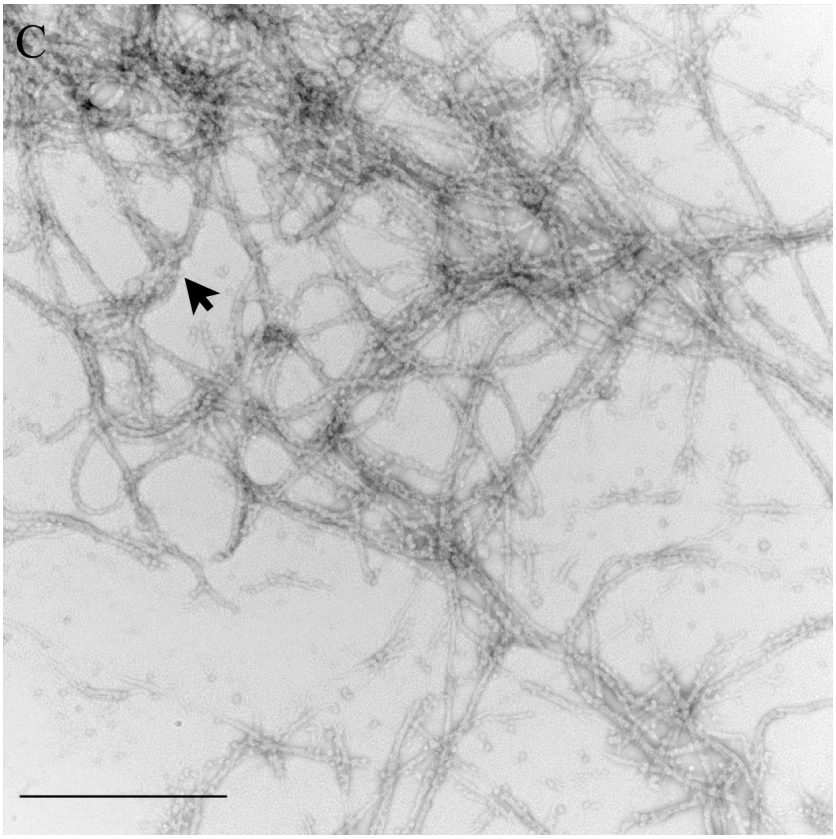

Figure 3.28 CRYAB increases binding to desmin, vimentin and GFAP at pH 6.3. TEM images were taken of A) GFAP at 23 ^{0}C, B) vimentin at 39 ^{0}C and C) desmin at 23 ^{0}C, all at pH 6.3 with CRYAB. Note the coating of the filaments with CRYAB particles and especially the regular spacing of the sHSP sandwiched between two vimentin filaments (oligomers are adjacent to each other with a repeat distance of approximately 20 nm (width of individual CRYAB particles) when situated between two filaments whereas with individual filaments the repeat distance of CRYAB is irregular). The repeat distance of CRYAB coating individual desmin filaments is also approximately 20 nm. Also note how the GFAP filaments have uneven widths, which tend to be thicker than the usual 10 nm. The arrows denote where CRYAB oligomers appear bound to the surfaces of the filaments. The scale bar is equal to 500 nm.

Protein		Protein widths (nm)		
	pH	6.3	6.8	7.3
GFAP		24 +/- 5	12 +/- 1	13 +/- 2
Desmin		12 +/- 1	12 +/- 3	10 +/- 1
Vimentin		11 +/- 2	10 +/- 1	15 +/- 2
CRYAB		15 +/- 5	10 +/- 1	10 +/- 1

Table 3.6 **Widths of IFs and CRYAB**

Three filament and CRYAB oligomer widths were measured and averaged from 23 ^{0}C. For the filaments, this was done on either three separate filaments or on the same filament from the TEM images in Figure 3.25-3.27 and CRYAB oligomers were measured in one image, on three separate oligomers, per pH (widths were similar in the presence of any of the IFs).

Filament width measurements were also taken at the higher temperatures and wider filaments were also observed for GFAP at pH 6.3 at the higher temperatures but not at pH 6.8 or 7.3. Since the above data show a trend of increased binding under certain pH and temperature conditions when CRYAB has been present for the whole of the filament assemblies, another experiment was carried out investigating whether a similar trend would be observed with the addition of CRYAB oligomers to assembled GFAP filaments. This did show a similar trend demonstrating that increased interactions can be seen when CRYAB is presented to filaments at different stages of formation (Figure 3.29). However it was shown that binding was less at 39 ^{0}C when CRYAB was added after the filaments had been formed at pH 6.3 and 7.3 (c.f. Table A.20 and A.22).

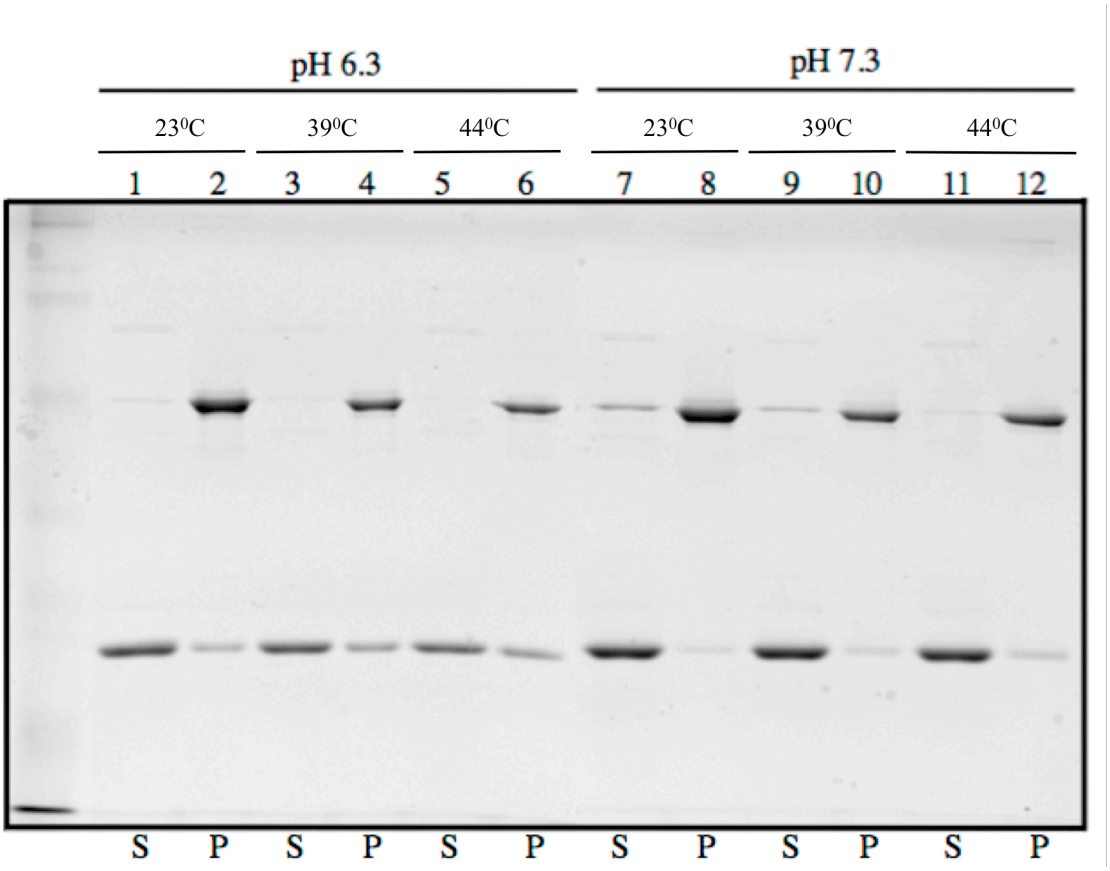

Figure 3.29 Binding of CRYAB to assembled GFAP IFs is increased upon a drop in pH and an increase in temperature.

High speed sedimentations were carried out on assembled WT GFAP with WT CRYAB added after filaments were formed. Similar increased binding of CRYAB can be seen at the lower pH and higher temperatures as shown in Figure 3.23 when CRYAB was added before the filaments had formed, however there is a significant decrease in binding of CRYAB at 39 ^{0}C at pH 6.3 ($p<0.05$) and 7.3 ($p= 0.051$) when CRYAB is added after filament assembly compared to its addition before filament assembly. S= supernatant and P= pellet.

The above sedimentation binding data were averaged and are shown in Figure 3.30. It can be seen that at pH 6.3 there is much more binding to WT GFAP compared to pH 7.3 and this is temperature dependent.

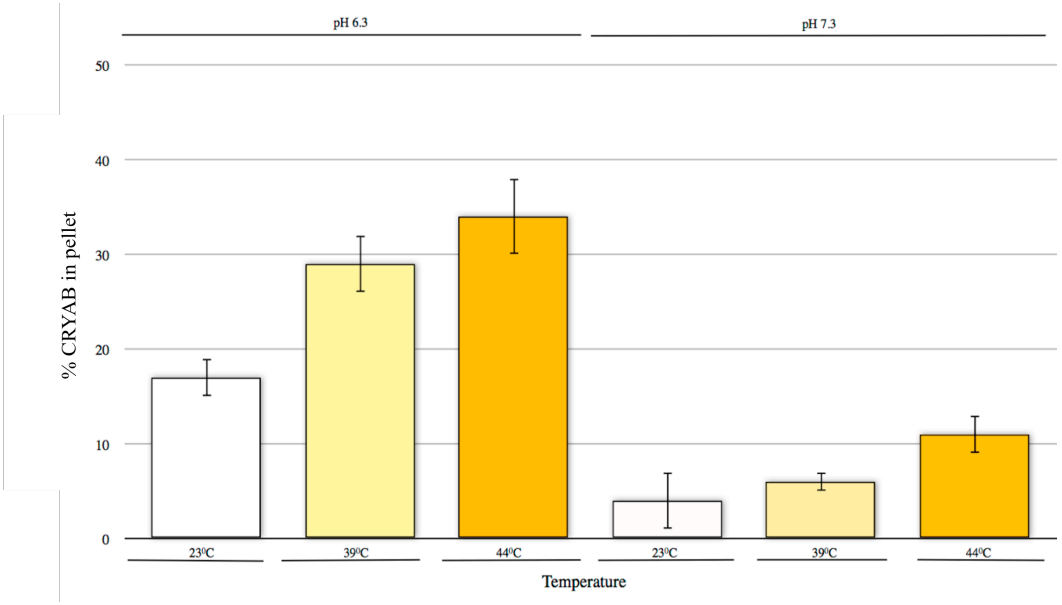

Figure 3.30 Chart of binding of WT CRYAB to assembled WT GFAP IFs.
CRYAB was added to assembled WT GFAP filaments, at pH 6.3 or 7.3 at three different temperatures. This showed increased binding at low pH and increased temperatures similar to when CRYAB is added before filaments have formed. At pH 6.3 and 7.3 at 39 ^{0}C there is a statistically significant smaller quantity of CRYAB co-pelleted with WT GFAP when CRYAB has been added to assembled filaments compared with CRYAB addition before filaments have formed (c.f. Table A.20 and A.22). Data are represented as the average values of three independent experiments with error bars showing +/- one SD. There is no significant difference observed at 23 or 44 ^{0}C.

Another experiment involved assembling WT GFAP filaments at pH 6.3 where most binding is observed and then dialysing back into pH 7.3 for 1.5 hr. The purpose was to see if the filaments retain any memory of their previous state or if the time of dialysis is sufficient to revert back to a state where lower binding is observed. From Figure 3.31 it can be seen that the binding is not as much at 23 and 39 ^{0}C (approximately 10% CRYAB is in the pellet fraction at both temperatures) compared to when GFAP has been formed at pH 6.3 and CRYAB from pH 6.3 is added in Figure 3.30 (17 and 29% of the total CRYAB is present in the pellet at 23 and 39 ^{0}C, respectively).

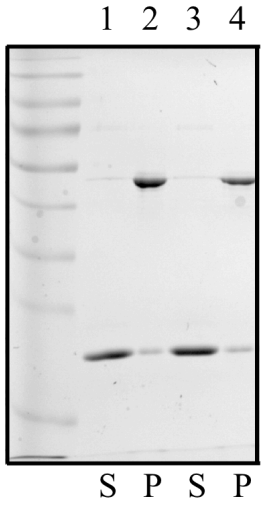

Figure 3.31 Plasticity of GFAP filaments in response to pH influences CRYAB interactions.

The filaments were formed at pH 6.3 at 23 ^{0}C, dialysed into pH 7.3 buffer for 1.5 hr and WT CRYAB formed at pH 7.3 was added and incubated at 23 (lanes 1-2) and 39 ^{0}C (lanes 3-4). It appears that the time for exchange of the pH 6.3 for the higher pH 7.3, for the assembled filaments, was sufficient to revert the higher binding, seen in Figure 3.29, to a lower binding (c.f. Figure 3.29 lanes 1-4 for pH 6.3 and 7-10 for pH 7.3). S= supernatant and P= pellet.

3.1.4 Discussion.

GFAP assembly is susceptible to its divalent cation environment.

Divalent cations are highly important for GFAP assembly and when they are removed this significantly affects the final compaction stage. EDTA does not chelate the sodium ions present and so this remains free to influence the assembly of the filaments, which highlights the specificity of magnesium ions for promoting normal assembly of GFAP.

When CRYAB is added to these filaments it can be seen that it has an effect to reduce the filament interactions and in fact it can be seen more clearly that these altered filaments are made up of shortened filaments that have not elongated fully, although they are longer than ULFs. These filaments also appear longer than those obtained with bovine GFAP in the absence of divalent cations (Tanaka et al., 1989). The lengths vary but some of the shorter filaments are approximately 300 nm. The filaments are also thicker than normal and often reach over 20 nm. There is a slight ability to reduce filament-filament interactions, visible after a low speed sedimentation assay has been carried out (Figure 3.2). However the chaperone-like activity of CRYAB is not great enough to overcome the full extent of the increased interactions of the GFAP filaments since there is still a much higher proportion of pelleted material compared to filaments assembled in the presence of magnesium ions (Figure 3.2 and 2.18) showing that either the chaperone-like activity of CRYAB has been exhausted at these concentrations and/or CRYAB would require an ATP-dependent chaperone to then re-fold the filaments to a more assembly-competent state, likely in the presence of magnesium. For future work it would be interesting to dialyse these filaments into a buffer with magnesium ions to see if the process is reversible. In addition, in comparison to normal WT GFAP filaments, which have minimal binding to CRYAB at 23 ^{0}C in Tris assembly, it appears that when the filaments have no magnesium ions CRYAB binds much more to these structures. Filament architecture is disrupted upon an increase in temperature through Tris assembly where CRYAB also binds much more, which may be due to a change in pH as well as temperature. The GFAP protein has an essential divalent cation binding site in the 2B rod domain (determined from flow dialysis experiments with a radioisotope of calcium), which is 70% identical with the similar region in desmin and 60% identical with the similar region in vimentin, as assessed using ClustalW2

(EMBL-EBI, UK) and BLAST (National Library of Medicine, US) (Yang Z W., 1988) and this region is shown in Figure 3.32. Since the GFAP filaments have been compromised in assembly formation when divalent cations are absent, it is likely that the mutations within the critical site of amino acid residues 320-349, for divalent metal ion binding, found associated with AxD would result in similar properties of altered filaments, although this is not the only region in GFAP that has been correlated with binding divalent cations (Yang Z W., 1988). The mutations found in this region include L331P that has a mild phenotype (Shiihara et al., 2004), E332del that is also mild (Jefferson et al., 2010) and the R330G and E332K mutations on the same allele which have a mild phenotype and lead to less aggregation compared to other cases (Bachetti et al., 2008). The *in vitro* properties of these assembled mutant filaments have not been assessed up to now but it could be the case that the mutations do not affect the metal binding and this is why the phenotypes are not as severe as would be expected if filaments were formed similar to Figure 3.4 A).

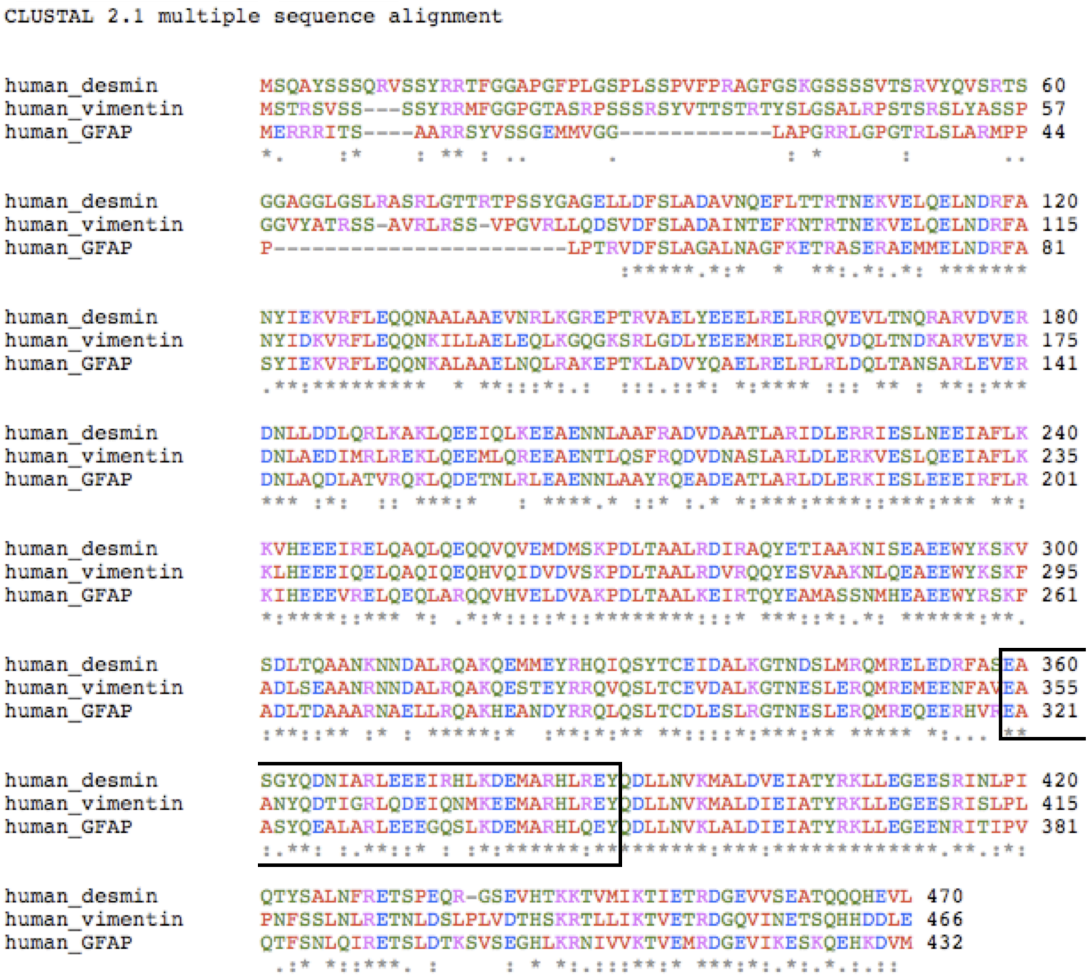

Figure 3.32 Sequence alignment of GFAP divalent cation binding site against desmin and vimentin.

The ClustalW2 alignment of WT human GFAP (GenBank: J04569.1), desmin (GenBank: NM_001927.3) and vimentin (GenBank: NM_003380.3) has been carried out and the boxed area represents the important Mg^{2+}-Ca^{2+} binding site in GFAP (Yang Z W., 1988, Larkin MA, 2007). Most variability between the three sequences occurs in the N-terminal head domain. Symbols: * indicates a single, fully conserved residue, : indicates conservation between groups with strongly similar properties, . indicates conservation between groups with weakly similar properties.

The region of residues 320-349 constitutes 24% of rod 2B and alteration of this domain in GFAP with mutation of the KLLEGEE sequence at the C-terminal end of rod 2B along with removal of the tail domain causes more perturbed assembly than when just the tail domain is removed, seen from transfection studies with a higher incidence of aggregate formation as the result of alteration to the conserved

TYRKLLEGEE sequence (Chen and Liem, 1994). However the tail region seems less important as long as the RDGE motif is maintained that is situated at amino acid position 416-419, since complete removal of the tail results in some aggregate formation after transfection into vimentin positive cells. This shows the importance of the 2B domain, which may be not only a reflection on the available amino acid residues for ionic interactions with other dimers but also the potential to bind divalent cations. This is in contrast to the head domain, which results in altered assembly when parts are removed (Chen and Liem, 1994). The head domain has been shown to be important for alignment and lateral interactions of IFs during assembly (Yang and Babitch, 1988). The magnesium-calcium binding site in the C-terminal tail mediates cross-linking from the divalent cations, which is in the last 11 amino acids of the tail region in vimentin in addition to the site in the rod 2B region shown in Figure 3.32 (Lin et al., 2010a). Therefore even if filaments have formed after truncation of the end of the tail region it is likely that filament properties will have been altered leading to weaker networks and lowered resistance to mechanical stress since it was shown that vimentin with the last 11 amino acids removed from the C-terminus was not effectively cross-linked by magnesium despite the presence of the 2B rod domain binding site (Lin et al., 2010a). The C-terminal tail is crucial for determining the diameters of IFs and therefore alterations in their interactions from different divalent cations likely influence this, as shown by thicker filaments for GFAP (Herrmann et al., 1996).

Unlike with Tris and magnesium ion assembly, where CRYAB can inhibit filament assembly at 23 ^{0}C, when no divalent cations are present this is not the case as seen in Figure 3.3. Perhaps in the diseased state there is a reduction in available divalent cations to bind to GFAP and this adds to the problem of aggregate formation.

From low speed sedimentation assays the filaments assembled in Tris assembly with 1mM Ca^{2+} give similar sedimentation values to those assembled in magnesium ions and they also are morphologically similar (Figure 3.6 and 3.7). With 5mM Ca^{2+}, GFAP filaments appeared to have a range of widths, which were thicker than 10 nm seen with 1 mM Ca^{2+} ions, like Xenopus vimentin (Figure 3.12). With the manganese ions, the filaments appear to associate together more as seen by a greater increase in proportion of protein in the pellet fraction in low speed sedimentation assays and this increased association is also seen from the TEM images where sheet-like structures are formed (Figure 3.5 and 3.7). This is also further supported by the

appearance of a higher molecular weight band positioned above the 130 kDa marker band corresponding to a potential dimer of GFAP, showing higher oligomeric GFAP structures are being formed (Figure 3.7). This higher molecular weight band is investigated further in the next section. An approximation of the molecular weight was derived from a natural log-log plot of arbitrary distance travelled against molecular weights of standards, utilising the arbitrary distance travelled of the higher molecular weight species and this derived a value of approximately 220 kDa (Figure A.3 in the appendix). In fact from the TEM pictures the filaments appear to align alongside each other apparently forming sheet-like structures. With manganese associated ALS, there is an upregulation in GFAP expression as this has been seen in mouse models of ALS mice due to the stress response in Schwann cells and therefore the manganese ions *in vivo* will perhaps be influencing altered GFAP filament formation which may add to the pathogenesis of the disease (Keller et al., 2009).

The diameters of filaments assembled in 1 mM Ca^{2+} ions are a similar width to the usual 10 nm for all three filaments. However the filament widths of the GFAP manganese-induced filaments can reach up to 30 nm, thus highlighting potential problems with filament compaction. This is likely to add to the paradigm of filament assembly, specifically with ULFs and support for their formation which then under go compaction after annealing (Georgakopoulou et al., 2009).

CRYAB has been shown to reduce filament-filament interactions of GFAP solutions assembled in the absence of magnesium and calcium ions and thus this heat shock protein was co-assembled with GFAP formed in the presence of manganese ions to see if it could also reduce the increased filament interactions here. CRYAB was unable to prevent the formation of the dimer and could not reduce filament-filament interactions of GFAP filaments formed with 1 mM Mn^{2+} ions at 23 ^{0}C (51 +/- 17% GFAP in the supernatant alone compared to 49 +/- 25% GFAP in the supernatant with CRYAB) as averaged from three independent repeats however effects were seen at 39 ^{0}C (from 4 +/- 1.5 % GFAP in the supernatant alone compared to 28 +/- 10 % GFAP in the supernatant with CRYAB) resulting in more protein in the supernatant fraction after low speed centrifugation (Figure 3.8). It has been found previously that CRYAB has reduced chaperone abilities when assembled with 1 mM Ca^{2+} ions, however from low speed in this instance with 1 mM Ca^{2+} assembled at 23 ^{0}C (83 +/- 7% GFAP in the supernatant alone changing to 89.0 +/- 1.3% GFAP in the supernatant with CRYAB) and 39 ^{0}C (2.3 +/- 1.4% GFAP in the supernatant alone

changing to 20.8 +/- 7.9% GFAP in the supernatant with CRYAB), the CRYAB seems to be able to reduce the filament-filament interactions shown in Figure 3.8 B), therefore showing that there is some difference between chaperone ability to reduce aggregation in a heat shock assay and to reduce interactions between non-aggregating filaments (Ganadu et al., 2004). Also the buffer conditions are different in this assay compared to the heat shock assay that will play a major part in the activity of the protein. In all three divalent cation environments looked at, CRYAB is able to reduce filament interactions at 39 ^{0}C, although the heat shock protein does not alter the apparent morphology of filaments which have not assembled properly such as with the manganese ions, likely due to higher temperatures increasing available hydrophobic binding regions. For both manganese and calcium assemblies, after high-speed sedimentation the WT GFAP was mostly pelleted showing effective filament formation albeit altered interactions detected from the low speed assays (Figure 3.15 and 3.16). Regarding binding with WT GFAP at 23 ^{0}C, WT CRYAB is 28 +/- 1.98% in the pellet with manganese ions compared to 8.07 +/- 4.6% with magnesium ions and at 39 ^{0}C WT CRYAB is 29 +/- 2% in the pellet with manganese ions compared to 17 +/- 5% that co-sediments with WT GFAP formed with magnesium ions, showing that manganese ions promote increased filament-CRYAB interactions.

Manganese ions promote increased binding of CRYAB to GFAP, desmin and vimentin filaments.

The divalent cations appear to influence the binding of CRYAB to the filaments studied here, as it was found from Tris assembly that CRYAB binds much more to vimentin, desmin and GFAP filaments in the presence of manganese ions as opposed to magnesium ions when pH is not controlled for, which was discussed in the previous section.

	% CRYAB pellet Mg^{2+} 23-28 ^{0}C	% CRYAB pellet Mg^{2+} 39-44 ^{0}C	% CRYAB pellet Mn^{2+} 23-28 ^{0}C	% CRYAB pellet Mn^{2+} 39-44 ^{0}C
Vimentin	12 +/- 3	19 +/- 2	15 +/- 12	31 +/- 13
GFAP	8 +/- 4.5	17 +/- 5	28 +/- 2	29 +/- 2
Desmin	13 +/- 4	53 +/- 7	25 +/- 5	64 +/- 10

Table 3.6 **Percentage of WT CRYAB binding to filaments**.
Mean values +/- one SD of percentages of WT CRYAB binding to filaments.

Manganese ions only appear to result in increased filament interactions with GFAP and desmin (Figure 3.13). This will be expected since desmin has more pronounced filament bundling than vimentin and thus has greater interactions between the filaments (Schopferer et al., 2009). The desmin filaments assembled with manganese ions can be seen coated with WT CRYAB oligomers after assembly at 39-44 ^{0}C, more so than after being assembled with calcium ions and this highlights that although the filaments look similar when assembled with both ions, there are subtle changes that reflect greater binding with manganese ions to CRYAB (Figure 3.11). Also this greater binding appearing on TEM images is reflected in the sedimentation quantification results (Figure 3.15 and 3.16). Interestingly, CRYAB appears to bind much more to desmin filaments under these conditions compared to the other two filaments and this will be discussed in more detail in the next section.

There is a high quantity of mitochondria in skeletal and cardiac muscle and mitochondrial dysregulation has been shown in desmin-related cardiomyopathy such as a lack of organisation important for providing ATP and a reduction in maximal respiration rate (Schroder et al., 2003, Vendelin et al., 2005). Mitochondria contain manganese in a complex with superoxide dismutase, which protects against oxidative damage and therefore superoxide dismutase binds to manganese in the sarcoplasm before being transported to the mitochondrial matrix. Muscle contains a relatively low quantity of manganese ions with a higher amount found within cardiac than skeletal muscle tissue and also red muscle as opposed to white muscle. Additionally the interfibrillar population of mitochondria, which have greater oxygen consumption, also have higher levels of manganese than the subsarcolemmal population of mitochondria (Sanchez-Morito et al., 1999, Kondo et al., 1991).

Desmin interacts with mitochondria since desmin K/O mice have displaced mitochondria although interactions with manganese ions have not been studied (Milner et al., 2000). Perhaps desmin is sensitive to manganese ions because of its presence in muscle. The induction of dimers of the three IFs studied here from the divalent manganese cation-catalysed disulfide bond formations, but not from magnesium ions, will be partly due to the greater ionic radius of the ion increasing interactions between IFs (Lin et al., 2010b). Copper is noted for being able to oxidise cysteinyl residues, although the mechanism is not fully known and in this case manganese also appears to have the same property (Niazi, 2007). Protein dimers are associated with AD and increased levels of Aβ dimers that are induced from copper ions (Shankar et al., 2008, Barnham et al., 2004, Proctor et al., 2012). Perhaps in AxD there is an increase in GFAP dimer formation although mutations have been correlated with a decrease in dimerisation with homodimers of the mutants, however heterodimers with GFAPα resulted in a similar capacity for dimerisation as GFAPα alone and will be the situation in the disease state due to populations of both WT and mutant GFAP because of the heterozygosity of the disease (Nielsen et al., 2002)

The higher molecular weight band from the manganese assembled GFAP samples corresponds to an oligomer as proved from the immunoblot using the assembled WT GFAP and the Ab specific for human GFAP of SMI-21 (Figure 3.17). Sending a sample for mass spectrometric analysis further proved this. Therefore one hypothesis was that as the manganese ions induce the formation of these oligomers, these might act to inhibit the normal compaction step in IF assembly and this oligomer may explain the increased widths of the GFAP filaments. It has been proposed previously however that filament oligomer bundles likely play a role in stabilisation of glia and neurons with strong filament-filament interactions (Shaw and Hou, 1990). The cysteine residue in vimentin is also highly important and has been proposed to be involved in binding to other proteins during oxidative stress through disulfide bonds (Rogers et al., 1991).

The next question that was answered was whether or not this species was formed from oxidative cross-linking of the GFAP filaments or whether it could be from covalent coupling. Manganese ions usually protect cells from oxidative damage however it is possible that the ions increase the associations between the filaments resulting in oxidative cross-links. GFAP has one cysteine residue in the 2B rod

domain and the oligomer is thus likely due to the formation of disulfide bonds between these groups. After treatment with 50 mM DTT for 1 hr at 37 ^{0}C it was found that the higher molecular weight oligomer was removed (Figure 3.18). This is unlike higher molecular weight oligomers of GFAP which have been discovered previously that were created from glutamine-lysine cross-links mediated *in vivo* from tissue transglutaminases and thus more stable (Shaw and Hawkins, 1992). The oligomer will most likely be a dimer as GFAP dimers were reported previously to run at an unexpected mobility of approximately 170 kDa and in this case it was approximately 220 kDa (Quinlan and Franke, 1982, Quinlan and Franke, 1983). In mice over-expressing GFAP, genes encoding for iron homeostasis and metallothioneins 1, 2 and 3 that bind toxic metals are elevated (Hagemann et al., 2005). Astrocytes are also the main manganese store in the CNS and perhaps GFAP is more responsive to altered levels in manganese ions because of this (Agustina Alaimo, 2011).

Assembly of GFAP, desmin and vimentin was carried out in the presence of 5 mM Ca^{2+}, showing increased filament widths for GFAP. Previous studies looking at assembly of bovine GFAP in 5 mM Ca^{2+} also showed increased filament widths at this concentration, but also filament bundling which is not seen in this instance (Tanaka et al., 1989, Yang and Babitch, 1988). Vimentin and desmin appear unaffected however and form usual 10 nm filaments (Figure 3.12).

CRYAB binding is dependent upon pH, time for pH change, temperature, structure of filament surface (altered either from a mutation, pH or temperature) and also the structure of the CRYAB surface (altered either from a mutation, pH or temperature). The hypothesis is that under normal filament assembly conditions the CRYAB does not bind very much to the filament surfaces but binds very transiently and this allows the protein to reduce filament-filament interactions but when this is altered to non-ideal filament structures (aggregates, disassembly of coils) such as with a rise in temperature, drop in pH or a mutation, the CRYAB binds much more but no longer can a reduction in filament interactions be seen in some cases because the aggregation has exhausted the ability of CRYAB to reduce the aggregation.

WT GFAP assembled in HEPES at pH 6.9 with manganese ions forms the usual dimer seen from Tris assembly and the same is seen for vimentin (Figure 3.21). HEPES buffer can however form free radicals (responsible for cross-linking protein) and since the oligomer is due to a redox reaction this buffer will give an incorrect

representation on the influences of the metal ions alone. However the morphology of the filaments look similar to those from Tris assembly with magnesium ions, except for GFAP where an uneven width distribution can be seen, similar to that seen in Tris buffer with manganese ions where widths of up to approximately 30 nm are seen (Figure 3.20). The amount of co-pelleting of CRYAB is statistically greater at pH 6.9 with the manganese ions than 6.8 with magnesium ions for vimentin at 39 and 44 ^{0}C and GFAP at 23 ^{0}C thus highlighting that the manganese ions promote increased associations of CRYAB to the filaments in these conditions (Figure 3.21). Divalent cations are known to affect the chaperone activity of CRYAB with copper reported to increase it and it was shown that copper has a binding site on the protein and interactions with three histidines via coordination sites on the imidazole rings (Ganadu et al., 2004). Calcium ions however have been shown to inhibit the chaperone-like reduction in aggregation of the insulin B-chain upon reduction, however CRYAB seems to be able to still reduce filament-filament interactions assessed from low speed sedimentation assays in Figure 3.8 B). The copper binding of CRYAB is implicated in cytoprotection by sequestering copper ions and thus preventing the oxidation of other proteins and when copper is applied to lens epithelial cells there is an up-regulation in CRYAB and αA-crystallin (Ahmad et al., 2008). Therefore, similar with copper ions it may be the case that CRYAB chaperone activity is increased since there's an increase in interactions observed from high speed sedimentation assays with manganese ions, although investigations without filaments would need to be carried out to assess this.

GFAP filament assembly appears to be the most sensitive to different divalent cations, compared to desmin and vimentin. This has been shown by the formation of different filament structures after assembly in the absence of magnesium ions, in the presence of 5 mM Ca^{2+} ions in Tris buffer and in the presence of 1 mM Mn^{2+} ions in Tris and HEPES buffers. Increased GFAP filament widths are also noted in the next section at pH 6.3.

Lower pH and increased temperature values promote increased binding of CRYAB to GFAP, desmin and vimentin filaments.

HEPES buffers were used for these experiments in preference to phosphate buffers, which do not change pH with temperature fluctuations, as they have limited divalent

metal chelation unlike phosphate buffers where nearly all divalent metals will precipitate out of solution (Zeyer et al., 1986). Additionally, an overnight assembly procedure was used as opposed to a final assembly step for 1 hr in a water bath, which has been carried out previously in the laboratory (Perng et al., 1999a). The reason for not using the shortened method in this case was to allow the filament structures to resemble those *in vivo* as close as possible since the shortened assembly always leads to filaments that have not compacted as well which would likely influence the interactions with CRYAB; compare Figure 3.9 and 3.25.

At pH 7.3 even upon raising the temperature to 44 ^{0}C, the binding does not increase significantly of WT CRYAB to all of the filaments looked at, however upon lowering the pH to 6.8 and 6.3 there is an increase in binding at 23 ^{0}C, which can be increased further upon raising the temperature (Figure 3.22). Therefore pH is the crucial determining factor to result in increased binding of the small heat shock protein and temperature increases are also dependent upon this variable. A 0.2 mg/mL concentration of IFs was used for the sedimentation assays to help reduce the propensity for the filaments to stick to the pipette tips and the samples were vortexed after assembly. WT GFAP filament assembly inhibition from WT CRYAB occurs at pH 6.8 and 7.3, but not at pH 6.3 and is not the case for desmin and vimentin (Figure 3.23). A similar trend of inhibition from native bovine phosphorylated CRYAB on native *in vitro* assembled bovine GFAP filaments at higher pH values has been seen before however the extent of inhibition is not as great in this chapter (Nicholl and Quinlan, 1994). All three filaments formed usual 10 nm wide filaments under all nine conditions apart from GFAP at pH 6.3 and vimentin at pH 7.3 at 23 ^{0}C which both had more variable and wider widths (Figure 3.28 A) and 3.27). This demonstrates how GFAP assembly appears more sensitive than desmin and vimentin assembly. Desmin also seemed to have more variable widths at the lower pH values. The data also show how increased temperature not only increase filament entanglement but also the efficiency of compaction and their surface structure since at 39 and 44 ^{0}C GFAP filaments at pH 6.3 are still wider than 10 nm but not as wide as at 23 ^{0}C (Figure 3.26). The increase in binding to the filaments at the lower pHs is likely due to changes in the charge of histidine residues in CRYAB, which are sensitive to pH changes near the physiological range, to a more positive charge. It is the only amino acid that is electrically neutral around pH 7.3 and there are many of these residues situated in the dimer interface of CRYAB (Clark et al., 2011).

Therefore any charge changes in this region will affect the ability of the oligomers to form dimers and potentially result in a preference for monomer formation. Table 3.6 demonstrates that the CRYAB oligomer widths are wider and more variable at the lower pH value of 6.3 thus showing that the pH is affecting oligomer size of the sHSP as well as the assembly equilibrium of filaments. The repeat distance of CRYAB binding to vimentin at pH 6.3, between two filaments, is equivalent to the width of a CRYAB oligomer (20 nm) and therefore difficult to assess what part of the filament structure they are binding to. Studies have been carried out to assess what sequence in CRYAB binds to the filaments but not what filament sequence interacts with CRYAB (Ghosh et al., 2007). Further studies would need to be carried out to assess what sequence/s CRYAB is interacting with, such as protein pin arrays. There are limitations of using negative staining for quantifying filament and CRYAB widths, which include low resolution and artifacts (uneven stain). Positive staining can also occur where the uranyl acetate complexes with the filaments and therefore will likely alter the chemistry and thus values of widths. Cryogenic electron microscopy would be a better method to use since the true shape of the proteins can be viewed (they don't get flattened against a carbon film as the sample is kept hydrated and frozen) and can aid in deriving the secondary and tertiary structures. This would be especially useful for CRYAB to assess how its secondary and quaternary structures are altered where an increase in oligomer width is observed at the lower pH.

CRYAB can reduce filament interactions more readily at increased pH values (Figure 3.24). The exception here appears to be desmin, which has high filament-filament interactions at all pH values; this is unusual as generally there is a correlation between lowered binding with CRYAB and lowered filament-filament interactions, demonstrated with vimentin and GFAP filaments (Figure 3.23 and 3.24). Increased temperatures however result in an increase in filament-filament interactions. Increased temperature increases the binding of CRYAB to the filaments (Figure 3.23 and 3.29), acting as an activator for CRYAB. Subunits exchange constantly in the sHSP and temperature increases will increase the on- and off- rates of subunit exchange, reported previously, thus triggering increased activity of CRYAB (Liu et al., 2006).

When CRYAB reduces filament interactions, its association (binding) to filaments is increased and vice versa regarding GFAP and vimentin filaments. In one study at

acidic pH it was shown that stable oligomers of CRYAB, with a reduction in dissociation, are preferred alongside a drop in chaperone activity demonstrated from SPR experiments, which is in contrast to higher pH values with smaller oligomers and increased chaperone activity. Increased temperatures were also associated with increased chaperone activity (Liu et al., 2006). Other studies suggest that lower pH increases the chaperone activity of the sHSP and it is likely that the drop in pH results in a preference for monomers. From the data in this chapter it can be hypothesised that both scenarios are likely whereby at acidic pH there will potentially be an initial increase in active monomer states, which have been observed previously from NMR studies, which then bind to filaments and then formation of stable oligomers which will lead larger complexes alongside a drop in chaperone activity (Liu et al., 2006, Jehle et al., 2009). At this moment in time it is not known how CRYAB dissociates and associates and what the functional unit is which interacts with IFs. CRYAB monomers have been shown to bind to microtubules and act to inhibit their assembly at high molar ratios and it is the monomers, which bind and the larger oligomers, which associate with unassembled tubulin, therefore this also supports the idea that when binding is promoted of CRYAB to filaments there would be a preference for CRYAB monomers (Houck and Clark, 2010). At physiological pH the autoinhibitory IXI motif (amino acids 159-161) in the C-terminal tail of CRYAB binds within the β4-β8 groove and competes with hydrophobic substrate proteins for interaction whereas at acidic pH 6.5 the IXI motif is released from this binding site thus increasing the available substrate binding regions (Jehle et al., 2010). At increased temperatures the ability of CRYAB to bind to substrates is increased due likely to a preference for monomer formation and an increase in chaperone-like activity (Spinozzi et al., 2006). It is also likely that at low pH and higher temperatures the extent of aggregation of the filaments is too great for the CRYAB to overcome and thus there is no longer a reduction in filament-filament interactions but instead increased binding, seen for GFAP and vimentin (Figure 3.24). This is the opposite scenario that is seen with tail truncated Q151X mutated CRYAB where an increase in binding is observed with a reduction in filament interactions; the increased binding may be due to the fact that the autoinhibitory motif in the C-terminal tail, as mentioned earlier, is no longer able to mask the β4-β8 groove for binding in addition to a change in tertiary structure (Hayes et al., 2008).

From these experiments, which kept constant pH and temperature values and also

from those in the previous section assessing binding in the presence of different divalent cations, which did not control for pH, it can be seen that CRYAB binds the most to desmin IFs. The reason for this will lie with the desmin amino acid sequence, which likely contains many more hydrophobic binding sites for CRYAB compared to the other two IFs. This was observed from a sequence analysis of the grand average of hydropathy (GRAVY) for the three IFs and desmin has the highest hydrophobic profile (-0.723) compared to GFAP (-0.773) and vimentin (-0.823) (Stothard, 2000). Also the fact that mutations in CRYAB have only so far been discovered associated with desminopathies and not gliopathies highlights how the interactions between CRYAB and desmin are perhaps stronger. However the preference for desmin will likely not only lie with desmin's amino acid sequence since it has been shown that CRYAB has different specific sites for interacting with desmin and GFAP and thus the CRYAB sequences will also influence the extent of interactions (Ghosh et al., 2007). Vimentin is able to co-assemble with both desmin and GFAP and since it has the least binding to CRYAB it is likely that it aids in modulating GFAP and desmin networks rather than playing an important functional role in interacting with the sHSP (Wickert et al., 2005, Menet et al., 2001). The dimer-monomer transition of CRYAB mediates increased chaperone activity and any deletion of amino acids which reduces the oligomer size acts to increase its chaperone ability, such as with the removal of ^{54}FLRAPSWF^{61} residues near the end of the head domain (residues 1-67) which increased the oligomer hydrophobicity (Santhoshkumar et al., 2009). Figure 3.28 B) shows how at pH 6.3 CRYAB appears to line up along the vimentin filament surface in a regular periodicity showing that the interaction between the sHSP and the filaments is specific, despite observing the lowest interactions out of the three IFs studied and this demonstrates how there are hydrophobic areas on CRYAB which become adsorbed to the target protein to prevent aggregation (Spinozzi et al., 2006). Similar periodic coating of GFAP filaments has been observed with α-crystallin and therefore since vimentin is expressed in the lens fibre cells with α-crystallin, specific interactions must occur (Nicholl and Quinlan, 1994).

In addition, the interactions between CRYAB and the filaments were investigated with CRYAB added to assembled filaments to compare to the interactions seen with its addition before their formation. There was a significantly lower amount of CRYAB binding to the GFAP filaments at 39 ^{0}C at pH 6.3 and 7.3, when CRYAB was added to formed filaments compared to its addition before the filaments had

formed showing that the filament surface is crucial for mediating CRYAB-filament interactions (Figure 3.29). However the same general trend was observed of increased binding at the low pH and raised temperatures thus supporting the notion that *in vivo* where there will be both soluble and insoluble filaments which are assembling and disassembling, when the pH is dropped and the temperature is increased there is a promotion of increased CRYAB interactions with the filaments. Another facet to this was investigated with the GFAP filaments being formed at pH 6.3 and then the buffer exchanged for the higher pH 7.3 over 1.5 hr before CRYAB was added, from pH 7.3. This showed a lower binding of CRYAB compared to the binding seen from the GFAP filaments formed at pH 6.3 and CRYAB from the same pH having been added (Figure 3.31). Therefore under the conditions of the experiment, the 1.5 hr was sufficient time to reduce the binding seen showing that the filaments are in a seesaw state which can be tipped in favour of higher or lower binding and it is likely that once formed they are still capable of altering their surfaces depending on the pH environment they are placed in. However the lower binding seen is also likely due to the fact that CRYAB was formed at the higher pH compared to the previous experiments where the filaments formed at pH 6.3 had CRYAB added which was formed at the same pH.

In the next chapter more information about how CRYAB interacts with IFs will be gained by looking at the interactions between desmin and CRYAB in their equilibrium state. These experiments look at the elasticity of the filaments and also the viscosity of the solutions and how CRYAB acts to alter these factors.

Chapter 4; Rheometrical properties of desmin filament networks and the influence of CRYAB.

4.1 Introduction and aims.

This work is a progression from the influences of human WT CRYAB upon GFAP and desmin filament-filament interactions seen from chapters 2 and 3 and is another method to quantify this utilising an equilibrium method. Sedimentation and bulk viscometry have been used before to assess how CRYAB reduces filament-filament interactions, however microrheology is a more sensitive technique as it allows local elastic and viscous components to be derived (Perng et al., 1999a, Mizuno et al., 2008). It is a non-invasive technique to study the interactions between desmin and CRYAB and is an important complementary technique to the methods used in chapter 2 and 3. Optical tweezers have the greatest frequency range compared to other methods such as passive video particle tracking and diffusing-wave-spectroscopy (DWS). The alpha-crystallin domain has been crystallised. This encompasses the R120G point mutation position responsible for cataract, desminopathy and myopathy (Clark A.R. et al. 2011). It is hypothesised that this mutant results in larger oligomeric complexes that perturb the normal chaperone and functional activities present *in vivo* between WT CRYAB and desmin filaments. *In vitro* work has also already shown that this mutant results in aggregation and increased binding to filaments. Here the viscosity changes associated with these interactions were investigated. One question is: does WT CRYAB act to increase pore width in the meshwork or does it act to promote assembly-disassembly at the level of individual filaments? A series of experiments were set up to help elucidate this and also delve deeper into filament network properties. Elasticity has been studied for various filament solutions, which are all seen as being elastic solids capable of deformation in phase with the imposed strains. There are a few constants that can be derived from rheological measurements of filament networks, such as G' (elastic modulus) and G'' (loss modulus) from single trap passive microrheology.

4.2 Materials and methods.

4.2.1 Filament and chaperone sample preparation.

4.2.1.1 Single Trap Rheology.

4.2.1.1.1 Assembly.

Desmin filaments were assembled either alone or in a mixture with CRYAB, according to Figure 4.1 up to the penultimate step, as shown below. For the 1:1 molar ratio, concentrations of 0.2 mg/mL desmin and 0.07 mg/mL CRYAB were used and for the 1:0.2 ratio of desmin: R120G CRYAB, 0.2 and 0.015 mg/mL were used respectively. PLL(20)-g[3.5]-PEG(2) (PEG-PLL) (SuSos, Zurich) -coated carboxylate-modified polystyrene 2.0 μm yellow-green fluospheres (Invitrogen, UK) were added at a mass of 0.0125 mg to each sample before the final overnight assembly step.

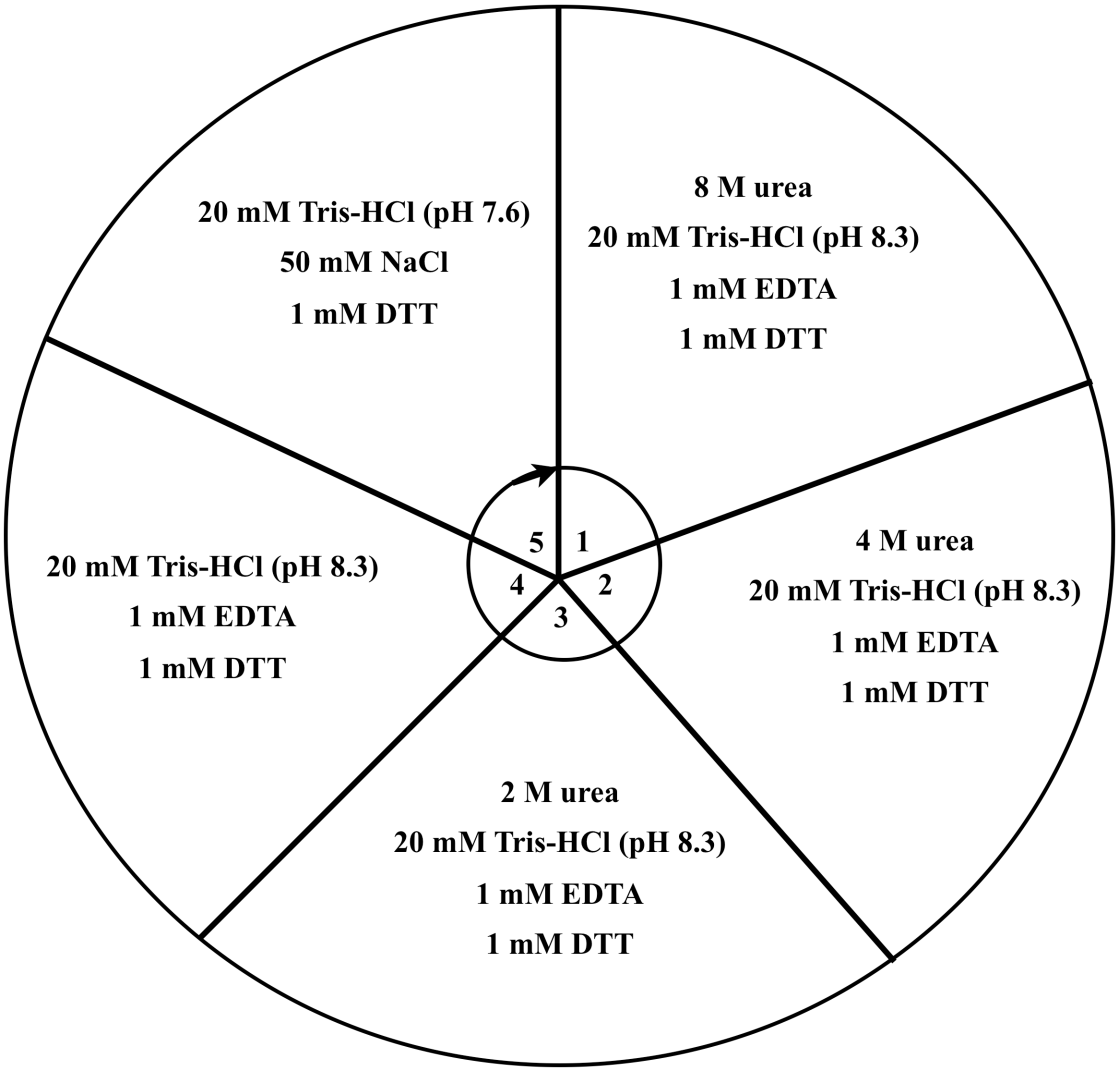

Figure 4.1 Desmin assembly.

4.2.1.1.2 Microsphere coating.

For coating of the fluospheres, the stock bead solution was initially diluted to 0.5% (w/v) upon dilution with Milli-Q® (Millipore, UK) water and then an equal volume of 1 mg/mL stock of PEG-PLL polymer was added and incubated for 15 min, 16 rpm at room temperature on a spinning wheel (Agar Scientific, UK). PEG-PLL is made up of L-lysine that is charged, thus binding to the beads and ethylene glycol that prevents the beads from clumping to each other and attaching to filament and glass surfaces, as it is inert. This was centrifuged down (5,200 xg_{av}, 15 min, room temperature) and resuspended in 200 µL of 20 mM Tris-HCl (pH 8.3) buffer and 5 µL of this was added to each sample of 195 µL. Protein samples were then transferred into the final overnight assembly buffer.

4.2.1.2 AMOLF two particle single trap rheology.

4.2.1.2.1 Desmin and vimentin with/without CRYAB assembly.

Assembly was carried out, for desmin and vimentin samples, the same as for the single trap rheology except 1 mM $MgCl_2$ was added to the final overnight assembly buffer. Concentrations of proteins used were 1 mg/mL IFs with or without 3.7 mg/mL WT CRYAB. A 200 or 100 µL volume was used for assembly using a slide-A-Lyzer MINI dialysis unit with a 20 kDa molecular weight cut-off (MWCO) (Thermo Scientific, UK). Microspheres were added to the final assembled material either before or after the final assembly step and it was shown that there was no difference in the *G'* and *G''* moduli between the two conditions (Figure 4.7). The beads were added after the final dialysis step in the samples analysed.

4.2.1.2.2 Microsphere coating.

Protein lobind tubes (Eppendorf, DE) were used and 15 µL of a stock preparation of microspheres were added (1 µm diameter polystyrene) and sonicated for 5 min in a floater in a sonic water bath and centrifuged (16,300 $xg_{av,}$ 5 min, room temperature). The supernatant was removed and 300 µL of PEG-PLL solution was added and incubated on a rotating wheel (22 rpm, 30 min, room temperature). This was centrifuged again (7,400 xg_{av}, 5 min, room temperature) and the supernatant was again removed. 65 µL of Tris-HCl (pH 8.0) buffer solution was added to resuspend the beads and they were left at 4 ^{0}C until use. 1.75 µL was added to the assembled samples.

4.2.2 Data acquisition for passive viscosity measurements using a 1064 nm single-trap for microrheology.

100 µL of the assembled protein and microsphere samples were placed into circular well slides (Agar Scientific, UK) and coverslips (Scientific Laboratory Supplies Ltd., UK) of depth 0 sealed on top with nail varnish. They were then inverted and placed onto a metal stage with a circular cut-out for the trapping objective to make contact with the coverslip. Citifluor (Agar Scientific, UK) was used as oil for the objective imaging. An optical tweezer trapping instrument was utilised, built by Scott Silburn,

to record the motion of a trapped bead in the protein solutions to gather passive viscosity measurements. An Nd:YAG laser at 1064 nm was used to trap beads through a 100x, 1.25 numerical aperture (NA) oil-immersion objective lens (Nikon, UK), with 10mW of laser power. White light was provided from a tungsten-halogen KL1500 light source (Schott, USA) from above and the slides were placed onto a translation stage movable in the x-, y- and z- axes, using micrometers. The laser beam was expanded initially using a Galilean beam expander and split through a 50/50 splitter so that a recording of the power could be taken with a power meter and the rest sent via an infrared (IR) optimised mirror to the trapping objective (Figure 4.2). An image of the trapped microsphere travelled back down the optical path of the trapping laser. This then passed through a beam splitter and was sent to the camera after passing through two filters (650 nm short-pass). A lens of 200 mm was used to focus the image onto the camera sensor. A high-speed DSi camera (Durham Smart Imaging, UK) built by Dr Christopher Saunter recorded the position of single trapped microspheres using centroids on the DSi smart GUI camera software with a centre-of-mass (CoM) algorithm on-camera. Microspheres were trapped and analysed using a 4.6 kHz camera frame rate for 1.5 min. A K-type thermocouple was used to record the ambient temperature of the samples, since it was impossible to directly measure the temperature of the protein samples as they were enclosed on the microscope slides, despite there being slight heating effects from the infrared laser which were minimal. On the DSI camera software, a tracking region was created for each trapped bead to give a threshold for the algorithm to record data. Pixels below a certain luminosity weren't included and those above were included. The 2 μm microspheres used were relatively uniform in size with the coefficient of variation being relatively low; 5% for sizes of 0.1 μm decreasing to 1% for 10-15 μm diameters, for Invitrogen Molecular Probes fluospheres. MATLAB R2007b (MathWorks, UK) was used to process the data retrieved from the position utilising scripts written by Scott Silburn (calculations in appendix). The output files were in the form of .csv, opened in Excel 2008 (Microsoft Corporation, US) and contained the X and Y frequency dependent viscosity values (Pa.s), which were then averaged and plotted against frequency (Hz). Initially calibration was required of the recording system to enable conversion of the data recorded in pixels to physical lengths. A microscope graticule (Agar Scientific, UK), with 100 x 0.01 mm divisions, was used and a still image captured with the 10 μm divisions. This was

put into ImageJ 1.43r (National Institutes of Health, USA) from which three separate rectangular selections were made, to give an average of the whole image, covering the whole length of the image to then derive a luminosity profile, from the Analyze > Plot Profile options. The luminosity profile was copied directly into Excel. A central difference was used upon the luminosity values, giving a chart plotted with pixels (x-axis) against central luminosity differences (y-axis), as the derivative of the profile plot. For the central luminosity differences, for each pixel the average luminosity was taken for the pixel values from the previous two to the two after. As an example, for pixel 2, the difference was calculated by subtracting the value for pixel 0 from the value for pixel 4 and divided by 4. The peaks on the chart were separated by 10 microns and thus the distance between the peaks gave the number of pixels per 10 microns. The distances were finally divided by 10 to get the conversion to pixels per μm, which were then used in MATLAB for data analysis. The bead diameter was calculated to be 9.5 +/- 0.02 pixels per μm, with the standard error representing the error for the top, middle and bottom of the graticule picture, from three independent luminosity charts. The trap stiffness (spring constant) from the laser was derived from three buffer only samples and this was then subtracted from subsequent analysed sample data in MATLAB.

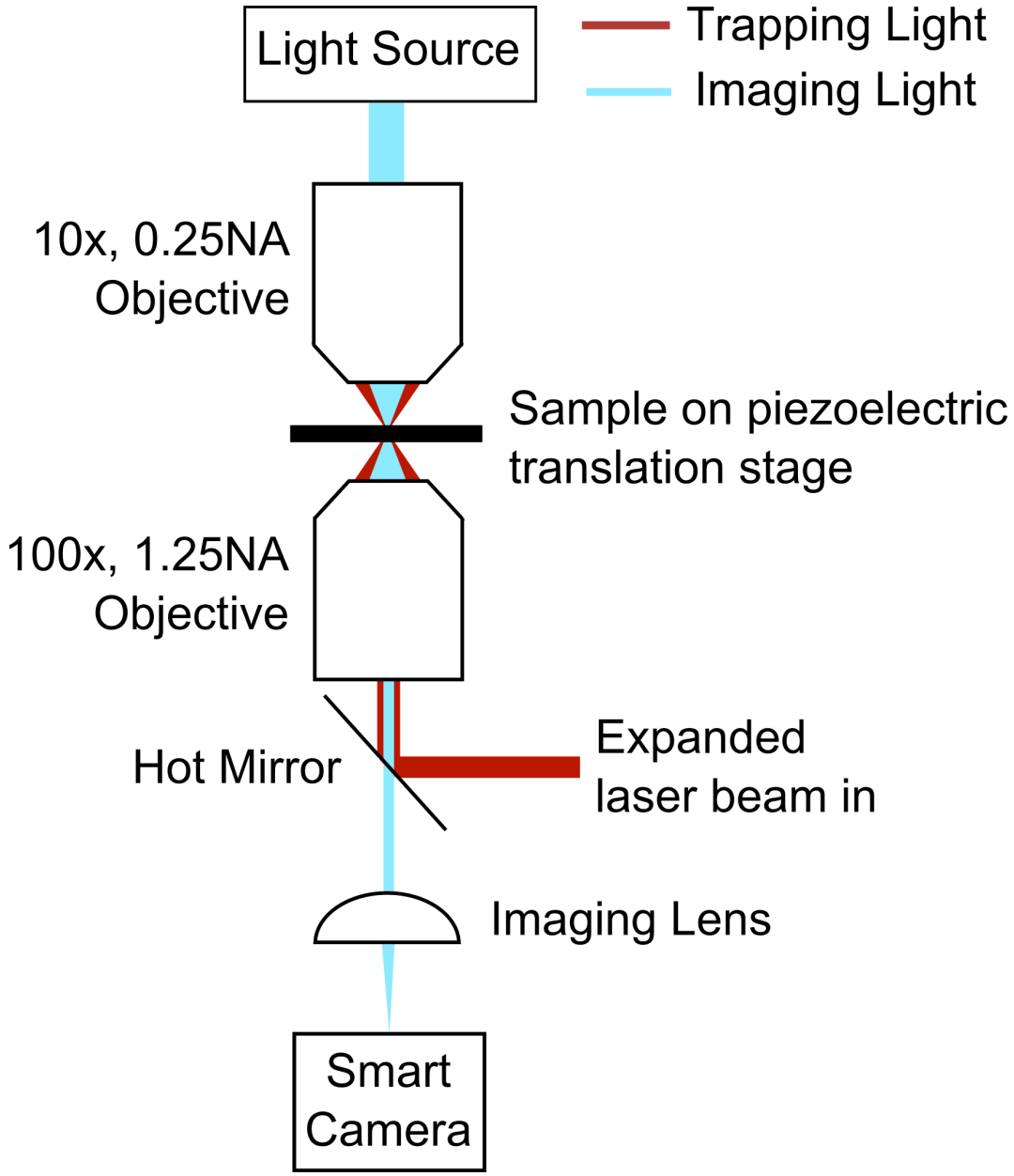

Figure 4.2 Optical tweezer set-up for single trap data.

Image kindly provided by Scott Silburn.

4.2.3 Data acquisition for passive viscosity measurements using 1064 and 808 nm single trap microrheology.

Experiments were carried out at the FOM Institute for Atomic and Molecular Physics (AMOLF), Amsterdam (NL).

Samples were placed in sample chambers prepared using a small glass microscope slide attached to a larger slide after melting parafilm strips between the two to hold them together to leave a gap for the sample, on a hot plate set to 50 ^{0}C with the use of tweezers to gently press the smaller glass slide against the larger slide to melt the parafilm. The samples were pipetted in the side after the chambers had cooled, drawn in by capillary action. Evaporation was prevented by sealing with a thin layer of vacuum grease from a syringe. Sample microscope slide chambers were analysed on an inverted Nikon Eclipse Ti microscope (Nikon, NL), which used two lasers of 808 and 1064 nm wavelengths, controlled by a custom-written programme in C++ of microRheology (version 1.0.4350.20571 copyright ©FOM AMOLF 2010, Amsterdam) and was used to optically trap microspheres in the filament samples. The samples were focused with a 100x oil-immersion objective lens (NA 1.4) (Nikon, NL). Objective oil was also used for the condenser, which was lowered on top of the chamber after the sample had been focused with the aid of a CoolSNAP HQ^{2} camera (Photometrics, AZ). A magnetic dichroic mirror was then placed above the condenser so as to divert the laser beams from the path of imaging. A laser detection card was used to check whether or not bubbles were present in the oil, which would distort the lasers and the bubbles were removed if necessary.

Back-focal-plane laser interferometry was used to detect the displacement intensity fluctuations of the microspheres from the focus of the sample plane and the data was recorded with a 100 kHz bandwidth with quadrant photodiodes (QPDs) used to record the thermal motion of the trapped microspheres; the oscillation of the drive laser was switched off for these passive measurements (Gittes F., 1998). The 1064 nm laser was set to 1 W (approximate power of 24 mW) and the 808 nm laser was set to 45 mW (approximate power of 20 mW). The acoustic optical deflector (AOD)-X was set to 30% and the AOD-Y was set to 100%. The cross-hair was assessed to see if the QPD detectors were saturated or not; if they were the lenses were adjusted to allow the laser spots to be centered if they deviated from the centre of the traps. The position of the 1064 nm laser spot in relation to the 808 nm laser

spot could be moved using the cursor in the microRheology programme. Once beads were trapped, the camera and light box were switched off to reduce noise in the power spectrum at lower frequencies before measurements were recorded. Calibration was carried out for just buffer at a 10 μm distance from the coverslip surface, to avoid surface effects. Separate power spectral densities were recorded and fit with a Lorentzian in the microRheology programme. The corner frequency was used to derive the trap stiffness (N/m) and displacement (μm/V) values from 10 independent measurements of 7MS of data for individually trapped microspheres in both the 808 and 1064 nm lasers for buffer, which were averaged and used to derive the real shear (*G'*) and imaginary loss (*G''*) moduli from the samples in the microRheology programme. For the buffer calibration values, a Lorentzian graph for each separate file and laser trap was fit using the two graph-cursors available in the programme to derive the trap stiffness and displacement. The output data were plotted in Excel, averaging the parallel (para-) direction values that contained less noise for *G'* and *G''*, against frequency (Hz). The calculations were the same as those used for the analysis of the single 1064 nm trap data in Durham based on the fluctuation-dissipation theorem (FDT), except the true values were used for Figure 4.7 and only the apparent in the generalised Stokes relation, to derive the *G'* values in Figure 4.8 (Atakhorrami et al., 2006). The elastic modulus was calculated from G_app by subtracting the apparent modulus in buffer thus compensating for the presence of the optical trap (Addas et al., 2004). The apparent *G'* values were used instead of the true values since the buffer initially appeared to have an unexpected high elastic response using just the true values in the generalised Stokes relation equation. The programme calculates the real ($\alpha'(f)$) and imaginary ($\alpha''(f)$) parts of the transfer function (apparent response) using the power spectral density, the fluctuations-dissipation theorem (FDT) and the Kramers-Kronig relation. The apparent responses ($\alpha'(f)$ and $\alpha''(f)$) are then used in the GSER to derive *G(f)* for the shear and loss moduli. *G''* sample was calculated as: *G''* apparent sample- solvent viscosity (2*Pi*frequency*viscosity of water at 21 ^{0}C).

The following conditions were present of: 1 W (24 mW) laser power for the 1064 nm laser, 45 mW (20mW) laser power for the 808 nm laser, QPD for the 1064 nm laser of Gain 1x and filter 100kHz, QPD for the 808 nm laser of Gain 1x and filter 100 kHz, 293.15 kelvin.

4.2.4 High speed sedimentation assays.

Sedimentation assays were carried out the same as in 2.1.2.12.

4.3 Results.

4.3.1 Single-trap microrheology.

R120G CRYAB gave such dramatic aggregation of desmin filaments that initially the viscosity appeared no different to buffer alone at a 1:1 molar ratio (Figure 4.5); the hypothesis is that the desmin filaments clumped together leaving large spaces in which the beads were trapped giving the same viscosity as buffer. Thus lower ratios of desmin: heat shock protein were used and it was found that a 1:0.2 molar ratio of desmin: R120G CRYAB gave an increase, likely due to the ability to position the beads next to the filament networks. However at the same ratio, WT CRYAB had lost its ability to chaperone the desmin filaments and only until a ratio of 1:1 was used was there a decrease in viscosity observed from desmin alone, due likely to an increase in mesh pore size (Figure 4.6). As biochemical evidence for R120G CRYAB having increased interactions with desmin filaments, assembly in HEPES buffers as in 3.1.3.3 at pH 7.3 was carried out showing greater binding for R120G CRYAB to desmin filaments compared to WT CRYAB; compare Figure 4.3 to 3.23. WT CRYAB acts as a stealth protein in reducing filament-filament interactions as seen by a reduction in viscosity of desmin solutions (Figure 4.6).

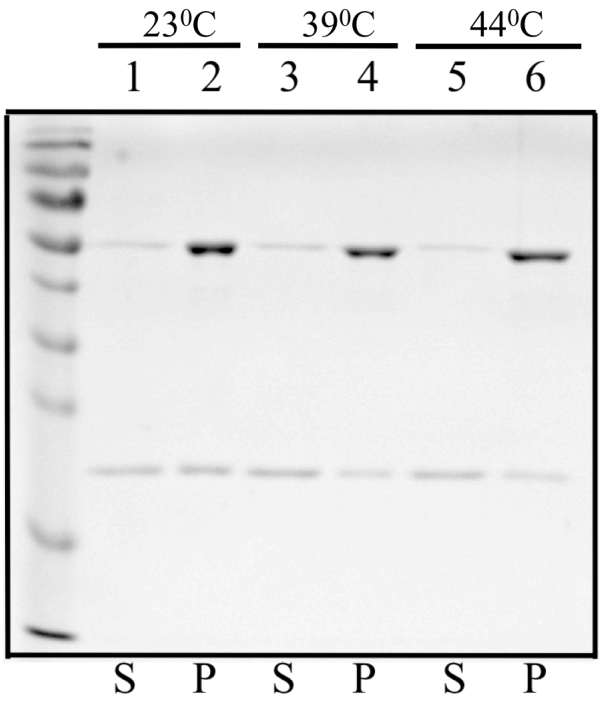

Figure 4.3 Binding of R120G CRYAB to desmin IFs at pH 7.3 is temperature dependent and greater compared to WT CRYAB.

High speed sedimentation assays were carried out on WT desmin and R120G CRYAB samples assembled through HEPES buffers at pH 7.3. A clear increase in co-pelleting of R120G CRYAB can be seen with desmin compared to WT CRYAB at the same pH, c.f. Figure 3.23 A).

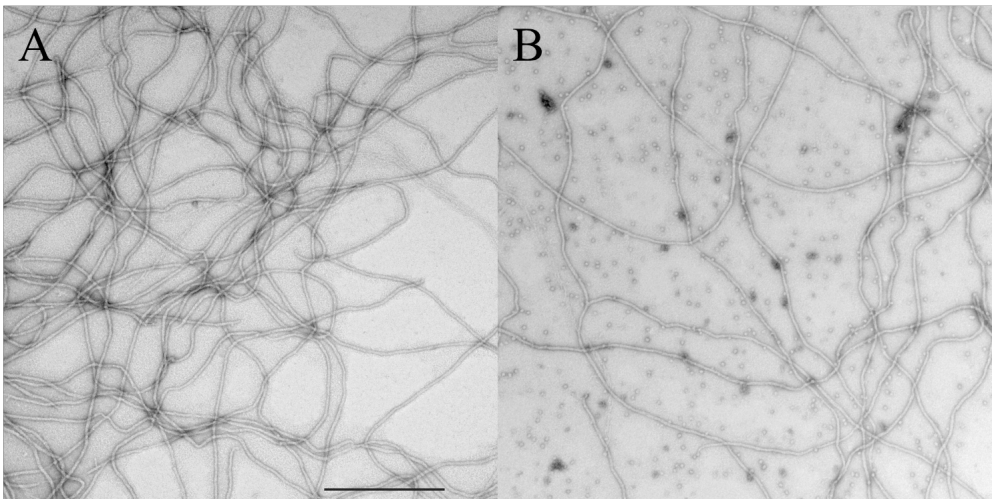

Figure 4.4 Desmin filament morphology in the absence and presence of WT CRYAB.

Desmin filaments were assembled according to Figure 4.1 of A) WT desmin alone and B) WT desmin with WT CRYAB in a 1:1 molar ratio. The scale bar is equal to 500 nm.

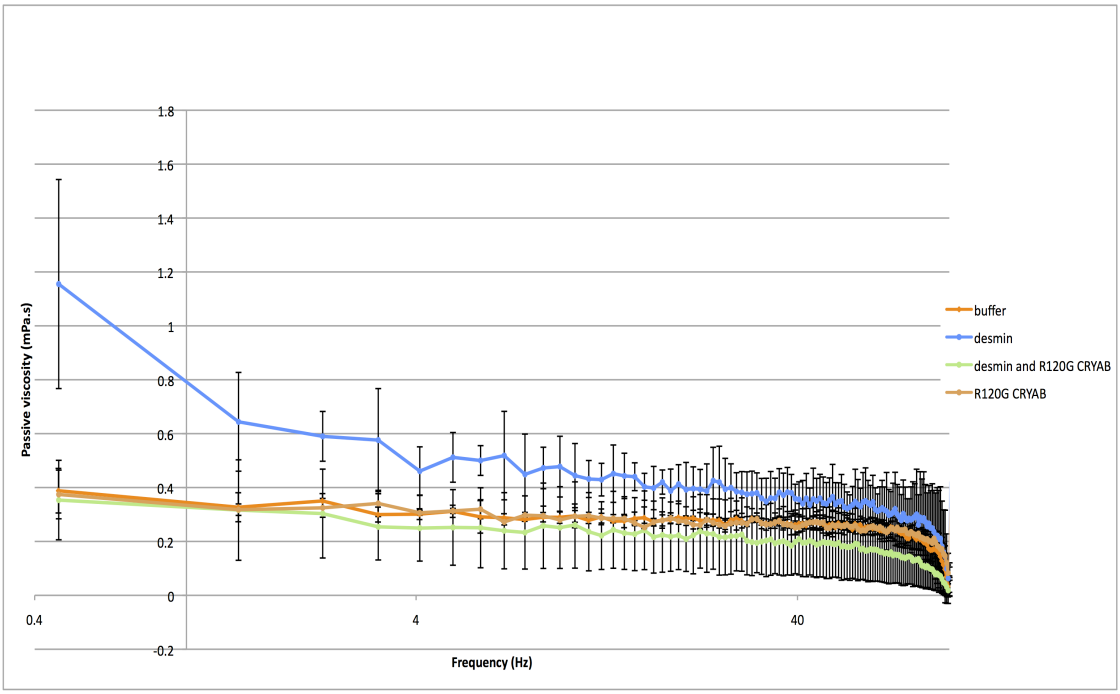

Figure 4.5 A 1:1 molar ratio of WT desmin: R120G mutant CRYAB gives a similar passive frequency-dependent viscosity as buffer from single-trap microrheology.

Averages from three independently trapped beads were taken and error bars are shown as +/- one SD. Desmin has a higher frequency-dependent viscosity than buffer as expected. However using the 1:1 molar ratio of desmin: R120G CRYAB used here, the frequency-dependent viscosity is the same as buffer. Honey, buffer and water are purely viscous solutions whereas desmin is a complex solution that has varying viscosity dependent upon the stress applied. Honey has a higher viscosity than water and also desmin filaments.

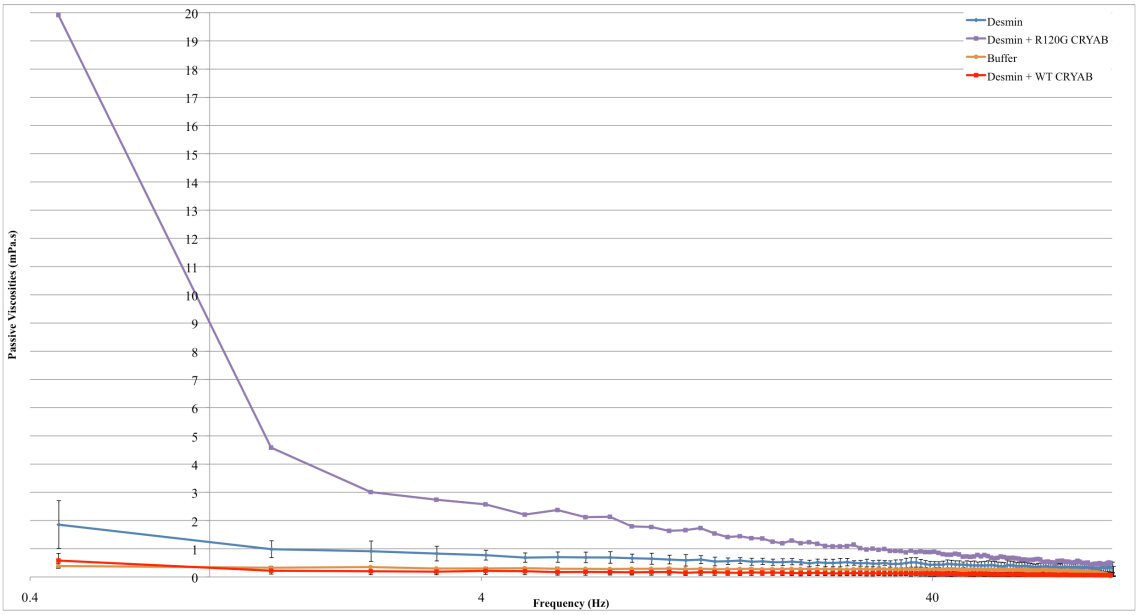

Figure 4.6 WT CRYAB has the ability to reduce the frequency-dependent passive viscosity of desmin filament networks, whereas the R120G mutant increases filament bundling and viscosity.

Microspheres were trapped and their natural thermal motion recorded for 1.5 min at 4.6 kHz in a 1064 nm laser. All data are the average of 3 (buffer), 3 (desmin) and 5 (desmin + WT CRYAB) independently trapped microspheres apart from the sample of desmin and R120G CRYAB (1:0.2 molar ratio), which is the average of 2 microspheres. Error bars are +/- 1 SD.

4.3.2 Two particle- single-trap microrheology (AMOLF).

The elastic, shear moduli data were averaged from at least 5 independent beads per sample. The parallel (para-) directions were taken in most cases, excluding the perpendicular (perp-) values, as these generally have less noise.

1064 nm		808 nm	
Displacement (μm/v)	Trap stiffness (N/m)	Displacement (μm/v)	Trap stiffness (N/m)
X 0.771228	2.60364E-05	X 0.398946	7.52E-05
Y 0.769733		Y 0.5078	

Table 4.1 **Calibration results for two-particle single tracking used in the analysis of samples for which the microRheology programme calculated the real and imaginary modulus values from the true responses**.

An average of 10 beads were taken to derive the calibration values for sample analysis.

1064 nm		808 nm	
Displacement (μm/v)	Trap stiffness (N/m)	Displacement (μm/v)	Trap stiffness (N/m)
X 0.741816667	2.23967E-05	X 0.43502	6.80E-05
Y 0.873783		Y 0.42802	

Table 4.2 **Calibration results for two-particle single tracking used in the analysis of samples where the modulus real and imaginary values were calculated from the apparent response functions**.

An average of 5 beads were taken to derive the calibration values for the 1064 nm laser and 10 for the 808 nm laser.

A small elastic response difference was detected for 1 mg/mL desmin when WT CRYAB had been added at a 1:10 molar ratio, shown in Figure 4.8, from the 808 nm laser trap. However the *G''* values were no different, shown in the frequency range of 0.1 - 100 Hz in Figure A.4, since negative values were obtained for desmin. The data from the 1064 nm laser were negative for both desmin and desmin + WT CRYAB for *G'* values.

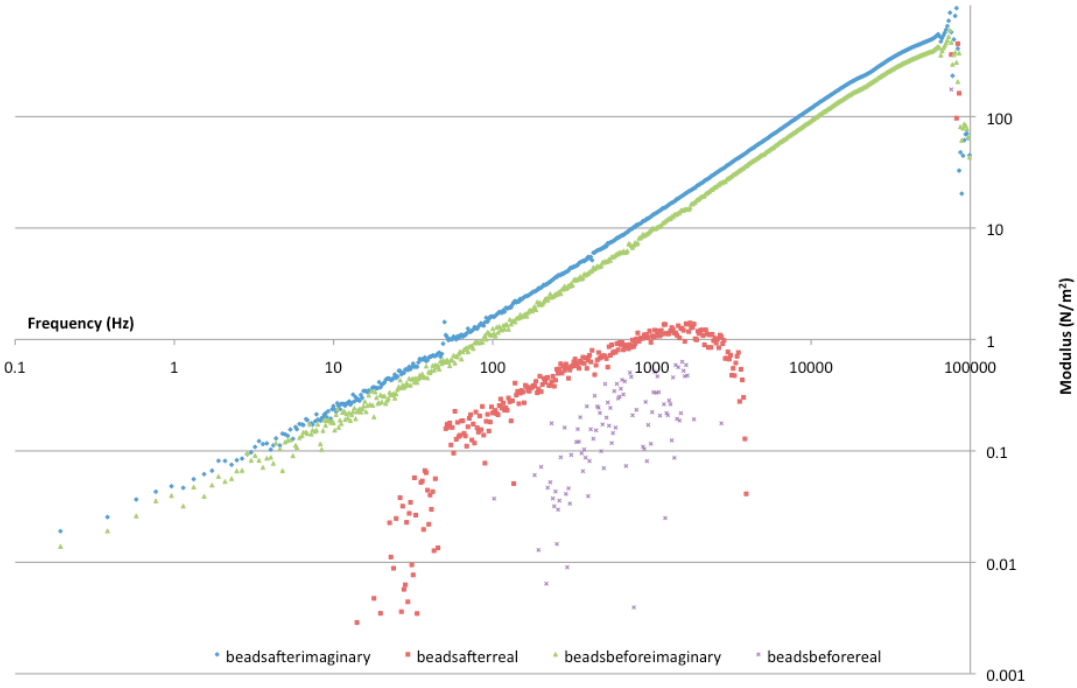

Figure 4.7 No great difference is observed in the *G'* and *G''* moduli of desmin filaments assembled with microsphere addition before and after the final assembly step.

G' and *G''* derived from the true responses, of 1 mg/mL desmin measured from 5 independently trapped beads in the 1064 nm laser are plotted as averages with beads added before and after the final assembly step. More of a viscous component (imaginary) can be seen compared to an elastic response (real). Line colours; beads added after the final assembly buffer: blue = *G''* and red = *G'*; beads added before the final assembly buffer; green = *G''* and purple = *G'*.

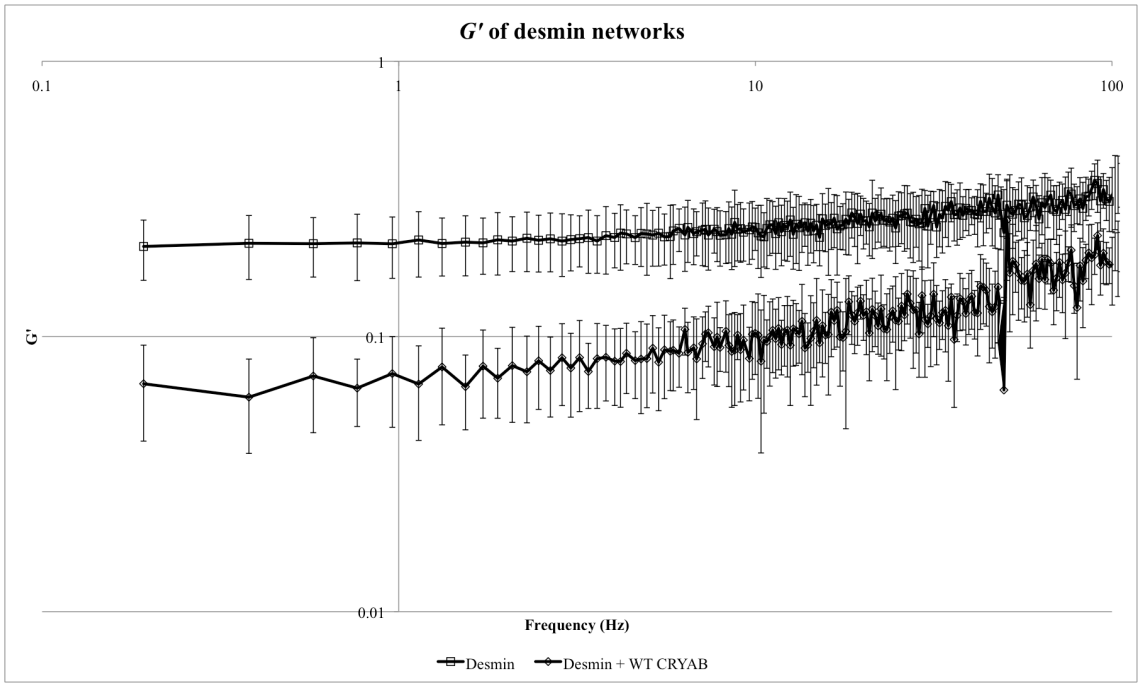

Figure 4.8 WT CRYAB in a 10-fold molar excess to desmin reduces the elastic response of desmin networks.

Microspheres were trapped in an 808 nm laser trap and their motion was recorded; 5 beads were analysed for 1 mg/mL desmin and 10 for 1 mg/mL desmin + 3.7 mg/mL WT CRYAB. Sample files were analysed in the microRheology programme and the apparent real and imaginary responses used to calculate *G',* which is plotted against frequency. Error bars represent +/- 1 SD. WT CRYAB can be seen to reduce the apparent *G'* of the desmin networks.

4.4 Discussion.

The advantage of passive microrheology is that it is a valid tool for observing the mechanical properties of an equilibrium system in a non-invasive way since there is no need to strain the system to measure local viscoelastic properties. Sedimentation assays will potentially shift the equilibrium of protein assembly, balanced between disassembled and assembled filaments, to more disassembled filaments than would be seen with filaments *in vivo*. Therefore microrheology is a preferred method for assessing filament interactions, as the trapping of microspheres will not affect the equilibrium. Microrheology also is advantageous as it measures local responses instead of taking an average of the viscoelastic properties, which is the case for DWS and this is especially essential for the desmin and R120G CRYAB samples in this chapter where filaments are entangled and thus the passive viscosity measurements that give higher values are found close to the filament networks and if an average was taken as with DWS, such a difference in the frequency-dependent passive viscosity might not be seen. Microrheology is useful for studying the interactions of CRYAB with filament networks since the usual method for assessing interactions has been high and low speed sedimentation assays, which have a disadvantage in that they are assessing protein interactions in a non-equilibrium system. The fact that CRYAB can reduce the elasticity of desmin networks shows that it may be influencing the structures of the filaments and not just the network mesh pore size as shown by a reduction in passive viscosity. However it can't be seen just from microrheology whether the reduction in elasticity is due to effects at the filament or network level. When low speed sedimentation assays have been showing reductions in filament-filament interactions such as for desmin in Figure 2.21 and R239H GFAP in Figure 2.18, this has been due to a reduction in the elastic response and viscosity of the networks from CRYAB. The elasticity is a reflection on the bending, sliding and potential breaking of the filaments in response to deformation and when it has been lowered due to WT CRYAB this may mean the filaments are more dynamic and flexible. Divalent cations are highly important for IF assembly, as demonstrated in chapter 3 with impaired GFAP filament elongation and compaction in their absence. It has been demonstrated that divalent cation cross-linking influences the elastic behaviour of vimentin filaments and thus desmin and they act as effective molecular cross-links similar in action to the F-actin network molecular cross-links

(Lin et al., 2010a). Therefore divalent cations are crucial for the *G'* values observed here. Divalent cations act to mediate attractive interactions between negatively charged side arms of IFs and this cross-linking will contribute to the observed *G'* values (Lin et al., 2010b).

To answer the question of how CRYAB reduces elasticity of desmin networks, rheology will need to be complemented with other information such as thermal fluctuation of individual filaments which could provide information on the mesh pore size in the presence and absence of CRYAB (Koster et al., 2010, Noding and Koster, 2012). Additionally, beads that are smaller than the network pore size could be used, as these should not get trapped in the meshwork and the use of mean square displacements (MSDs) could derive the mesh size (Koster et al., 2010).

Despite a clear reduction in the *G'* of the desmin filament networks from the presence of WT CRYAB, no difference was observed in the *G''* values and in fact the values were negative from the data analysis and so could not be used.

Chapter 5; Final discussion and future directions.

5.1 Main results.

With AxD and cardiomyopathy, CRYAB-IF interactions are increased and thus their interactions have been studied in this thesis to assess any potential functional interactions. The main conclusions from this thesis are outlined within Table 5.1. They demonstrate that desmin-CRYAB interactions are functional since CRYAB binds to desmin the most out of all three type III IFs studied here and CRYAB is able to alter the biomechanical properties of desmin filaments, shown by a reduction in the plastic modulus. R120G mutant CRYAB causes cardiomyopathy and has increased interactions with desmin filaments and since it was shown that it increases the viscosity of the filaments compared to WT CRYAB, this shows that the mutant CRYAB is affecting the way the filament networks are interacting. CRYAB also interacts with GFAP, relevant for AxD and was shown to have increased binding to AxD mutants compared to WT CRYAB. Two main mutations were studied of R239H and R79C and CRYAB was shown to reduce R239H filament-filament interactions despite the formation of aggregates and also have a slight inhibitory effect upon WT GFAP filament formation. The dominant nature of the R79C and R239H mutants was investigated by assembling varying percentages of the mutants with WT GFAP. R239H had a dominant effect at a 50% level from low speed sedimentation assays in comparison to R416W with effects only seen at a 100% level under the conditions of assembly used. Both the R239H and R79C mutants are predicted to disrupt the ionic interactions within the dimers thus disrupting assembly that will lead to an increase in exposed surfaces for interaction with CRYAB and also explain the disruption of WT GFAP filaments when co-assembled with the mutants. R239H also appeared to bind much more CRYAB than R416W thus highlighting the greater severity of the R239H mutant compared to R416W. Temperature was shown to influence the CRYAB-filament interactions as higher temperatures promoted increased binding of CRYAB to the filaments, also likely due to potential unfolding of the IFs. As well as mutation of IFs, the influence of divalent cations on IF assembly was studied. Manganese ions were shown to increase the filament-filament interactions of GFAP and desmin and result in dimer formation. GFAP is compromised the most by alterations in its assembly environment as it was shown to form thicker filaments in the presence of manganese,

absence of divalent cations, low pH and 5 mM calcium. CRYAB interactions were investigated in all conditions apart from 5 mM calcium and these conditions led to much greater binding of CRYAB compared to assembly conditions with 1 mM magnesium ions and pH 7.4. Desmin however was found to bind the most to CRYAB and it was shown for all three IFs that low pH results in increased interactions and higher temperatures also promote greater interactions. High temperature and low pH usually shift protein assembly to more disassembled states and thus it's likely that the IFs become more destabilised leading to increased interactions with CRYAB. These experiments are important as they show that the interaction between desmin and CRYAB is functional and thus predisposes to disease with the R120G mutation in myocytes. The widths of the CRYAB oligomers were measured and found to be wider at pH 6.3 compared to 6.8 and 7.3 that may be a reflection on a shift to CRYAB monomers that are known to have higher affinity for client proteins. Wider GFAP and desmin filaments were also observed at pH 6.3 compared to the higher pH values thus demonstrating how pH can disrupt filament interactions. Importantly a difference was observed in the amount of binding of CRYAB to GFAP filaments dependent upon the assembly stage it was added, showing that with CRYAB present throughout the whole of filament assembly there is much greater binding compared to when CRYAB is added to formed filaments.

Chapter 2				
Structure	**Mutant**	**AxD phenotype**	**Location in coiled-coils**	**Morphology**
	R79C	I and J	Position g	ULF lengths
	R239H	I	Position e	Aggregates of ULF lengths
	R416W	I, J and A	Random coil (RDGE motif)	Aggregates of short filaments
CRYAB-IF interactions	**TEM and sedimentation data**			
	Interactions greatest with the R239H mutant GFAP			
Chapter 3				
	Morphology of IFs	**Widths of CRYAB**	**Interactions of CRYAB-IFs**	**Effects of increased temperature**
pH 6.3	GFAP widths are greater and more variable	More variable and wider than pH 6.8 and 7.3	Greater binding to all IFs; especially desmin. Repeat distance on vimentin is regular (20 nm) between 2 filaments	Increased temperature increases the binding of CRYAB to IFs (also for pH 6.8 and 7.3)
Chapter 4	WT CRYAB reduces the plastic modulus and viscosity of desmin filaments and R120G mutant CRYAB increases the viscosity			

Table 5.1 Summary table of main results.

I = infantile, J = juvenile and A = adult.

5.2 Mutants of GFAP and interactions with CRYAB.

GFAP mutation is linked to AxD and it was shown in chapter 2 that the R239H mutant has a much greater association with CRYAB compared to WT, R79C and R416W GFAP, as observed from high speed sedimentation assays. This links in with the discovery that Rosenthal fibres contain aggregates of mutated GFAP alongside p62, HSP27 and CRYAB and thus CRYAB is sequestered to the aggregated filaments (Der Perng et al., 2006). In addition the amino acid sequence of an IF is crucial for normal assembly and when mutated in the case of AxD the filaments are no longer normal, as demonstrated in chapter 2 by shortened ULF-like filaments of 60-100 nm in length for both the R79C and R239H mutants with the latter leading to aggregates, as with R416W. Type III IFs assemble with the formation of ULFs initially and then the longitudinal annealing and compaction of these and therefore the two mutants studied here appear to have a halted assembly before the annealing step (Parry and Steinert, 1995). Removal of crucial residues can also disrupt assembly such as removal of the head domain in GFAP, which always leads to disrupted filaments showing that the entire head domain is needed for efficient assembly, also removal of the entire tail domain results in aggregate formation when no other filament network is present, which is recovered to normal filaments if in the presence of vimentin (Chen and Liem, 1994). Removal of the initial half of the RP-box in the head domain of GFAP also leads to shortened filaments (Ralton et al., 1994). Shown in chapter 2, the R239H mutant which is correlated only with infantile cases of AxD was more severe in terms of its dominant effect over WT filament formation and increased binding with CRYAB compared to R416W which is associated with infantile, juvenile and adult onset cases of AxD (Kinoshita et al., 2003). R416 is located at the beginning of the RDGE motif, conserved in all type III IFs, in the tail domain and the R239 site is situated in the 2A rod domain (Chen and Liem, 1994). It will be a combination of the location and also the type of amino acid (either basic histidine or neutral tryptophan), which leads to differences in the aggregates and severity of the disease. Since the entire tail domain can be removed and filaments can still form if in the presence of vimentin whereas the head domain is necessary for filament formation, this demonstrates that the head domain is more crucial for assembly than the tail region. Histidine is more prone to charge change at the pH of assembly since one of the side chains has a pK

close to pH 7 and therefore a negative charge will result at pH 7.3 for this group, which is unlike arginine that will be more positively charged since it is a basic amino acid with a side group that has a much higher pK. The amino acid position of 239 is also in position e of the heptad repeat in the coiled coil responsible for inter-ionic interactions and therefore mutation will disrupt how neighbouring monomers interact and the formation of dimers and this may be why the R239H is more severe than R416W since the RDGE motif of GFAP has been proposed to not be sufficient alone for GFAP assembly, demonstrated when amino acids were deleted between the end of the rod 2B domain and the start of the RDGE sequence, whereas with desmin the RDGE motif is sufficient (Chen and Liem, 1994). R79 mutations (in the LNDR motif of rod 1A also in a crucial position for inter-ionic interactions at position g in the heptad repeat) have been correlated with less severe phenotypes than the R239 mutations and the R239H has a more severe clinical course than the R239C mutation phenotypes (Rodriguez et al., 2001, Smith et al., 2002). The heptad assignment of coiled coils is derived from the research of David Parry and is demonstrated in Figure 2.32 (Parry, 1982). The LNDR motif is crucial for normal functioning of many IFs since mutations have been linked to diseases other than AxD, such as skin blistering with type I keratins (Yamanishi et al., 1994). The arginine to cysteine mutation in the LNDR motif also appears to occur at a relatively high frequency in diseases (Pittenger et al., 2007). As well as the GFAP R79C mutant, BFSP2 also has a cysteine replacing an arginine residue within the LNDR motif (LGGC), unique to IFs, however this is present normally in the sequence and it has been shown with K18 that if two glycines are present alongside the cysteine, filament assembly is restored whereas if only LNDC is present the filaments are perturbed, as seen in this instance with R79C GFAP (Pittenger et al., 2007).

It was demonstrated in chapter 2 that the R79C mutant binds less to CRYAB than the R239H and R416W mutants and has a dominant effect upon filament morphology at a 50% level, as opposed to R239H that is dominant at a 10% level, thus demonstrating its less severe phenotype.

CRYAB was shown to influence filament-filament interactions and could reduce the propensity for the R239H mutant GFAP shortened filaments to associate, observed with $p<0.05$. CRYAB didn't have any affect on WT or the R79C mutant quantities in the pellet fractions at low speed, perhaps a reflection on WT GFAP filaments that do not need any alteration of filament-filament interactions and also R79C that is

predominantly soluble and has low interactions already. CRYAB interactions influencing filament behaviour are dependent upon the buffer environment, demonstrated from the apparent increase in WT GFAP filament-filament interactions from imidazole assembly when CRYAB was present compared to its absence with a p value of 0.05, which is in contrast to assembly through Tris where levels of GFAP are unchanged with the addition of CRYAB after low speed centrfiguation. Therefore pH and ionic strength are factors that influence these interactions. The buffer conditions also influence filament-filament interactions in the absence of CRYAB as discussed in the next section and demonstrated with R416W and WT GFAP mixtures. Ionic strength is crucial for IF assembly and it requires monovalent cations for type III IFs, alongside divalent cations for GFAP. When ions are removed the IFs do not form long filaments but instead assembly is halted at the elongation step and most of the species are dimers, tetramers and a few higher order oligomers (Kooijman et al., 1995).

CRYAB was also shown to have a slight inhibition on WT GFAP filament formation in section 2.1.3.3, observed by an increase in non-pelleted GFAP in its presence. This has been shown before with phosphorylated CRYAB and bovine GFAP, however with these the inhibition was much greater as no filaments were observed whereas in this thesis filaments are still present but there has been an increase in the soluble portion of GFAP, likely due to modifications of the proteins that are absent in this thesis (Nicholl and Quinlan, 1994).

Three different temperatures of assembly were used in chapter 2 assessing the interactions between CRYAB and the different mutants of GFAP. R239H bound the most to CRYAB and for all of the mutants including WT GFAP there was an increase in interactions with increased temperature. However this could not be attributed solely to a temperature-dependent effect since the pH of the Tris buffers changed with temperature, therefore the next section discusses the findings from experiments that investigated the temperature and pH-dependent effects of CRYAB-GFAP interactions.

The morphology of the R239H mutant GFAP and the fact that it has the greatest interactions with CRYAB demonstrate how it is associated with the most severe phenotype of AxD. AxD is the direct result of GFAP mutations and it is likely that CRYAB is acting to reduce the increased interactions between the altered filaments. Importantly one of the main functional roles of CRYAB in the disease is to reverse

the inhibition of proteasome activity from the GFAP mutants (Tang et al., 2010). By interacting directly with the filaments, CRYAB also reduces the sizes of aggregate oligomers (Figure 2.15) and can result in smaller GFAP oligomers alongside monomers, which are believed to occur alongside proteasome re-activation (Tang et al., 2010).

5.3 Divalent metal ions, pH and temperature influences on IFs and interactions with CRYAB.

The removal of divalent metal ions from GFAP assembly was assessed in chapter 3 since divalent cations are crucial for GFAP assembly and it was demonstrated previously that bovine GFAP forms rod structures without divalent cations (Tanaka et al., 1989). Divalent metal ions also impart IFs with elasticity, acting as effective molecular cross-linkers and thus the *G'* of desmin networks could be assessed in chapter 4 (Lin et al., 2010b). However the elasticity will not only be due to bending of the filaments in response to deformation but also rearrangement since the cross-links won't be as strong as for instance avidin with actin filaments which have almost covalent bonds with the filaments (Wachsstock et al., 1994).

Human GFAP was shown to form shortened (approx. 300 nm), wider (approx. over 20 nm) filaments that were longer than ULFs in the absence of divalent metal ions and had an altered appearance with greater filament-filament interactions and thus unlike the mutants of R79C and R239H assembled with divalent cations which had ULF lengths, these structures annealed longitudinally past the ULF stage but not as much as WT filaments. When higher concentrations of ions were used such as with 5 mM Ca^{2+}, much thicker filaments were observed and this will be because the positive ions attract the negative amino acids of the IFs and lead to bundling of parallel fibres, which has been correlated with increased stability of networks (Wen and Tang, 2006, Shaw and Hou, 1990). The increased widths in filament morphology in manganese ions were absent for vimentin and desmin filaments and will likely be due to the fact that astrocytes, the predominant site of GFAP expression, are the main stores of manganese ions and thus GFAP is more receptive to alterations in its concentrations (Agustina Alaimo, 2011). Divalent cations are also stronger at promoting assembly of GFAP than monovalent ions, which is a

reflection on their different sites of binding to the filaments (Yang and Babitch, 1988).

The absence of divalent cations results in increased associations with CRYAB and is likely due to a similar mechanism as seen with R239H whereby the aggregates likely have increased hydrophobic sites leading to increased CRYAB-filament interactions. Also, manganese ions result in increased interactions of desmin, GFAP and vimentin with CRYAB. The increased filament associations are also supported by the oxidative dimer formed for GFAP. Divalent metal ions are important since alterations in the concentrations of different metal ions have been associated with various disease states, such as AD and PD and since alterations in morphology of filaments and interactions with CRYAB have been observed *in vitro*, the divalent cations likely contribute to what is seen *in vivo*, such as co-localisation to amyloid fibrils alongside increased expression of CRYAB in AD (Shammas et al., 2011). Copper levels have been found reduced and iron levels increased in the amygdala of AD brains, but manganese ions remain unaltered (Akatsu et al., 2012). Perhaps in desminopathies and AxD there is a sequestering of manganese ions to the muscle fibres and astrocytes resulting in greater associations between CRYAB and the IFs, although increased levels of manganese have not been reported.

GFAP filaments were much more susceptible to assembly changes than vimentin and desmin, as shown from assembly in manganese ions and also 5 mM Ca^{2+} ions, which both resulted in thicker filament widths. This highlights how the three IFs have very distinct properties and in addition, adding to the discussion below, at the lower pH of 6.3 where increased interactions of CRYAB with IFs is observed there is also an observed alteration in the filament morphology of GFAP which also appears much thicker (Figure 3.28). Only in 5 mM Ca^{2+} ions was the full-length GFAP filaments seen despite wider filaments in contrast to the other conditions mentioned, also resulting in thicker filaments, where the filaments were shorter in length. This shows that elongation is halted from manganese, a lack of divalent cations and a drop in pH whereas the 5 mM calcium ions do not appear to impede elongation despite hindering filament compaction. In addition, CRYAB binding to vimentin and GFAP was assessed in the presence of 1 mM manganese ions at pH 6.9 and was shown to be significantly greater, for vimentin and GFAP, than the binding seen in the presence of magnesium ions at pH 6.8 (Table 3.5 and A.11 and A.14). The fact that binding was greater at the higher pH also supports the fact that the manganese ions

promote increased CRYAB-filament associations, since usually greater interactions are seen at lower pH values (section 3.1.3.3) and if experiments had been carried out at pH 6.8 with manganese ions then there would have likely been a greater difference observed.

Filament bundling has been observed previously with 5 mM calcium ions and appears to occur with manganese ions observed by an increase in side-by-side interactions (Figure 3.5 B)) however CRYAB was able to reduce some of the increased interactions, observed from low speed sedimentation assays (Figure 3.8 A)), which is supported by the finding that CRYAB has been shown to debundle IFs and inhibit aggregate formation whilst not altering filament lengths (Head et al., 2000, Perng et al., 1999a, Yang and Babitch, 1988). The ability to debundle IFs appears to be affected by the local pH since the IFs had fewer interactions, assessed from low speed sedimentation assays, at the higher pH values (Figure 3.24). Additionally the ability for CRYAB to inhibit GFAP IF formation is favoured at the higher pH values (Figure 3.23 B)). CRYAB has been shown to be able to inhibit IF formation but appears to act to stabilise microtubules especially promoting mitosis and nucleation and plays a crucial role in preventing disorganisation of actin filaments upon heat stress by increasing its associations, which are believed to aid in prevention of heart failure, where actin filaments are found to have degenerated that precede changes in polymerisation of actin fibres (Nishida et al., 1987, Xi et al., 2006). Thus it is likely that the increased affinity of CRYAB for IFs upon heat stress and lowered pH plays a functional role in keeping the cells in a normal physiological state and aids in prevention of disease (Singh et al., 2007).

Outlining the importance of the ionic environment for filament formation, it was shown in chapter 2 that imidazole buffer resulted in GFAP filaments with much greater interactions than those assembled in Tris buffer. This was demonstrated from low speed sedimentation assays where most of the GFAP was pelleted and also from high speed sedimentation assays whereby CRYAB didn't have the same inhibitory effect upon WT GFAP formation as it did in Tris buffer. This will also likely account for the increased effect of the R416W mutant over WT protein observed previously in the laboratory after an imidazole assembly at a 25% level whereas when Tris assembly was used the dominant effect was not seen even at a 50% level by low speed sedimentation, however the dominant effect was seen using the TEM (Der Perng et al., 2006). Additionally there appears to be a theme throughout with

CRYAB binding, as the imidazole buffer demonstrated with increased interactions of CRYAB with GFAP compared to Tris buffer and therefore it seems that increased ionic strength or changes in the divalent cation environment, leading to increased interactions between filaments, can lead to increased interactions between CRYAB and the filaments.

Type III IFs were studied, of vimentin, desmin and GFAP as they belong to the same group and evolved at a similar time, looking at interactions with CRYAB. Therefore any difference observed in interactions with the CRYAB is likely not going to be due to the general assembly mechanism of the filaments as they have the same method of assembly, but the variation in amino acid sequences. CRYAB mutation has only been linked to the disease of desminopathy and this highlights the importance of CRYAB-desmin interactions and also why desmin-CRYAB interactions are the most compared to GFAP and vimentin (Djabali et al., 1997).

Studies have previously investigated the binding of CRYAB to purified native desmin and actin filaments showing an increase in interactions between the filaments and the sHSP at lower pH and increased temperatures, however this is the first time that recombinant human desmin has been studied and compared to vimentin and GFAP (Bennardini et al., 1992). However similar binding patterns have been observed with increased interactions between the sHSP and IFs at the lower pH values and increased temperatures. At 39 and 44 ^{0}C at pH 6.3, more than 35% of the total CRYAB co-pelleted with GFAP and desmin filaments after high speed sedimentation and much less CRYAB was associated with vimentin (less than 30%). Desmin bound the most to CRYAB, likely a reflection on the fact that it has the highest hydrophobic profile out of the three IFs and reflects how desmin-CRYAB interactions are crucial for physiological states in muscles since myopathy is the result of either desmin or CRYAB mutations which result in desmin aggregates that associate with CRYAB (Maloyan et al., 2009). The pH will also influence how the magnesium divalent cations can bind to the IFs and thus will also contribute to altered structures of the filaments and partly explain why CRYAB binds with preference at the lower pH value of 6.3 (Ghalebani et al., 2012). When pH is lowered in muscle, sHSPs translocate to the Z-discs and this highlights therefore their crucial role in being targeted to desmin filaments (Golenhofen et al., 1998). Regarding structural changes in the CRYAB oligomers influenced by pH, at the lower pH values there is perhaps a preference for monomer formation as

demonstrated from experiments where the α-crystallin domain was isolated and assessed (Jehle et al., 2009). However it has also been reported that low pH acts to stabilise oligomers and they will likely cluster together to form large complexes, as demonstrated in Figure 5.1 (Liu et al., 2006). It is not currently known what the mechanism is of CRYAB dissociation and association in favoured environments for interacting with IFs. However it is likely that monomers are able to dissociate from the complexes as phosphorylated CRYAB has been found to consist of odd numbered units, which is in contrast to other HSPs such as HSP16.5, which consist of much greater units such as 24 in this case to retain the symmetry (Aquilina et al., 2004, Haslbeck et al., 2008). The Q151X, missing the C-terminal tail region, mutant CRYAB also supports the dissociation of dimers/monomers since TEM images revealed an absence of CRYAB particles highlighting how the oligomers are much smaller than WT CRYAB (Hayes et al., 2008). Additionally these smaller oligomers were more effective chaperones. Although the TEM images in chapter 3 show that the lower pH and increased temperatures result in increased clustering of WT CRYAB oligomers around the filaments, these have not been quantified and therefore future work would need to measure this to see if the number of CRYAB oligomers bound to filaments is increased at low pH. The C-terminal tail region in one monomer of CRYAB is able to dissociate from another monomer upon a drop in pH as shown in Figure 5.1, thus increasing potential hydrophobic substrate binding domains and explaining how CRYAB is able to increase its association with target proteins (Jehle et al., 2010). The C-terminal tail has been reported previously to be more flexible in αA-crystallin than CRYAB and is likely due to the fact that in the lens the chaperone complex needs to be soluble for longer due to lower rates of protein turnover, however this demonstrates the importance of the flexibility of the tail region in the chaperone's interactions (Lindner et al., 1998).

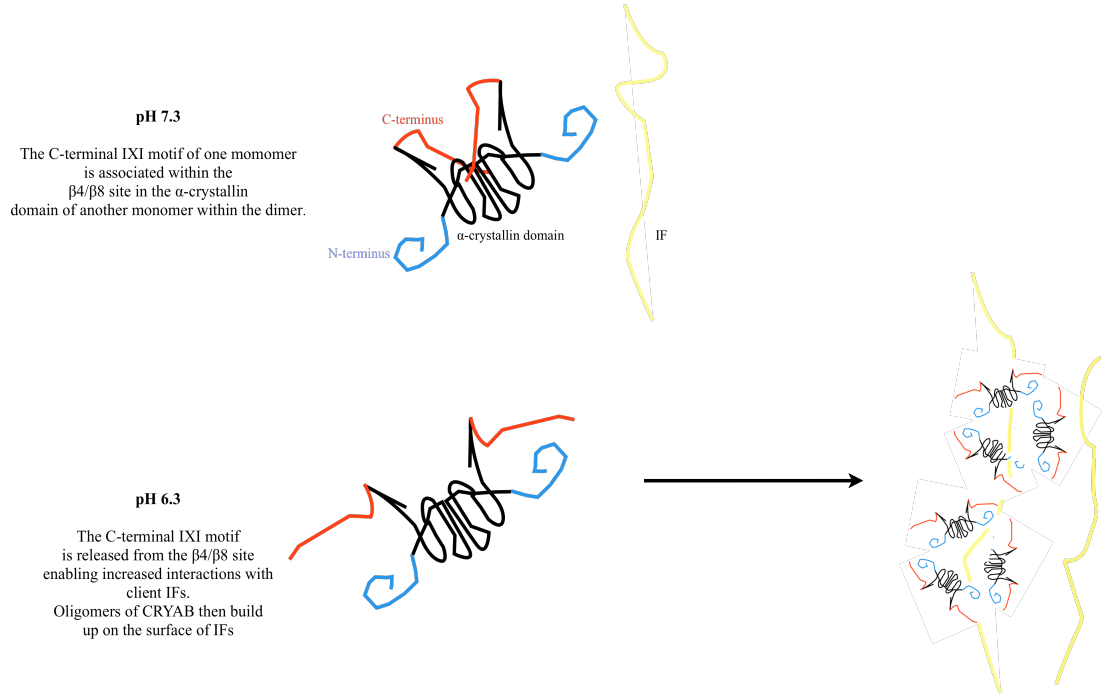

Figure 5.1 CRYAB-IF interactions influenced by pH.
The C-terminal tail from one monomer is released from the β4/β8 site within the other monomer, thus increasing target protein affinity (Jehle et al., 2010).

As well as pH influencing the interactions, increased temperature also promotes increased associations between the filaments and CRYAB. High temperatures increase the dynamics of CRYAB oligomers due to increased association and dissociation rates (Liu et al., 2006). It was also observed from alpha-crystallin complexes with ovotransferrin that increased temperatures increase the hydrophobicity of the protein complexes, likely explaining the increased associations between CRYAB and target substrates at higher temperatures (Lindner et al., 1998). Additionally higher temperatures reduce the critical concentration of divalent cations required for filament assembly (Chou et al., 1990).

Regarding the increased CRYAB interactions with IFs in different divalent cation environments, it is likely that structural changes are occurring for CRYAB as well as the filament surfaces.

CRYAB-IF interactions are important as CRYAB is able to influence the size of IF oligomers which can impact on proteasome function in AxD for instance and during stress there is a translocation of CRYAB to the insoluble formed IFs, from the soluble IF subunit pool, showing that the interactions are functional (Tang et al., 2010, Nicholl and Quinlan, 1994). The altered filament structures therefore from

higher temperatures and different divalent cations act as a cue for CRYAB to increase its interactions and alter the organisation of IF networks as seen *in vivo* whereby more diffuse networks are observed without an alteration in polymerisation state (Muchowski et al., 1999, Head et al., 2000). Increased temperatures and decreased pH act to shift the assembly equilibrium of proteins to disassembled states. Therefore the increased binding of CRYAB to the filaments under these conditions, as observed from sedimentation assays, may be due to increased interactions between the partially unfolded and soluble IFs rather than just the fully formed filaments. Mutations also result in disassembly of proteins in most cases and a similar reason for increased interactions with CRYAB will likely be occurring.

Mutations in CRYAB are associated with muscle myopathies and also cataracts, such as the R120G mutant, which hinders dimer formation since this residue is directly involved in monomer-monomer interactions (Sacconi et al., 2012). However no gliopathies associated with CRYAB have been found; the cataracts are likely the cause of aberrant interactions with BFSP1/2 and vimentin in addition to a loss of its ability to prevent apoptosis by protecting cytochrome c against oxidation within mitochondria (McGreal et al., 2012). The R120G mutation results in desmin aggregates within muscles of affected patients and also vimentin aggregation alongside increased binding of vimentin to CRYAB within the lenses of mouse knock-in models thus showing that vimentin-CRYAB interactions are also important (Andley et al., 2011). It has been noted that the R120G mutation likely favours monomer formation and this correlates with increased binding to desmin and vimentin filaments and the potential pattern of monomer preference for increased interactions of CRYAB with filaments has also been demonstrated in chapter 3 at the lower pH values, which also will perhaps promote monomer formation (Clark et al., 2011, Andley et al., 2011). The R120G mutant also forms larger complexes than WT CRYAB demonstrating a bigger quaternary structure (Perng et al., 1999b). It has also been shown that the R120G mutant CRYAB is partially unfolded which leads to decreased subunit exchange and stability (Liang and Liu, 2006). Therefore the increased interactions of the mutant will be due to altered oligomer sizes and also partial unfolding. The altered oligomer size will be due to a change in the equilibrium of dissociation, likely contributed to by a time-dependent truncation of the C-terminus, which has been implicated in the process of subunit exchange in CRYAB (Aquilina et al., 2005). However it was reported that the decrease in

subunit exchange as measured from FRET was not very much and is due to most of the C-terminus still being present (Liang and Liu, 2006). Terminally truncated αA-crystallin has been found associated with cataracts and the αA-crysallin$_{1-168}$ has been found only in the water-insoluble lens fraction, thus showing how the hydrophilic C-terminal tail is essential for normal functioning of this protein, which will also be the case for CRYAB (Aquilina et al., 2005). It was found that when CRYAB was present throughout GFAP assembly the interactions were increased compared to its addition after filament formation for pH 6.3 and 7.3 at 39 ^{0}C. This highlights how important the presenting filament surface is for mediating interactions with CRYAB and the difference will either be the result of a different filament surface mediated by the presence/absence of CRYAB and/or different interactions with the oligomer dependent on the stage of filament formation when the sHSP oligomer is present.

Developing on chapter 3 data, future work should investigate whether the altered GFAP filaments induced from a lack of magnesium ions can be promoted to form normal filaments if they are dialysed into a buffer with magnesium ions. It would also be important to see if chaperone proteins can actively re-fold these structures once CRYAB has bound to them, in the presence of ATP and magnesium ions. Experiments without CRYAB would also be carried out to assess how CRYAB aids in the re-folding process.

In chapter 3, the ability for GFAP filaments to revert to a different CRYAB binding preferential structure was assessed by assembling filaments at pH 6.3 where the greatest binding has been shown, dialysing into pH 7.3 where lower binding was observed and adding CRYAB from pH 7.3. This showed that low binding was present, however this could have been because the CRYAB was assembled at pH 7.3 and not 6.3, instead of the fact that the GFAP filament surface changed. GFAP should be assembled at pH 7.3 where low binding is observed, then dialysed into pH 6.3 and CRYAB from pH 6.3 added to see if the reverse can be observed with an increase in binding, although again the same issue of CRYAB having been assembled at the final pH will complicate the interpretation. A true test to eliminate whether the change in binding is due to the filament or CRYAB structure would involve adding CRYAB assembled at the first pH to the filaments, however this is limited by the experimental set-up since adding CRYAB to the latest pH buffer that GFAP is in could potentially change the CRYAB structure again. Therefore other methods are needed that analyse the surfaces of the CRYAB and GFAP filaments.

There are a few techniques that could be used such as measuring hydrophobicity with bis-ANS although as outlined before it is difficult to correlate hydrophobicity with chaperone activity, as other factors will also play a role (Kumar et al., 2005). Ideally NMR and crystallographic analyses would need to be carried out. Sedimentation velocity experiments on CRYAB assembled at pH 6.3 and 7.3 at 23, 39 and 44 ^{0}C would help understand how the oligomeric species might be changing responsible for the differences in interactions (Prabhu et al., 2012). Circular dichroism would aid in determining the secondary structure of the CRYAB and IFs under the different conditions and small angle X-ray scattering (SAXS) would give an idea of any un-folding or aggregation. Size exclusion chromatography would be another method to assess what basic unit is preferred in the lower pH conditions for CRYAB where increased interactions are seen with the IFs. In addition fluorescence resonance energy transfer microscopy (FRET) could be used, labelling individual monomers of CRYAB with different fluorophores and then assessing how these associate at the low and high pH values. Two different populations of CRYAB would have to be fused with separate donar/acceptor fluorophores and then mixed to assess interactions (Sreelakshmi and Sharma, 2005). This would be useful to gauge how subunits may be exchanging and their rate of exchange but would not give much insight into what units are associating/dissociating. Ideally there needs to be a sequence in CRYAB which is only exposed as a monomer and can be attached to a fluorescent label via a conjugated antibody and then quantified to assess the actual number of monomers in the CRYAB solutions. This may be problematic since CRYAB is polydisperse and thus buried residues are likely to change between the different oligomer sizes.

5.4 Desmin and CRYAB interactions assessed from microrheology.

WT CRYAB acts to reduce the *G'* of desmin networks and the frequency-dependent viscosity, unlike the cardiomyopathy- and cataract- causing R120G mutant.

Regarding rheological measurements of desmin filament networks and the influence of CRYAB, it would be useful to use polarised light to assess where the networks are in relation to the microspheres being trapped. Other studies would need to be carried out to complement the elastic responses of desmin in the absence and presence of CRYAB to ascertain if its effects are at the individual filament or overall network

level in reducing desmin elasticity. Thermal fluctuation would be a useful method to assess persistence lengths of the filaments, which would give some idea on the filament widths and also bundling (Noding and Koster, 2012). The plateau modulus would also be a useful constant to derive the mesh size of the networks. This would require measurements of the *G'* where it is independent of frequency at different concentrations of protein and then a direct impact on mesh size from CRYAB could be derived (Schopferer et al., 2009).

Appendix

Purification methods for chapter 2.

2.1.2.4 Purification of GFAP, desmin and vimentin insoluble protein.

The final pellet from the insoluble protein preparation was dissolved in 5 mL of extraction buffer (8 M urea, 10 mM Tris-HCl (pH 8.0), 5 mM EDTA and 0.2 mM PMSF) at room temperature for 2 hr. The urea buffer had charged particles removed using amberlite (Merck, DE), with stirring at room temperature for 30 min and was vacuum filtered through a cellulose nitrate 0.2 μm pore-sized filter (Whatman, NJ, USA), to prevent carbamylation of protein. Then the extracted protein was homogenised to extract more from the inclusion bodies, using a 15 mL Dounce homogeniser (Wheaton, USA). The sample was centrifuged in a TLS-55 rotor, at 201,247xg_{av}, for 20 min at 4 ^{0}C in the TL-100 Bench Top ultracentrifuge (Beckman Coulter, UK). 1 μL of supernatant was removed and dissolved with 2x Laemmli SB in an equal volume and run on a SDS-PAGE gel to check the quality of the inclusion body preparation (an adequate preparation had at least 80% of the total protein as the target protein). Then the supernatant was dialysed overnight at 4 ^{0}C, regarding GFAP, into: 6 M urea, 10 mM Tris-HCl (pH 8.0), 1 mM EDTA, 20 mM NaCl, 0.2 mM PMSF and 1 mM DTT for anion exchange chromatography on a Fractogel-EMD trimethylaminoethyl (TMAE)-650(S) column (Merck, UK). For desmin and vimentin these were dialysed into: 7M urea, 10 mM Tris-HCl (pH 8.0), 1 mM EDTA, 20 mM NaCl, 0.2 mM PMSF and 1 mM DTT. Rehydrated cellulose dialysis tubing was used (Scientific Laboratory Supplies Ltd., UK) and rinsed with de-ionised water before use. Before loading the sample onto the column, the dialysate was filtered through a 0.45 μm and then a 0.2 μm polyethersulfone (PES) filter (Whatman, NJ, USA) using a 5 mL syringe.

2.1.2.5 Purification of WT and R120G CRYAB.

The bacterial pellet was resuspended in 20 mL TEN buffer (50 mM Tris-HCl (pH 8.0), 1 mM EDTA, 300 mM NaCl and 0.2 mM PMSF) and underwent three freeze thaw cycles. The cells were then defrosted to room temperature and lysozyme added at a final concentration of 1.0 mg/mL and mixed using the 40 mL Dounce

homogeniser and tight pestle (Wheaton, USA). This was shaken for 15 min, at 70 rpm and 37 ^{0}C. Then the solution was homogenised and centrifuged at room temperature for 15 min in the JA-20 rotor, 30,000xg_{av} (Beckman JA-20-I). Benzonase nuclease (Novagen, UK) at a final concentration of 100 units/mL was added to the homogenate, mixed well and incubated at room temperature for 30 min with gentle shaking. Polyethyleneimine (PEI) at a final concentration of 0.005% (w/v) was added to remove contaminating DNA and incubated on ice for 10 min. This was then centrifuged in the JA-20 rotor, using 31,360xg_{av}, at 4 ^{0}C for 30 min to pellet any DNA and RNA (Beckman JA-20-I). The supernatant was then dialysed overnight into buffer A (20 mM Tris (pH 7.4), 1 mM $MgCl_2$, 1 mM EDTA, 1 mM DTT and 0.2 mM PMSF), used as the anion exchange buffer.

2.1.2.6 GFAP, desmin and vimentin TMAE anion and COO^- cation exchange chromatography.

The dialysate was injected into the 5 mL capacity loop on the Merck-Hitachi Chromatography System (Merck-Hitachi, UK) and the column (either TMAE-650(S) Fractogel-EMD or COO^--650(S) Fractogel-EMD) was equilibrated overnight with at least 10 column volumes of buffer A (TMAE: 6/7 M urea, 10 mM Tris-HCl (pH 8.0), 1 mM EDTA, 20 mM NaCl, 0.2 mM PMSF and 1 mM DTT). 6 M urea was used for GFAP purification and 7 M urea was used for desmin and vimentin purifications according to previous laboratory protocols. After the sample was loaded onto the column, one column volume of buffer A was run through before a 0.02 (to elute some contaminants in the wash step) - 1 M linear NaCl gradient was initiated. The flow rate was 1 mL/min. Fractions were collected using the BioFrac^{TM} fraction collector (Bio-Rad, UK). The protein content of the eluate fractions was monitored using the ultraviolet (UV) spectrometer and data processed using a Chromelean Client (Dionex, UK) to give a chromatogram plot. Peak fractions on the chromatogram were run on SDS-PAGE gels to assess if proteins were present, loading 10 µL sample from 10 µL mixed with 10 µL SB. Target fractions were pooled together. These were then dialysed overnight into COO^- buffer (6 M urea, 20 mM sodium formate (pH 4.0), 5 mM EDTA and 1 mM DTT) whilst the COO^- column was also equilibrated in the same buffer. The column was also run using a linear gradient, this time of 0 - 1 M NaCl with a 1 mL/min flow rate. For WT

desmin and vimentin, 7 M urea was used in all the buffers, as has been used previously in the laboratory, as opposed to 6 M urea. WT and mutant GFAP eluted in the range of 0.2 - 0.4 M NaCl for TMAE and COO^-. WT desmin eluted in the range of 0.2 - 0.3 M NaCl with TMAE purification and 0.3 - 0.4M NaCl for COO^- purification. WT vimentin eluted at 0.3 - 0.4 M NaCl for TMAE and COO^- purifications.

2.1.2.7 WT and R120G CRYAB TMAE anion and size exclusion chromatography.

The dialysate was injected into the 5 mL capacity loop on the Merck-Hitachi Chromatography System and the TMAE column was equilibrated overnight with at least 10 column volumes of buffer A (20 mM Tris-HCl (pH 7.4), 1 mM $MgCl_2$, 1 mM EDTA, 1 mM DTT and 0.2 mM PMSF). After the sample was loaded onto the column, one column volume of buffer A was run through the column before a linear NaCl gradient was run from 0 - 1 M; the flow rate was 1 mL/min. Fractions were collected using the fraction collector (Bio-Rad, UK). WT CRYAB eluted in the range of 0 - 0.1 M NaCl, as it does not stick to the column; the contaminants stick however. Most of the R120G CRYAB also eluted at this concentration of NaCl. For size exclusion chromatography, the pooled fractions were spin concentrated in an Amicon Ultra Centrifugal filter device with a 10 kDa molecular weight cut-off filter (Millipore, Bedford, MA), to 0.5 mL, injected into the 2 mL capacity loop and then run in the buffer: 20 mM Tris-HCl (pH 7.4) and 300 mM NaCl, on the Fractogel EMD BioSEC-650(S) (Merck, UK) column with a flow rate of 1 mL/min. WT CRYAB eluted between 30 - 45 min and R120G eluted between 30 - 48 min.

Ionic strength calculations.

In Figure 2.13, the *I* of buffer 5 (0.0607 M) was calculated taking into account the conjugate base of Tris being electrostatically neutral and the only charges present being contributed from the weak acid dissociation products of Tris-H^+ and Cl^-; including the contributions from the Mg^{2+}, Na^+ and Cl^- ions, whose *I* is calculated collectively. The F_{WA} was calculated to be 0.87 for pH 7.3 using the Henderson-Hasselbach equation and pKa of 8.114:

$$pH = pK_a + \log[A]/[HA]$$

and the following: F_{WA} = [HA]/([A] + [HA]). Then the following equation was used just for the Tris species components (Tris-H^+ and Cl^-); where z_i is equal to the charge and m_i is equal to the concentration of the ion, giving a value of 0.0087 for the Tris species:

$$I = 1/2 \cdot \sum z_i^2 \cdot m_i \cdot F_{WA}$$

The Mg^{2+}, Na^+ and Cl^- ions used the above equation without the F_{WA} component. The Tris and ion *I* values were then summed to give the overall *I*. Below is a plot showing the relationship between *I* and pH for Tris-HCl buffers.

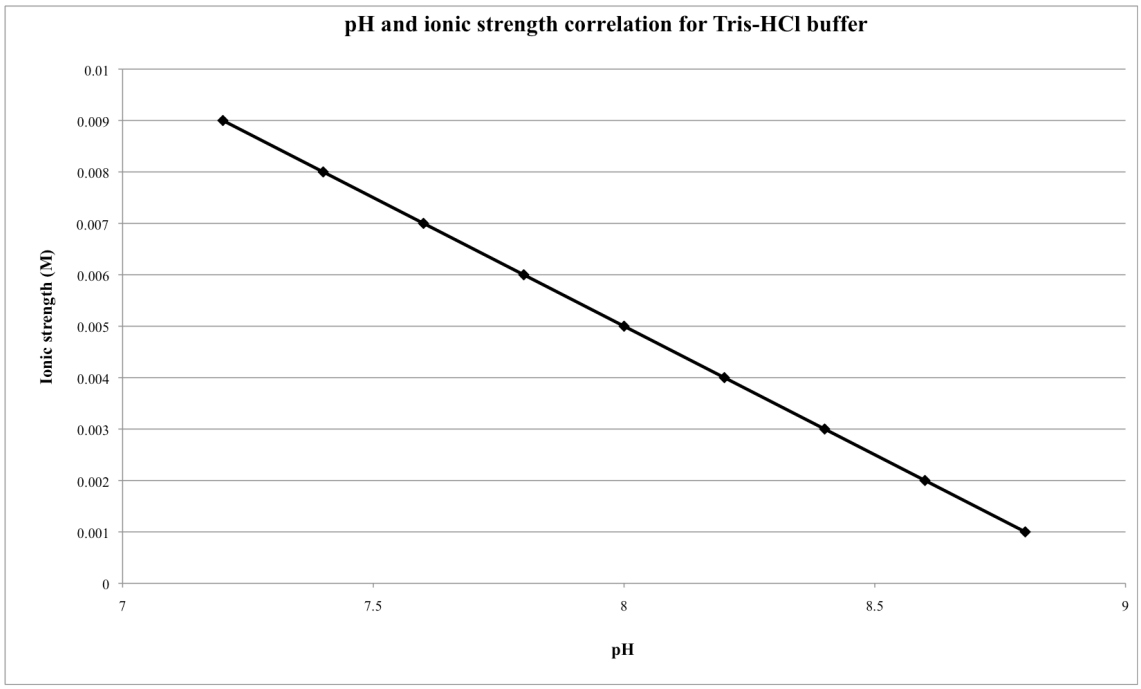

Figure A.1 PH-dependent ionic strength of 10mM Tris-HCl buffers.

The above chart outlines the *I* for a 10mM Tris-HCl buffer, using the pKa of 8.114, minus other species and this is dependent upon concentration, as shown in the ionic strength calculation.

Statistical tests for chapter 2.

This section shows the statistical results from the data obtained in chapter 2. Parametric two-sided, type-2 Student's T tests or non-parametric Mann-Whitney U tests were carried out on the data. For T test analysis, the data were pasted into Excel and initially normalised from an arcsine-root transformation since the proportions assessed from the gels are distributed binomially (Zar, 1996). Two-sided tests were used since the observed values in one group were equally likely to be bigger or smaller than the mean in the other group. A type-2 test was used assuming equal variances for the two groups. The Shapiro-Wilk test was performed on the transformed data before the T test analyses to make sure that the data had been normalised, in the SPSS Statistics version 21 programme (IBM, US) (Barnard et al., 2007). The data were pasted into the programme and the Analyze > Descriptive Statistics > Explore options selected. The data were transferred to the Dependent List and the Descriptive statistics option was chosen with a confidence interval of 95% for the mean. The data were then processed using the Normality plots with tests and Histograms options. The output file gave Shapiro-Wilk test results; with significance above 0.05 the data could be inferred to have a normal distribution. Below is one of the output tables for the first sample in Table A.2.

Tests of Normality

	Kolmogorov-Smirnov[a]			Shapiro-Wilk		
	Statistic	df	Sig.	Statistic	df	Sig.
VAR00001	.242	5	.200*	.963	5	.826

*. This is a lower bound of the true significance.

a. Lilliefors Significance Correction

Figure A.2 Shapiro-Wilk test result example.

A Mann-Whitney U test was used on those data that weren't successfully normalised after transformation, i.e. had a significance less than 0.05 from the Shapiro-Wilk test. The data were ranked in ascending order of magnitude and for those values that were the same these were given an average rank.

The total ranks were summed for each group and then the U value was calculated for each group, with an example for group A, using:

$$U_A = n_A \times n_B + ((n(n+1))/2) - R_A.$$

Where n_A and n_B represent the total number of samples in group A and B respectively, n is equal to the number of observations in group A and R_A has been given as an example of the sum total of ranks in group A. U_B is calculated using the same formula except R_B is used instead of R_A and n is the total number of observations in group B. To calculate significance, the smallest U value was compared to critical values of U using a one-tailed test and $\alpha = 0.05$ (Gravetter and Wallnau, 2009). A U value smaller than the critical value achieved significance.

n_B		n_A	1	2	3	4	5
1			-	-	-	-	-
2			-	-	-	-	0
3			-	-	0	0	1
4			-	-	0	1	2
5			-	0	1	2	3

Table A.1 **Critical U values**.

Values were obtained from published values, with n_A representing the number of samples in group A and n_B representing the number of samples in group B (Gravetter and Wallnau, 2009).

For each test there is a null hypothesis, which states that there is no difference between the two group means and that they come from the same population. The null hypotheses have been rejected when $p<0.05$.

Overall these results show that CRYAB can reduce R239H filament-filament interactions, CRYAB inhibits a proportion of WT and R416W GFAP filament assembly and CRYAB has increased binding to filaments at 44 ^{0}C compared to 23 ^{0}C for the WT and mutant GFAP.

Sample assembled	Proportion of GFAP in supernatant	Arcsine-root transformation (2 d.p.)	F value (critical F value)	p-value	Significance at 5%
WT	0.85	1.17			
	0.9	1.25			
	0.88	1.22			
	0.94	1.32			
	0.9	1.25			
WT + CRYAB	0.94	1.32			
	0.86	1.19			
	0.9	1.25			
	0.85	1.17			
	0.88	1.22	1.18 (**9.6**)	0.72	Not Significant
R416W	0.096	0.32			
	0.021	0.15			
	0.2	0.46			
R416W + CRYAB	0.57	0.86			
	0.33	0.61			
	0.11	0.34	2.64 (**39**)	0.30	Not significant

Table A.2 **Filament-filament interactions of GFAP in the presence and absence of CRYAB through Tris assembly assessed from the Student's T-test**.

P-values from arcsine-root transformed proportions of GFAP protein in supernatants from low speed sedimentation assays and two-sided, type-2 Student's T-test analyses comparing those assembled with/without WT CRYAB are shown.

Sample assembled	Proportion of GFAP in supernatant	Rank	Sum of Ranks	U value (Critical U value)	Significance
R79C	0.82	2			
	0.79	1			
	0.84	3			
	0.91	9			
	0.9	6.5	21.5	18.5 (3)	
R79C + CRYAB	0.95	10			
	0.9	6.5			
	0.9	6.5			
	0.88	4			
	0.9	6.5	33.5	6.5 (3)	Not Significant
R239H	0.066	3			
	0.057	2			
	0.05	1			
	0.072	4	10	16 (1)	
R239H + CRYAB	0.45	7			
	0.55	8			
	0.36	6			
	0.2	5	26	0 (1)	Significant

Table A.3 **Filament-filament interactions of GFAP in the presence and absence of CRYAB through Tris assembly assessed from the Mann-Whitney U test**.

WT CRYAB reduces R239H filament-filament interactions as demonstrated by a smaller U value then the critical U value for the R239H + CRYAB sample.

Sample assembled	Proportion of GFAP in supernatant	Arcsine-root transformation (2 d.p.)	F value (critical F value)	p-value	Significance at 5%
WT	0.48	0.77			
	0.44	0.73			
	0.24	0.51			
WT + CRYAB	0.24	0.51			
	0.11	0.34			
	0.086	0.30	1.43 (**39**)	0.05	Significant
R79C	0.66	0.95			
	0.84	1.16			
	0.81	1.12			
R79C + CRYAB	0.85	1.17			
	0.87	1.20			
	0.88	1.22	25.23 (**39**)	0.14	Not significant

Table A.4 **Filament-filament interactions of GFAP in the presence and absence of CRYAB through imidazole assembly assessed from the Student's T test**.
P-values from arcsine-root transformed proportions of GFAP protein in supernatants from low speed sedimentation assays and two-sided, type-2 Student's T-test analyses comparing those assembled with/without WT CRYAB are shown.

Sample assembled	Proportion of GFAP in supernatant	Rank	Sum of Ranks	U value (Critical U value)	Significance
R239H	0.11	5.5			
	0.074	2			
	0.11	5.5			
	0.1	4	17	9 (1)	
R239H + CRYAB	0.05	1			
	0.087	3			
	0.24	8			
	0.22	7	19	7 (1)	Not Significant

Table A.5 **Filament-filament interactions of GFAP in the presence and absence of CRYAB through imidazole assembly assessed from the Mann-Whitney U test**.

Sample assembled	Proportion of GFAP in supernatant	Arcsine-root transformation (2 d.p.)	F value (critical F value)	p-value	Significance at 5%
WT	0.09	0.31			
	0.06	0.25			
	0.13	0.36			
	0.09	0.30			
WT + CRYAB	0.33	0.61			
	0.25	0.52			
	0.38	0.66	2.05 (**39.2**)	0.001	Significant
R239H	0	0			
	0	0			
	0.02	0.14			
	0.12	0.35			
R239H + CRYAB	0.01	0.10			
	0.02	0.14			
	0.05	0.23			
	0.04	0.20	8.64 (**15.4**)	0.63	Not significant

Table A.6 **Inhibition of assembly of GFAP through Tris assembly by CRYAB assessed from the Student's T test**.

P-values from arcsine-root transformed proportions of protein in supernatants from high speed sedimentations and two-sided, type-2 Student's T-test analyses are shown. WT CRYAB inhibits WT GFAP assembly.

Sample assembled	Proportion of GFAP in supernatant	Rank	Sum of Ranks	U value (Critical U value)	Significance
R79C	0.32	2			
	0.44	5			
	0.15	1	8	7 (0)	
R79C + CRYAB	0.57	6			
	0.43	3.5			
	0.43	3.5	13	2 (0)	Not significant
R416W	0	2.5			
	0	2.5			
	0	2.5			
	0	2.5	10	16 (1)	
R416W + CRYAB	0.14	8			
	0.01	5			
	0.03	6.5			
	0.03	6.5	26	0 (1)	Significant

Table A.7 **Inhibition of assembly of GFAP through Tris assembly by CRYAB assessed from the Mann-Whitney U test**.

CRYAB appears to reduce the amount of assembled mutant R416W GFAP material with $p<0.05$.

GFAP type assembled and temperature	Proportion of CRYAB in pellet	Arcsine-root transformation (2 d.p.)	F value (critical F value)	p-value	Significance at 5%
WT 23 ^{0}C	0.17	0.43			
	0.16	0.41			
	0.18	0.44			
	0.03	0.17			
	0.06	0.25			
WT 44 ^{0}C	0.71	1.00			
	0.37	0.65			
	0.39	0.67	2.63 (**39**)	0.008	Significant
R79C 23 ^{0}C	0.12	0.35			
	0.14	0.38			
	0.07	0.27			
	0.07	0.27			
	0.11	0.34			
R79C 44 ^{0}C	0.7	0.99			
	0.41	0.69			
	0.45	0.74	9.44 (**39**)	0.001	Significant
R239H 23 ^{0}C	0.23	0.50			
	0.06	0.25			
	0	0			
	0.20	0.47			
	0.15	0.39			
R239H 44 ^{0}C	0.89	1.23			
	0.84	1.16			
	0.47	0.76	1.58 (**39**)	0.004	Significant
R416W 23 ^{0}C	0.14	0.38			
	0.12	0.35			
	0.19	0.45			
R416W 44 ^{0}C	0.43	0.72			
	0.36	0.64			
	0.55	0.84	3.79 (**39**)	0.006	Significant

Table A.8 **Binding of WT CRYAB to GFAP through Tris assembly at 23 and 44 ^{0}C assessed from the Student's T test**.

P-values from arcsine-root transformed proportions of WT CRYAB in pellets from high speed sedimentation assays and two-sided, type-2 Student's T-test analyses are shown comparing the amount of pelleted WT CRYAB between 23 and 44 ^{0}C.

GFAP type assembled and temperature	Proportion of CRYAB in pellet	Arcsine-root transformation (2 d.p.)	F-value (critical F value)	p-value	Significance at 5%
WT 23 ^{0}C	0.26	0.54			
	0.13	0.37			
	0.14	0.38			
WT 44 ^{0}C	0.74	1.04			
	0.61	0.90			
	0.95	1.34	6.24 (**39**)	0.010	Significant

Table A.9 **Binding of WT CRYAB to GFAP through imidazole assembly at 23 and 44 ^{0}C assessed from the Student's T test**.

The p-value from arcsine-root transformed proportions of CRYAB co-pelleting with WT GFAP from high speed sedimentation assays and two-sided, type-2 Student's T-test analysis between 23 and 44 ^{0}C is shown.

Appendix of GFAP oligomer approximation chapter 3.

A standard curve was derived from the standard protein ladder bands' distances travelled on a gel versus their molecular weights, with values shown in the table below.

Molecular Weight Standards (kDa)	Distance Travelled (units)
250	0.4
130	0.8
95	1.5
72	2.2
55	3.1
36	4.8
28	6
17	9

Table A.10 **Standard curve values.**

The distance travelled of the GFAP oligomer was equivalent to 0.5 units and this was used in the equation of the standard curve shown in Figure A.3 to give an approximate size of 220 kDa for the oligomer.

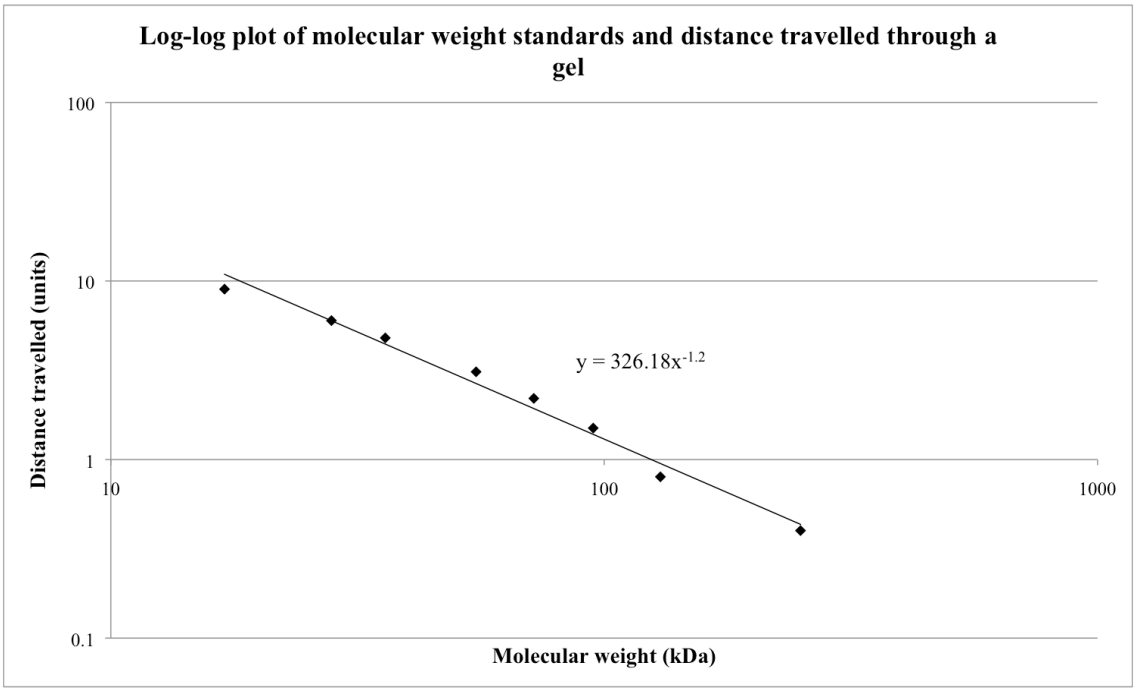

Figure A.3 Denatured protein SDS-PAGE gel standard curve.

Appendix of statistical analyses chapter 3.1.3.2, section 2.

Sample assembled and conditions	Proportion of CRYAB in pellet	Arcsine-root transformation (2 d.p.)	F value (critical F value)	p-value	Significance at 5%
Vimentin 39 ^{0}C Mn^{2+}	0.1	0.32			
	0.16	0.41			
	0.12	0.35			
Vimentin 39 ^{0}C Mg^{2+}	0.059	0.25			
	0.068	0.26			
	0.093	0.31	1.87 (**39**)	0.052	Significant
Vimentin 44 ^{0}C Mn^{2+}	0.2	0.46			
	0.15	0.40			
	0.12	0.35			
Vimentin 44 ^{0}C Mg^{2+}	0.085	0.30			
	0.096	0.32			
	0.103	0.33	12.60 (**39**)	0.049	Significant

Table A.11 **There is a significant increase in binding of CRYAB to vimentin filaments formed with manganese ions at pH 6.9 compared to magnesium ions at pH 6.8 at 39 and 44 ^{0}C assessed from the Student's T test**.

The amounts of CRYAB binding to vimentin filaments assembled at pH 6.9 with manganese ions compared to pH 6.8 with magnesium ions are shown.

Sample assembled	Proportion of CRYAB in pellet	Rank	Sum of Ranks	U value (Critical U value)	Significance
Vimentin 23 ^{0}C Mn^{2+}	0.12	6			
	0.09	4			
	0.07	1	11	4 (0)	
Vimentin 23 ^{0}C Mg^{2}	0.076	3			
	0.074	2			
	0.093	5	10	5 (0)	Not Significant

Table A.12 **There is no significant increase in binding of CRYAB to vimentin filaments formed with manganese ions at pH 6.9 compared to magnesium ions at pH 6.8 at 23 ^{0}C assessed from the Mann-Whitney U test**.

Sample	Proportion of CRYAB in pellet	Arcsine-root transformation (2 d.p.)	F value (critical F value)	p-value	Significance at 5%
39 ^{0}C Mn^{2+} GFAP	0.14	0.38			
	0.15	0.40			
	0.1	0.32			
39 ^{0}C Mg^{2+} GFAP	0.146	0.39			
	0.128	0.37			
	0.135	0.38	9.37 (**39**)	0.69	Not Significant
44 ^{0}C Mn^{2+} GFAP	0.31	0.59			
	0.2	0.46			
	0.4	0.68			
44 ^{0}C Mg^{2+} GFAP	0.213	0.48			
	0.232	0.50			
	0.267	0.54	11.97 (**39**)	0.35	Not Significant

Table A.13 **There is no significant difference in binding of CRYAB to GFAP filaments formed with manganese ions at pH 6.9 compared to magnesium ions at pH 6.8 at 39 and 44 ^{0}C assessed from the Student's T test**.

The amounts of CRYAB binding to GFAP filaments assembled at pH 6.9 with manganese ions compared to pH 6.8 with magnesium ions are shown.

Sample assembled	Proportion of CRYAB in pellet	Rank	Sum of Ranks	U value (Critical U value)	Significance
23 ^{0}C Mn^{2+} GFAP	0.1	7			
	0.08	5			
	0.13	8			
	0.09	6	26	0 (1)	
23 ^{0}C Mg^{2+} GFAP	0.075	3			
	0.06	1			
	0.077	4			
	0.069	2	10	16 (1)	Significant

Table A.14 **There is a significant difference in binding of CRYAB to GFAP filaments formed with manganese ions at pH 6.9 compared to magnesium ions at pH 6.8 at 23 ^{0}C assessed from the Mann-Whitney U test**.

Appendix of quantifications from chapter 3.1.3.3.

Overall these results demonstrate that a drop in pH and an increase in temperature result in increased co-pelleting of CRYAB with GFAP, vimentin and desmin.

Section 1 pH and temperature dependence of binding of CRYAB to GFAP, vimentin and desmin with addition prior to filament formation.

Table values are shown as averages +/- their standard deviations.

	% CRYAB pellet Mg^{2+} 23 ^0C	% CRYAB pellet Mg^{2+} 39 ^0C	% CRYAB pellet Mg^{2+} 44 ^0C
Vimentin	14 +/- 3	22 +/- 1	28 +/- 2
GFAP	15 +/- 4	38 +/- 1	40 +/- 2
Desmin	54 +/- 2	64 +/- 14	47 +/- 19

Table A.15 **% binding of CRYAB to filaments in HEPES buffers at pH 6.3.**

	% CRYAB pellet Mg^{2+} 23 ^0C	% CRYAB pellet Mg^{2+} 39 ^0C	% CRYAB pellet Mg^{2+} 44 ^0C
Vimentin	8 +/- 1	8 +/- 3	10 +/- 1
GFAP	7 +/- 1	14 +/- 1	24 +/- 3
Desmin	16 +/- 2	15 +/- 2	20 +/- 4

Table A.16 **% binding of CRYAB to filaments in HEPES buffers at pH 6.8.**

	% CRYAB pellet Mg^{2+} 23 ^0C	% CRYAB pellet Mg^{2+} 39 ^0C	% CRYAB pellet Mg^{2+} 44 ^0C
Vimentin	8 +/- 4	7 +/- 2	8 +/- 6
GFAP	7 +/- 5	11 +/- 3	15 +/- 3
Desmin	10 +/- 2	12 +/- 1	11 +/- 1

Table A.17 **% binding of CRYAB to filaments in HEPES buffers at pH 7.3.**

pH	% CRYAB pellet Mg^{2+} 23 ^{0}C	% CRYAB pellet Mg^{2+} 39 ^{0}C	% CRYAB pellet Mg^{2+} 44 ^{0}C
7.3	13 +/- 3	10 +/- 1	13 +/- 1
6.8	11 +/- 3	13 +/- 2	16 +/- 2
6.3	15 +/- 5	14 +/- 5	12 +/- 4

Table A.18 **% of CRYAB pelleting in HEPES buffers.**

Section 2 pH and temperature dependence of binding of CRYAB, to assembled GFAP filaments, at the same pH.

	% CRYAB pellet Mg^{2+} 23 ^{0}C	% CRYAB pellet Mg^{2+} 39 ^{0}C	% CRYAB pellet Mg^{2+} 44 ^{0}C
GFAP pH 6.3	17 +/- 2	29 +/- 3	34 +/- 4
GFAP pH 7.3	4 +/- 3	6 +/- 1	11 +/- 2

Table A.19 **% binding of CRYAB to filaments in HEPES buffers at pH 6.3 and 7.3.**

Appendix of statistical analyses chapter 3.1.3.3.

Sample	Proportion of CRYAB in pellet	Arcsine-root transformation (2 d.p.)	F value (critical F value)	p-value	Significance at 5%
pH 7.3					
23 ^{0}C CRYAB before	0.05	0.23			
	0.037	0.19			
	0.131	0.37			
23 ^{0}C CRYAB after	0.012	0.11			
	0.075	0.28			
	0.04	0.20	1.25 (**39**)	0.41	Not Significant
39 ^{0}C CRYAB before	0.15	0.40			
	0.09	0.30			
	0.09	0.31			
39 ^{0}C CRYAB after	0.055	0.24			
	0.05	0.23			
	0.07	0.27	6.02 (**39**)	0.051	Significant

Table A.20 **CRYAB interactions are significantly greater at pH 7.3 at 39 ^{0}C with addition of CRYAB before GFAP has formed compared to CRYAB addition after GFAP formation assessed from the Student's T test**.

The data in Table A.20 and A.21 show p-values from arcsine-root transformed proportions of CRYAB protein in pellets from high speed sedimentation assays and two-sided, type-2 Student's T-test analyses comparing the difference, at pH 7.3 at the same temperatures, of pelleted CRYAB to filaments either after being added to the filaments before or after they had assembled. Table A.22 shows the data for pH 6.3.

Sample assembled	Proportion of GFAP in supernatant	Rank	Sum of Ranks	U value (Critical U value)	Significance
44 ^{0}C CRYAB before	0.16	5			
	0.18	6			
	0.12	3	14	1 (0)	
44 ^{0}C CRYAB after	0.10	1.5			
	0.14	4			
	0.10	1.5	7	8 (0)	Not Significant

Table A.21 **CRYAB interactions are not significantly greater at pH 7.3 at 44 ^{0}C with addition of CRYAB before GFAP has formed compared to CRYAB addition after GFAP formation assessed from the Mann-Whitney U test**.

Sample assembled	Proportion of GFAP in supernatant	Rank	Sum of Ranks	U value (Critical U value)	Significance
pH 6.3					
23 ^{0}C CRYAB before	0.21	6			
	0.20	5			
	0.13	1	12	3 (0)	
23 ^{0}C CRYAB after	0.18	3.5			
	0.15	2			
	0.18	3.5	9	6 (0)	Not Significant
39 ^{0}C CRYAB before	0.39	6			
	0.38	4.5			
	0.38	4.5	15	0 (0)	
39 ^{0}C CRYAB after	0.30	2			
	0.31	3			
	0.26	1	6	9 (0)	Significant
44 ^{0}C CRYAB before	0.37	3			
	0.39	5			
	0.42	6	14	1 (0)	
44 ^{0}C CRYAB after	0.30	1			
	0.38	4			
	0.33	2	7	8 (0)	Not Significant

Table A.22 **CRYAB interactions are significantly greater at pH 6.3 at 39 ^{0}C with addition of CRYAB before GFAP has formed compared to CRYAB addition after GFAP formation assessed from the Mann-Whitney U test**.

Appendix of the microrheology calculations for single bead trapping from chapter 4.

For the rheology experiments carried out in Durham, MATLAB R2007b was used for calculating the passive frequency dependent viscosity values; the "modulus" script was run to derive the complex shear modulus:

$$G(f)=G'(f)+iG''(f)$$

Initially the power spectral density was calculated, where the discrete Fourier transform is used on the bead positions relative to the camera frames, using the following discrete Fourier transform equation:

$$Y(k) = \sum_{j=1}^{N} y(j) \exp\left(\frac{2\pi i(j-1)(k-1)}{N}\right)$$

N represents the total number of data points and $y(j)$, j, and k are integers labeling the input/output data points.

It then applied the following to fit a Lorentzian function to the data:

$$S(f) = \left(\frac{2Y(f>0)}{N}\right)^2$$

This gave the power spectrum for data up to half the camera frame rate, from which the imaginary apparent and real apparent part of the transfer function were derived to give the complex transfer function:

$$\alpha = \alpha' + i\alpha''$$

The imaginary apparent part is calculated from:

$$\alpha''(f) = \frac{\pi}{2k_bT}S(f)$$

T is the temperature in kelvin and k_b is the Boltzmann's constant.

The real apparent part was calculated using the Kramers-Kronig relation:

$$\alpha'(\omega) = \frac{2}{\pi}\int_0^\infty \cos(\omega t)\int_0^\infty \alpha''(\omega)\sin(\omega' t)d\omega' dt.$$

The true responses were then derived from the apparent responses using:

$$\alpha(f) = \frac{A(f)}{1 - k \cdot A(f)}$$

A(f) is the apparent response and k is the trap stiffness.

The true responses were then put into the Stokes relation:

$$G(f) = \frac{1}{6\pi a \alpha(f)}$$

G'' was calculated as: (1/(6*Pi*bead radius ($2*10^{-06}$)))*-(-$\alpha''/(\alpha'^2 + \alpha''^2)$) and then subtraction of solvent viscosity. The passive frequency dependent viscosity was then derived from *G''* (loss modulus) in the following equation:

$$\eta(f) = \frac{G''(f)}{2\pi f}$$

As for the analysis in Durham, the data at AMOLF used the complex transfer function $\alpha(f)$ ($\alpha' + i\alpha''$) to calculate the apparent $G(f)$, using the generalised Stokes relation, with *a* as the bead radius. The general operation formula for dividing complex numbers was applied to separate out the real and imaginary parts (Chow, 2000):

$$\frac{a+ib}{c+id} = \frac{(a+ib)(c-id)}{(c+id)(c-id)} = \frac{ac+bd}{c^2+d^2} + i\frac{bc-ad}{c^2+d^2}.$$

The following values were used: $a = 1$, $b = 0$, $c = \alpha'$ and $d = \alpha''$.

This derived α' apparent as: $\alpha'/(\alpha'^2 + \alpha''^2)$ and α'' apparent as: $-\alpha''/(\alpha'^2 + \alpha''^2)$ (with α' as the apparent real and α'' as the apparent imaginary response values) to then separately derive *G'* apparent and *G''* apparent respectively from the Stokes relation.

Therefore *G'* apparent was calculated:

(1/(6*Pi*bead radius (10^{-06})))*($\alpha'/(\alpha'^2 + \alpha''^2)$)

and *G''* apparent was calculated: (1/(6*Pi*bead radius))*-(-$\alpha''/(\alpha'^2 + \alpha''^2)$).

G' sample was then: *G'* apparent sample- *G'* apparent buffer.

G'' sample was: *G''* apparent sample- solvent viscosity (2*Pi*frequency*viscosity of water at 21 ^{0}C).

G'' values for 1 mg/mL desmin in the presence and absence of WT CRYAB.

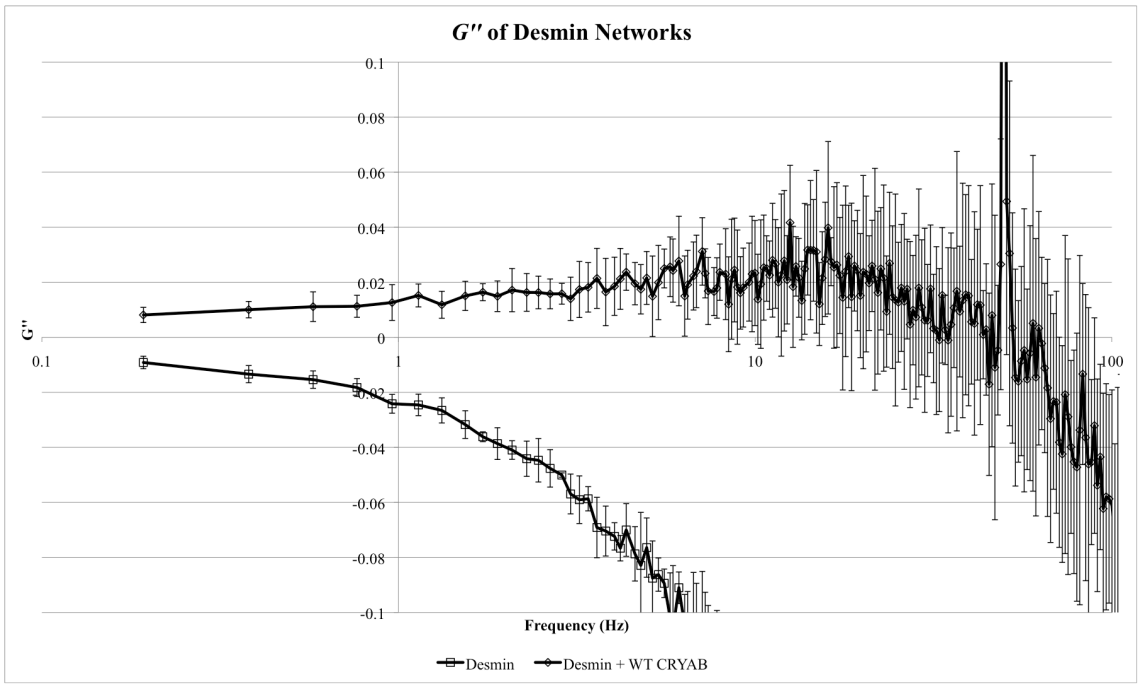

Figure A.4 *G''* values of desmin networks in the presence and absence of WT CRYAB show no difference at this concentration.

Values represent the average of 9 microspheres for desmin + WT CRYAB and 5 microspheres for desmin alone +/- one SD shown as error bars.

References

ADDAS, K. M., SCHMIDT, C. F. & TANG, J. X. 2004. Microrheology of solutions of semiflexible biopolymer filaments using laser tweezers interferometry. *Physical review E, Statistical, nonlinear, and soft matter physics,* 70**,** 021503.

AGUSTINA ALAIMO, R. M. G., MÓNICA L. KOTLER 2011. The extrinsic and intrinsic apoptotic pathways are involved in manganese toxicity in rat astrocytoma C6 cells. *Neurochemistry International,* 59**,** 297-308.

AHMAD, M. F., SINGH, D., TAIYAB, A., RAMAKRISHNA, T., RAMAN, B. & RAO CH, M. 2008. Selective Cu2+ binding, redox silencing, and cytoprotective effects of the small heat shock proteins alphaA- and alphaB-crystallin. *J Mol Biol,* 382**,** 812-24.

AKATSU, H., HORI, A., YAMAMOTO, T., YOSHIDA, M., MIMURO, M., HASHIZUME, Y., TOOYAMA, I. & YEZDIMER, E. M. 2012. Transition metal abnormalities in progressive dementias. *Biometals : an international journal on the role of metal ions in biology, biochemistry, and medicine,* 25**,** 337-50.

ALEXANDER, W. S. 1949. Progressive fibrinoid degeneration of fibrillary astrocytes associated with mental retardation in a hydrocephalic patient. *Brain,* 72**,** 373-81.

AMARANTE-MENDES, G. P. & GREEN, D. R. 1999. The regulation of apoptotic cell death. *Braz J Med Biol Res,* 32**,** 1053-61.

ANDLEY, U. P., HAMILTON, P. D., RAVI, N. & WEIHL, C. C. 2011. A knock-in mouse model for the R120G mutation of alphaB-crystallin recapitulates human hereditary myopathy and cataracts. *PLoS One,* 6**,** e17671.

AQUILINA, J. A., BENESCH, J. L., DING, L. L., YARON, O., HORWITZ, J. & ROBINSON, C. V. 2004. Phosphorylation of alphaB-crystallin alters chaperone function through loss of dimeric substructure. *J Biol Chem,* 279**,** 28675-80.

AQUILINA, J. A., BENESCH, J. L. P., DING, L. L., YARON, O., HORWITZ, J. & ROBINSON, C. V. 2005. Subunit exchange of polydisperse proteins: mass spectrometry reveals consequences of alphaA-crystallin truncation. *The Journal of biological chemistry,* 280**,** 14485-91.

ASHKIN, A., DZIEDZIC, J. M., BJORKHOLM, J. E. & CHU, S. 1986. Observation of a single-beam gradient force optical trap for dielectric particles. *Optics letters,* 11**,** 288.

ATAKHORRAMI, M., SULKOWSKA, J. I., ADDAS, K. M., KOENDERINK, G. H., TANG, J. X., LEVINE, A. J., MACKINTOSH, F. C. & SCHMIDT, C. F. 2006. Correlated fluctuations of microparticles in viscoelastic solutions: quantitative measurement of material properties by microrheology in the presence of optical traps. *Phys Rev E Stat Nonlin Soft Matter Phys,* 73**,** 061501.

BACHETTI, T., CAROLI, F., BOCCA, P., PRIGIONE, I., BALBI, P., BIANCHERI, R., FILOCAMO, M., MARIOTTI, C., PAREYSON, D., RAVAZZOLO, R. & CECCHERINI, I. 2008. Mild functional effects of a novel GFAP mutant allele identified in a familial case of adult-onset Alexander disease. *Eur J Hum Genet,* 16**,** 462-70.

BAGNERIS, C., BATEMAN, O. A., NAYLOR, C. E., CRONIN, N., BOELENS, W. C., KEEP, N. H. & SLINGSBY, C. 2009. Crystal structures of alpha-crystallin domain dimers of alphaB-crystallin and Hsp20. *J Mol Biol,* 392**,** 1242-52.

BANDYOPADHYAY, U., SRIDHAR, S., KAUSHIK, S., KIFFIN, R. & CUERVO, A. M. 2010. Identification of regulators of chaperone-mediated autophagy. *Mol Cell,* 39**,** 535-47.

BAR, H., SCHOPFERER, M., SHARMA, S., HOCHSTEIN, B., MUCKE, N., HERRMANN, H. & WILLENBACHER, N. 2010. Mutations in desmin's carboxy-terminal "tail" domain severely modify filament and network mechanics. *J Mol Biol,* 397**,** 1188-98.

BARNARD, C., GILBERT, F. & MCGREGOR, P. 2007. *Asking Questions in Biology, A Guide to Hypothesis-testing, Analysis and Presentation in Practical Work and Research,* London, Pearson Education Limited.

BARNHAM, K. J., HAEFFNER, F., CICCOTOSTO, G. D., CURTAIN, C. C., TEW, D., MAVROS, C., BEYREUTHER, K., CARRINGTON, D., MASTERS, C. L., CHERNY, R. A., CAPPAI, R. & BUSH, A. I. 2004. Tyrosine gated electron transfer is key to the toxic mechanism of Alzheimer's disease beta-amyloid. *FASEB J,* 18**,** 1427-9.

BAYLESS, K. J. & JOHNSON, G. A. 2011. Role of the cytoskeleton in formation and maintenance of angiogenic sprouts. *J Vasc Res,* 48**,** 369-85.

BCHETNIA, M., TREMBLAY, M. L., LECLERC, G., DUPEREE, A., POWELL, J., MCCUAIG, C., MORIN, C., LEGENDRE-GUILLEMIN, V. & LAPRISE, C. 2012. Expression signature of epidermolysis bullosa simplex. *Hum Genet,* 131**,** 393-406.

BENNARDINI, F., WRZOSEK, A. & CHIESI, M. 1992. Alpha B-crystallin in cardiac tissue. Association with actin and desmin filaments. *Circ Res,* 71**,** 288-94.

BEYNON, R. J. & EASTERBY, J. S. 1996. *Buffer Solutions: The Basics,* US, Oxford University Press.

BONGCAM-RUDLOFF E, N. M., BETSHOLTZ C, WANG JL, STENMAN G, HUEBNER K, CROCE CM, WESTERMARK B 1991. Human glial fibrillary acidic protein: complementary DNA cloning, chromosome localization, and messenger RNA expression in human glioma cell lines of various phenotypes. *Cancer Res.,* 51**,** 1553-60.

BORNHEIM, R., MULLER, M., REUTER, U., HERRMANN, H., BUSSOW, H. & MAGIN, T. M. 2008. A dominant vimentin mutant upregulates Hsp70 and the activity of the ubiquitin-proteasome system, and causes posterior cataracts in transgenic mice. *Journal of cell science,* 121**,** 3737-46.

BOVA, M. P., MCHAOURAB, H. S., HAN, Y. & FUNG, B. K. 2000. Subunit exchange of small heat shock proteins. Analysis of oligomer formation of alphaA-crystallin and Hsp27 by fluorescence resonance energy transfer and site-directed truncations. *J Biol Chem,* 275**,** 1035-42.

BOVENSHULTE, M., RIEMER, D. & WEBER, K. 1995. The structure of a cytoplasmic intermediate filament (IF) protein from the annelid Lumbricus terrestris emphasizes a distinctive feature of protostomic IF proteins. *FEBS Lett,* 360**,** 223-6.

BOZˇANIC´, D., BOCˇINA, I. & SARAGA-BABIC, M. 2006. Involvement of cytoskelatal proteins and growth factor receptors during development of the human eye. *Anat Embryol,* 211**,** 367-377.

BRASNO, G. & OTIS, T. S. 2001. Neuronal Glutamate Transporters Control Activation of Postsynaptic Metabotropic Glutamate Receptors and Influence Cerebellar Long-Term Depression. *Neuron,* 31**,** 607-616.

BRENNER, M., GOLDMAN, J. E., QUINALN, R. A. & MESSING, A. 2009. *Astrocytes in (Patho)Physiology of the Nervous System,* New York, Springer.

BRENNER, M., JOHNSON, A. B., BOESPFLUG-TANGUY, O., RODRIGUEZ, D., GOLDMAN, J. E. & MESSING, A. 2001. Mutations in GFAP, encoding glial fibrillary acidic protein, are associated with Alexander disease. *Nat Genet,* 27**,** 117-20.

BROWN, S. C., TORELLI, S., UGO, I., DE BIASIA, F., HOWMAN, E. V., POON, E., BRITTON, J., DAVIES, K. E. & MUNTONI, F. 2005. Syncoilin upregulation in muscle of patients with neuromuscular disease. *Muscle Nerve,* 32**,** 715-25.

BRUNKENER, M. & GEORGATOS, S. D. 1992. Membrane-binding properties of filensin, a cytoskeletal protein of the lens fiber cells. *J Cell Sci,* 103 (Pt 3)**,** 709-18.

BULLARD, B., FERGUSON, C., MINAJEVA, A., LEAKE, M. C., GAUTEL, M., LABEIT, D., DING, L., LABEIT, S., HORWITZ, J., LEONARD, K. R. & LINKE, W. A. 2004. Association of the chaperone alphaB-crystallin with titin in heart muscle. *J Biol Chem,* 279**,** 7917-24.

BYUN, Y., CHEN, F., CHANG, R., TRIVEDI, M., GREEN, K. J. & CRYNS, V. L. 2001. Caspase cleavage of vimentin disrupts intermediate filaments and promotes apoptosis. *Cell Death Differ,* 8**,** 443-50.

CALNE, D. B., CHU, N. S., HUANG, C. C., LU, C. S. & OLANOW, W. 1994. Manganism and idiopathic parkinsonism: similarities and differences. *Neurology,* 44**,** 1583-6.

CARTER, J. M., HUTCHESON, A. M. & QUINLAN, R. A. 1995. In vitro studies on the assembly properties of the lens proteins CP49, CP115: coassembly with alpha-crystallin but not with vimentin. *Exp Eye Res,* 60**,** 181-92.

CARY, R. B., KLYMKOWSKY, M. W., EVANS, R. M., DOMINGO, A., DENT, J. A. & BACKHUS, L. E. 1994. Vimentin's tail interacts with actin-containing structures in vivo. *J Cell Sci,* 107 (Pt 6)**,** 1609-22.

CAULIN, C., SALVESEN, G. S. & OSHIMA, R. G. 1997. Caspase cleavage of keratin 18 and reorganization of intermediate filaments during epithelial cell apoptosis. *J Cell Biol,* 138**,** 1379-94.

CHALLA, A. A. & STEFANOVIC, B. 2011. A novel role of vimentin filaments: binding and stabilization of collagen mRNAs. *Mol Cell Biol,* 31**,** 3773-89.

CHAMCHEU, J. C., SIDDIQUI, I. A., SYED, D. N., ADHAMI, V. M., LIOVIC, M. & MUKHTAR, H. 2011. Keratin gene mutations in disorders of human skin and its appendages. *Arch Biochem Biophys,* 508**,** 123-37.

CHANG, I. A., OH, M. J., KIM, M. H., PARK, S. K., KIM, B. G. & NAMGUNG, U. 2012. Vimentin phosphorylation by Cdc2 in Schwann cell controls axon growth via beta1-integrin activation. *FASEB J*.

CHASTEK, T. Q., IIDA, K., AMIS, E. J., FASOLKA, M. J. & BEERS, K. L. 2008. A microfluidic platform for integrated synthesis and dynamic light scattering measurement of block copolymer micelles. *Lab Chip,* 8**,** 950-957.

CHEN, F., CHANG, R., TRIVEDI, M., CAPETANAKI, Y. & CRYNS, V. L. 2003. Caspase proteolysis of desmin produces a dominant-negative inhibitor of intermediate filaments and promotes apoptosis. *J Biol Chem,* 278**,** 6848-53.

CHEN, W. J. & LIEM, R. K. 1994. The endless story of the glial fibrillary acidic protein. *Journal of cell science,* 107 (Pt 8)**,** 2299-311.

CHEN, Y. S., LIM, S. C., CHEN, M. H., QUINLAN, R. A. & PERNG, M. D. 2011. Alexander disease causing mutations in the C-terminal domain of GFAP are deleterious both to assembly and network formation with the potential to both activate caspase 3 and decrease cell viability. *Exp Cell Res,* 317**,** 2252-66.

CHEUNG, Z. H. & IP, N. Y. 2011. Autophagy deregulation in neurodegenerative diseases - recent advances and future perspectives. *J Neurochem,* 118**,** 317-25.

CHIANG, H. L., TERLECKY, S. R., PLANT, C. P. & DICE, J. F. 1989. A role for a 70-kilodalton heat shock protein in lysosomal degradation of intracellular proteins. *Science,* 246**,** 382-5.

CHOU, R. G., STROMER, M. H., ROBSON, R. M. & HUIATT, T. W. 1990. Determination of the critical concentration required for desmin assembly. *Biochem J,* 272**,** 139-45.

CHOU, Y. H., ROSEVEAR, E. & GOLDMAN, R. D. 1989. Phosphorylation and disassembly of intermediate filaments in mitotic cells. *Proceedings of the National Academy of Sciences of the United States of America,* 86**,** 1885-9.

CHOW, T. L. 2000. *Mathematical Methods for Physicists: A Concise Introduction,* Cambridge, Cambridge University Press.

CLARK, A. R., NAYLOR, C. E., BAGNERIS, C., KEEP, N. H. & SLINGSBY, C. 2011. Crystal structure of R120G disease mutant of human alphaB-crystallin domain dimer shows closure of a groove. *J Mol Biol,* 408**,** 118-34.

COLAKOGLU, G. & BROWN, A. 2009. Intermediate filaments exchange subunits along their length and elongate by end-to-end annealing. *J Cell Biol,* 185**,** 769-77.

CONWAY, J. F. & PARRY, D. A. 1988. Intermediate filament structure: 3.Analysis of sequence homologies. *Int. J. Biol. Macromol.,,* 10**,** 79-98.

COOPER, D. N. & YOUSSOUFIAN, H. 1988. The CpG dinucleotide and human genetic disease. *Hum Genet,* 78**,** 151-5.

CORREIA, I., CHU, D., CHOU, Y. H., GOLDMAN, R. D. & MATSUDAIRA, P. 1999. Integrating the actin and vimentin cytoskeletons. adhesion-dependent formation of fimbrin-vimentin complexes in macrophages. *J Cell Biol,* 146**,** 831-42.

COULOMBE, P. A., HUTTON, M. E., LETAI, A., HEBERT, A., PALLER, A. S. & FUCHS, E. 1991. Point mutations in human keratin 14 genes of epidermolysis bullosa simplex patients: genetic and functional analyses. *Cell,* 66**,** 1301-11.

COX, P. A. 2004. *Instant Notes Inorganic Chemistry,* New York, BIOS Scientific Publishers.

CUI, X., GAO, L., JIN, Y., ZHANG, Y., BAI, J., FENG, G., GAO, W., LIU, P., HE, L. & FU, S. 2007. The E233del mutation in BFSP2 causes a progressive autosomal dominant congenital cataract in a Chinese family. *Mol Vis,* 13**,** 2023-9.

DATTA, S. A. & RAO, C. M. 1999. Differential temperature-dependent chaperone-like activity of alphaA- and alphaB-crystallin homoaggregates. *J Biol Chem,* 274**,** 34773-8.

DER PERNG, M., SU, M., WEN, S. F., LI, R., GIBBON, T., PRESCOTT, A. R., BRENNER, M. & QUINLAN, R. A. 2006. The Alexander disease-causing glial fibrillary acidic protein mutant, R416W, accumulates into Rosenthal fibers by a pathway that involves filament aggregation and the association of alpha B-crystallin and HSP27. *Am J Hum Genet,* 79**,** 197-213.

DHORI, P. K., GIACOMIN, A. J. & SLATTERY, J. C. 1997. Common line motion II: sliding plate rheometry. *Journal of Non-Newtonian Fluid Mechanics,* 71**,** 215-229.

DJABALI, K., DE NECHAUD, B., LANDON, F. & PORTIER, M. M. 1997. AlphaB-crystallin interacts with intermediate filaments in response to stress. *J Cell Sci,* 110 (Pt 21)**,** 2759-69.

DONG, D. L., XU, Z. S., CHEVRIER, M. R., COTTER, R. J., CLEVELAND, D. W. & HART, G. W. 1993. Glycosylation of mammalian neurofilaments. Localization of multiple O-linked N-acetylglucosamine moieties on neurofilament polypeptides L and M. *J Biol Chem,* 268**,** 16679-87.

DORNMAIR, K. & MCCONNELL, H. M. 1990. Refolding and reassembly of separate a and f8 chains of class II molecules of the major histocompatibility complex leads to increased peptide-binding capacity. *Proc. Natl. Acad. Sci. USA,* 87**,** 4134-4138.

DUCRAY, F., CRINIERE, E., IDBAIH, A., MOKHTARI, K., MARIE, Y., PARIS, S., NAVARRO, S., LAIGLE-DONADEY, F., DEHAIS, C., THILLET, J., HOANG-XUAN, K., DELATTRE, J. Y. & SANSON, M. 2009. alpha-Internexin expression identifies 1p19q codeleted gliomas. *Neurology,* 72**,** 156-61.

EATON, P., FULLER, W., BELL, J. R. & SHATTOCK, M. J. 2001. AlphaB crystallin translocation and phosphorylation: signal transduction pathways and preconditioning in the isolated rat heart. *J Mol Cell Cardiol,* 33**,** 1659-71.

ELIASSON, C., SAHLGREN, C., BERTHOLD, C. H., STAKEBERG, J., CELIS, J. E., BETSHOLTZ, C., ERIKSSON, J. E. & PEKNY, M. 1999. Intermediate filament protein partnership in astrocytes. *J Biol Chem,* 274**,** 23996-4006.

ENGEL A, E. R., AEBI U. 1985. Polymorphism of reconstituted human epidermal keratin filaments: determination of their mass-per-length and width by scanning transmission electron microscopy (STEM). *J Ultrastruct Res. ,* 90**,** 323-335.

ERIKSSON, J. E., HE, T., TREJO-SKALLI, A. V., HARMALA-BRASKEN, A. S., HELLMAN, J., CHOU, Y. H. & GOLDMAN, R. D. 2004. Specific in vivo phosphorylation sites determine the assembly dynamics of vimentin intermediate filaments. *J Cell Sci,* 117**,** 919-32.

ERIKSSON, K. S., ZHANG, S. N., LARIVIÈRE, R. C., JULIEN, J. P. & MIGNOT, E. 2008. The type III neurofilament peripherin is expressed in the tuberomammillary neurons of the mouse. *BMC Neurosci,* 9.

FAGERHOLM, P. P., PHILIPSON, B. T. & LINDSTROM, B. 1981. Normal human lens - the distribution of protein. *Exp Eye Res,* 33**,** 615-20.

FERRARO, A., EUFEMI, M., CERVONI, L., MARINETTI, R. & TURANO, C. 1989. Glycosylated forms of nuclear lamins. *FEBS Lett,* 257**,** 241-6.

FOWLER JIM, C. L. A. J. P. 1998. *Practical Statistics for Field Biology,* Chichester, John Wiley and SOns Inc.

FUJIWARA, I., TAKAHASHI, S., TADAKUMA, H., FUNATSU, T. & ISHIWATA, S. 2002. Microscopic analysis of polymerization dynamics with individual actin filaments. *Nat Cell Biol,* 4**,** 666-73.

GALOU, M., COLUCCI-GUYON, E., ENSERGUEIX, D., RIDET, J. L., GIMENEZ Y RIBOTTA, M., PRIVAT, A., BABINET, C. & DUPOUEY, P. 1996. Disrupted glial fibrillary acidic protein network in astrocytes from vimentin knockout mice. *J Cell Biol,* 133**,** 853-63.

GANADU, M. L., ARU, M., MURA, G. M., COI, A., MLYNARZ, P. & KOZLOWSKI, H. 2004. Effects of divalent metal ions on the alphaB-crystallin chaperone-like activity: spectroscopic evidence for a complex between copper(II) and protein. *J Inorg Biochem,* 98**,** 1103-9.

GAO, Y. & SZTUL, E. 2001. A novel interaction of the Golgi complex with the vimentin intermediate filament cytoskeleton. *J Cell Biol,* 152**,** 877-94.

GEISLER, N., SCHUNEMANN, J., WEBER, K., JHANER, M. & AEBI, U. 1998. Assembly and architecture of invertebrate cytoplasmic intermediate filaments reconcile features of vertebrate cytoplasmic and nuclear lamin-type intermediate filaments. *J Mol Biol,* 282**,** 601-17.

GEISLER, N. & WEBER, K. 1982. The amino acid sequence of chicken muscle desmin provides a common structural model for intermediate filament proteins. *EMBO J,* 1**,** 1649-56.

GEORGAKOPOULOU, S., MOLLER, D., SACHS, N., HERRMANN, H. & AEBI, U. 2009. Near-UV circular dichroism reveals structural transitions of vimentin subunits during intermediate filament assembly. *J Mol Biol,* 386**,** 544-53.

GEORGATOS, S. D., WEBER, K., GEISLER, N. & BLOBEL, G. 1987. Binding of two desmin derivatives to the plasma membrane and the nuclear envelope of avian erythrocytes: evidence for a conserved site-specificity in intermediate filament-membrane interactions. *Proc Natl Acad Sci U S A,* 84**,** 6780-4.

GHALEBANI, L., WAHLSTROM, A., DANIELSSON, J., WARMLANDER, S. K. & GRASLUND, A. 2012. pH-dependence of the specific binding of Cu(II) and Zn(II) ions to the amyloid-beta peptide. *Biochem Biophys Res Commun,* 421**,** 554-60.

GHOSAL, D., OMELCHENKO, M. V., GAIDAMAKOVA, E. K., MATROSOVA, V. Y., VASILENKO, A., VENKATESWARAN, A., ZHAI, M., KOSTANDARITHES, H. M., BRIM, H., MAKAROVA, K. S., WACKETT, L. P., FREDRICKSON, J. K. & DALY, M. J. 2005. How radiation kills cells: survival of Deinococcus radiodurans and Shewanella oneidensis under oxidative stress. *FEMS microbiology reviews,* 29**,** 361-75.

GHOSH, J. G., HOUCK, S. A. & CLARK, J. I. 2007. Interactive sequences in the stress protein and molecular chaperone human alphaB crystallin recognize and modulate the assembly of filaments. *Int J Biochem Cell Biol,* 39**,** 1804-15.

GITTES F., S. C. F. 1998. Interfrence model for back-focal-plane displacement detection in optical tweezers. *OPTICS LETTERS,* 23**,** 7-9.

GLASS, C. A., GLASS, J. R., TANIURA, H., HASEL, K. W., BLEVITT, J. M. & GERACE, L. 1993. The alpha-helical rod domain of human lamins A and C contains a chromatin binding site. *EMBO J.,* 12**,** 4413-4424.

GOLENHOFEN, N., NESS, W., KOOB, R., HTUN, P., SCHAPER, W. & DRENCKHAHN, D. 1998. Ischemia-induced phosphorylation and translocation of stress protein alpha B-crystallin to Z lines of myocardium. *Am J Physiol,* 274**,** H1457-64.

GOMI, H., YOKOYAMA, T. & ITOHARA, S. 2010. Role of GFAP in morphological retention and distribution of reactive astrocytes induced by scrapie encephalopathy in mice. *Brain Res,* 1312**,** 156-67.

GOOD, N. E. & IZAWA, S. 1972. Hydrogen ion buffers. *Methods Enzymol,* 24**,** 53-68.

GOULIELMOS, G., GOUNARI, F., REMINGTON, S., MULLER, S., HANER, M., AEBI, U. & GEORGATOS, S. D. 1996. Filensin and phakinin form a novel

type of beaded intermediate filaments and coassemble de novo in cultured cells. *J Cell Biol,* 132**,** 643-55.

GOUNARI, F., MERDES, A., QUINLAN, R., HESS, J., FITZGERALD, P. G., OUZOUNIS, C. A. & GEORGATOS, S. D. 1993. Bovine filensin possesses primary and secondary structure similarity to intermediate filament proteins. *J Cell Biol,* 121**,** 847-53.

GRAVETTER, F. J. & WALLNAU, L. B. 2009. *Statistics for the Behavioral Sciences,* California, Wadsworth.

GREGO, S., CANTILLANA, V. & SALMON, E. D. 2001. Microtubule treadmilling in vitro investigated by fluorescence speckle and confocal microscopy. *Biophys J,* 81**,** 66-78.

HAGEMANN, T. L., BOELENS, W. C., WAWROUSEK, E. F. & MESSING, A. 2009. Suppression of GFAP toxicity by alphaB-crystallin in mouse models of Alexander disease. *Hum Mol Genet,* 18**,** 1190-9.

HAGEMANN, T. L., CONNOR, J. X. & MESSING, A. 2006. Alexander disease-associated glial fibrillary acidic protein mutations in mice induce Rosenthal fiber formation and a white matter stress response. *J Neurosci,* 26**,** 11162-73.

HAGEMANN, T. L., GAETA, S. A., SMITH, M. A., JOHNSON, D. A., JOHNSON, J. A. & MESSING, A. 2005. Gene expression analysis in mice with elevated glial fibrillary acidic protein and Rosenthal fibers reveals a stress response followed by glial activation and neuronal dysfunction. *Hum Mol Genet,* 14**,** 2443-58.

HALEY, D. A., HORWITZ, J. & STEWART, P. L. 1999. Image restrained modeling of alphaB-crystallin. *Exp Eye Res,* 68**,** 133-6.

HANSON, S. R., HASAN, A., SMITH, D. L. & SMITH, J. B. 2000. The major in vivo modifications of the human water-insoluble lens crystallins are disulfide bonds, deamidation, methionine oxidation and backbone cleavage. *Exp Eye Res,* 71**,** 195-207.

HARRIS, J. & HORNE, R. 1991. *Electron Microscopy in Biology,* Oxford, IRl Press.

HARTIG, R., SHOEMAN, R. L., JANETZKO, A., TOLSTONOG, G. V. & TRAUB, P. 1998. DNA-mediated transport of the intermediate filament protein vimentin into the nucleus of cultured cells. *J Cell Sci,* 111**,** 3573-84.

HASLBECK, M., KASTENMULLER, A., BUCHNER, J., WEINKAUF, S. & BRAUN, N. 2008. Structural dynamics of archaeal small heat shock proteins. *J Mol Biol,* 378**,** 362-74.

HATZFELD, M. & WEBER, K. 1991. Modulation of keratin intermediate filament assembly by single amino acid exchanges in the consensus sequence at the C-terminal end of the rod domain. *Journal of cell science,* 99 (Pt 2)**,** 351-62.

HAYES, V. H., DEVLIN, G. & QUINLAN, R. A. 2008. Truncation of alphaB-crystallin by the myopathy-causing Q151X mutation significantly destabilizes the protein leading to aggregate formation in transfected cells. *J Biol Chem,* 283**,** 10500-12.

HEAD, M. W., HURWITZ, L., KEGEL, K. & GOLDMAN, J. E. 2000. AlphaB-crystallin regulates intermediate filament organization in situ. *Neuroreport,* 11**,** 361-5.

HEIMBURG, T., SCHUENEMANN, J., WEBER, K. & GEISLER, N. 1996. Specific recognition of coiled coils by infrared spectroscopy: analysis of the three structural domains of type III intermediate filament proteins. *Biochemistry,* 35**,** 1375-82.

HEITLINGER, E., PETER, M., LUSTIG, A., VILLIGER, W., NIGG, E. A. & AEBI, U. 1992. The role of the head and tail domain in lamin structure and assembly: analysis of bacterially expressed chicken lamin A and truncated B2 lamins. *J Struct Biol,* 108**,** 74-89.

HENDRIX, M. J., SEFTOR, E. A., SEFTOR, R. E. & TREVOR, K. T. 1997. Experimental co-expression of vimentin and keratin intermediate filaments in human breast cancer cells results in phenotypic interconversion and increased invasive behavior. *Am J Pathol,* 150**,** 483-95.

HENNEKES, H., PETER, M., WEBER, K. & NIGG, E. A. 1993. Phosphorylation on protein kinase C sites inhibits nuclear import of lamin B2. *J Cell Biol,* 120**,** 1293-304.

HERRMANN, H. & AEBI, U. 1999. Intermediate filament assembly: temperature sensitivity and polymorphism. *Cell Mol Life Sci,* 55**,** 1416-31.

HERRMANN, H., HANER, M., BRETTEL, M., KU, N. O. & AEBI, U. 1999. Characterization of distinct early assembly units of different intermediate filament proteins. *J Mol Biol,* 286**,** 1403-20.

HERRMANN, H., HANER, M., BRETTEL, M., MULLER, S. A., GOLDIE, K. N., FEDTKE, B., LUSTIG, A., FRANKE, W. W. & AEBI, U. 1996. Structure and assembly properties of the intermediate filament protein vimentin: the role of its head, rod and tail domains. *J Mol Biol,* 264**,** 933-53.

HESS, J. F., BUDAMAGUNTA, M. S., FITZGERALD, P. G. & VOSS, J. C. 2005. Characterization of structural changes in vimentin bearing an epidermolysis bullosa simplex-like mutation using site-directed spin labeling and electron paramagnetic resonance. *J Biol Chem,* 280**,** 2141-6.

HESS, J. F., CASSELMAN, J. T., KONG, A. P. & FITZGERALD, P. G. 1998. Primary sequence, secondary structure, gene structure, and assembly properties suggests that the lens-specific cytoskeletal protein filensin represents a novel class of intermediate filament protein. *Exp Eye Res,* 66**,** 625-44.

HILL, W. D., ARAI, M., COHEN, J. A. & TROJANOWSKI, J. Q. 1993. Neurofilament mRNA is reduced in Parkinson's disease substantia nigra pars compacta neurons. *J Comp Neurol,* 329**,** 328-36.

HOFEMEISTER, H., WEBER, K. & STICK, R. 2000. Association of prenylated proteins with the plasma membrane and the inner nuclear membrane is mediated by the same membrane-targeting motifs. *Molecular biology of the cell,* 11**,** 3233-46.

HOFMANN, I., HERRMANN, H. & FRANKE, W. W. 1991. Assembly and structure of calcium-induced thick vimentin filaments. *Eur J Cell Biol,* 56**,** 328-41.

HOUCK, S. A. & CLARK, J. I. 2010. Dynamic subunit exchange and the regulation of microtubule assembly by the stress response protein human alphaB crystallin. *PLoS One,* 5**,** e11795.

HSIAO, V. C., TIAN, R., LONG, H., DER PERNG, M., BRENNER, M., QUINLAN, R. A. & GOLDMAN, J. E. 2005. Alexander-disease mutation of GFAP causes filament disorganization and decreased solubility of GFAP. *J Cell Sci,* 118**,** 2057-65.

HUGHES, E. G., MAGUIRE, J. L., MCMINN, M. T., SCHOLZ, R. E. & SUTHERLAND, M. L. 2004. Loss of glial fibrillary acidic protein results in decreased glutamate transport and inhibition of PKA-induced EAAT2 cell surface trafficking. *Brain Res Mol Brain Res,* 124**,** 114-23.

ICENOGLE, L. M., HENGEL, S. M., COYE, L. H., STREIFEL, A., COLLINS, C. M., GOODLETT, D. R. & MOSELEY, S. L. 2012. Molecular and Biological Characterization of Streptococcal SpyA-mediated ADP-ribosylation of Intermediate Filament Protein Vimentin. *J Biol Chem,* 287**,** 21481-91.

INAGAKI, M., GONDA, Y., MATSUYAMA, M., NISHIZAWA, K., NISHI, Y. & SATO, C. 1988. Intermediate filament reconstitution in vitro. The role of phosphorylation on the assembly-disassembly of desmin. *J Biol Chem,* 263**,** 5970-8.

INAGAKI, M., GONDA, Y., NISHIZAWA, K., KITAMURA, S., SATO, C., ANDO, S., TANABE, K., KIKUCHI, K., TSUIKI, S. & NISHI, Y. 1990. Phosphorylation sites linked to glial filament disassembly in vitro locate in a non-alpha-helical head domain. *J Biol Chem,* 265**,** 4722-9.

INAGAKI, M., TAKAHARA, H., NISHI, Y., SUGAWARA, K. & SATO, C. 1989. Ca2+-dependent deimination-induced disassembly of intermediate filaments involves specific modification of the amino-terminal head domain. *The Journal of biological chemistry,* 264**,** 18119-27.

IRELAND, M. E., KLETTNER, C. & NUNLEE, W. 1993. Cyclic AMP-mediated phosphorylation and insolubilization of a 49-kDa cytoskeletal marker protein of lens fiber terminal differentiation. *Exp Eye Res,* 56**,** 453-61.

ISHIDA-YAMAMOTO, A., IIZUKA, H., MANABE, M., O'GUIN, W. M., HOHL, D., KARTASOVA, T., KUROKI, T., ROOP, D. R. & EADY, R. A. 1995. Altered distribution of keratinization markers in epidermolytic hyperkeratosis. *Arch Dermatol Res,* 287**,** 705-11.

ISHIKAWA, H., BISCHOFF, R. & HOLTZER, H. 1968. Mitosis and intermediate-sized filaments in developing skeletal muscle. *J Cell Biol,* 38**,** 538-55.

ISHIWATA, T., MATSUDA, Y. & NAITO, Z. 2011. Nestin in gastrointestinal and other cancers: effects on cells and tumor angiogenesis. *World J Gastroenterol,* 17**,** 409-18.

ITAKURA, E. & MIZUSHIMA, N. 2010. Characterization of autophagosome formation site by a hierarchical analysis of mammalian Atg proteins. *Autophagy,* 6**,** 764-76.

ITO, H., KAMEI, K., IWAMOTO, I., INAGUMA, Y., NOHARA, D. & KATO, K. 2001. Phosphorylation-induced change of the oligomerization state of alpha B-crystallin. *J Biol Chem,* 276**,** 5346-52.

ITO, M. & KANO, M. 1982. Long-lasting depression of parallel fiber–Purkinje cell transmission induced by conjunctive stimulation of parallel fibers and climbing fibers in the cerebellar cortex. *Neurosci. Lett.,* 33**,** 253-258.

JEFFERSON, R. J., ABSOUD, M., JAIN, R., LIVINGSTON, J. H., MS, V. D. K. & JAYAWANT, S. 2010. Alexander disease with periventricular calcification: a novel mutation of the GFAP gene. *Dev Med Child Neurol,* 52**,** 1160-3.

JEHLE, S., RAJAGOPAL, P., BARDIAUX, B., MARKOVIC, S., KUHNE, R., STOUT, J. R., HIGMAN, V. A., KLEVIT, R. E., VAN ROSSUM, B. J. & OSCHKINAT, H. 2010. Solid-state NMR and SAXS studies provide a structural basis for the activation of alphaB-crystallin oligomers. *Nat Struct Mol Biol,* 17**,** 1037-42.

JEHLE, S., VAN ROSSUM, B., STOUT, J. R., NOGUCHI, S. M., FALBER, K., REHBEIN, K., OSCHKINAT, H., KLEVIT, R. E. & RAJAGOPAL, P. 2009. alphaB-crystallin: a hybrid solid-state/solution-state NMR investigation reveals structural aspects of the heterogeneous oligomer. *J Mol Biol,* 385**,** 1481-97.

JEONG, S. Y., RATHORE, K. I., SCHULZ, K., PONKA, P., AROSIO, P. & DAVID, S. 2009. Dysregulation of iron homeostasis in the CNS contributes to disease progression in a mouse model of amyotrophic lateral sclerosis. *J Neurosci,* 29**,** 610-9.

JERÁBKOVÁ, B., MAREK, J., BUCKOVÁ, H., KOPECKOVÁ, L., VESELÝ, K., VALÍCKOVÁ, J., FAJKUS, J. & FAJKUSOVÁ, L. 2010. Keratin mutations in patients with epidermolysis bullosa simplex: correlations between phenotype severity and disturbance of intermediate filament molecular structure. *Br J Dermatol,* 162**,** 1004-13.

JIANG, J., PRASAD, K., LAFER, E. M. & SOUSA, R. 2005. Structural basis of interdomain communication in the Hsc70 chaperone. *Mol Cell,* 20**,** 513-24.

JIN, J. K., WHITTAKER, R., GLASSY, M. S., BARLOW, S. B., GOTTLIEB, R. A. & GLEMBOTSKI, C. C. 2008. Localization of phosphorylated alphaB-crystallin to heart mitochondria during ischemia-reperfusion. *Am J Physiol Heart Circ Physiol,* 294**,** H337-44.

KALISMAN, N., ADAMS, C. M. & LEVITT, M. 2012. Subunit order of eukaryotic TRiC/CCT chaperonin by cross-linking, mass spectrometry, and combinatorial homology modeling. *PNAS,* 109**,** 2884-2889.

KARPLUS, M., GAO, Y. Q., MA, J., VAN DER VAART, A. & YANG, W. 2005. Protein structural transitions and their functional role. *Phil. Trans. R. Soc. A,* 363**,** 331-356.

KAWAUCHI, T., CHIHAMA, K., NABESHIMA, Y. & HOSHINO, M. 2006. Cdk5 phosphorylates and stabilizes p27kip1 contributing to actin organization and cortical neuronal migration. *Nat Cell Biol,* 8**,** 17-26.

KELLER, A. F., GRAVEL, M. & KRIZ, J. 2009. Live imaging of amyotrophic lateral sclerosis pathogenesis: disease onset is characterized by marked induction of GFAP in Schwann cells. *Glia,* 57**,** 1130-42.

KINOSHITA, T., IMAIZUMI, T., MIURA, Y., FUJIMOTO, H., AYABE, M., SHOJI, H., OKAMOTO, Y., TAKASHIMA, H., OSAME, M. & NAKAGAWA, M. 2003. A case of adult-onset Alexander disease with Arg416Trp human glial fibrillary acidic protein gene mutation. *Neuroscience letters,* 350**,** 169-72.

KLEEBERGER, W., BOVA, G. S., NIELSEN, M. E., HERAWI, M., CHUANG, A.-Y., EPSTEIN, J. I. & BERMAN, D. M. 2007. Roles for the stem cell associated intermediate filament Nestin in prostate cancer migration and metastasis. *Cancer research,* 67**,** 9199-206.

KONDO, H., KIMURA, M. & ITOKAWA, Y. 1991. Manganese, copper, zinc, and iron concentrations and subcellular distribution in two types of skeletal muscle. *Proc Soc Exp Biol Med,* 196**,** 83-8.

KOOIJMAN, M., VAN AMERONGEN, H., TRAUB, P., VAN GRONDELLE, R. & BLOEMENDAL, M. 1995. The assembly state of the intermediate filament proteins desmin and glial fibrillary acidic protein at low ionic strength. *FEBS Lett,* 358**,** 185-8.

KOSTER, S., LIN, Y. C., HERRMANN, H. & WEITZ, D. A. 2010. Nanomechanics of vimentin intermediate filament networks. *Soft Matter,* 6**,** 1910-1914.

KOTEICHE, H. A. & MCHAOURAB, H. S. 2003. Mechanism of chaperone function in small heat-shock proteins. Phosphorylation-induced activation of two-mode binding in alphaB-crystallin. *J Biol Chem,* 278**,** 10361-7.

KREPLAK, L., BAR, H., LETERRIER, J. F., HERRMANN, H. & AEBI, U. 2005. Exploring the mechanical behavior of single intermediate filaments. *J Mol Biol,* 354**,** 569-77.

KU, N. O., LIAO, J. & OMARY, M. B. 1998. Phosphorylation of human keratin 18 serine 33 regulates binding to 14-3-3 proteins. *EMBO J,* 17**,** 1892-906.

KU, N. O., TOIVOLA, D. M., STRNAD, P. & OMARY, M. B. 2010. Cytoskeletal keratin glycosylation protects epithelial tissue from injury. *Nat Cell Biol,* 12**,** 876-85.

KUMAR, M. S., KAPOOR, M., SINHA, S. & REDDY, G. B. 2005. Insights into hydrophobicity and the chaperone-like function of alphaA- and alphaB-crystallins: an isothermal titration calorimetric study. *The Journal of biological chemistry,* 280**,** 21726-30.

KUNA, A. T. 2012. Mutated citrullinated vimentin antibodies in rheumatoid arthritis. *Clin Chim Acta,* 413**,** 66-73.

LAGANOWSKY, A., BENESCH, J. L., LANDAU, M., DING, L., SAWAYA, M. R., CASCIO, D., HUANG, Q., ROBINSON, C. V., HORWITZ, J. & EISENBERG, D. 2010. Crystal structures of truncated alphaA and alphaB crystallins reveal structural mechanisms of polydispersity important for eye lens function. *Protein Sci,* 19**,** 1031-43.

LARKIN MA, B. G., BROWN NP, CHENNA R, MCGETTIGAN PA, MCWILLIAM H, VALENTIN F, WALLACE IM, WILM A, LOPEZ R, THOMPSON JD, GIBSON TJ AND HIGGINS DG 2007. *ClustalW2* [Online]. Available: http://www.ebi.ac.uk/Tools/msa/clustalw2/ 2012].

LEE, M. K., XU, Z., WONG, P. C. & CLEVELAND, D. W. 1993. Neurofilaments are obligate heteropolymers in vivo. *J Cell Biol,* 122**,** 1337-50.

LENGYEL, I., VOSS, K., CAMMAROTA, M., BRADSHAW, K., BRENT, V., MURPHY, K. P., GIESE, K. P., ROSTAS, J. A. & BLISS, T. V. 2004. Autonomous activity of CaMKII is only transiently increased following the induction of long-term potentiation in the rat hippocampus. *Eur J Neurosci.,* 20**,** 3063-72.

LI, G., TOLSTONOG, G. V., SABASCH, M. & TRAUB, P. 2003. Type III intermediate filament proteins interact with four-way junction DNA and facilitate its cleavage by the junction-resolving enzyme T7 endonuclease I. *DNA Cell Biol,* 22**,** 261-91.

LI, H., GUO, Y., TENG, J., DING, M., YU, A. C. & CHEN, J. 2006. 14-3-3gamma affects dynamics and integrity of glial filaments by binding to phosphorylated GFAP. *J Cell Sci,* 119**,** 4452-61.

LI, R., JOHNSON, A. B., SALOMONS, G., GOLDMAN, J. E., NAIDU, S., QUINLAN, R., CREE, B., RUYLE, S. Z., BANWELL, B., D'HOOGHE, M., SIEBERT, J. R., ROLF, C. M., COX, H., REDDY, A., GUTIERREZ-SOLANA, L. G., COLLINS, A., WELLER, R. O., MESSING, A., VAN DER KNAAP, M. S. & BRENNER, M. 2005. Glial fibrillary acidic protein mutations in infantile, juvenile, and adult forms of Alexander disease. *Ann Neurol,* 57**,** 310-26.

LIANG, J. J. & LIU, B. F. 2006. Fluorescence resonance energy transfer study of subunit exchange in human lens crystallins and congenital cataract crystallin mutants. *Protein Sci,* 15**,** 1619-27.

LIM, L., MANSER, E., LEUNG, T. & HALL, C. 1996. Regulation of phosphorylation pathways by p21 GTPases. The p21 Ras-related Rho subfamily and its role in phosphorylation signalling pathways. *Eur J Biochem,* 242**,** 171-85.

LIN, Y. C., BROEDERSZ, C. P., ROWAT, A. C., WEDIG, T., HERRMANN, H., MACKINTOSH, F. C. & WEITZ, D. A. 2010a. Divalent cations crosslink vimentin intermediate filament tail domains to regulate network mechanics. *J Mol Biol,* 399**,** 637-44.

LIN, Y. C., YAO, N. Y., BROEDERSZ, C. P., HERRMANN, H., MACKINTOSH, F. C. & WEITZ, D. A. 2010b. Origins of elasticity in intermediate filament networks. *Phys Rev Lett,* 104**,** 058101.

LINDNER, R. A., KAPUR, A., MARIANI, M., TITMUSS, S. J. & CARVER, J. A. 1998. Structural alterations of alpha-crystallin during its chaperone action. *Eur J Biochem,* 258**,** 170-83.

LIU, L., GHOSH, J. G., CLARK, J. I. & JIANG, S. 2006. Studies of alphaB crystallin subunit dynamics by surface plasmon resonance. *Anal Biochem,* 350**,** 186-95.

LONG, H. A. 2003. *Mutations in Glial Fibrillary Acidic Protein (GFAP) associated with Alexander Disease.* Doctor of Philosophy, University of Dundee.

LOVERING, R. M., O'NEILL, A., MURIEL, J. M., PROSSER, B. L., STRONG, J. & BLOCH, R. J. 2011. Physiology, structure, and susceptibility to injury of skeletal muscle in mice lacking keratin 19-based and desmin-based intermediate filaments. *Am J Physiol Cell Physiol,* 300**,** C803-13.

LOVICU, F. J., SCHULZ, M. W., HALES, A. M., VINCENT, L. N., OVERBEEK, P. A., CHAMBERLAIN, C. G. & MCAVOY, J. W. 2002. TGFbeta induces morphological and molecular changes similar to human anterior subcapsular cataract. *Br J Ophthalmol,* 86**,** 220-6.

LOWRIE, D. J., JR., STICKNEY, J. T. & IP, W. 2000. Properties of the nonhelical end domains of vimentin suggest a role in maintaining intermediate filament network structure. *J Struct Biol,* 132**,** 83-94.

LUDEMANN, N., CLEMENT, A., HANS, V. H., LESCHIK, J., BEHL, C. & BRANDT, R. 2005. O-glycosylation of the tail domain of neurofilament protein M in human neurons and in spinal cord tissue of a rat model of amyotrophic lateral sclerosis (ALS). *J Biol Chem,* 280**,** 31648-58.

LV, Z., JIANG, H., XU, H., SONG, N. & XIE, J. 2011. Increased iron levels correlate with the selective nigral dopaminergic neuron degeneration in Parkinson's disease. *J Neural Transm,* 118**,** 361-9.

MACHIELS, B. M., ZORENC, A. H., ENDERT, J. M., KUIJPERS, H. J., VAN EYS, G. J., RAMAEKERS, F. C. & BROERS, J. L. 1996. An alternative splicing product of the lamin A/C gene lacks exon 10. *J Biol Chem,* 271**,** 9249-53.

MALOYAN, A., OSINSKA, H., LAMMERDING, J., LEE, R. T., CINGOLANI, O. H., KASS, D. A., LORENZ, J. N. & ROBBINS, J. 2009. Biochemical and mechanical dysfunction in a mouse model of desmin-related myopathy. *Circ Res,* 104**,** 1021-8.

MANETTO, V., STERNBERGER, N. H., PERRY, G., STERNBERGER, L. A. & GAMBETTI, P. 1988. Phosphorylation of neurofilaments is altered in amyotrophic lateral sclerosis. *J Neuropathol Exp Neurol.,* 47**,** 642-53.

MAO, Y. W., LIU, J. P. & LI, D. W. 2004. Human A- and B-crystallins bind to Bax and Bcl-X(S) to sequester their translocation during staurosporine-induced apoptosis. *Cell Death Differ.,* 11**,** 512-26.

MATSUOKA, Y., NISHIZAWA, K., YANO, T., SHIBATA, M., ANDO, S., TAKAHASHI, T. & INAGAKI, M. 1992. Two different protein kinases act on a different time schedule as glial filament kinases during mitosis. *The EMBO journal,* 11**,** 2895-902.

MAYER, M., KIES, U., KAMMERMEIER, R. & BUCHNER, J. 2000. BiP and PDI cooperate in the oxidative folding of antibodies in vitro. *J Biol Chem,* 275**,** 29421-5.

MCCALL, M. A., GREGG, R. G., BEHRINGER, R. R., BRENNER, M., DELANEY, C. L., GALBREATH, E. J., ZHANG, C. L., PEARCE, R. A., CHIU, S. Y. & MESSING, A. 1996. Targeted deletion in astrocyte intermediate filament (Gfap) alters neuronal physiology. *Proc Natl Acad Sci U S A,* 93**,** 6361-6.

MCDONALD, E. T., BORTOLUS, M., KOTEICHE, H. A. & MCHAOURAB, H. S. 2012. Sequence, structure, and dynamic determinants of Hsp27 (HspB1) equilibrium dissociation are encoded by the N-terminal domain. *Biochemistry,* 51**,** 1257-68.

MCGREAL, R. S., LEE KANTOROW, W., CHAUSS, D. C., WEI, J., BRENNAN, L. A. & KANTOROW, M. 2012. alphaB-crystallin/sHSP protects cytochrome c and mitochondrial function against oxidative stress in lens and retinal cells. *Biochim Biophys Acta,* 1820**,** 921-30.

MCHAOURAB, H. S., LIN, Y.-L. & SPILLER, B. W. 2012. Crystal structure of an activated variant of small heat shock protein hsp16.5. *Biochemistry,* 51**,** 5105-12.

MCLACHLAN, D. R., LUKIW, W. J., WONG, L., BERGERON, C. & BECH-HANSEN, N. T. 1988. Selective messenger RNA reduction in Alzheimer's disease. *Brain Res,* 427**,** 255-61.

MCNULTY, A. K. & SAUNDERS, M. J. 1992. Purification and immunological detection of pea nuclear intermediate filaments: evidence for plant nuclear lamins. *J Cell Sci,* 103 (Pt 2)**,** 407-14.

MENET, V., GIMÉNEZ Y RIBOTTA, M., CHAUVET, N., DRIAN, M. J., LANNOY, J., COLUCCI-GUYON, E. & PRIVAT, A. 2001. Inactivation of the Glial Fibrillary Acidic Protein Gene, But Not That of Vimentin, Improves Neuronal Survival and Neurite Growth by Modifying Adhesion Molecule Expression *The Journal of Neuroscience,* 21**,** 6147-6158.

MENG, J. J., KHAN, S. & IP, W. 1996. Intermediate Filament Protein Domain Interactions as Revealed by Two-hybrid Screens. *J Biol Chem,* 271**,** 1599-604.

MESSING, A. 2012. *Alexander Disease* [Online]. Available: http://www.waisman.wisc.edu/alexander-disease/diagram.html 2012].

MIDDELDORP, J. & HOL, E. M. 2011. GFAP in health and disease. *Prog Neurobiol,* 93**,** 421-43.

MILNER, D. J., MAVROIDIS, M., WEISLEDER, N. & CAPETANAKI, Y. 2000. Desmin cytoskeleton linked to muscle mitochondrial distribution and respiratory function. *J Cell Biol,* 150**,** 1283-98.

MIOT, M., REIDY, M., DOYLE, S. M., HOSKINS, J. R., JOHNSTON, D. M., GENEST, O., VITERY, M. C., MASISON, D. C. & WICKNER, S. 2011. Species-specific collaboration of heat shock proteins (Hsp) 70 and 100 in thermotolerance and protein disaggregation. *Proc Natl Acad Sci U S A,* 108**,** 6915-20.

MIYATA, S., NAKAMURA, S., NAGATA, H. & KAMEYAMA, M. 1983. Increased manganese level in spinal cords of amyotrophic lateral sclerosis determined by radiochemical neutron activation analysis. *Journal of the neurological sciences,* 61**,** 283-93.

MIZUNO, D., HEAD, D. A., MACKINTOSH, F. C. & SCHMIDT, C. F. 2008. Active and Passive Microrheology in Equilibrium and Nonequilibrium Systems. *Macromolecules,* 41**,** 7194-7202.

MOIR, R. D., DONALDSON, A. D. & STEWART, M. 1991. Expression in Escherichia coli of human lamins A and C: influence of head and tail domains on assembly properties and paracrystal formation. *J Cell Sci,* 99 (Pt 2)**,** 363-72.

MOORWOOD, C. 2008. Syncoilin, an intermediate filament-like protein linked to the dystrophin associated protein complex in skeletal muscle. *Cell Mol Life Sci,* 65**,** 2957-63.

MORRISON, L. E., HOOVER, H. E., THUERAUF, D. J. & GLEMBOTSKI, C. C. 2003. Mimicking phosphorylation of alphaB-crystallin on serine-59 is necessary and sufficient to provide maximal protection of cardiac myocytes from apoptosis. *Circ Res,* 92**,** 203-11.

MOUSER, P. E., HEAD, E., HA, K. H. & ROHN, T. T. 2006. Caspase-mediated cleavage of glial fibrillary acidic protein within degenerating astrocytes of the Alzheimer's disease brain. *Am J Pathol,* 168**,** 936-46.

MUCHOWSKI, P. J., VALDEZ, M. M. & CLARK, J. I. 1999. AlphaB-crystallin selectively targets intermediate filament proteins during thermal stress. *Invest Ophthalmol Vis Sci,* 40**,** 951-8.

MURAKAMI, K., KONDO, T., KAWASE, M., LI, Y., SATO, S., CHEN, S. F. & CHAN, P. H. 1998. Mitochondrial susceptibility to oxidative stress exacerbates cerebral infarction that follows permanent focal cerebral ischemia in mutant mice with manganese superoxide dismutase deficiency. *The Journal of neuroscience : the official journal of the Society for Neuroscience,* 18**,** 205-13.

MURUGESAN, R., SANTHOSHKUMAR, P. & SHARMA, K. K. 2008. Role of alphaBI5 and alphaBT162 residues in subunit interaction during oligomerization of alphaB-crystallin. *Mol Vis,* 14**,** 1835-44.

NAKAJIMA, N. & ABE, K. 1995. Genomic structure of the mouse A-type lamin gene locus encoding somatic and germ cell-specific lamins. *FEBS Lett,* 365**,** 108-14.

NIAZI, S. K. 2007. *Handbook of Preformulation. Chemical, Biological and Botanical Drugs*, Informa Healthcare USA.

NICHOLAS, A. P., KING, J. L., SAMBANDAM, T., ECHOLS, J. D., GUPTA, K. B., MCINNIS, C. & WHITAKER, J. N. 2003. Immunohistochemical localization of citrullinated proteins in adult rat brain. *J Comp Neurol,* 459**,** 251-66.

NICHOLL, I. D. & QUINLAN, R. A. 1994. Chaperone activity of alpha-crystallins modulates intermediate filament assembly. *EMBO J,* 13**,** 945-53.

NIELSEN, A. L. & JORGENSEN, A. L. 2004. Self-assembly of the cytoskeletal glial fibrillary acidic protein is inhibited by an isoform-specific C terminus. *J Biol Chem,* 279**,** 41537-45.

NIELSEN, A. L., JORGENSEN, P. & JORGENSEN, A. L. 2002. Mutations associated with a childhood leukodystrophy, Alexander disease, cause deficiency in dimerization of the cytoskeletal protein GFAP. *J Neurogenet,* 16**,** 175-9.

NIEMINEN, M., HENTTINEN, T., MERINEN, M., MARTTILA-ICHIHARA, F., ERIKSSON, J. E. & JALKANEN, S. 2006. Vimentin function in lymphocyte adhesion and transcellular migration. *Nat Cell Biol,* 8**,** 156-62.

NISHIDA, S., HIRUMA, S. & HASHIMOTO, S. 1987. Immunohistochemical change of actin in experimental myocardial ischemia. Its usefulness to detect very early myocardial damages. *Histology and histopathology,* 2**,** 417-28.

NODING, B. & KOSTER, S. 2012. Intermediate filaments in small configuration spaces. *Phys Rev Lett,* 108**,** 088101.

OKADA, M., HATAKEYAMA, T., ITOH, H., TOKUTA, N., TOKUMITSU, H. & KOBAYASHI, R. 2004. S100A1 is a novel molecular chaperone and a member of the Hsp70/Hsp90 multichaperone complex. *The Journal of biological chemistry,* 279**,** 4221-33.

OMARY, M. B. 2009. "IF-pathies": a broad spectrum of intermediate filament-associated diseases. *J Clin Invest,* 119**,** 1756-62.

PALMER, A., XU, J., KUO, S. C. & WIRTZ, D. 1999. Diffusing wave spectroscopy microrheology of actin filament networks. *Biophysical Journal,* 76**,** 1063-71.

PANA, T. L., WANG, P. W., HUANG, C. C., YEH, C. T., HU, T. H. & YU, J. S. 2012. Network analysis and proteomic identification of vimentin as a key regulator associated with invasion and metastasis in human hepatocellular carcinoma cells. *J Proteomics*.

PANKHURST, Q., HAUTOT, D., KHAN, N. & DOBSON, J. 2008. Increased levels of magnetic iron compounds in Alzheimer's disease. *J Alzheimers Dis,* 13**,** 49-52.

PARDO, J. V., D'ANGELO SILICIANO, J. & CRAIG, S. W. 1983. A vinculin-containing cortical lattice in skeletal muscle: Transverse lattice elements ("costameres") mark sites of attachment between myofibrils and sarcolemma. *Proc. Natl. Acad. Sci. USA,* 80**,** 1008-1012.

PARRY, D. A. 1982. Coiled-coils in alpha-helix-containing proteins: analysis of the residue types within the heptad repeat and the use of these data in the prediction of coiled coils in other proteins. *Biosci Rep.,* 2**,** 1017-24.

PARRY, D. A. & STEINERT, P. M. 1995. *Intermediate Filament Structure (molecular Biology Intelligence Unit),* Texas, U.S.A., R.G.Landes Company.

PERMYAKOV, E. & KRETSINGER, R. H. 2011. *Calcium Binding Proteins,* New Jersey, John Wiley and Sons.

PERNG, M. D., CAIRNS, L., VAN DEN, I. P., PRESCOTT, A., HUTCHESON, A. M. & QUINLAN, R. A. 1999a. Intermediate filament interactions can be altered by HSP27 and alphaB-crystallin. *J Cell Sci,* 112 (Pt 13)**,** 2099-112.

PERNG, M. D., MUCHOWSKI, P. J., VAN DEN, I. P., WU, G. J., HUTCHESON, A. M., CLARK, J. I. & QUINLAN, R. A. 1999b. The cardiomyopathy and lens cataract mutation in alphaB-crystallin alters its protein structure, chaperone activity, and interaction with intermediate filaments in vitro. *J Biol Chem,* 274**,** 33235-43.

PERNG, M. D., WEN, S. F., GIBBON, T., MIDDELDORP, J., SLUIJS, J., HOL, E. M. & QUINLAN, R. A. 2008. Glial fibrillary acidic protein filaments can tolerate the incorporation of assembly-compromised GFAP-delta, but with consequences for filament organization and alphaB-crystallin association. *Mol Biol Cell,* 19**,** 4521-33.

PERNG, M. D., WEN, S. F., VAN DEN, I. P., PRESCOTT, A. R. & QUINLAN, R. A. 2004. Desmin aggregate formation by R120G alphaB-crystallin is caused by altered filament interactions and is dependent upon network status in cells. *Mol Biol Cell,* 15**,** 2335-46.

PERNG, M. D., ZHANG, Q. & QUINLAN, R. A. 2007. Insights into the beaded filament of the eye lens. *Exp Cell Res,* 313**,** 2180-8.

PITTENGER, J. T., HESS, J. F. & FITZGERALD, P. G. 2007. Identifying the role of specific motifs in the lens fiber cell specific intermediate filament phakosin. *Invest Ophthalmol Vis Sci,* 48**,** 5132-41.

POULAIN, P., GELLY, J. C. & FLATTERS, D. 2010. Detection and architecture of small heat shock protein monomers. *PLoS One,* 5**,** e9990.

PRABHU, S., RAMAN, B., RAMAKRISHNA, T. & RAO, C. M. 2012. HspB2/myotonic dystrophy protein kinase binding protein (MKBP) as a novel molecular chaperone: structural and functional aspects. *PloS one,* 7**,** e29810.

PREEDY, V. R., WASSIF, W. S., BALDWIN, D., JONES, J., FALKOUS, G., MARWAY, J. S., MANTLE, D. & SCOTT, D. L. 2001. Skeletal muscle protein loss due to D-penicillamine results from reduced protein synthesis. *The international journal of biochemistry & cell biology,* 33**,** 1013-26.

PROCTOR, C. J., PIENAAR, I. S., ELSON, J. & KIRKWOOD, T. B. 2012. Aggregation, impaired degradation and immunization targeting of amyloid-beta dimers in Alzheimer's disease: a stochastic modelling approach. *Mol Neurodegener,* 7**,** 32.

QUINLAN, R. A. & FRANKE, W. W. 1982. Heteropolymer filaments of vimentin and desmin in vascular smooth muscle tissue and cultured baby hamster kidney cells demonstrated by chemical crosslinking. *Proc Natl Acad Sci U S A,* 79**,** 3452-6.

QUINLAN, R. A. & FRANKE, W. W. 1983. Molecular interactions in intermediate-sized filaments revealed by chemical cross-linking. Heteropolymers of vimentin and glial filament protein in cultured human glioma cells. *Eur J Biochem,* 132**,** 477-84.

RADMACHER, M., TILLMANN, R. W. & GAUB, H. E. 1993. Imaging viscoelasticity by force modulation with the atomic force microscope. *Biophysical Journal,* 64**,** 735-42.

RALTON, J. E., LU, X., HUTCHESON, A. M. & QUINLAN, R. A. 1994. Identification of two N-terminal non-alpha-helical domain motifs important in the assembly of glial fibrillary acidic protein. *J Cell Sci,* 107 (Pt 7)**,** 1935-48.

RAMACHANDRAN, R. D., PERUMALSAMY, V. & HEJTMANCIK, J. F. 2007. Autosomal recessive juvenile onset cataract associated with mutation in BFSP1. *Hum Genet,* 121**,** 475-82.

RAVIOL, H., BUKAU, B. & MAYER, M. P. 2006. Human and yeast Hsp110 chaperones exhibit functional differences. *FEBS Lett,* 580**,** 168-74.

ROBINSON, H. W. 1929. The Influence of Neutral Salts on the pH of Phosphate Buffer Mixtures. *J. Biol. Chem.,* 82**,** 775-802.

RODRIGUEZ, D., GAUTHIER, F., BERTINI, E., BUGIANI, M., BRENNER, M., N'GUYEN, S., GOIZET, C., GELOT, A., SURTEES, R., PEDESPAN, J. M., HERNANDORENA, X., TRONCOSO, M., UZIEL, G., MESSING, A., PONSOT, G., PHAM-DINH, D., DAUTIGNY, A. & BOESPFLUG-TANGUY, O. 2001. Infantile Alexander disease: spectrum of GFAP mutations and genotype-phenotype correlation. *Am J Hum Genet,* 69**,** 1134-40.

ROGERS, K. R., MORRIS, C. J. & BLAKE, D. R. 1991. Oxidation of thiol in the vimentin cytoskeleton. *Biochem J,* 275 (Pt 3)**,** 789-91.

SACCONI, S., FEASSON, L., ANTOINE, J. C., PECHEUX, C., BERNARD, R., COBO, A. M., CASARIN, A., SALVIATI, L., DESNUELLE, C. &

URTIZBEREA, A. 2012. A novel CRYAB mutation resulting in multisystemic disease. *Neuromuscul Disord,* 22**,** 66-72.

SAHLGREN, C. M., MIKHAILOV, A., VAITTINEN, S., PALLARI, H.-M., KALIMO, H., PANT, H. C. & ERIKSSON, J. E. 2003. Cdk5 regulates the organization of Nestin and its association with p35. *Molecular and cellular biology,* 23**,** 5090-106.

SAHLGREN, C. M., PALLARI, H. M., HE, T., CHOU, Y. H., GOLDMAN, R. D. & ERIKSSON, J. E. 2006. A nestin scaffold links Cdk5/p35 signaling to oxidant-induced cell death. *EMBO J,* 25**,** 4808-19.

SALIS, A., BILANICOVA, D., NINHAM, B. W. & MONDUZZI, M. 2007. Hofmeister effects in enzymatic activity: weak and strong electrolyte influences on the activity of Candida rugosa lipase. *The journal of physical chemistry B,* 111**,** 1149-56.

SANCHEZ-MORITO, N., PLANELLS, E., ARANDA, P. & LLOPIS, J. 1999. Magnesium-manganese interactions caused by magnesium deficiency in rats. *J Am Coll Nutr,* 18**,** 475-80.

SANDILANDS, A., PRESCOTT, A. R., CARTER, J. M., HUTCHESON, A. M., QUINLAN, R. A., RICHARDS, J. & FITZGERALD, P. G. 1995a. Vimentin and CP49/filensin form distinct networks in the lens which are independently modulated during lens fibre cell differentiation. *J Cell Sci,* 108 (Pt 4)**,** 1397-406.

SANDILANDS, A., PRESCOTT, A. R., HUTCHESON, A. M., QUINLAN, R. A., CASSELMAN, J. T. & FITZGERALD, P. G. 1995b. Filensin is proteolytically processed during lens fiber cell differentiation by multiple independent pathways. *European journal of cell biology,* 67**,** 238-53.

SANDOVAL, I. V., COLACO, C. A. & LAZARIDES, E. 1983. Purification of the intermediate filament-associated protein, synemin, from chicken smooth muscle. Studies on its physicochemical properties, interaction with desmin, and phosphorylation. *The Journal of biological chemistry,* 258**,** 2568-76.

SANTHOSHKUMAR, P., MURUGESAN, R. & SHARMA, K. K. 2009. Deletion of (54)FLRAPSWF(61) residues decreases the oligomeric size and enhances the chaperone function of alphaB-crystallin. *Biochemistry,* 48**,** 5066-73.

SAWADA, K., AGATA, J., EGUCHI, G., QUINLAN, R. & MAISEL, H. 1995. The predicted structure of chick lens CP49 and a variant thereof, CP49ins, the

first vertebrate cytoplasmic intermediate filament protein with a lamin-like insertion in helix 1B. *Curr Eye Res,* 14**,** 545-53.

SCHOPFERER, M., BAR, H., HOCHSTEIN, B., SHARMA, S., MUCKE, N., HERRMANN, H. & WILLENBACHER, N. 2009. Desmin and vimentin intermediate filament networks: their viscoelastic properties investigated by mechanical rheometry. *J Mol Biol,* 388**,** 133-43.

SCHRODER, R., GOUDEAU, B., SIMON, M. C., FISCHER, D., EGGERMANN, T., CLEMEN, C. S., LI, Z., REIMANN, J., XUE, Z., RUDNIK-SCHONEBORN, S., ZERRES, K., VAN DER VEN, P. F., FURST, D. O., KUNZ, W. S. & VICART, P. 2003. On noxious desmin: functional effects of a novel heterozygous desmin insertion mutation on the extrasarcomeric desmin cytoskeleton and mitochondria. *Hum Mol Genet,* 12**,** 657-69.

SELCEN, D., OHNO, K. & ENGEL, A. G. 2004. Myofibrillar myopathy: clinical, morphological and genetic studies in 63 patients. *Brain,* 127**,** 439-51.

SHAH, S. B., DAVIS, J., WEISLEDER, N., KOSTAVASSILI, I., MCCULLOCH, A. D., RALSTON, E., CAPETANAKI, Y. & LIEBER, R. L. 2004. Structural and functional roles of desmin in mouse skeletal muscle during passive deformation. *Biophys J,* 86**,** 2993-3008.

SHAH, S. B., LOVE, J. M., O'NEILL, A., LOVERING, R. M. & BLOCH, R. J. 2012. Influences of desmin and keratin 19 on passive biomechanical properties of mouse skeletal muscle. *J Biomed Biotechnol,* 2012**,** 704061.

SHAMMAS, S. L., WAUDBY, C. A., WANG, S., BUELL, A. K., KNOWLES, T. P., ECROYD, H., WELLAND, M. E., CARVER, J. A., DOBSON, C. M. & MEEHAN, S. 2011. Binding of the molecular chaperone alphaB-crystallin to Abeta amyloid fibrils inhibits fibril elongation. *Biophys J,* 101**,** 1681-9.

SHANKAR, G. M., LI, S., MEHTA, T. H., GARCIA-MUNOZ, A., SHEPARDSON, N. E., SMITH, I., BRETT, F. M., FARRELL, M. A., ROWAN, M. J., LEMERE, C. A., REGAN, C. M., WALSH, D. M., SABATINI, B. L. & SELKOE, D. J. 2008. Amyloid-beta protein dimers isolated directly from Alzheimer's brains impair synaptic plasticity and memory. *Nat Med,* 14**,** 837-42.

SHARMA, S., MUCKE, N., KATUS, H. A., HERRMANN, H. & BAR, H. 2009. Disease mutations in the "head" domain of the extra-sarcomeric protein

desmin distinctly alter its assembly and network-forming properties. *J Mol Med*.

SHARP, G., OSBORN, M. & WEBER, K. 1982. Occurrence of two different intermediate filament proteins in the same filament in situ within a human glioma cell line. An immunoelectron microscopical study. *Experimental cell research,* 141**,** 385-95.

SHAW, G. & HAWKINS, J. 1992. Identification of spinal cord polypeptides related to glial fibrillary acidic protein (GFAP). *Neuroreport,* 3**,** 461-4.

SHAW, G. & HOU, Z. C. 1990. Bundling and cross-linking of intermediate filaments of the nervous system. *J Neurosci Res,* 25**,** 561-8.

SHIIHARA, T., SAWAISHI, Y., ADACHI, M., KATO, M. & HAYASAKA, K. 2004. Asymptomatic hereditary Alexander's disease caused by a novel mutation in GFAP. *J Neurol Sci,* 225**,** 125-7.

SHIN, J. H., JEONG, J. Y., JIN, Y., KIM, I. D. & LEE, J. K. 2011. p38beta MAPK affords cytoprotection against oxidative stress-induced astrocyte apoptosis via induction of alphaB-crystallin and its anti-apoptotic function. *Neurosci Lett,* 501**,** 132-7.

SHIROMA, N., KANAZAWA, N., IZUMI, M., SUGAI, K., FUKUMIZU, M., SASAKI, M., HANAOKA, S., KAGA, M. & TSUJINO, S. 2001. Diagnosis of Alexander disease in a Japanese patient by molecular genetic analysis. *J Hum Genet,* 46**,** 579-82.

SIMMONS, D. A., CASALE, M., ALCON, B., PHAM, N., NARAYAN, N. & LYNCH, G. 2007. Ferritin accumulation in dystrophic microglia is an early event in the development of Huntington's disease. *Glia,* 55**,** 1074-84.

SINGH, B. N., RAO, K. S., RAMAKRISHNA, T., RANGARAJ, N. & RAO CH, M. 2007. Association of alphaB-crystallin, a small heat shock protein, with actin: role in modulating actin filament dynamics in vivo. *J Mol Biol,* 366**,** 756-67.

SMITH, T. A., STRELKOV, S. V., BURKHARD, P., AEBI, U. & PARRY, D. A. 2002. Sequence comparisons of intermediate filament chains: evidence of a unique functional/structural role for coiled-coil segment 1A and linker L1. *J Struct Biol,* 137**,** 128-45.

SOKOLOWSKA, M. & BAL, W. 2005. Cu(II) complexation by "non-coordinating" N-2-hydroxyethylpiperazine-N'-2-ethanesulfonic acid (HEPES buffer). *J Inorg Biochem,* 99**,** 1653-60.

SPINOZZI, F., MARIANI, P., RUSTICHELLI, F., AMENITSCH, H., BENNARDINI, F., MURA, G. M., COI, A. & GANADU, M. L. 2006. Temperature dependence of chaperone-like activity and oligomeric state of alphaB-crystallin. *Biochim Biophys Acta,* 1764**,** 677-87.

SREELAKSHMI, Y. & SHARMA, K. K. 2005. Recognition sequence 2 (residues 60-71) plays a role in oligomerization and exchange dynamics of alphaB-crystallin. *Biochemistry,* 44**,** 12245-52.

SRINIVAS, P. N., REDDY, P. Y. & REDDY, G. B. 2008. Significance of alpha-crystallin heteropolymer with a 3:1 alphaA/alphaB ratio: chaperone-like activity, structure and hydrophobicity. *Biochem J,* 414**,** 453-60.

STEINERT, P. M., CHOU, Y. H., PRAHLAD, V., PARRY, D. A., MAREKOV, L. N., WU, K. C., JANG, S. I. & GOLDMAN, R. D. 1999. A high molecular weight intermediate filament-associated protein in BHK-21 cells is nestin, a type VI intermediate filament protein. Limited co-assembly in vitro to form heteropolymers with type III vimentin and type IV alpha-internexin. *J Biol Chem,* 274**,** 9881-90.

STENGEL, F., BALDWIN, A. J., PAINTER, A. J., JAYA, N., BASHA, E., KAY, L. E., VIERLING, E., ROBINSON, C. V. & BENESCH, J. L. 2010. Quaternary dynamics and plasticity underlie small heat shock protein chaperone function. *Proc Natl Acad Sci U S A,* 107**,** 2007-12.

STERNLICHT, H., FARR, G. W., STERNLICHT, M. L., DRISCOLL, J. K., WILLISON, K. & YAFFE, M. B. 1993. The t-complex polypeptide 1 complex is a chaperonin for tubulin and actin in vivo. *Proc Natl Acad Sci USA.,* 90**,** 9422-6.

STIERLE, V., COUPRIE, J., OSTLUND, C., KRIMM, I., ZINN-JUSTIN, S., HOSSENLOPP, P., WORMAN, H. J., COURVALIN, J. C. & DUBAND-GOULET, I. 2003. The carboxyl-terminal region common to lamins A and C contains a DNA binding domain. *Biochemistry,* 42**,** 4819-28.

STORM, C., PASTORE, J. J., MACKINTOSH, F. C., LUBENSKY, T. C. & JANMEY, P. A. 2005. Nonlinear elasticity in biological gels. *Nature,* 435**,** 191-4.

STOTHARD, P. 2000. *Sequence Manipulation Suite Protein GRAVY* [Online]. Available: http://www.bioinformatics.org/sms2/protein_gravy.html 2012].

STRELKOV, S. V., HERRMANN, H., GEISLER, N., WEDIG, T., ZIMBELMANN, R., AEBI, U. & BURKHARD, P. 2002. Conserved segments 1A and 2B of the intermediate filament dimer: their atomic structures and role in filament assembly. *EMBO J,* 21**,** 1255-66.

STROMER, M. H., RITTER, M. A., PANG, Y. Y. & ROBSON, R. M. 1987. Effect of cations and temperature on kinetics of desmin assembly. *Biochem J,* 246**,** 75-81.

STRYER, L. 1996. *Biochemistry,* New York, W. H. Freeman and Company.

STYERS, M. L., KOWALCZYK, A. P. & FAUNDEZ, V. 2006. Architecture of the vimentin cytoskeleton is modified by perturbation of the GTPase ARF1. *Journal of cell science,* 119**,** 3643-54.

SU, P. H., WANG, T. C., WONG, Z. R., HUANG, B. M. & YANG, H. Y. 2011. The expression of nestin delineates skeletal muscle differentiation in the developing rat esophagus. *J Anat,* 218**,** 311-23.

SUZUKI, Y., KANAZAWA, N., TAKENAKA, J., OKUMURA, A., NEGORO, T. & TSUJINO, S. 2004. A case of infantile Alexander disease with a milder phenotype and a novel GFAP mutation, L90P. *Brain Dev,* 26**,** 206-8.

SWAMY, M. S. & ABRAHAM, E. C. 1991. Reverse-phase HPLC analysis of human alpha crystallin. *Curr Eye Res,* 10**,** 213-20.

SYBERT, V. P., FRANCIS, J. S., CORDEN, L. D., SMITH, L. T., WEAVER, M., STEPHENS, K. & MCLEAN, W. H. 1999. Cyclic ichthyosis with epidermolytic hyperkeratosis: A phenotype conferred by mutations in the 2B domain of keratin K1. *Am J Hum Genet,* 64**,** 732-8.

SZEVERENYI, I., CASSIDY, A. J., CHUNG, C. W., LEE, B. T., COMMON, J. E., OGG, S. C., CHEN, H., SIM, S. Y., GOH, W. L., NG, K. W., SIMPSON, J. A., CHEE, L. L., ENG, G. H., LI, B., LUNNY, D. P., CHUON, D., VENKATESH, A., KHOO, K. H., MCLEAN, W. H., LIM, Y. P. & LANE, E. B. 2008. The Human Intermediate Filament Database: comprehensive information on a gene family involved in many human diseases. *Hum Mutat,* 29**,** 351-60.

TAKEMURA, M., GOMI, H., COLUCCI-GUYON, E. & ITOHARA, S. 2002. Protective role of phosphorylation in turnover of glial fibrillary acidic protein in mice. *J Neurosci,* 22**,** 6972-9.

TANAKA, J., TADA, K., TAKEDA, M., HARIGUCHI, S. & NISHIMURA, T. 1989. Effect of metallic cations and pH on reassembly of glial fibrillary acidic protein. *Neurochem Int,* 15**,** 421-8.

TANG, G., PERNG, M. D., WILK, S., QUINLAN, R. & GOLDMAN, J. E. 2010. Oligomers of mutant glial fibrillary acidic protein (GFAP) Inhibit the proteasome system in alexander disease astrocytes, and the small heat shock protein alphaB-crystallin reverses the inhibition. *J Biol Chem,* 285**,** 10527-37.

TANG, G., XU, Z. & GOLDMAN, J. E. 2006. Synergistic effects of the SAPK/JNK and the proteasome pathway on glial fibrillary acidic protein (GFAP) accumulation in Alexander disease. *J Biol Chem,* 281**,** 38634-43.

TAWK, M., TITEUX, M., FALLET, C., LI, Z., DAUMAS-DUPORT, C., CAVALCANTE, L. A., PAULIN, D. & MOURA-NETO, V. 2003. Synemin expression in developing normal and pathological human retina and lens. *Exp Neurol,* 183**,** 499-507.

TRAUB, P., NELSON, W. J., KUHN, S. & VORGIAS, C. E. 1983. The interaction in vitro of the intermediate filament protein vimentin with naturally occurring RNAs and DNAs. *J Biol Chem,* 258**,** 1456-66.

TSUTSUMI, S., MOLLAPOUR, M., PRODROMOU, C., LEE, C. T., PANARETOU, B., YOSHIDA, S., MAYER, M. P. & NECKERS, L. M. 2012. Charged linker sequence modulates eukaryotic heat shock protein 90 (Hsp90) chaperone activity. *Proc Natl Acad Sci U S A,* 109**,** 2937-42.

VAN BOEKEL, M. A., DE LANGE, F., DE GRIP, W. J. & DE JONG, W. W. 1999. Eye lens alphaA- and alphaB-crystallin: complex stability versus chaperone-like activity. *Biochim Biophys Acta,* 1434**,** 114-23.

VAN MONTFORT, R. L., BASHA, E., FRIEDRICH, K. L., SLINGSBY, C. & VIERLING, E. 2001. Crystal structure and assembly of a eukaryotic small heat shock protein. *Nat Struct Biol,* 8**,** 1025-30.

VARGOVA, L. & SYKOVA, E. 2009. *Astrocytes in (Patho)Physiology of the Nervous System,* New York, Springer.

VEERANNA, AMIN, N. D., AHN, N. G., JAFFE, H., WINTERS, C. A., GRANT, P. & PANT, H. C. 1998. Mitogen-activated protein kinases (Erk1,2) phosphorylate Lys-Ser-Pro (KSP) repeats in neurofilament proteins NF-H and NF-M. *J Neurosci,* 18**,** 4008-21.

VENDELIN, M., BERAUD, N., GUERRERO, K., ANDRIENKO, T., KUZNETSOV, A. V., OLIVARES, J., KAY, L. & SAKS, V. A. 2005. Mitochondrial regular arrangement in muscle cells: a "crystal-like" pattern. *Am J Physiol Cell Physiol,* 288**,** C757-67.

VICART, P., CARON, A., GUICHENEY, P., LI, Z., PREVOST, M. C., FAURE, A., CHATEAU, D., CHAPON, F., TOME, F., DUPRET, J. M., PAULIN, D. & FARDEAU, M. 1998. A missense mutation in the alphaB-crystallin chaperone gene causes a desmin-related myopathy. *Nat Genet,* 20**,** 92-5.

WACHSSTOCK, D. H., SCHWARZ, W. H. & POLLARD, T. D. 1994. Cross-linker dynamics determine the mechanical properties of actin gels. *Biophys J,* 66**,** 801-9.

WAGNER, O. I., LIFSHITZ, J., JANMEY, P. A., LINDEN, M., MCINTOSH, T. K. & LETERRIER, J. F. 2003. Mechanisms of mitochondria-neurofilament interactions. *J Neurosci,* 23**,** 9046-58.

WANG, J., MARTIN, E., GONZALES, V., BORCHELT, D. R. & LEE, M. K. 2008. Differential regulation of small heat shock proteins in transgenic mouse models of neurodegenerative diseases. *Neurobiol Aging,* 29**,** 586-97.

WANG, R., LI, Q. & TANG, D. D. 2006. Role of vimentin in smooth muscle force development. *Am J Physiol Cell Physiol,* 291**,** C483-9.

WANG, Z., OBIDIKE, J. E. & SCHEY, K. L. 2010. Posttranslational modifications of the bovine lens beaded filament proteins filensin and CP49. *Invest Ophthalmol Vis Sci,* 51**,** 1565-74.

WATERS, E. R., LEE, G. J. & VIERLING, E. 1996. Evolution, structure and function of the small heat shock proteins in plants. *J. Exp. Bot.,* 47**,** 325-338.

WEISLEDER, N., SOUMAKA, E., ABBASI, S., TAEGTMEYER, H. & CAPETANAKI, Y. 2004. Cardiomyocyte-specific desmin rescue of desmin null cardiomyopathy excludes vascular involvement. *J Mol Cell Cardiol,* 36**,** 121-8.

WEN, Q. & TANG, J. X. 2006. Temperature effects on threshold counterion concentration to induce aggregation of fd virus. *Physical Review Letters,* 97**,** 048101.

WENDLER, P., SHORTER, J., PLISSON, C., CASHIKAR, A. G., LINDQUIST, S. & SAIBIL, H. R. 2007. Atypical AAA+ subunit packing creates an expanded

cavity for disaggregation by the protein-remodeling factor Hsp104. *Cell,* 131**,** 1366-77.

WESTERMANN, S. & WEBER, K. 2003. Post-translational modifications regulate microtubule function. *Nat Rev Mol Cell Biol,* 4**,** 938-47.

WICKERT, U., MUCKE, N., WEDIG, T., MULLER, S. A., AEBI, U. & HERRMANN, H. 2005. Characterization of the in vitro co-assembly process of the intermediate filament proteins vimentin and desmin: mixed polymers at all stages of assembly. *European journal of cell biology,* 84**,** 379-91.

WILLENBACHER, N. & OELSCHLAEGER, C. 2007. Dynamics and structure of complex fluids from high frequency mechanical and optical rheometry. *Current Opinion in Colloid & Interface Science,* 12**,** 43-49.

XI, J.-H., BAI, F., MCGAHA, R. & ANDLEY, U. P. 2006. Alpha-crystallin expression affects microtubule assembly and prevents their aggregation. *FASEB journal : official publication of the Federation of American Societies for Experimental Biology,* 20**,** 846-57.

YAMANISHI, K., MATSUKI, M., KONISHI, K. & YASUNO, H. 1994. A novel mutation of Leu122 to Phe at a highly conserved hydrophobic residue in the helix initiation motif of keratin 14 in epidermolysis bullosa simplex. *Human molecular genetics,* 3**,** 1171-2.

YANG, H., HUANG, S., DAI, H., GONG, Y., ZHENG, C. & CHANG, Z. 1999. The Mycobacterium tuberculosis small heat shock protein Hsp16.3 exposes hydrophobic surfaces at mild conditions: conformational flexibility and molecular chaperone activity. *Protein science : a publication of the Protein Society,* 8**,** 174-9.

YANG, S. H., CHANG, S. Y., REN, S., WANG, Y., ANDRES, D. A., SPIELMANN, H. P., FONG, L. G. & YOUNG, S. G. 2011. Absence of progeria-like disease phenotypes in knock-in mice expressing a non-farnesylated version of progerin. *Hum Mol Genet,* 20**,** 436-44.

YANG, X., WANG, J., LIU, C., GRIZZLE, W. E., YU, S., ZHANG, S., BARNES, S., KOOPMAN, W. J., MOUNTZ, J. D., KIMBERLY, R. P. & ZHANG, H. G. 2005. Cleavage of p53-vimentin complex enhances tumor necrosis factor-related apoptosis-inducing ligand-mediated apoptosis of rheumatoid arthritis synovial fibroblasts. *Am J Pathol,* 167**,** 705-19.

YANG Z W., K. C. F., AND BABITCH J A. 1988. Characterization and location of divalent cation binding sites in bovine glial fibrillary acidic protein. *Biochemistry,* 27**,** 7045-7050.

YANG, Z. W. & BABITCH, J. A. 1988. Factors modulating filament formation by bovine glial fibrillary acidic protein, the intermediate filament component of astroglial cells. *Biochemistry,* 27**,** 7038-45.

YODER, C. H. 2006. *Ionic Compunds: Applications of Chemistry to Mineralogy,* New Jersey, John Wiley and Sons.

ZANDY, A. J., LAKHANI, S., ZHENG, T., FLAVELL, R. A. & BASSNETT, S. 2005. Role of the executioner caspases during lens development. *J Biol Chem,* 280**,** 30263-72.

ZAR, J. H. 1996. *Biostatistical Analysis,* London, Prentice-Hall International, Inc.

ZEYER, J., KOCHER, H. P. & TIMMIS, K. N. 1986. Influence of para-substituents on the oxidative metabolism of o-nitrophenols by Pseudomonas putida B2. *Appl Environ Microbiol,* 52**,** 334-9.

ZHANG, J., MA, B., DIMAIO, F., DOUGLAS, N. R., JOACHIMIAK, L. A., BAKER, D., FRYDMAN, J., LEVITT, M. & CHIU, W. 2011. Cryo-EM structure of a group II chaperonin in the prehydrolysis ATP-bound state leading to lid closure. *Structure,* 19**,** 633-9.

ZHENG, Y. L., LI, B. S., VEERANNA & PANT, H. C. 2003. Phosphorylation of the head domain of neurofilament protein (NF-M): a factor regulating topographic phosphorylation of NF-M tail domain KSP sites in neurons. *J Biol Chem,* 278**,** 24026-32.

ZOU, P., PINOTSIS, N., LANGE, S., SONG, Y. H., POPOV, A., MAVRIDIS, I., MAYANS, O. M., GAUTEL, M. & WILMANNS, M. 2006. Palindromic assembly of the giant muscle protein titin in the sarcomeric Z-disk. *Nature,* 439**,** 229-33.